X-ray Tomography study on the impact of microstructural defects on the rupture and fatigue properties of a filled elastomer

Muhamed Jesbeer Kallungal Abdul Jaleel

N°d'ordre NNT : 2022LYSEI015

THESE de DOCTORAT DE L'UNIVERSITE DE LYON
opérée au sein de
(l'Institut National des Sciences Appliquées de Lyon)

Ecole Doctorale N° EDA 034
(Matériaux de Lyon)

Spécialité/ discipline de doctorat : Matériaux

Soutenue publiquement/à huis clos le 02/03/2022, par :
Muhamed Jesbeer Kallungal Abdul Jaleel

X-ray Tomography study on the impact of microstructural defects on the rupture and fatigue properties of a filled elastomer

---

Devant le jury composé de :

Castagnet, Sylvie	Directrice de Recherche, CNRS-Université de Poitiers-ISAE ENSMA	Rapportrice
Peuvrel-Disdier, Edith	Chargée de recherche, CNRS MINES ParisTech – PSL	Rapportrice
Marco, Yann	Professeur des Universités, ENSTA Bretagne	Examinateur
Wilde, Fabian	Docteur, PETRA III, Helmholtz-Zentrum Hereon, Hamburg, Germany	Examinateur
Chazeau, Laurent	Professeur des Universités, MATEIS/INSA Lyon	Directeur de thèse
Chenal, Jean-Marc	Professeur des Universités, MATEIS/INSA Lyon	Co-directeur de thèse
Barrès, Claire	Maître de Conférences HDR, IMP/INSA Lyon	Co-encadrante
Selles, Nathan	Docteur, LRCCP	Invité

Département FEDORA – INSA Lyon - Ecoles Doctorales

SIGLE	ECOLE DOCTORALE	NOM ET COORDONNEES DU RESPONSABLE
CHIMIE	**CHIMIE DE LYON** **https://www.edchimie-lyon.fr** Sec. : Renée EL MELHEM Bât. Blaise PASCAL, 3e étage secretariat@edchimie-lyon.fr	**M. Stéphane DANIELE** C2P2-CPE LYON-UMR 5265 Bâtiment F308, BP 2077 43 Boulevard du 11 novembre 1918 69616 Villeurbanne **directeur@edchimie-lyon.fr**
E.E.A.	**ÉLECTRONIQUE, ÉLECTROTECHNIQUE, AUTOMATIQUE** **https://edeea.universite-lyon.fr** Sec. : Stéphanie CAUVIN Bâtiment Direction INSA Lyon Tél : 04.72.43.71.70 secretariat.edeea@insa-lyon.fr	**M. Philippe DELACHARTRE** INSA LYON Laboratoire CREATIS Bâtiment Blaise Pascal, 7 avenue Jean Capelle 69621 Villeurbanne CEDEX Tél : 04.72.43.88.63 **philippe.delachartre@insa-lyon.fr**
E2M2	**ÉVOLUTION, ÉCOSYSTÈME, MICROBIOLOGIE, MODÉLISATION** **http://e2m2.universite-lyon.fr** Sec. : Sylvie ROBERJOT Bât. Atrium, UCB Lyon 1 Tél : 04.72.44.83.62 secretariat.e2m2@univ-lyon1.fr	**M. Philippe NORMAND** Université Claude Bernard Lyon 1 UMR 5557 Lab. d'Ecologie Microbienne Bâtiment Mendel 43, boulevard du 11 Novembre 1918 69 622 Villeurbanne CEDEX **philippe.normand@univ-lyon1.fr**
EDISS	**INTERDISCIPLINAIRE SCIENCES-SANTÉ** **http://ediss.universite-lyon.fr** Sec. : Sylvie ROBERJOT Bât. Atrium, UCB Lyon 1 Tél : 04.72.44.83.62 secretariat.ediss@univ-lyon1.fr	**Mme Sylvie RICARD-BLUM** Institut de Chimie et Biochimie Moléculaires et Supramoléculaires (ICBMS) - UMR 5246 CNRS - Université Lyon 1 Bâtiment Raulin - 2ème étage Nord 43 Boulevard du 11 novembre 1918 69622 Villeurbanne Cedex Tél : +33(0)4 72 44 82 32 **sylvie.ricard-blum@univ-lyon1.fr**
INFOMATHS	**INFORMATIQUE ET MATHÉMATIQUES** **http://edinfomaths.universite-lyon.fr** Sec. : Renée EL MELHEM Bât. Blaise PASCAL, 3e étage Tél : 04.72.43.80.46 infomaths@univ-lyon1.fr	**M. Hamamache KHEDDOUCI** Université Claude Bernard Lyon 1 Bât. Nautibus 43, Boulevard du 11 novembre 1918 69 622 Villeurbanne Cedex France Tél : 04.72.44.83.69 **hamamache.kheddouci@univ-lyon1.fr**
Matériaux	**MATÉRIAUX DE LYON** **http://ed34.universite-lyon.fr** Sec. : Yann DE ORDENANA Tél : 04.72.18.62.44 yann.de-ordenana@ec-lyon.fr	**M. Stéphane BENAYOUN** Ecole Centrale de Lyon Laboratoire LTDS 36 avenue Guy de Collongue 69134 Ecully CEDEX Tél : 04.72.18.64.37 **stephane.benayoun@ec-lyon.fr**
MEGA	**MÉCANIQUE, ÉNERGÉTIQUE, GÉNIE CIVIL, ACOUSTIQUE** **http://edmega.universite-lyon.fr** Sec. : Stéphanie CAUVIN Tél : 04.72.43.71.70 Bâtiment Direction INSA Lyon mega@insa-lyon.fr	**M. Jocelyn BONJOUR** INSA Lyon Laboratoire CETHIL Bâtiment Sadi-Carnot 9, rue de la Physique 69621 Villeurbanne CEDEX **jocelyn.bonjour@insa-lyon.fr**
ScSo	**ScSo*** **https://edsciencessociales.universite-lyon.fr** Sec. : Mélina FAVETON INSA : J.Y. TOUSSAINT Tél : 04.78.69.77.79 melina.faveton@univ-lyon2.fr	**M. Christian MONTES** Université Lumière Lyon 2 86 Rue Pasteur 69365 Lyon CEDEX 07 **christian.montes@univ-lyon2.fr**

*ScSo : Histoire, Géographie, Aménagement, Urbanisme, Archéologie, Science politique, Sociologie, Anthropologie

TABLE OF CONTENTS

Résumé français

Les produits en caoutchouc sont largement utilisés dans de nombreuses applications telles que les pneus, les joints d'étanchéité et les supports antivibratoires. Au fil des ans, leur production a augmenté de manière exponentielle pour répondre à une demande croissante. Ils sont cependant difficiles à recycler ou à réutiliser après leur défaillance. Les déchets de caoutchouc générés par ces applications ont un impact négatif sur l'environnement. Comme solution à court terme à ce problème, on peut améliorer la durée de vie des produits en caoutchouc afin de réduire les déchets qu'ils génèrent.

En général, la durée de vie des produits en caoutchouc est améliorée en ajoutant divers ingrédients à l'élastomère. Les ingrédients généralement utilisés sont des charges de renforcement, des additifs, des agents de réticulation, etc. Le noir de carbone est couramment utilisé pour le renforcement et optimiser les propriétés mécaniques pour diverses applications. La dispersion du noir de carbone dans l'élastomère est un problème important auquel l'industrie est confrontée et qui a été largement étudié au cours des dernières décennies. Elle dépend des paramètres du procédé de mise en œuvre, et de la formulation. Dans les faits, elle est surtout limitée par les coûts de production. Ainsi, les matériaux contiennent généralement des défauts indésirables tels que des agglomérats de noir de carbone (CB_{aggl}) qui peuvent provoquer une défaillance prématurée des produits. Pour éviter de telles défaillances et améliorer la durabilité, l'industrie a besoin de caractériser ces défauts. Cette caractérisation est également nécessaire dans les processus de contrôle qualité de ces produits. Au fil des années, l'industrie a utilisé pour cela de nombreuses techniques de caractérisation facilement disponibles telles que les techniques basées sur la microscopie optique, la microscopie électronique à balayage, etc... Cependant, ces techniques ne fournissent que des informations partielles puisqu'il s'agit principalement de techniques 2D et que la zone de l'échantillon observée est généralement limitée.

Récemment, les industriels ont commencé à explorer l'utilisation de techniques non destructives telles que la tomographie à rayons X en laboratoire pour une meilleure quantification de ces défauts de taille micronique. Ces appareils rencontrent un succès commercial croissant car leurs performances actuelles se rapprochent de celles de la tomographie à rayons X à source synchrotron. Cette technique permet l'observation de nombreux défauts. Néanmoins, jusqu'à présent, l'industrie manque d'une méthodologie appropriée pour quantifier leur concentration, leur morphologie, leur dispersion etc... De plus, elle ne dispose pas non plus d'informations claires sur la relation entre les caractéristiques de ces défauts et la durabilité du matériau. Ceci est lié au peu d'études bibliographiques sur ce sujet

et en particulier sur le lien entre ces caractéristiques et les mécanismes d'initiation et de propagation des fissures lors d'une sollicitation monotone/dynamique. Par conséquent, l'établissement de critères de contrôle qualité pour les produits en caoutchouc tenant compte de manière pertinente des caractéristiques des défauts reste une tâche difficile.

Ainsi, le but de cette thèse est d'abord d'élaborer une méthodologie robuste qui facilite la quantification de la dispersion et des caractéristiques morphologiques des agglomérats de noir de carbone présents dans un élastomère chargé en utilisant la tomographie à rayons X. En outre, cette étude cherche à comprendre comment la présence de ces agglomérats influence les propriétés de rupture et de fatigue du matériau en utilisant la possibilité offerte par la tomographie aux rayons X pour des observations in situ. Ce projet est réalisé en collaboration entre le LRCCP, Vitry-sur seine et le laboratoire MATEIS dans le cadre du CIFRE. Les travaux ont eu lieu dans le groupe "Polymères, verres et matériaux hètérogènes" (PVMH).

Afin d'atteindre le premier objectif, nous avons d'abord optimisé les paramètres de fonctionnement de la tomographie à rayons X en laboratoire pour l'acquisition d'images afin d'étudier efficacement des EPDM chargés au noir de carbone. Il est conseillé d'utiliser une tension de tube plus faible dans la tomographie à rayons X de laboratoire (40 kV) pour améliorer le contraste d'atténuation des défauts comme les CB_{aggl}. Le contraste peut être encore amélioré en appliquant divers algorithmes de traitement d'image. On peut ainsi facilement extraire des images 3D diverses caractéristiques morphologiques, mais certaines de ces caractéristiques peuvent être redondantes. Dans ce cas, des outils de sélection sont nécessaires pour les identifier. Avec les matériaux étudiés, nous avons trouvé que le volume, la structure et l'excentricité (liée au rapport d'aspect ou à l'élongation) peuvent décrire de manière appropriée les CB_{aggl}. Néanmoins, une simple analyse de leur distribution ne fournit pas d'informations claires sur les différences entre les différents matériaux. Pour cette raison, nous avons développé une méthode de classification des CB_{aggl} basée sur leurs trois caractéristiques morphologiques. Cette classification s'est avérée efficace pour distinguer nos matériaux. Dans le cas étudié, elle peut fournir des informations sur l'influence des paramètres de traitement tels que la vitesse du rotor, le protocole d'ajout de CB, etc. sur la morphologie finale des agglomérats. L'application possible de cette méthodologie est l'analyse de la conformité des produits en caoutchouc. Par exemple, elle peut être utilisée pour identifier les défauts indésirables et s'assurer que ceux présents dans les produits se situent dans des niveaux acceptables.

La rupture est la conséquence de l'initiation et de la propagation d'une ou plusieurs fissures à travers toute la section des matériaux. Nous avons étudié des matériaux avec différentes concentrations de CB_{aggl} ; un avec une concentration anormalement élevée de CB_{aggl} et un autre avec une concentration de CB_{aggl} représentative de celles couramment rencontrées dans la production industrielle. Dans les images de tomographie, les CB_{aggl} sont presque invisibles en présence de particules à fort contraste d'atténuation comme le ZnO (D'où le terme d'inclusions non visibles utilisé dans certaines études bibliographiques récentes faisant référence aux CB_{aggl}). Pour éviter ces problèmes, le ZnO a été enlevé des formulations étudiées. Malgré cela, les élastomères contiennent de faibles concentrations (moins de 0,05%) d'inclusions d'oxydes métalliques préexistantes. Nous avons mis en évidence que les CB_{aggl} sont les seuls précurseurs de l'initiation d'une fissure et que la décohésion au pôle de ces inclusions d'oxyde métallique n'initie pas une fissure lors des essais de traction. De plus, les propriétés de rupture (en traction) sont indépendantes de la concentration en CB_{aggl} dans les matériaux que nous avons étudiés. L'observation au cours de la traction in situ sous tomographie aux rayons X à source synchrotron a montré une cavitation à l'intérieur des CB_{aggl} lors de l'étirement. Une dépendance intéressante de type loi puissance a été trouvée entre la contrainte macroscopique au début de la cavitation et le diamètre équivalent des CB_{aggl}. Cette corrélation suggère que ces cavités pourraient avoir été créées par la décohésion à l'interface entre les couches de polymère et d'agrégats qui constituent les agglomérats. Ces cavités se développent pour devenir une fracture interne à l'intérieur de CB_{aggl}. Comme observé dans de nombreux agglomérats, tant que la fracture reste à l'intérieur de ceux-ci, il n'y a pas d'initiation de fissure dans l'échantillon. Pour observer cette initiation, le CBaggl fracturé doit se trouver dans ou à proximité d'une zone à forte contrainte triaxiale. De plus, le CB_{aggl} doit avoir une taille critique supérieure à 40µm. Les autres caractéristiques morphologiques du CB_{aggl}, comme la structure et l'excentricité, ne sont pas aussi critiques que la taille. De plus, la transition de la fracture interne de CB_{aggl} vers une fissure semble être retardée si CB_{aggl} subit des fractures multiples. Tous les matériaux étudiés avec des concentrations variables de CB_{aggl} contiennent ces CB_{aggl} critiques, ce qui explique leurs propriétés de rupture similaires. Ainsi, lors de la transformation du matériau, pour améliorer les propriétés de rupture, il faut s'efforcer d'éliminer les agglomérats ayant cette taille critique plutôt que de réduire la concentration globale d'agglomérats dans le matériau.

Comme attendu, le mécanisme d'initiation des fissures pendant les essais de fatigue reste le même qu'en traction, c'est-à-dire que l'origine de l'initiation des fissures est la rupture des CB_{aggl}. Nous avons étendu notre étude en comparant les CB_{aggl} dans les matériaux modèles avec

ceux d'un matériau industriel dont la formulation contient également de l'huile. La présence de cette huile modifie la morphologie des agglomérats ; ils sont plus gros, moins structurés et plus sphériques (excentricité plus faible). Il s'agit certainement de la conséquence d'un taux de cisaillement réduit au début du mélange en raison d'un module de cisaillement plus faible du polymère gonflé d'huile. Bien qu'il y ait une différence entre la morphologie et les propriétés mécaniques des matériaux industriels et des matériaux modèles, leur mécanisme d'initiation de fissure reste le même (croissance de la fissure/cavitation dans l'agglomérat qui se transforme en fissure dans la matrice). Cependant, les CB_{aggl} des matériaux industriels semblent plus résistants que ceux des matériaux modèles, et nécessitent un plus grand nombre de cycles de fatigue pour être fracturés.

La présence de CB_{aggl} influence la propagation des fissures. Ceci a été observé lors d'un essai classique de propagation de fissure, c'est-à-dire lors de la mesure de la vitesse de propagation de fissure en fonction du taux de restitution d'énergie (G) dans une éprouvette à géométrie de cisaillement pur. En présence de CB_{aggl}, la déformation au voisinage de la pointe de la fissure est plus élevée. Au voisinage de la fissure, soumis à des déformation élevées, les CB_{aggl} subissent une fracture interne (comme discuté précédemment). Ces mécanismes dissipatifs réduisent la vitesse de propagation des fissures pour un G macroscopique donné. Ils sont évidemment plus importants dans les matériaux à forte concentration de CB_{aggl}, et n'ont un impact significatif qu'à G élevé, lorsque le volume fortement déformé en pointe de fissure devient très important. De plus, nous avons observé d'autres mécanismes tels que la déviation/arrêt des fissures par les agglomérats (fracturés ou non) qui augmentent également l'énergie nécessaire à la rupture du matériau.

General introduction

Rubber products are widely used in many applications such as tires, sealants, and anti-vibration mounts. Over the years their production has increased to meet the growing demands. They are however difficult to recycle or reuse after their failure. The rubber waste generated from these applications has a negative impact on the environment. As a short-term solution to this issue, one can improve the service life of the rubber products to reduce the generated waste from them.

In general, the service life of rubber products is improved by adding various ingredients into the elastomer. The ingredients typically used are reinforcing fillers, additives, crosslinking agents etc. Carbon black is commonly used for the reinforcement and optimizing their mechanical properties for various applications. The dispersion of carbon black in elastomer is an important issue facing the industry that has been extensively studied over the past decades. It depends on the process parameters and the chosen formulation. In fact, it is mainly limited by the production costs. Thus, materials usually contain undesirable defects such as carbon black agglomerates (CB_{aggl}) that can cause premature product failures. To avoid such failure and improve the durability, the industry needs to characterize these defects. This characterization is also necessary in the quality control processes of these products. Over the years, the industry has used many easily available characterization techniques such as optical microscopy based techniques, Scanning Electron Microscopy, etc… However, these techniques provide only partial information since they are mostly 2D techniques and the area of the sample that can be observed is generally limited.

Recently, industries have started to explore the use of nondestructive techniques such as X-ray tomography using laboratory sourced for better quantification of these micron-sized defects. These devices have become more and more commercially successful. This technique enables the observation of many defects. Nevertheless, until now, the industry lacks an appropriate methodology to quantify their concentration, morphology, dispersion etc… Moreover, industry does not have clear information on the relationship between these defects characteristics and the material durability. This is related to the incomplete literature studies on this topic and in particular on the link between these characteristics on the crack initiation and propagation mechanisms during monotone/dynamic solicitation. Therefore, establishing relevant quality control benchmarks for rubber products taking into account the defects characteristics remains a challenging task.

Thus, the objective of this thesis is to a build a robust methodology that facilitates quantification of the dispersion and the morphology features of carbon black agglomerates present in a filled elastomer using X-ray Tomography. In addition, this study seeks to

understand how the presence of these agglomerates influences the rupture and fatigue properties of the material using the possibility offered by X-ray Tomography for in situ observations. This project is carried out in collaboration between LRCCP, Vitry-sur seine and MATEIS laboratory under the framework of CIFRE. The work took place in "Polymères, verres et matériaux hètérogènes" (PVMH) group.

In order to attain these objectives, we propose to study model materials containing mostly filler agglomerates as defects. We chose a material based on non-crystallizing Ethylene Propylene Diene Monomer Rubber (EPDM Keltan 4450). It contains 19.3% volume fraction of high furnace Carbon Black (N326) and uses unsupported Bis (α,α-dimethylbenzyl) peroxide for crosslinking. The volume fraction remains the same across all the model materials. We vary the compounding process conditions to modify the degree of CB_{aggl} present inside the materials. We also extend our study by comparing the CB_{aggl} in the model materials with the CB_{aggl} in an industrial compound that contains oil and higher concentration of carbon black. We developed a methodology to quantify the dispersion and morphology of CB_{aggl} in the above mentioned materials. We then conduct various mechanical experiments on these materials to characterize their rupture and fatigue properties. In order to understand the crack mechanisms at the micron scale, we performed various in-situ mechanical tests using laboratory and synchrotron sourced (P05, PETRA, Germany and Anatomix, SOLEIL, France) X-ray Tomography.

The chapter 1 of the thesis presents a state-of-the-art review on the influence of microstructural defects on the rupture and fatigue properties. The chapter is divided into 3 parts. The 1st part discusses the influence of process parameters and ingredients on the formation of defects. 2nd part presents various experimental results on the influence of defects on crack initiation and propagation under monotone and cyclic/dynamic solicitation. The last part aims to summarize the details of the available 2D and 3D characterization techniques used to quantify/observe the defects in the materials and their impact on different crack initiation and propagation mechanisms.

The second chapter provides an exhaustive description on materials formulations along with the processing protocols applied to fabricate them. It also presents the methods and protocols related to all the techniques implemented to characterize the physical properties of these materials. The last part of the chapter on the micro structural characterization describes the details of the used Laboratory and Synchrotron sourced X-ray Tomography instruments. It also gives information on the in-situ experiments protocols used in this thesis.

The rest of the thesis contains the results and discussion. These are divided into 4 chapters written in the form of articles. Due to this style of presentation, some information regarding the

material formulation, methods and protocols is redundant. To simplify the reading of the manuscript, the repeated information is written in italics.

The third chapter: 'Novel methodology for quantitative analysis of agglomerates morphology in elastomer composites based on X-ray Tomography' describes the methodology for quantifying the dispersion and morphology features of CB_{aggl} in a filled elastomer. The chapter provides details of the methodology implemented to identify distinct agglomerates based on their morphology. The chapter also discusses the impact of processing parameters on CB_{aggl} morphology using this methodology.

The fourth chapter: 'Crack propagation in filled elastomers: 3D study of mechanisms involving the filler agglomerates' suggests a new crack propagation mechanism, which takes into account the dissipative behaviour of CB_{aggl} at the crack tip. An in-situ tensile test using synchrotron source X-ray tomography was used to evidence this mechanism. This enables us to understand the influence of CB_{aggl} concentrations on crack propagation in our materials.

The chapter 5: 'Microscopic damage and crack initiation mechanisms during in-situ tensile test in a filled EPDM observed with in situ synchrotron X-ray tomography' aims at studying the crack initiation mechanism in the model materials using synchrotron sourced X-ray tomography. The chapter presents a 3D visualization of crack initiation chronology in a filled material during a tensile test along with the description of the critical morphological parameters.

The 6^{th} chapter talks about the fatigue properties of the material. This chapter follows the similar methodology presented in chapter 5. The objective of this chapter is to understand the role of CB_{aggl} in crack initiation during fatigue solicitation. This chapter also presents a comparative study on the influence CB_{aggl} on the crack initiation mechanisms in our model materials and an industrial formulation containing oil.

A general conclusion recapitulates all the main results of the aforementioned chapters. This chapter provides various insights by linking the results of all the chapters. Finally, we present possible future works to improve and to bring more insights on this thesis work in the perspective section.

CHAPTER 1

Literature review: Impact of microstructural defects on mechanical properties of a filled elastomer

TABLE OF CONTENTS

1 INTRODUCTION

The aim of this chapter is to revisit the bibliography on mechanisms and modeling approaches of fatigue and rupture in filled elastomers. The focus is put on the impact of "microstructural defects" or "flaws". The first section is devoted to the mechanisms of formation of these defects during material processing. A second section describes their impact on the mechanical properties during monotonic and cyclic uniaxial solicitations. The third section presents a state of the art on the various techniques available to observe, characterize and quantify these defects. Some of the information delivered in this chapter are already published in our recent review article "About the Influence of Materials Parameters on the Ultimate and Fatigue Properties of Elastomers"[1] (attached in Appendix 1).

2 HOW ARE MICROSTRUCTURAL DEFECTS FORMED?

2.1 Generalities

Elastomers are used in many applications such as tires, sealants, and anti-vibration. In these applications, they can undergo static or dynamic strain solicitations which reduce their durability. The optimization of their properties requires addition of many ingredients in the pristine polymers. Typical ingredients used in industrial grade rubber composites include elastomers (for instance, natural rubber: NR, ethylene propylene diene monomer rubber: EPDM, or styrene butadiene rubber: SBR), reinforcing fillers (such as carbon black, silica, clay), processing aids (paraffin wax, oils etc...), crosslinking agents (usually sulphur or peroxide type), cure activators (like ZnO and stearic acid) and accelerators for crosslinking reactions (based on sulfonamides, thiazole or dithiocarbamate etc.).

The mixing process of all these ingredients involves different steps. The first one requires an internal mixer, in which all the ingredients except the curing agents are added. The mix is further introduced into a two roll mill machine along with vulcanizing agents. The final step is curing of the material after forming by extrusion or compression or injection molding. Typically, four types of microstructural defects can be formed: filler agglomerates, metallic oxides inclusions, micro-bubbles or voids, and molding joints. For example, after curing, unreacted ZnO inclusions remain in the rubber compound as confirmed through SEM or X-ray Tomography measurements[2–4]. In addition to ZnO, other metallic oxides can be found in rubber compounds, e.g: $CaCO_3$, $Al(OH)_3$[2,5,6]. They are due to impurities already in the

elastomer or are introduced as supporting fillers to support peroxide molecules (when they are used for curing instead of sulphur)[7].

The concentration of all these defects depends on the various processing parameters and on the chosen formulation[8–11]. This is described in the following.

2.2 Processing parameters

Inorganic fillers like carbon black (CB) or silica exist in the form of pellets or granules with sizes ranging from 100µm to 2mm [12,13] before their introduction into the internal mixer. After this introduction, they are subdivided into big agglomerates, before their incorporation into the polymers[14–16] (Figure 1, 2). The time required for the wetting of the fillers by the polymer chain is short compared to the one needed for their subsequent dispersion into the polymer matrix. Agglomerate rupture occurs during the initial dispersion step[12,13,17] [18]. The rupture mechanism can be summarized as brutal breaking of agglomerates, when $F_h/F_{coh} \geq 1$, where F_h is the hydrodynamic drag forces applied on the filler (due to shearing of the material, i.e. polymer matrix + ingredients, in the internal mixer) and F_{coh} is the cohesive force between the aggregates inside the agglomerates[18,19]. This mechanism depends on the agglomerate size and is not influenced by the aggregate's characteristics[10]. As the agglomerate size reduces, its cohesive strength becomes stronger than F_h and rupture becomes more difficult. Then, erosion mechanism becomes prevalent. This erosion occurs by detaching small clusters of aggregates or small agglomerates from its surface. The shear stress required for erosion is low compared to rupture mechanism. The erosion mechanism could be by either “onion” or “ribbon” peeling depending on matrix viscosity (Figure 3). The matrix viscosity influences the impregnation of the elastomer chains into the agglomerates[17]. The volume eroded from the agglomerate surface during erosion can be described by $R_0^3 - R_t^3 = \alpha(\tau - \tau_c)\dot{\gamma}t$ [10,12,18,20], where t is the mixing time, $\dot{\gamma}$ the shear rate, τ the shear stress and α the erosion efficiency which depends on the characteristics of the carbon black. R_0 and R_t are the sizes of the agglomerate at time $t = 0$ and t respectively.

Thus, the efficiency of dispersion through these mechanisms (rupture and erosion mechanism) can be improved by varying different processing parameters, such as the rotor speed[8] (influencing the shear rate), the rotor type (e.g. Banbury or tangential rotor)[21], the filling ratio (% of the free volume in the mixer occupied by the ingredients)[8] etc… and of course, the mixing time[17]. In any case, there will always remain a certain fraction of

agglomerates that is not transformed into aggregates (Figure 2) at the end of the process, especially in industrial production.

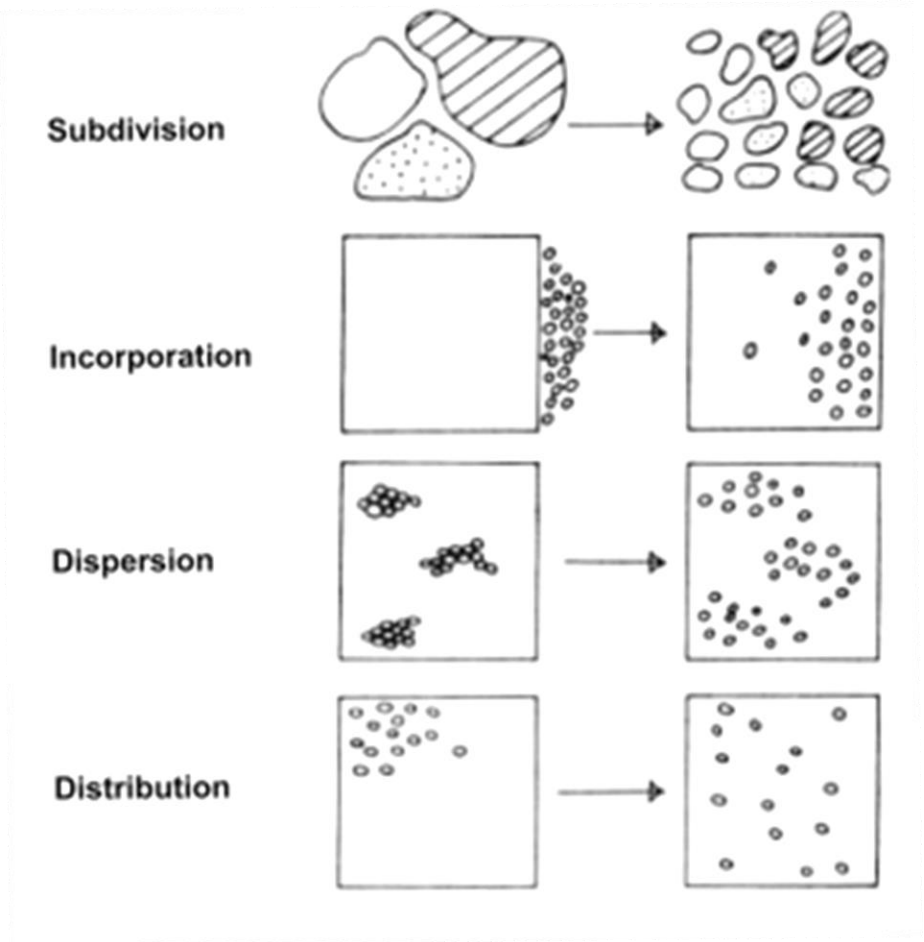

Figure 1 : Illustration of various steps of fillers dispersion [21]

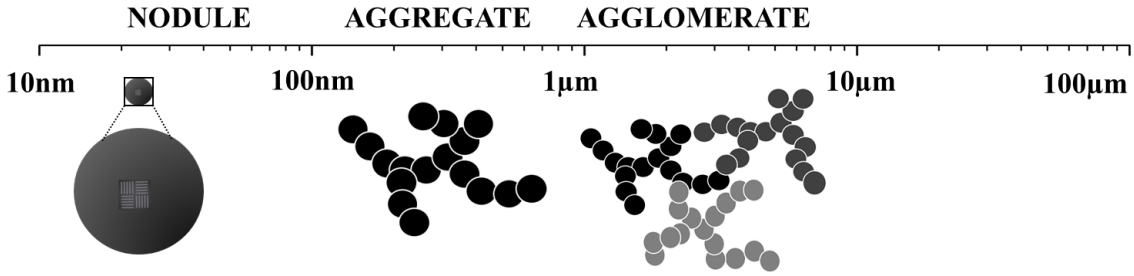

Figure 2: Illustration of carbon clack filler states that can exist inside a material. Aggregates of CB are indivisible structures and are the effective reinforcing and smallest entities that can be found in a polymeric material.

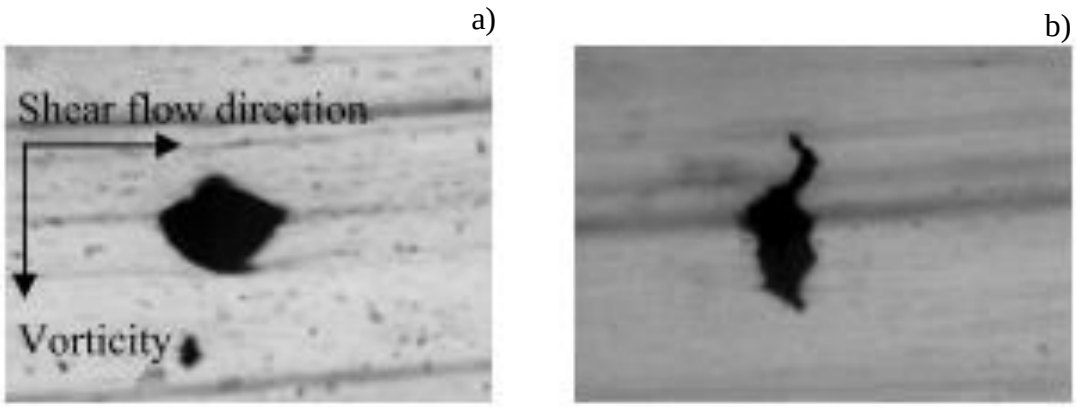

Figure 3: Erosion of filler agglomerates in Butadiene Rubber a) “Onion peeling mechanism”: small particles are detached from the agglomerate surface and they form a dark cloud around it, b) “Ribbon pealing mechanism”: detachment of particles in the form of ribbon [17].

After the internal mixer step, the material is further introduced into a two roll mill machine, along with vulcanizing agents required for curing. The machine is kept at a lower temperature so that the curatives are not activated during the process. The duration and the number of loading passes through the gap influence the dispersion and the distribution of the ingredients. Curing is carried out at high temperature (typically above 130°C) after that the final shape has been given to the product. The cure time of the material is estimated from the torque measurements in a Monsanto rheometer. In the case of compression or injection molding, mold geometry[22] and imperfections can create defects on the surface of the samples. In addition, microbubbles or voids can be trapped inside the cured material due to improper evacuation of the air or insufficient amount of material available for the molding process[23].

2.3 Influence of formulation

Variations in formulation can promote or reduce the dispersion quality of the different ingredients during compounding. E.g. polymer chains with high molecular weight can improve dispersion [14] as they increase the material viscosity and therefore generate higher shear stress during mixing. On the other hand, oil is a typical ingredient used for improving the processability of the compounds, by reducing the shear stress. However, depending on the elastomer matrix, processing parameters (addition of the oil along with the CB or after in the internal mixer, shearing time before this addition, shearing energy etc…), presence of oil can result in a good or bad dispersion of the filler in the matrix[8].

The characteristics of CB aggregates obviously have a strong influence on the quality of their dispersion. As mentioned earlier, the rupture mechanisms of the initial agglomerates are

not significantly influenced by the specific surface area or structure of the aggregates[10], unlike the erosion mechanisms. Thus, the erosion efficiency is given by $= A * \sqrt{CTAB} + B * DBP/\sqrt{CTAB}$, where CTAB is the specific area (cm^2/g) and DBP (in cm^3/g) is an indication of the aggregate structure and roughly corresponds to the voids available in a given weight of filler. Thus, higher structure promotes the efficiency of the dispersion, from agglomerates to aggregates.

2.4 Conclusion

The existence of defects is inevitable in rubber compounds, especially in industrial production. Different process parameters and ingredients influence their concentration in the materials. These defects affect the mechanical properties, particularly the rupture and fatigue properties. These are discussed in detail in the next section.

3 IMPACT OF MICROSTRUCTURAL DEFECTS ON RUPTURE AND FATIGUE PROPERTIES

From a general point of view, fatigue and rupture involve initiation and eventual propagation of one or more cracks over the entire section of a material. These mechanisms can occur under constant, monotonic, or cyclic loading or under a combination of these three. Here, a consolidation of experimental evidence on the impact of defects on crack initiation and propagation under monotone and cyclic/dynamic solicitation is presented.

3.1 Crack initiation

The definition of crack initiation depends on the scale at which crack mechanism is evaluated. E.g., crack initiation may be considered as the appearance of crack on the surface of a specimen at the macroscale. Crack initiation can also be identified at the microscale as the appearance of cavitation of pre-existing voids or as debonding from an inclusion or as cavitation at the poles of agglomerates or as breaking of agglomerates. Note that these different mechanisms do not necessarily lead to rupture. The defects from which the initiated crack leads to rupture are said to be critical.

Various sample geometries are used for characterizing crack initiation such as pancake[24,25], dogbone[26], diabolo[27], AE2[28] etc. Pancake and dogbone geometries are typically used for tensile tests whereas AE2 or diabolo geometries are mostly employed for fatigue tests. The samples can be observed post mortem, i.e. after rupture, or during deformation

using SEM[2,27,28] or X-ray Tomography [3,24,26,29]. Two kinds of solicitation can be explored: monotonic (e.g. tensile test) or dynamic (fatigue test) solicitation.

3.1.1 Monotonic solicitation (Tensile test)

Cavitation of pre-existing voids was first shown by Gent *et al.* [25] using a pancake specimen of a filled Natural rubber. Later on, many studies have shown similar phenomena for different elastomers [30–33]. When the critical hydrostatic pressure inside the voids reaches a constant value of $5E/6$, there is an onset of cavitation due to elastic instability. Gent and Tompkins [34] have shown that this is valid for micro cavities bigger than 100nm (Figure 4).

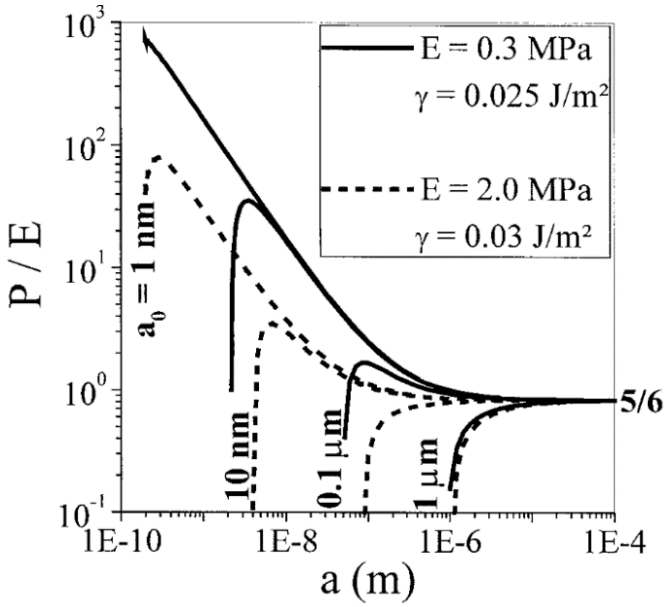

Figure 4: Ratio of hydrostatic pressure P over Young's Modulus E to evaluate the onset of cavitation by taking into account the surface tension. a is the size of the cavities[35] .

Cavitation was also observed with other specimen geometries. For instance, Oberth *et al.*[36] observed cavitation at the poles of spherical defect in a polyurethane matrix in a stretched tensile specimen. In 1984, Gent *et al.*[37] discussed the impact of micro-structural defect diameter and surface characteristics on cavitation under tensile loading, by using treated and untreated glass beads in PDMS (cf Figure 5). Inclusion in a polymer under a critical stress leads to the formation of cavity near its poles, provided it has good surface adhesion with the polymer (Figure 5a). For this particular case of spherical inclusion, the onset stress for cavitation can be written empirically as $t_c = A * E + B * d^{-1/2}$[32,37], where $A * E$ represents the elastic resistance to the unstable growth of pre-existing spherical voids under a triaxial tension, *d* the diameter of the inclusion, and *B* a constant. For a very large inclusion, the equation

reduces to $t_c = 5E/12$, i.e. as expected, half of the critical hydrostatic pressure for cavitation onset. If the inclusion diameter is small, the 2nd term in the equation becomes predominant, i.e. the cavitation stress becomes proportional to $d^{-0.5}$. t_c is smaller for an inclusion with prolate shape oriented parallel to the sollicitation axis compared to an oblate shaped inclusion oriented perpendicular to the solliciation axis[2] (Figure 6). t_c is reduced when there is another inclusion in the close vicinity (Figure 5b).

On the other hand, if there is no adhesion between the polymer and the spherical inclusion, there will be debonding at its poles as shown in Figure 5c. To deduce the criterion for debonding, it was assumed that stored strain energy is lost when a small circular portion of inclusion is debonded from the matrix at the pole in the direction of applied stress. The debonded area will grow if the reduction of this energy is greater than the one required for debonding. Thus, a criterion was developed, $\sigma_a^2 = 8\pi G_a E/3kr \sin 2\theta$. E is Young's modulus, k a numerical constant , r the radius of the inclusion, 2θ the angle subtended by a hypothetical initial debonded zone on the inclusions pole and G_a is the bond fracture energy per unit area of bonded surface (which is lower than the cohesive fracture energy of the inclusion). Note that at a scale below, under uniaxial strain, nano-cavitation has also been observed in the vicinity of the interface between filler aggregates and matrix (Figure 7)[38–40]. These filler aggregates are not considered as defects, however they can also influence the crack initiation mechanism.

In case of industrial compounds, which contain many different defects, there can be additional mechanisms. For instance, formation of cavities due to fracture of silica agglomerates was observed by X-ray tomography during a tensile test (Mullins test) of a silica-filled SBR material[26]. Similar studies for carbon black-based compounds are not available in literature. Moreover, the dependence of crack initiation mechanism on the defects morphology has not been experimentally observed in tensile test.

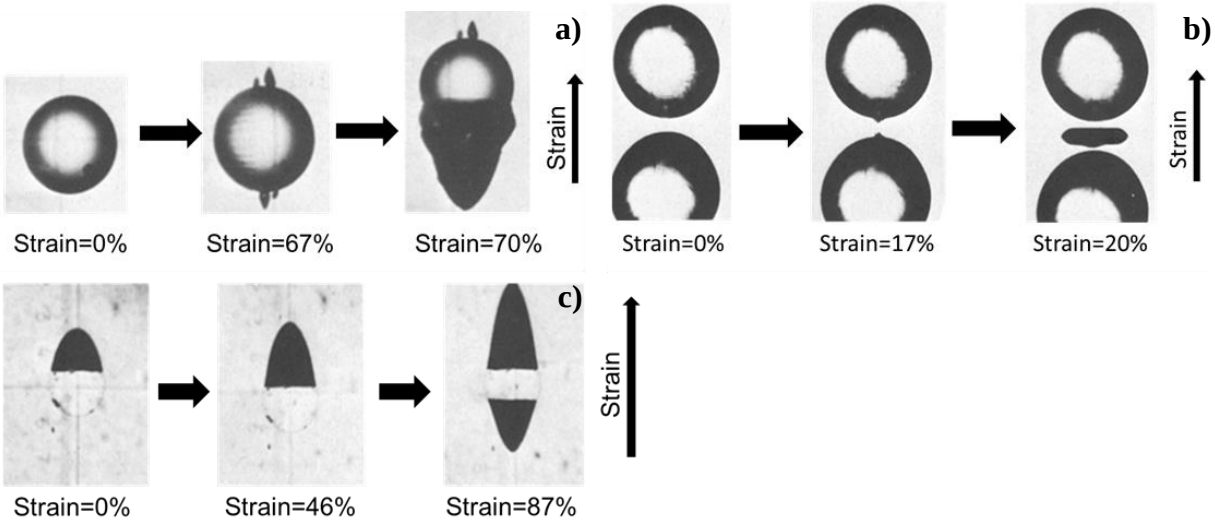

Figure 5: a) Cavitation near to the surface of an inclusion with good adhesion with the matrix, b) cavitation between two inclusions, c) debonding at the pole of the spherical inclusion when there is no adhesion between the inclusion and the matrix[37].

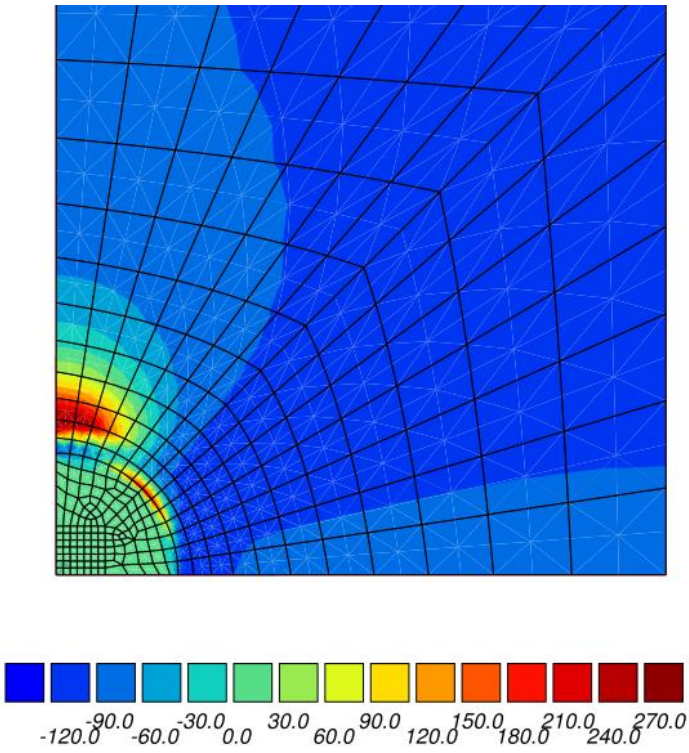

Figure 6: Stress profile in an elastomer with an inclusion which shows the triaxial stress concentration at the pole of the inclusion where there could be a potential cavitation[2].

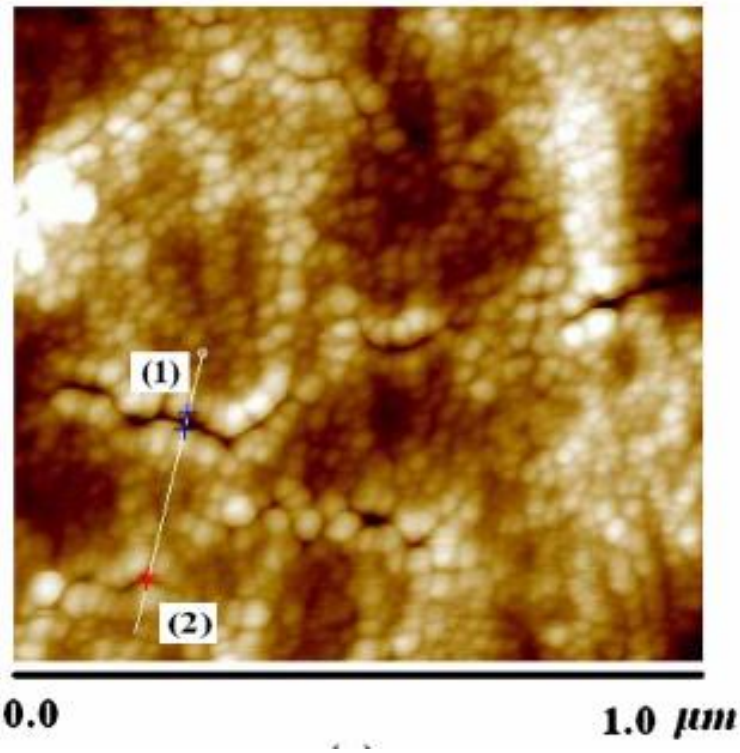

Figure 7: Crack propagation through polymer matrix along the interface between carbon black aggregates and polymer in a stretched sample[41].

3.1.2 Dynamic solicitation (Fatigue test)

Crack initiation studies in filled elastomer have been much more explored during fatigue tests than during tensile tests. Early studies have demonstrated the need for considering microstructural defects, like those of Gent and Lake[42–44] who assimilated the size of the defects with the size of a notch in the model describing the crack propagation rate. Applying this model to experimental results, it was deduced for an unfilled, non-crystallizing, vulcanized rubber that the fatigue properties are controlled by defects whose size is around 56μm. Similarly, for rubber compounds reinforced with carbon black, this size was found out to be ranging from 3 to 52μm, depending on the filler characteristics[45]. It was confirmed using a magnified photo of failed test piece that crack initiated from carbon black agglomerates. Similarly, SEM-based investigations on filled polymer compounds[2,22,46,47] under fatigue loading, after their failure or after a pre-determined number of fatigue cycles, also pointed out the existence of defects at the initiation sites of cracks[22]. For CB-filled rubber, it was deduced that the minimum size required to initiate the debonding around an agglomerate is 5.1μm in a fatigue test with 100% strain cycle (Figure 8a). Under similar condition, the size of an agglomerate for which a surrounding cavity could become a crack is 41μm, and this could happen as soon as 20% of the life duration is reached. These studies also showed that defects

such as ZnO inclusions can initiate debonding at their pole (Figure 8b, c). Cracks initiated by agglomerates appear to be more critical than cracks initiated at the ZnO inclusions[22,48]. Other inclusions like Al(OH)3 can also become precursor for crack initiation as demonstrated by Le Cam *et al.*[6]. Crack initiation also occurs at the fragile zones in the specimen (Figure 8d, e), e.g. the molding line in the diabolo specimen geometry[22].

The lifetime of the material can be correlated to the size of the critical defect (Figure 9) [27,28]. However, it is assumed that the critical defect found at the initiating site is the biggest defect found in the material, which might not always be the case. Other parameters must also be considered such the location in the sample, the internal properties of the defects[27] etc.. The mechanism of crack initiation is also influenced by the type of the elastomer, e.g. SBR vs natural rubber. Several studies show that for Natural rubber, crack propagates from multiple initiating sites, whereas for synthetic rubber, rupture is due to propagation from a single critical defect. This difference is due to the strain crystallization which can occur in NR.

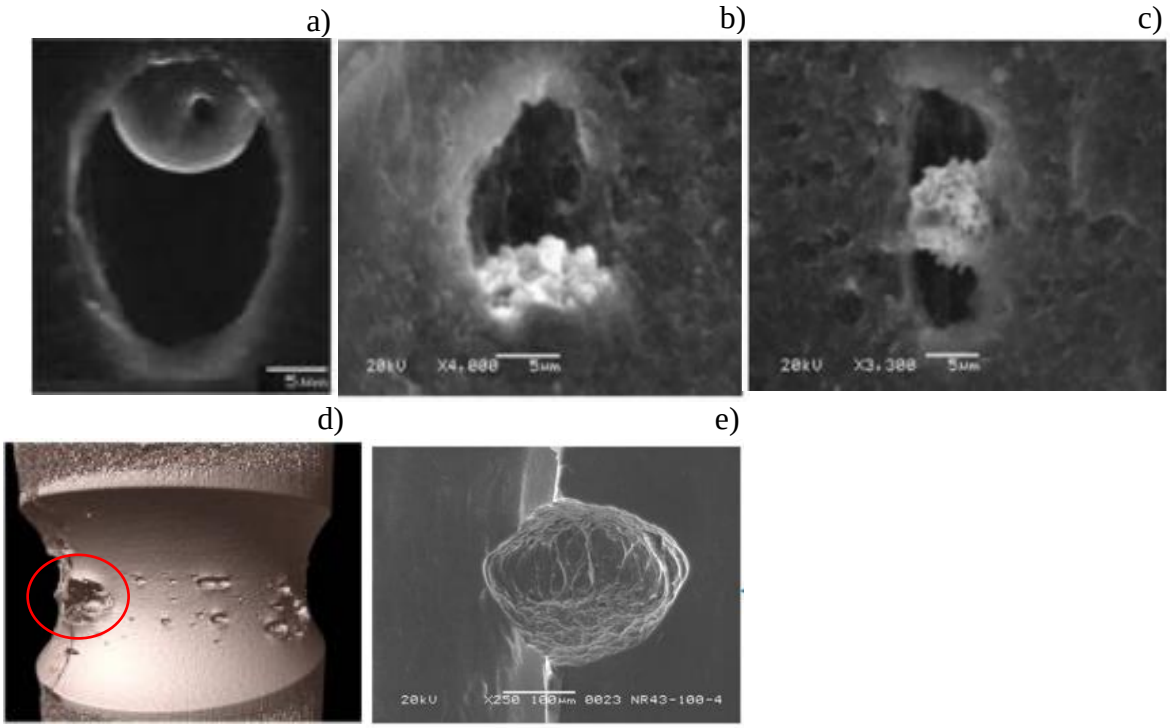

Figure 8: a) Cavitation around filler agglomerates, b) and c) debonding around ZnO inclusion, d) multiple crack initiations in an NR diabolo sample specimen at the molding line, e) Crack initiation at the molding line observed by SEM [22,48].

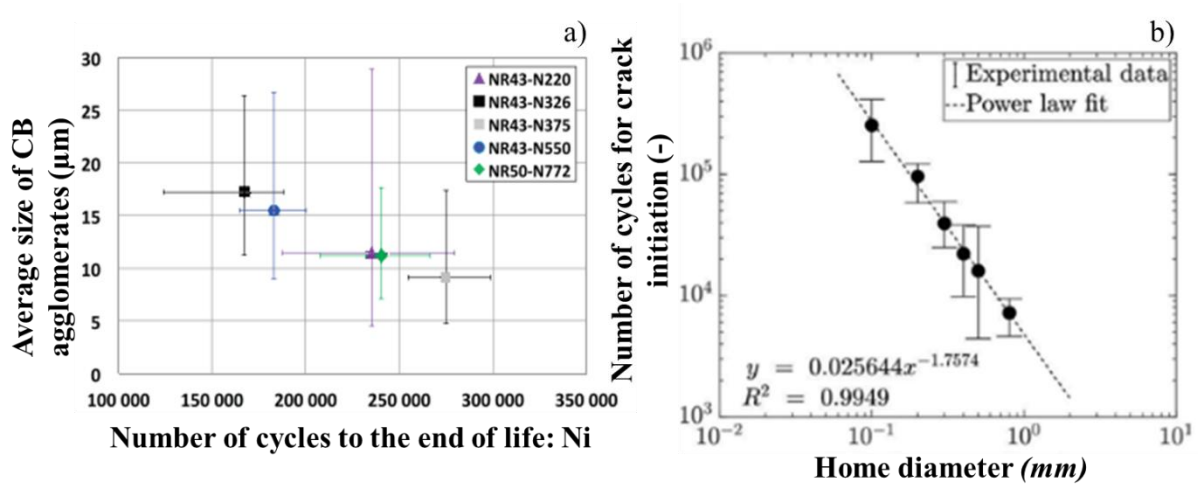

Figure 9: a) End of life of a filled NR material as a function of the CB_{aggl} size at 100% strain, for different types of CB, b) correlation between number of cycles for crack initiation and size of the artificial defect in a pure shear geometry specimen of filled EPDM[27,48].

3.2 Crack propagation (*extract from* [1])

In many cases, crack initiation(s) is not considered as the mechanism which dictates the lifetime. Thus, many works have been rather devoted to crack propagation. Different experimental protocols and specimen geometries can be used (the most commonly used geometries are pure shear, trouser, and tensile test-pieces). This can make comparison and generalisation of the results difficult. The test-piece can be strained, at a constant load force and then the crack propagation velocity Vp(t) can be measured. The trouser test-piece is the most suitable geometry for this so-called crack growth tests since the stretch of the two legs can be directly related to the crack propagation velocity[42]. Things are less straightforward on notched pure shear (PS) geometry or tensile specimens. In this case, the estimate of the propagation velocity requires a direct measurement of the crack length as a function of time. “Static cut growth test” corresponds to the measurement of the crack propagation velocity after a cut is made in a statically strained PS specimen. In the so called “fatigue crack growth tests”, the notched test-piece is subjected to a cyclic loading, controlled by deformation or stress, with or without polarization. (i.e. with or without complete unloading). The stabilised propagation rate is then measured per cycle[43] for different loading levels. Such protocols are built to mimic the conditions encountered in numerous applications, where loading levels are relatively low. In these applications, the load frequencies are often significantly higher than 1 Hz. This can lead to a significant rise in temperature of the material. To avoid this, or to at least limit it, haversine type loading conditions are often used. The term "stabilized" is important: indeed, faster propagation is generally observed during the first cycles, and the crack growth rate

decreases more or less rapidly towards a “stabilized” value. This is ascribed to the modification of the crack geometry (initially created from a razor cut), and of the mechanical properties of the material in its vicinity.

Irrespective of the type of solicitation applied (static, monotonic or cyclic), these experiments enable to relate Vp, expressed per time unit (for instance in static crack growth experiment) or per number of cycles (in fatigue crack growth tests) to a strain energy release rate G. G is defined as the variation of potential energy in the specimen per created crack area. Note that G is noted T (for tearing energy) in many articles. The resulting Vp(G) curve is indeed considered to be independent of the geometry[43,49], at least for those commonly used [50], if certain conditions of the geometries are fulfilled[51]. Using a Pure Shear (PS) geometry of initial height h_0 submitted to a stretching λ, G associated with the propagation of a crack of length c, is the product of $W(\lambda)$ by h_0, where $W(\lambda)$ is the strain energy density of the unnotched PS test piece submitted to the same stretching[50,52,53]. For a tensile strip geometry, the expression becomes $2kW(\lambda)c$, k being a parameter depending smoothly on λ[54,55]. In the case of an elastic material, $W(\lambda)$ simply is the area under the loading curve of the unnotched test piece, and G is then the stored elastic energy. The estimate is less trivial for viscoelastic materials, or when the mechanical behaviour irreversibly depends - over the time scale of the cycles and/or of the crack propagation - on the maximum loading (as it is the case in filled elastomers due to the Mullins effect). In fatigue crack growth, depending on the authors, $W(\lambda)$ will then be estimated from the area under the loading, or the unloading curve of the material, over a stabilized cycle, and will thus include, or not, the energy dissipated during the cycle (this having important consequences on the interpretation of the Vp(G) curves)[56].

$V_p(G)$ curves (or the reverse, $G(V_p)$ curves) from non-cyclic crack growth tests are found in literature with crack propagation rates which can extend over ten decades (Figure 10)[57]. The authors estimate a tearing energy G_t (with a significant error bar), akin to G_c, when Vp reaches several m/s. In the lower or higher velocity domains, the breaking surfaces are rough and smooth respectively, and the velocity is approximatively or completely stable, while stick-slip occurs in the transition domain[58,59]. These different behaviors are related to the ability of material to blunt the crack tip by cavitation[60]. This mechanism involving the viscoelastic response of the material, may or may not have the time to occur, depending on the propagation velocity[61]. The width of the transition domain decreases with the increase in the material crosslinking density. Note that the unstable stick-slip process may also result from a non-uniform temperature in the crack vicinity, that interacts with the local viscoelasticity of the

material[56]. Below G_t, two different domains can be distinguished : for G above a value named G_0, V_p roughly varies with a power law of G. Below G_0, an extremely low crack propagation rate is observed, independent of G, solely originating from a chemical degradation of the material at the crack tip[62]. G(V_p,T) data obeys the same time-temperature equivalence as dynamic moduli and makes possible the construction of a master curve over a very large domain. Incidentally, T and V_p being given, G grows with the loss modulus. G_0 has therefore to be estimated when the viscoelastic effects are minimized. The reduction of the dissipation zone can be obtained by pushing an ultra-sharp blade into the open crack. This inspired a new efficient protocol to rapidly evaluate G_0[63,64]. Values are found between 20 and 100 J/m^2 [65–69]. According to Lake and Thomas[70], they correspond to the breaking energy of the chains that cross the fracture plane. When a bond breaks, the entire chain between crosslinks relaxes to zero load, making the energy dissipation proportional to the number of Kuhn segments (N) between the crosslinks. Recent studies however suggest that chains rupturing out of the fracture plane are also involved in the fracture energy[71]. Despite its simplifying assumption (perfect network without entanglement), the Lake-Thomas model predicts the right order of magnitude for G_0 in unfilled amorphous polymers and the observed dependence of G_0 on $N^{-1/2}$.

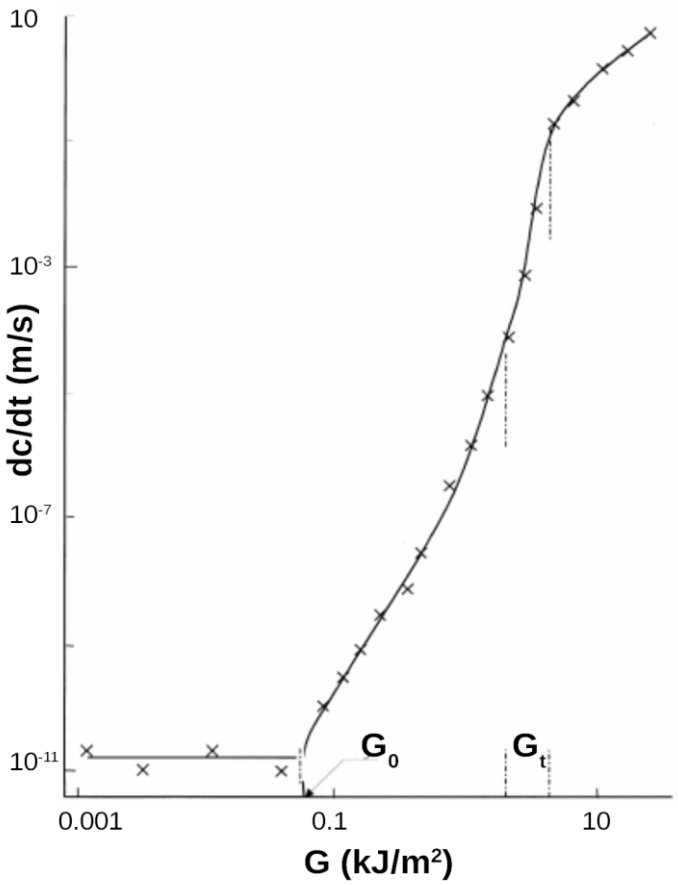

Figure 10: Crack growth velocity (dc/dt) as a function of the strain energy release rate G for Styrene Butadiene Rubber. G_0 is the threshold energy for mechanical crack growth and G_t indicates the transition region [30].

Regarding fatigue crack growth tests, the curves are generally given as dc/dn (i.e. the crack growth per cycle) versus G[72]. They have a typical shape, similar to those observed for other classes of materials[44] (Figure 11). Like in static crack growth, three domains are identified. For G values lower than G_0 (same meaning as in static), crack propagation is again ascribed to chemical degradation processes. Then one observes a transition on a restricted domain of G, where the $V_p(G)$ curve increases, usually according to a linear law. For higher G, dc/dn follows a Paris type law[73], i.e. dc/dn is equal to $A \cdot G^{\beta}$ where A and β are material parameters. Finally, beyond a certain critical value G_c, the crack propagates in a catastrophic way, causing the sample rupture within few cycles. A detailed review on the impact of various parameters (Tg effect, filled or unfilled system, temperature effect, different elastomers etc…) on the crack propagation resistance can be found in our recently published review (Appendix 1).

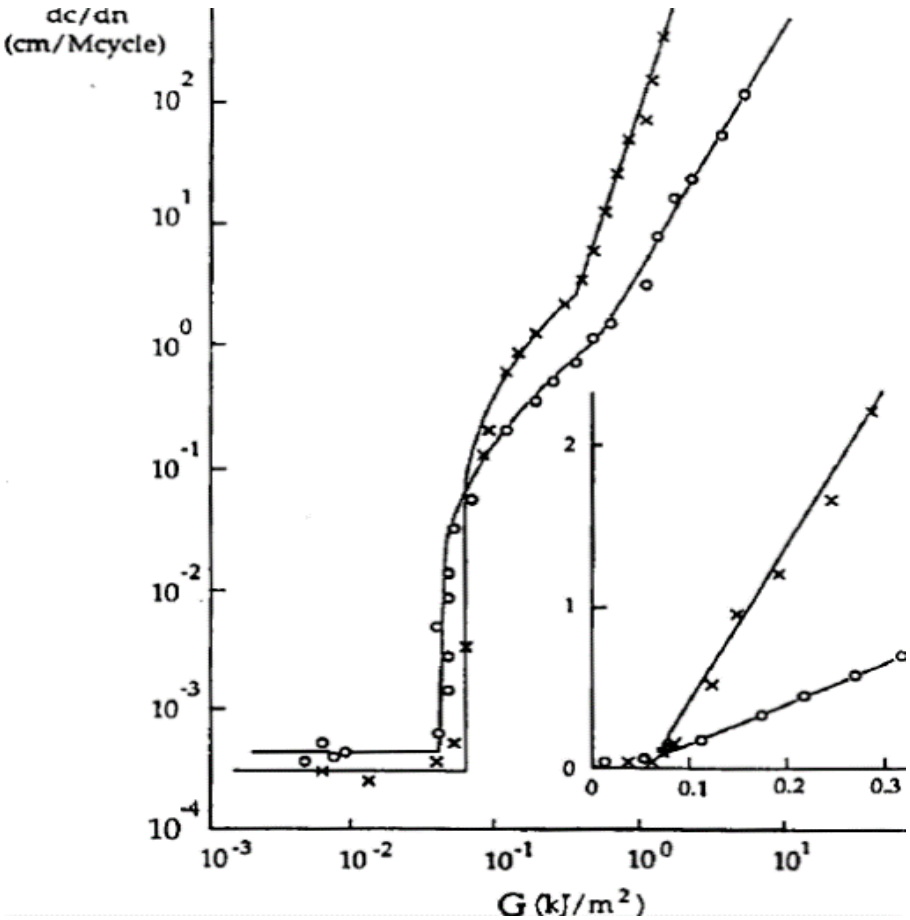

Figure 11: Crack propagation rate as a function of the maximum energy release rate G in fatigue crack growth test for unfilled Styrene Butadiene Rubber (x) and Natural Rubber (o) [74].

3.2.1 Impact of defects on the crack propagation path

By performing postmortem analysis using electron microscopy, the presence of defects like ZnO (Figure 12a, b), carbon black agglomerates (CB_{aggl}), and cavities was observed in the crack vicinity[2,46,75–77]. One mechanism of crack propagation involves cavities: the crack advances by breaking the ligaments between the crack tip and the cavities in front of it. These cavities can be formed at the poles of defects, given the high hydrostatic stress they undergo (Figure 12c). In case of filled elastomers, improvement in the crack propagation resistance is ascribed to the ability of the filler to deviate or arrest the crack[78]. Crack can follow the contours of the fillers, and are therefore deviated, increasing the crack path length[79]. The same mechanisms are suspected for filler agglomerates, but they have not been explored. The crack can also be arrested by the reinforced anisotropic structures (fibrillary structure) formed at the crack tip where the material is submitted to very large strain[80]. Even though all these mechanisms are often discussed in literature, their experimental observation, especially in situ, is much less reported.

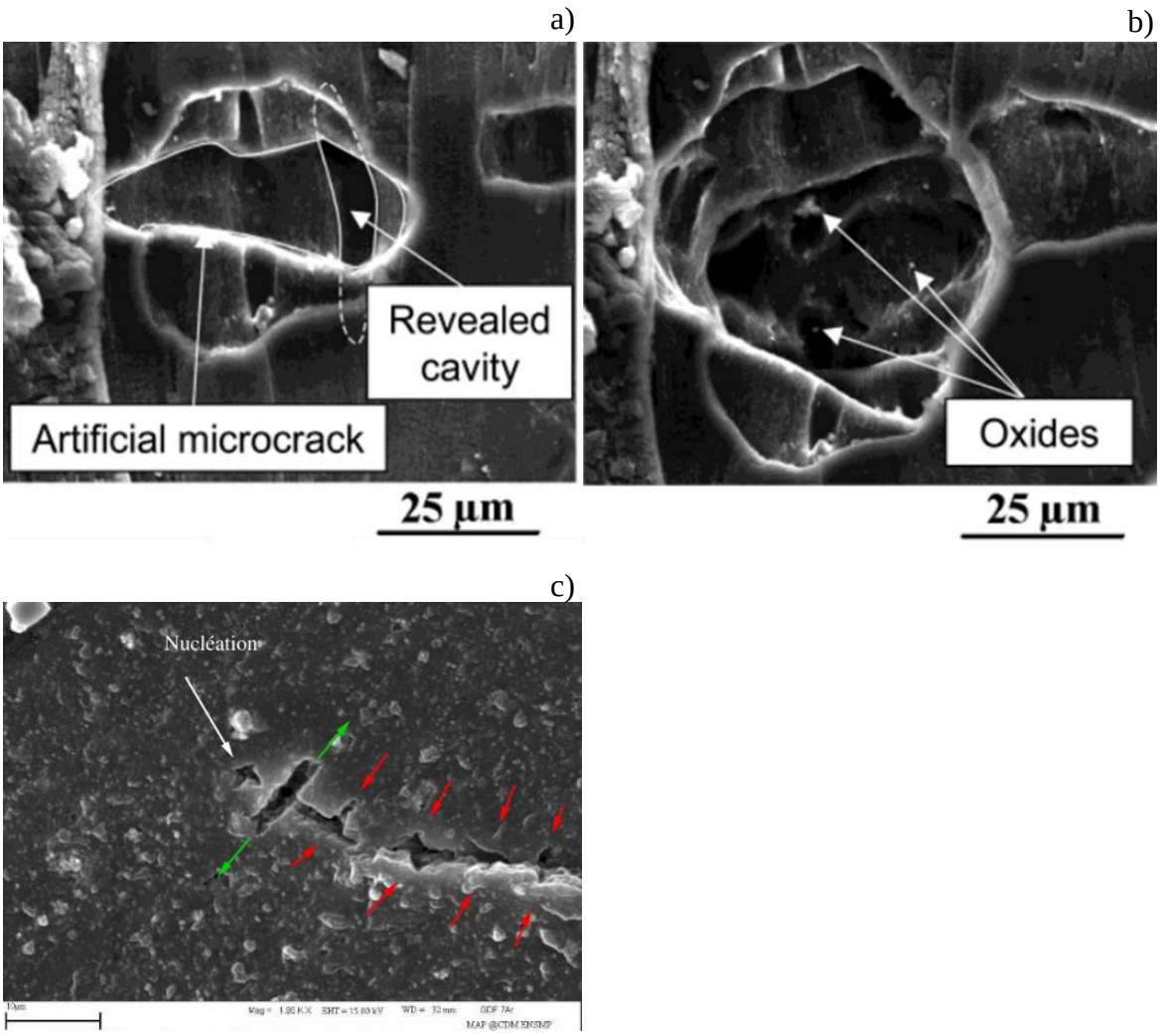

Figure 12: a) Artificial micro-cracks created to observe the morphology behind the crack tip, b) cavities observed at the poles of ZnO inclusions, c) nucleation of void around a crack tip for NR[46].

3.3 Conclusion

Microstructural defects in the materials are precursors for crack initiation and also impact the crack propagation. In-situ observation of the crack initiation and propagation along with these defects is difficult. The advantages and the limitations of different characterization techniques that are available for these observations are explained in the following section.

4 TECHNIQUES TO CHARACTERIZE MICROSTRUCTURAL DEFECTS

Many multiscale characterization techniques exist to characterize/observe the defects present in elastomers and the different mechanisms of crack initiation and propagation that they are

associated with. These characterizations can be destructive or nondestructive, 2-dimensional or 3-dimensional.

4.1 2D techniques

Optical microscope, atomic force microscopy (AFM), transmission electron microscopy (TEM), and scanning electron microscopy (SEM) are some of the techniques available for 2D characterization of materials. Since these are all 2D techniques, only "apparent" morphology information can be obtained, e.g., the diameter of the particle analyzed depends on the preparation of the thin slices of the sample. The resolution of each technique obviously determines the size range of the observed defects in the sample.

The Dispergrader technique is fast and simple to use, and has been applied in research studies to quantify the dispersion of filler agglomerates[12,22]. It works on the principles of reflected light microscope, where the light source is kept at an angle of 30^{o} with respect to the specimen surface. The surface is observed using a camera with a magnification of 100x. This technique cannot distinguish between the inclusions, surface roughness (e.g. due to improper sample slicing), voids and filler agglomerates. Its resolution capability is also limited (in between 3-57μm). Similar to Dispergrader, Optical microscope is also often used[17]. With the latter, one can conduct ex-situ tests, i.e. observation of the crack appearance on the surface sample during a fatigue test[22]. However, observations are limited by the resolution of the instrument to the micron scale.

A better resolution, at the nanoscale or even higher, can be achieved with AFM and TEM. Both techniques provide similar information such as filler structure, aggregate dispersion etc… in an elastomer[81–84], for instance, in silica filled elastomer matrix composites[82] (cf Figure 13). They are not very well suitable for characterizing micron sized defects due to the limited size of the observation area. Visualization of the crack mechanisms is also possible by these techniques by performing a postmortem analysis after a mechanical experiment. For instance, the rearrangement of silica agglomerates in natural rubber due to fatigue solicitation was observed by TEM[85]. Mdarhri and Brosseau[40,41] have observed the crack initiation and propagation in the vicinity of the filler aggregates – matrix interface in a stretched sample using AFM. However, in-situ characterization capabilities of these instruments remain limited.

SEM is another technique extensively used for characterization of microstructural defects and the crack mechanisms they are associated to. Typical SEM resolution is in microns, but it can reach 100 nm. Generally, secondary electron (SE) detector with low voltage electron

beam is used. A combination of SE and Energy dispersive X-ray (EDX) analysis enhances the contrast between the defects and the polymer matrix [2,6,48,77,86]. The capability of in-situ SEM observations was, for instance, demonstrated in a study devoted to characterization of the microstructural evolution behind a crack tip in a NR/CB composite. A high energy electronic beam was used to create artificial micro-cracks to observe the cavitation at the poles of inclusion during a crack propagation [46,77]. The main disadvantages of using SEM are the high chances of material damage by the electron beam during the observation and the low surface area of the observable specimen.

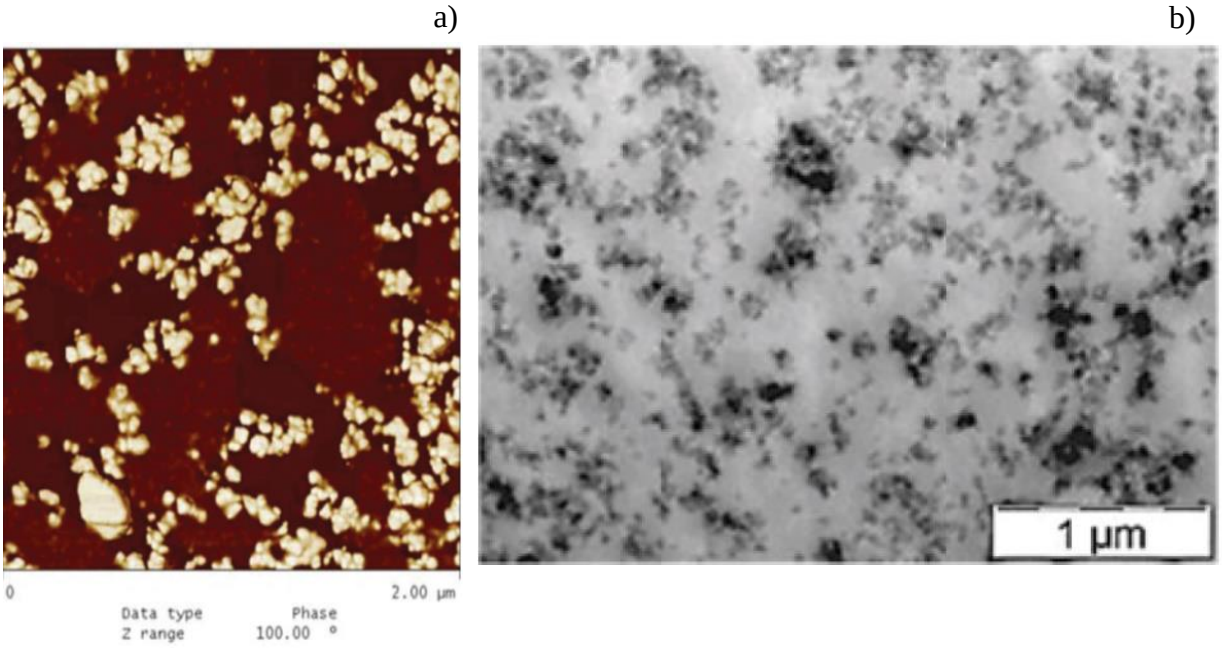

Figure 13: a) AFM image of silica filler in NR/ENR matrix b) TEM image of filler aggregates in an NR/SBR matrix[83]

4.2 3D characterization

4.2.1 Electron tomography

Electron Tomography uses TEM technique to obtain a 3D tomography of a specimen at a nanoscale resolution. TEM images are acquired by rotating the specimen around its center at an incremental degree. This can be used to characterize the morphology or spatial distribution of filler network or filler structure[84,87,88] (Figure 14) and also for visualizing the cavitation due to breakdown of silica aggregates upon stretching the matrix[38] (Figure 14). The main disadvantage of this technique is the small volume that can be analyzed ($500x500x100nm^3$), which limits in-situ mechanical experiments. Another drawback is the reduced phase contrast

between the fillers and the matrix in the presence of strongly scattering inclusions like ZnO [89,90].

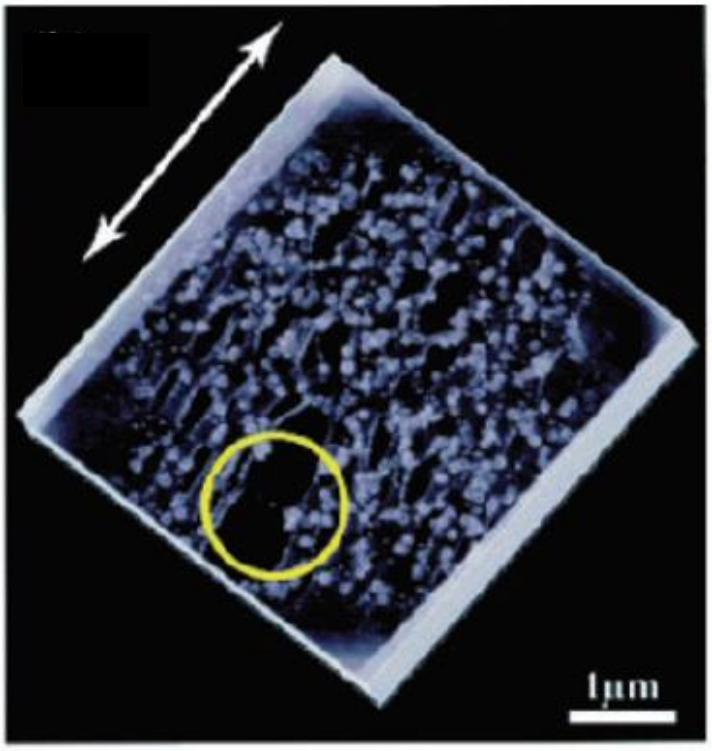

Figure 14: Nano cavitation is observed in SBR filled with silica particles. The specimen has been cut from the stretched sample[38].

4.2.1 FIB-SEM

Through a combination of focused ion beam (FIB) which sequentially mills the sample layers (around 10nm) and SEM (Figure 15), 3D information on the defects in an elastomer can be obtained at the SEM resolution. The volume that can be analyzed is in the range of 15x15x15 μm^3. The acquisition time for an image stack is relatively long due to the slow milling process. With FIB – SEM, Tunicliffe *et al.*[91] has imaged the 3D dispersion of silica aggregates, agglomerates and ZnO inclusion in a SBR matrix (Figure 16a). Koch *et al.*[92] has characterized polypropylene composites with various fillers like glass fibers, mica and talc particles (Figure 16b). Similar to electron tomography, FIB-SEM is a destructive characterization. Though, in-situ experiments are possible, they remain challenging[84].

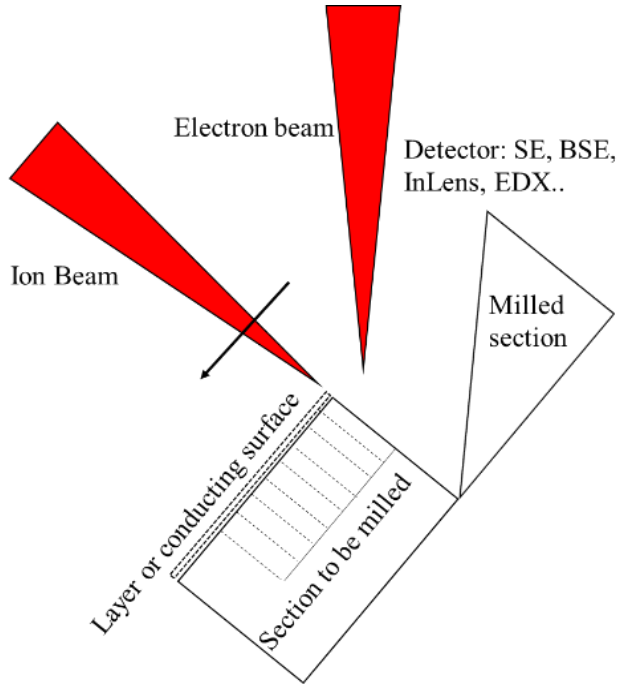

Figure 15: Configuration of FIB-SEM

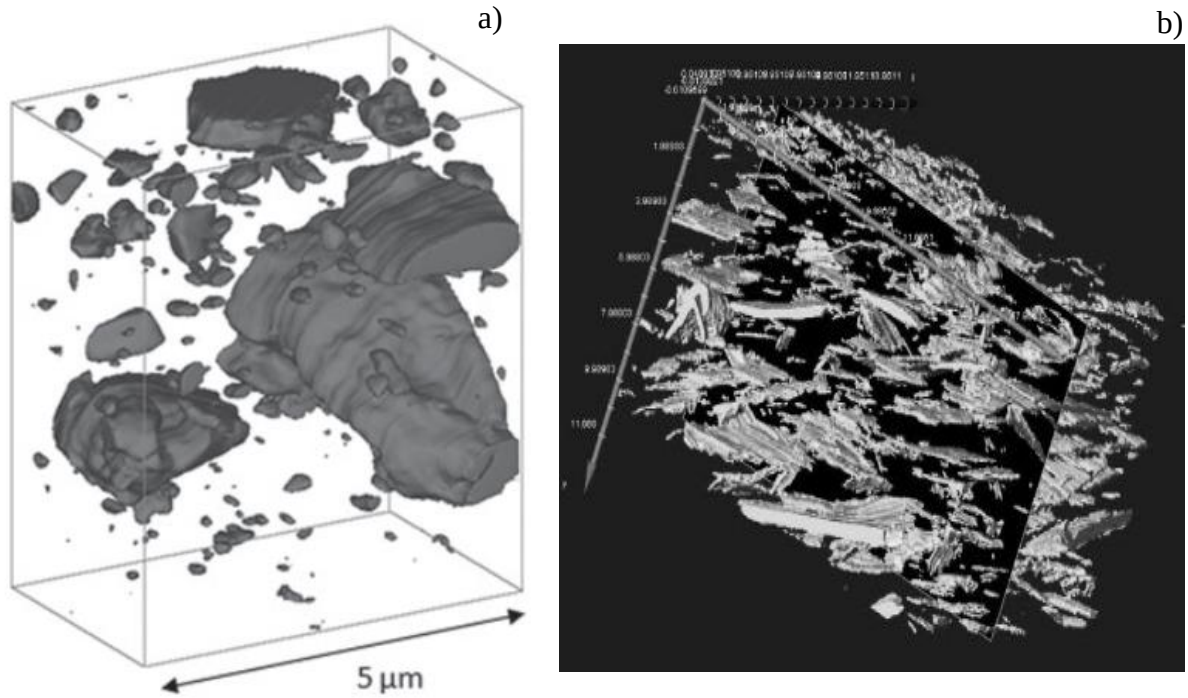

Figure 16: a) 3D-rendering of silica in SBR 1502 matrix from FIB-SEM observation b) 3D rendered volume of talc particles dispersed in polypropylene matrix observed by FIB-SEM [91,92].

4.2.2 X-ray tomography

X-ray tomography has the advantage to be a non-destructive method. It works on the principle of the Beer-Lambert law where the coefficient of absorption of a material depends on its interaction with the X-ray photons. The sample is rotated over 180° or 360° in front of the X-ray beam (Figure 17). Numerous projections are acquired during this rotation. A reconstruction of the obtained projections using various algorithms (e.g. filtered back projection algorithm) gives a 3D image of the sample. The biggest advantages of this technique are the possibility to observe large volumes in the range of cm^3 and to conduct in-situ experiments without damaging the materials[3,29,93–96]. Like for all tomo observation techniques, the disadvantages are the generation of different artifacts (ring artifact, beam hardening) during the acquisition, low attenuation contrast difference between particles of similar nature to that of polymer matrix, and the requirement of high computational power for the post processing of the 3D images. Various sources exist for X-ray Tomography, notably laboratory sources and synchrotron sources.

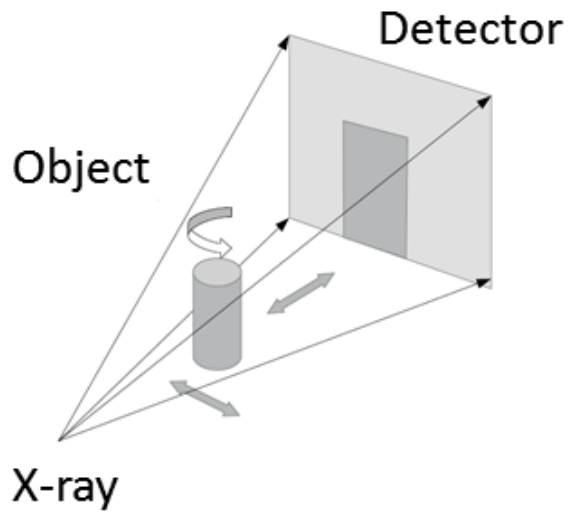

Figure 17: Illustration of the configuration of X-ray tomography imaging[96].

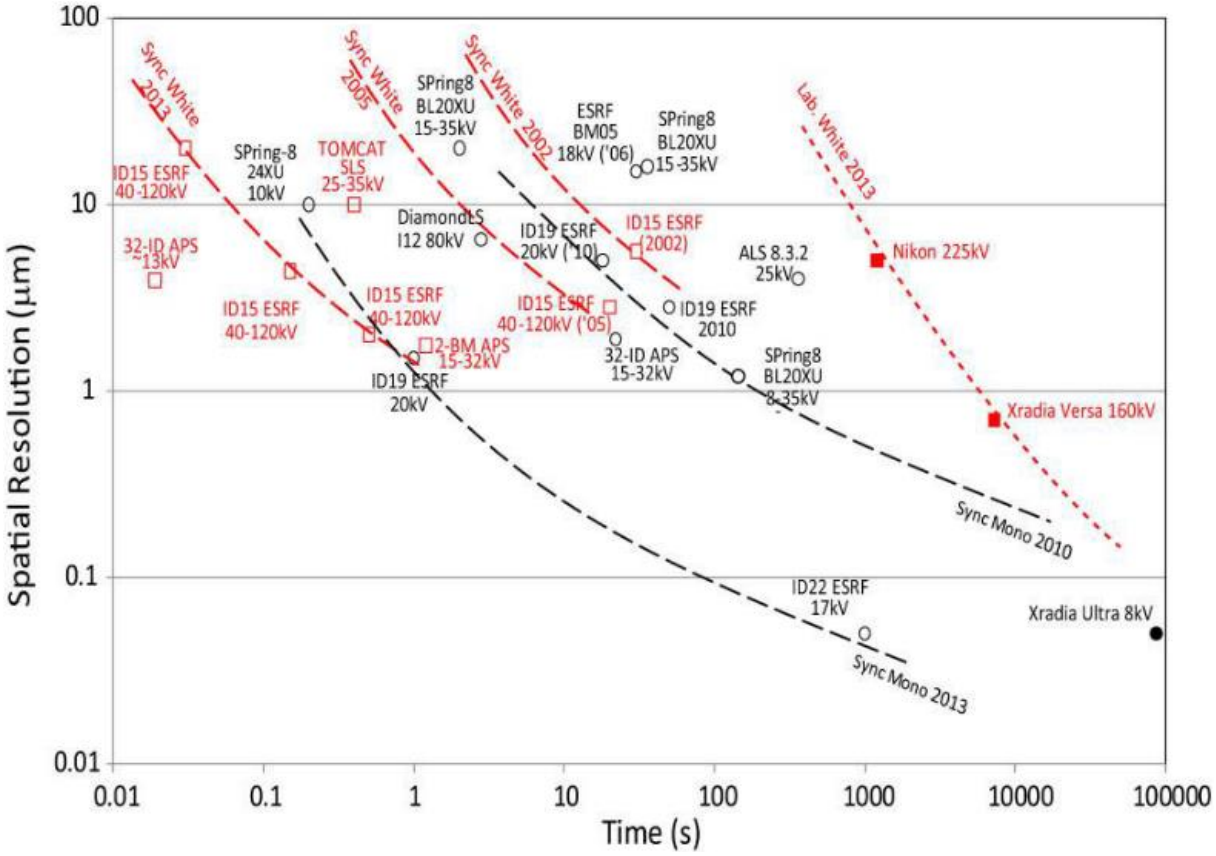

Figure 18: Historical development of spatial resolution vs scan time of X-ray Tomography. In case where spatial resolution is not cited in the references, an estimated resolution of twice the pixel is used. The filled symbols represent X-ray lab tomography and open symbols are for synchrotron sourced X-ray Tomography. The red squares denote X-ray Tomography with white beam and black circle is for monochromatic beam[97].

4.2.2.1 Laboratory source tomography

Laboratory sourced X-ray tomography has seen significant improvement in scan times and spatial resolution so that their performances get closer to the ones of synchrotron-sourced X-ray tomography (Figure 18). Thus they became more and more suitable for characterization of microstructures of various materials such as metals, ceramics or polymer composites[96–102]. In recent decades, this technique has also been used for characterizing cavitation in elastomers[3,26,29,103,104]. Voids or cavitations are easy to detect because of their good contrast with the matrix. This is also the case for silica agglomerates whose attenuation coefficient is much higher than the matrix one[26]. It is more difficult to detect defects such as carbon black agglomerates, since their attenuation contrast is close to the one of polymers. High attenuating inclusions like ZnO also perturb their detection as well as the one of cracks[105]. For these reasons (among others like the cost of the apparatus and the processing time required

to conduct the analysis) the rubber industry, which often uses ZnO particles and carbon blacks in their elastomer formulations, has not yet adopted X-ray Tomography for the routine characterization of their products.

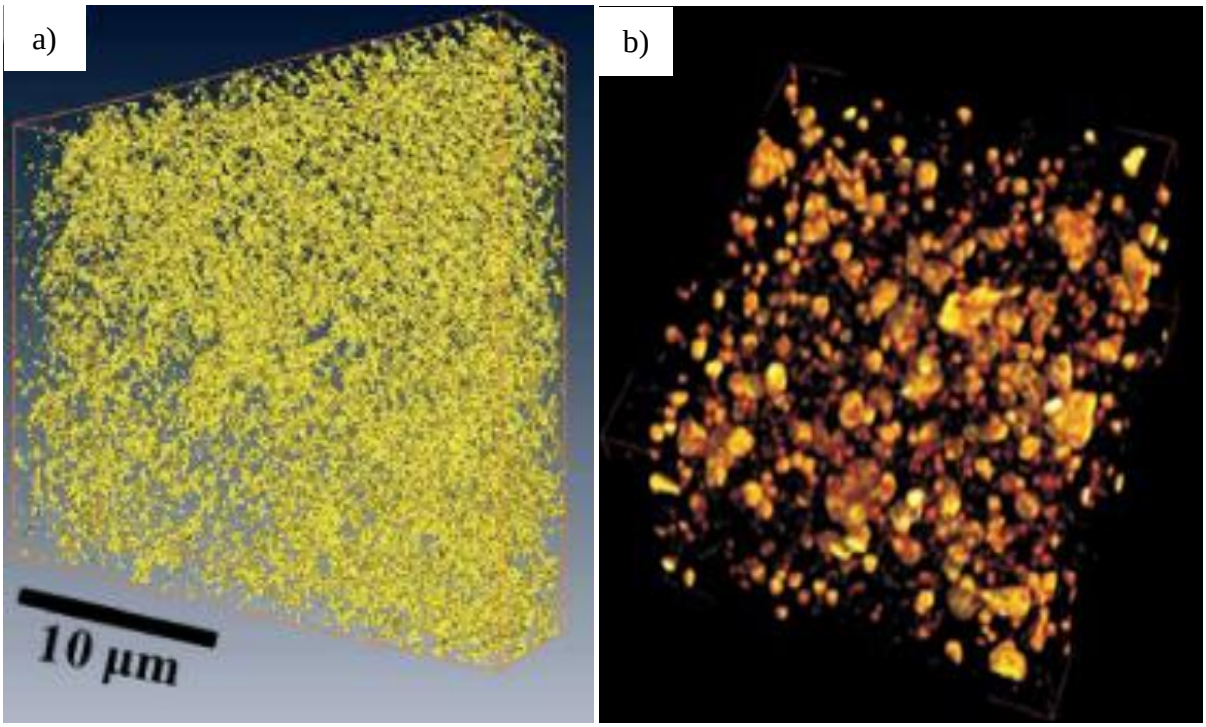

Figure 19: a) X-ray tomography imaging of carbon black aggregates distribution from reference [106], and b) silica distribution in SBR matrix [107].

4.2.2.2 Synchrotron-sourced tomography

The method of production of X-ray is different in synchrotron. Synchrotron radiations are emitted when electrons accelerate radially in a storage ring at ultrarelativistic speed. The radiation that is projected in tangential direction to the electron trajectory is captured by beamlines. Monochromatic parallel radiation is produced with broad spectrum of energies and high flux (with a ratio of 10^6 compared to a conventional source). In addition, due to spatial coherence of the emitted radiation, phase contrast imaging is possible, which helps in the detection of low attenuation coefficient materials (like e.g. CB_{aggl}). The resolution of X-ray Tomography ranges from 100nm up to more than 10µm. Thus, Zhou *et al.*[106,108] studied the evolution of the carbon black aggregate network in a rubber matrix and its impact on the mechanical properties during a tensile deformation (Figure 19a). To do so, they used X-ray energy of 8 keV and phase contrast imaging mode at a resolution of 100nm. Using this relatively high resolution, they observed that upon stretching, the aggregate network undergoes breakage and re-aggregation. A similar study was performed by Chen *et al.*[109] on carbon black in

natural rubber. Nusser *et al.* [107] characterized silica fillers dispersion and their cluster size distribution in silica filled SBR using a synchrotron radiation with a resolution below 1µm at 9.6 keV (Figure 19b). This study highlighted the ambiguities and misinterpretations that a 2D analysis can induce, especially when the existence of a percolating network is addressed.

It is noteworthy that all these studies only dealt with the characterization of filler aggregates structures and not with that of defects such as filler agglomerates or micron size voids, which actually requires a lower resolution and is therefore technically easier to perform. Moreover, thanks to its relatively fast acquisition time (of the order of few minutes), synchrotron source tomography is also suitable to study the impact of these defects on the rupture and fatigue properties in a filled elastomer by performing in-situ characterization. In-situ studies are commonly performed for metal or ceramic materials[99,101,110–114], but are yet rarely reported for elastomer materials.

4.3 Statistics of morphology and spatial distribution of defects

Whatever the techniques chosen for characterizing the material defects are, the obtained images require a quantitative analysis of their different features (volume, size aspect ratio, structure etc.). 2D techniques require a post treatment of the data with strong assumptions to extract the real morphological features from apparent dimensions[115] (Figure 20). 3D observations can provide a direct picture of the morphology of the microstructural defects along with their dispersion state. For instance, the equivalent diameter and sphericity (closeness of the shape of the object to that of a perfect sphere, e.g. sphericity is equal to one for perfect sphere) distributions of silica agglomerates in SBR, obtained from laboratory source X-ray tomography have been described in a recent publication[26] (Figure 21). To the author's knowledge, neither the analysis of spatial distribution of defects (e.g. inter-particle distance) and of their morphological characteristics (such as shape factor, structure etc.), nor the methodology to derive these features have ever been reported.

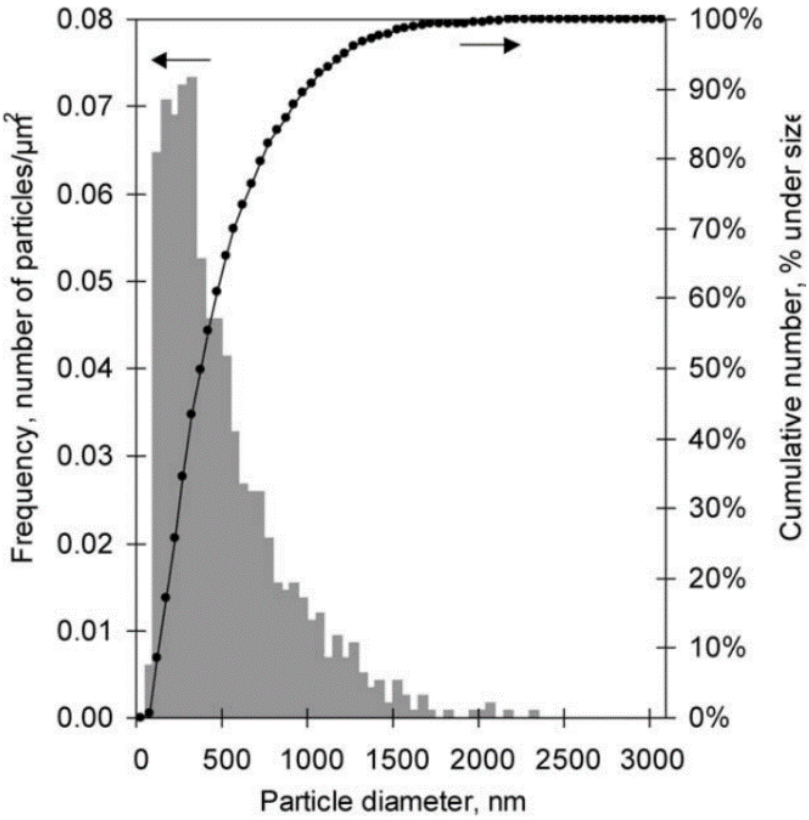

Figure 20: a) Distribution of the particle diameter obtained using TEM microscopy[115].

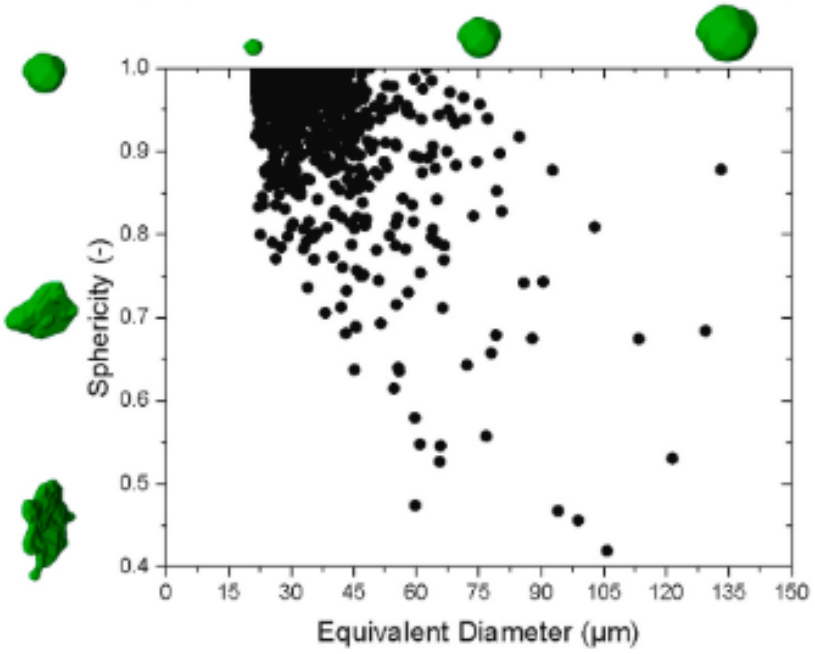

Figure 21: Sphericity as a function of Equivalent diameter of silica agglomerates in a silica filled SBR obtained using laboratory X-ray Tomography with spatial resolution of 20µm[26].

4.4 Conclusion

One can reliably characterize the morphology and spatial distribution of defects like CB_{aggl} and their impact on crack initiation and propagation mechanisms using synchrotron sourcing. This enables high spatial resolution, fast acquisition and phase-contrast imaging capabilities. Laboratory X-ray Tomography also appears as a useful technique. It is more easily accessible with a spatial resolution around 1µm, but it suffers from limitations regarding the acquisition times, the attenuation contrast between the materials etc. It also requires more research to optimize the parameters governing the image formation and acquisition, especially for a performant characterization of defects in an elastomer matrix. Moreover, whatever the X-ray source, tomography still needs the development of a dedicated image analysis routine (e.g. filters, segmentation etc...) and a methodology for powerful extraction of the morphological features of the defects (e.g. volume, diameter, aspect ratio etc.).

5 CONCLUSIONS AND PERSPECTIVES

Ideally, a material should be free from defects since the defects can lead to rupture. Yet, their existence is unavoidable in a filler-reinforced elastomer. The defects concentrations vary, depending on various processing parameters and on the chosen formulations. The most common defects found in filled elastomers are filler agglomerates. ZnO particles are also commonly observed in industrial materials since they are key ingredients in sulphur-based curing systems. The presence of these defects raises some important questions in the industry, regarding their potential impact on the mechanical properties and on the need to characterize them or not.

Rupture in a material is the consequence of initiation and propagation of one or more cracks through the entire section of the material. Past studies systematically showed the presence of a critical defect at the origin of cracks during a fatigue or tensile test. One of the seminal works in this domain is that of A.N. Gent and B. Park regarding cavitation of an elastomer matrix near a spherical inclusion[37]. However, with respect to industrial rubber, it is challenging to characterize the onset of a damage due to defects in the material and its evolution towards a crack initiation during solicitation. When a material contains varying fractions of defects or different kinds of defects, their characterization becomes complex. This becomes even more challenging when the defects considered are CB_{aggl} due to the low contrast between CB_{aggl} and the matrix. For that reason, many studies identify crack initiation scenarios by mostly performing postmortem analysis.

Similarly, crack propagation has been well studied by the scientific community, notably regarding the influence of the elastomer type, of the filler type and of the loading and temperature conditions. In the presence of a defect, a common crack advance mechanism is by breaking the ligaments between the crack tip and the cavities ahead of it. The cavities are created at the pole of defects by the high triaxial stress behind the crack tip. The presence of reinforcing filler also induces additional mechanisms such as crack deviation or crack arrest. Even though all these mechanisms are often discussed in the literature, their experimental observation is much less reported, especially in situ.

Indeed, there are certain limitations to study crack initiation and propagation in an industrial material containing defects, mostly due to the inadequacy of techniques that are currently available for the characterization of defects. The prevalent techniques in the industry are Dispergrader, Optical microscopy, SEM and TEM. They can extract some pertinent statistical information with certain strong assumptions. However, the main challenge with these techniques materializes when carrying out in-situ mechanical tests, as it requires samples with very small dimensions. To overcome these challenges, one can use X-ray Tomography with synchrotron or laboratory source. One can then characterize the morphology and spatial distribution of defects like CB_{aggl} and their impact on crack initiation and propagation mechanisms reliably using X-ray Tomography with synchrotron sourcing. This is facilitated by its high spatial resolution, its fast acquisition and phase-contrast imaging capabilities. Today, laboratory source X-ray Tomography can almost reach spatial resolution capabilities of synchrotron sourcing, making this technique suitable for characterization of the micro-size defects present in elastomer materials. However, the rubber industry is not yet ready to adopt X-ray Tomography for the routine characterization of their products even though these elastomer materials often contain carbon black, ZnO particles etc.. This is due to some limitations of this technique i.e. long acquisition time, insufficient attenuation contrast between materials (e.g. CB_{aggl} and elastomer), lack of methodology to characterize and process the data, etc… In addition, given the questions regarding the influence of the defects on the mechanical properties of their products, the industry still lacks pertinent information on the relevancy of this characterization in the specifications of their products.

Thus this thesis work has two objectives:

1. Develop a robust methodology to quantify the dispersion and the morphological features of defects that are present in a CB filled elastomer (the matrix chosen here being EPDM, commonly used in many applications) using synchrotron source *and* laboratory source X-ray Tomography.

2. Understand the impact of these defects on the materials properties with the help of the tomography, which means:
    a. Characterize the damage mechanism associated to different defects present in the materials and identify how this damage mechanism can lead to crack initiation
    b. Establish the characteristics of the defects critical for crack initiation
    c. Determine the consequences of the presence of defects like CB_{aggl} on the crack propagation mechanisms.

6 REFERENCES

[1] Chazeau, L.; Chenal, J.-M.; Gauthier, C.; Kallungal, J.; Caillard, J. About the Influence of Materials Parameters on the Ultimate and Fatigue Properties of Elastomers; In *Fatigue Crack Growth in Rubber Materials. Advances in Polymer Science*; G., H.; R., K.; R., S., Eds.; Springer, Cham., **2020**; pp 297; 10.1007/12_2020_80.

[2] Saintier, N. Thesis,. Fatigue multiaxiale dans un élastomère de type NR chargé : mécanismes d'endommagment et critère local d'amorçage de fissure, Ecole Nationale Supérieure d'Arts et Métiers, **2001**.

[3] Marco, Y.; Le Saux, V.; Calloch, S.; Charrier, P. X-ray computed μ-tomography: A tool for the characterization of fatigue defect population in a polychloroprene rubber *Procedia Engineering* **2010**, *2*, 2131, 10.1016/j.proeng.2010.03.229.

[4] Horiuchi, S.; Dohi, H. Nanoimaging and spectroscopic analysis of rubber/ZnO interfaces by energy-filtering transmission electron microscopy *Langmuir* **2006**, *22*, 4607, 10.1021/la052308f.

[5] Saintier, N.; Cailletaud, G.; Piques, R. Crack initiation and propagation under multiaxial fatigue in a natural rubber *International Journal of Fatigue* **2006**, *28*, 61, 10.1016/j.ijfatigue.2005.03.006.

[6] Le Cam, J.-B.; Huneau, B.; Verron, E. Fatigue damage in carbon black filled natural rubber under uni- and multiaxial loading conditions *International Journal of Fatigue* **2013**, *52*, 82, 10.1016/j.ijfatigue.2013.02.022.

[7] Kallungal, J.; Chazeau, L.; Chenal, J.-M.; Adrien, J.; Maire, E.; Barres, C.; Cantaloube, B.; Heuillet, P. Methodology for 3D characterization of microstructural defects in filled polymer using X-ray Tomography; In *Constitutive Models for Rubber XI*; CRC Press, **2019**; pp 77; 10.1201/9780429324710-14.

[8] Hess, W. M.; Swor, R. A.; Micek, E. J. The Influence of Carbon Black, Mixing, and Compounding Variables on Dispersion *Rubber Chemistry and Technology* **1984**, *57*, 959, 10.5254/1.3536052.

[9] Grunert, F. Thesis,. Analytical method development to predict the in-rubber dispersibility of silica, University of Twente, **2018**.

[10] Collin, V.; Boudimbou, I.; Peuvrel-Disdier, E. New insights in dispersion mechanisms of carbon black in a polymer matrix under shear by rheo-optics *Journal of Applied Polymer Science* **2013**, *127*, 2121, 10.1002/app.37769.

[11] Dizon, E. S. Processing in an Internal Mixer as Affected by Carbon Black Properties. *Rubber Chem. Technol.* **1976**, *49*, 12–27.

[12] Collin, V. Thesis,. Étude rhéo-optique des mécanismes de dispersion du noir de carbone dans des élastomères, **2009**.

[13] Boudimbou, I. Thesis,. Mécanismes élémentaires de dispersion de charges de silice dans une matrice élastomère, l ' École Nationale Supérieure des Mines de Paris, **2011**.
[14] Tokita, N.; Pliskin, I. The Dependence of Processability on Molecular Weight Distribution of Elastomers *Rubber Chemistry and Technology* **1973**, *46*, 1166, 10.5254/1.3547426.
[15] Cotten, G. R. Mixing of Carbon Black with Rubber I. Measurement of Dispersion Rate by Changes in Mixing Torque *Rubber Chemistry and Technology* **1984**, *57*, 118, 10.5254/1.3535988.
[16] Cotten, G. R.; Murphy, L. J. Mixing of Carbon Black with Rubber. VI. Analysis of NR/SBR Blends *Rubber Chemistry and Technology* **1988**, *61*, 609, 10.5254/1.3536207.
[17] Astruc, M. Thesis,. Étude rhéo-optique des mécanismes de dispersion de mélanges sous cisaillement simple . 1 Mélanges concentrés de polymères immiscibles . 2 Mélanges polymères-charges poreuse, l'École des Mines de Paris, **2008**.
[18] Rwei, S. P.; Feke, D. L. Simple Shear Flows **1990**, *30*, 701.
[19] Manas-Zloczower, I.; Nir, A.; Tadmor, Z. Dispersive Mixing in Internal Mixers - a Theoretical Model Based on Agglomerate Rupture. *Rubber Chem. Technol.* **1982**, *55*, 1250–1285.
[20] Rwei, S. P.; Manas-Zloczower, I.; Feke, D. L. Characterization of agglomerate dispersion by erosion in simple shear flows *Polymer Engineering & Science* **1991**, *31*, 558, 10.1002/pen.760310804.
[21] Palmgren, H. Processing Conditions in the Batch-Operated Internal Mixer *Rubber Chemistry and Technology* **1975**, *48*, 462, 10.5254/1.3547462.
[22] Masquelier, I. Thesis,. Influence de la formulation sur les propriétés en fatigue d'élastomères industriels, Université De Bretagne Occidentale, **2014**.
[23] Gent, A. N. Strength of Elastomers *Science & Technology of Rubber* **1978**, 419, 10.1016/b978-0-12-234360-5.50015-8.
[24] Euchler, E.; Bernhardt, R.; Schneider, K.; Heinrich, G.; Wießner, S.; Tada, T. In-situ dilatometry and X-ray microtomography study on the formation and growth of cavities in unfilled styrene-butadiene-rubber vulcanizates subjected to constrained tensile deformation *i*.
[25] Gent, A. N.; Lindley, P. B. Internal Rupture of Bonded Rubber Cylinders in Tension *Proceedings of the Royal Society A: Mathematical, Physical and Engineering Sciences* **1959**, *249*, 195, 10.1098/rspa.1959.0016.
[26] Federico, C. E.; Padmanathan, H. R.; Kotecký, O.; Rommel, R.; Rauchs, G.; Fleming, Y.; Addiego, F. Resolving cavitation in silica-filled styrene-butadiene rubber composites upon cyclic tensile testing *Polymer Testing* **2021**, *100*, 107274, 10.1016/j.polymertesting.2021.107274.
[27] Balutch, T.; Huneau, B.; Marco, Y.; Charrier, P.; Champy, C. Influence of defects size on the fatigue properties of an industrial EPDM; In *Constitutive Models for Rubber XI*; CRC Press, **2019**; pp 357; 10.1201/9780429324710-62.
[28] Masquelier, I. Thesis,. Influence de la formulation sur les propriétés en fatigue d'élastomères industriels, Université De Bretagne Occidentale, **2014**.
[29] Le Saux, V.; Marco, Y.; Calloch, S.; Charrier, P. Evaluation of the fatigue defect population in an elastomer using X-ray computed micro-tomography *Polymer Engineering & Science* **2011**, *51*, 1253, 10.1002/pen.21872.
[30] Bayraktar, E.; Isac, N.; Bessri, K.; Bathias, C. Damage mechanisms in natural (NR) and synthetic rubber (SBR): Nucleation, growth and instability of the cavitation *Fatigue and Fracture of Engineering Materials and Structures* **2008**, *31*, 184, 10.1111/j.1460-2695.2007.01213.x.
[31] Bayraktar, E.; Bessri, K.; Bathias, C. Deformation behaviour of elastomeric matrix

composites under static loading conditions *Engineering Fracture Mechanics* **2008**, *75*, 2695, 10.1016/j.engfracmech.2007.03.016.
[32] Cho, K.; Gent, A. N. Cavitation in model elastomeric composites *Journal of Materials Science* **1988**, *23*, 141, 10.1007/BF01174045.
[33] Lindsey, G. H. Triaxial fracture studies *Journal of Applied Physics* **1967**, *38*, 4843, 10.1063/1.1709232.
[34] Gent, A. N.; Tompkins, D. A. Surface Energy Effects for Small Holes or Particles in Elastomers *J Polym Sci Part A-2 Polym Phys* **1969**, *7*, 1483, 10.5254/1.3547296.
[35] Fond, C. Cavitation criterion for rubber materials: A review of void-growth models *Journal of Polymer Science, Part B: Polymer Physics* **2001**, 10.1002/polb.1183.
[36] Oberth, A. E.; Bruenner, R. S. Tear Phenomena around Solid Inclusions in Castable Elastomers *Transactions of the Society of Rheology* **1965**, *9*, 165, 10.1122/1.548997.
[37] Gent, A. N.; Park, B. Failure processes in elastomers at or near a rigid spherical inclusion *Journal of Materials Science* **1984**, *19*, 1947, 10.1007/BF00550265.
[38] Dohi, H.; Kimura, H.; Kotani, M.; Kaneko, T.; Kitaoka, T.; Nishi, T.; Jinnai, H. Three-dimensional imaging in polymer science: Its application to block copolymer morphologies and rubber composites *Polymer Journal* **2007**, *39*, 749, 10.1295/polymj.PJ2006259.
[39] Cao, X.; Zhou, X.; Weng, G. Nanocavitation in silica filled styrene-butadiene rubber regulated by varying silica-rubber interfacial bonding *Polymers for Advanced Technologies* **2018**, *29*, 1779, 10.1002/pat.4284.
[40] Mdarhri, A.; Elies, P.; Brosseau, C. Stress induced cracks in carbon black filled elastomers probed by atomic force microscopy *Journal of Applied Physics* **2008**, *104*, 10.1063/1.3042218.
[41] Brosseau, C.; Mdarhri, A.; Vidal, A. Mechanical fatigue and dielectric relaxation of carbon black/polymer composites *Journal of Applied Physics* **2008**, *104*, 10.1063/1.2988269.
[42] Gent, A. N.; Lindley, P. B.; Thomas, A. G. Cut growth and fatigue of rubbers. I. The relationship between cut growth and fatigue *Journal of Applied Polymer Science* **1964**, *8*, 455, 10.1002/app.1964.070080129.
[43] Lake, G. J.; Lindley, P. B. Cut growth and fatigue of rubbers. II. Experiments on a noncrystallizing rubber *Journal of Applied Polymer Science* **1964**, *8*, 707, 10.1002/app.1964.070080212.
[44] Lake, G. J.; Lindley, P. B. The mechanical fatigue limit for rubber *Journal of Applied Polymer Science* **1965**, *9*, 1233, 10.1002/app.1965.070090405.
[45] Dizon, E. S.; Hicks, A. E.; Chirico, V. E. The Effect of Carbon Black Parameters on the Fatigue Life of Filled Rubber Compounds. *Rubber Chem. Technol.* **1974**, *47*, 231–249.
[46] Le Cam, J. B.; Huneau, B.; Verron, E.; Gornet, L. Mechanism of fatigue crack growth in carbon black filled natural rubber *Macromolecules* **2004**, *37*, 5011, 10.1021/ma0495386.
[47] Grandcoin, J.; Boukamel, A.; Lejeunes, S. A micro-mechanically based continuum damage model for fatigue life prediction of filled rubbers *International Journal of Solids and Structures* **2014**, *51*, 1274, 10.1016/j.ijsolstr.2013.12.018.
[48] Huneau, B.; Masquelier, I.; Marco, Y.; Le Saux, V.; Noizet, S.; Schiel, C.; Charrier, P. Fatigue crack initiation in a carbon black-filled natural rubber *Rubber Chemistry and Technology* **2016**, *89*, 126, 10.5254/rct.15.84809.
[49] Lindley, P. B. Non-Relaxing Crack Growth and Fatigue in a Non-Crystallizing Rubber *Rubber Chemistry and Technology* **1974**, *47*, 1253, 10.5254/1.3540497.
[50] Rivlin, R. S.; Thomas, A. G. Rupture of rubber. I. Characteristic energy for tearing

Journal of Polymer Science **1953**, *10*, 291, 10.1002/pol.1953.120100303.
[51] Roucou, D.; Diani, J.; Brieu, M.; Witz, J. F.; Mbiakop-Ngassa, A. Experimental investigation of elastomer mode I fracture: an attempt to estimate the critical strain energy release rate using SENT tests *International Journal of Fracture* **2018**, *209*, 163, 10.1007/s10704-017-0251-x.
[52] Yeoh, O. H. Fracture mechanics of bond failure in the "pure shear" test piece *Rubber Chemistry and Technology* **2003**, *76*, 483, 10.5254/1.3547755.
[53] Thomas, A. G. The Development of Fracture Mechanics for Elastomers *Rubber Chemistry and Technology* **1994**, *67*, 50, 10.5254/1.3538688.
[54] Greensmith, H. W. Rupture of rubber. X. The change in stored energy on making a small cut in a test piece held in simple extension *Journal of Applied Polymer Science* **1963**, *7*, 993, 10.1002/app.1963.070070316.
[55] Lindley, P. B. Energy for crack growth in model rubber components *Change* **1972**, *132*.
[56] Carbone, G.; Persson, B. N. J. Crack motion in viscoelastic solids: The role of the flash temperature *The European Physical Journal E* **2005**, *17*, 261, 10.1140/epje/i2005-10013-y.
[57] Lake, G. J.; Lawrence, C. C.; Thomas, A. G. High-speed fracture of elastomers: Part I *Rubber Chemistry and Technology* **2000**, *73*, 801, 10.5254/1.3547620.
[58] Tsunoda, K.; Busfield, J. J. C.; Davies, C. K. L.; Thomas, A. G. Effect of materials variables on the tear behaviour of a non-crystallizing elastomer *Journal of Materials Science* **2000**, *35*, 5187, 10.1023/A:1004860522186.
[59] Papadopoulos, I. C.; Thomas, A. G.; Busfield, J. J. C. Rate transitions in the fatigue crack growth of elastomers *Journal of Applied Polymer Science* **2008**, *109*, 1900, 10.1002/app.28086.
[60] Fukahori, Y.; Sakulkaew, K.; Busfield, J. J. C. Elastic-viscous transition in tear fracture of rubbers *Polymer* **2013**, *54*, 1905, 10.1016/j.polymer.2013.01.019.
[61] Horst, T.; Heinrich, G. Crack propagation behavior in rubber materials *Polymer Science Series A* **2008**, *50*, 583, 10.1134/S0965545X08050131.
[62] Mullins, L. Rupture of rubber – Part IX : role of hysteresis in the tearing of rubber *Transactions and Proceedings of the Institution of the Rubber Industry* **1959**, *35*, 213.
[63] Robertson, C. G.; Stoček, R.; Kipscholl, C.; Mars, W. V. Characterizing the Intrinsic Strength (Fatigue Threshold) of Natural Rubber/Butadiene Rubber Blends *Tire Science and Technology* **2019**, *47*, 292, 10.2346/tire.19.170168.
[64] Lake, G. J.; Yeoh, O. H. Measurement of rubber cutting resistance in the absence of friction *International Journal of Fracture* **1978**, *14*, 509, 10.1007/BF01390472.
[65] Mueller, H. K.; Knauss, W. G. The Fracture Energy and Some Mechanical Properties of a Polyurethane Elastomer *Transactions of the Society of Rheology* **1971**, *15*, 217, 10.1122/1.549209.
[66] Ahagon, A.; Gent, A. N. Threshold fracture energies for elastomers *Journal of Polymer Science: Polymer Physics Edition* **1975**, *13*, 1903, 10.1002/pol.1975.180131005.
[67] Bhowmick, A.; Gent, A. N.; Pulford, C. T. R. Tear Strength of Elastomers Under Threshold Conditions. *Rubber Chem. Technol.* **1983**, *56*, 226–232.
[68] Gent, A. N.; Tobias, R. H. Threshold Tear Strength of Some Molecular Networks; **1982**; pp 367; 10.1021/bk-1982-0193.ch019.
[69] Stoček, R.; Stěnička, M.; Zádrapa, P. Future trends in predicting the complex fracture behaviour of rubber materials *Continuum Mechanics and Thermodynamics* **2021**, *33*, 291, 10.1007/s00161-020-00887-z.
[70] Lake, G. J.; Thomas, A. G. The strength of highly elastic materials *Proceedings of the Royal Society of London. Series A. Mathematical and Physical Sciences* **1967**, *300*,

108, 10.1098/rspa.1967.0160.
[71] Slootman, J. Thesis,. Quantitative detection of damage in soft materials using mechano-fluorescence, l'Ecole Supérieure de Physique et de Chimie Industrielles de la ville de Paris (ESPCI Paris), **2019**.
[72] Kadir, A.; Thomas, A. G. Tear Behavior of Rubbers Over a Wide Range of Rates. *Rubber Chem. Technol.* **1981**, *54*, 15–23.
[73] Paris, P.; Erdogan, F. A Critical Analysis of Crack Propagation Laws *Journal of Basic Engineering* **1963**, *85*, 528, 10.1115/1.3656900.
[74] Lake, G. J. Fatigue and Fracture of Elastomers *Rubber Chemistry and Technology* **1995**, *68*, 435, 10.5254/1.3538750.
[75] Roland, C. M.; Smith, C. R. Defect Accumulation in Rubber. *Rubber Chem. Technol.* **1985**, *58*, 806–814.
[76] Aglan, H.; Chudnovsky, A.; Moet, A.; Fleischman, T.; Stalnaker, D. Crack layer analysis of fatigue crack propagation in rubber compounds *International Journal of Fracture* **1990**, *44*, 167, https://doi.org/10.1007/BF00035514.
[77] Beurrot, S.; Huneau, B.; Verron, E. In situ SEM study of fatigue crack growth mechanism in carbon black-filled natural rubber *Journal of Applied Polymer Science* **2010**, *43*, NA, 10.1002/app.31707.
[78] Kraus, G. Reinforcement of elastomers by carbon black; In *Fortschritte der Hochpolymeren-Forschung*; Springer Berlin Heidelberg: Berlin, Heidelberg; pp 155; 10.1007/3-540-05483-9_12.
[79] Lorenz, H.; Steinhauser, D.; Klüppel, M. Morphology and Micro-mechanics of Filled Elastomer Blends: Impact on Dynamic Crack Propagation; **2013**; pp 81; 10.1007/978-3-642-37910-9_3.
[80] Stacer, R. G.; Yanyo, L. C.; Kelley, F. N. Observations on the Tearing of Elastomers. *Rubber Chem. Technol.* **1985**, *58*, 421–435.
[81] Baeza, G. P.; Genix, A.-C.; Degrandcourt, C.; Petitjean, L.; Gummel, J.; Couty, M.; Oberdisse, J. Multiscale Filler Structure in Simplified Industrial Nanocomposite Silica/SBR Systems Studied by SAXS and TEM *Macromolecules* **2013**, *46*, 317, 10.1021/ma302248p.
[82] Grau, P. Étude de la structuration de mélanges d ' élastomères chargés silice ; influence sur leurs propriétés dissipatives et de renfort To cite this version : HAL Id : tel-01128263 **2015**.
[83] Clément, F.; Lapra, A.; Bokobza, L.; Monnerie, L.; Ménez, P. Atomic force microscopy investigation of filled elastomers and comparison with transmission electron microscopy - Application to silica-filled silicone elastomers *Polymer* **2001**, *42*, 6259, 10.1016/S0032-3861(01)00058-1.
[84] Yang, L. ' Tri - 3D ' electron microscopy tomography by FIB , SEM and TEM : Application to polymer nanocomposites **2013**, 166.
[85] Zhang, F.; Chen, Y.; Sun, C.; Wen, S.; Liu, L. Network evolutions in both pure and silica-filled natural rubbers during cyclic shear loading *RSC Advances* **2014**, *4*, 26706, 10.1039/c4ra02003k.
[86] Pal, P. K.; Bhowmick, A. K.; De, S. K. Scanning Electron Microscopy Studies on Failure of Natural Rubber. *Int. J. Polym. Mater. Polym. Biomater.* **1982**, *9*, 139–149.
[87] Ikeda, Y.; Katoh, A.; Shimanuki, J.; Kohjiya, S. Nano-structural observation of in situ silica in natural rubber matrix by three dimensional transmission electron microscopy *Macromolecular Rapid Communications* **2004**, *25*, 1186, 10.1002/marc.200400053.
[88] Jinnai, H.; Shinbori, Y.; Kitaoka, T.; Akutagawa, K.; Mashita, N.; Nishi, T. Three-dimensional structure of a nanocomposite material consisting of two kinds of nanofillers and rubbery matrix studied by transmission electron microtomography

Macromolecules **2007**, *40*, 6758, 10.1021/ma071102d.
[89] Kohjiya, S.; Katoh, A.; Shimanuki, J.; Hasegawa, T.; Ikeda, Y. Three-dimensional nano-structure of in situ silica in natural rubber as revealed by 3D-TEM/electron tomography *Polymer* **2005**, *46*, 4440, 10.1016/j.polymer.2005.02.026.
[90] Kohjiya, S.; Kato, A.; Ikeda, Y. Visualization of nanostructure of soft matter by 3D-TEM: Nanoparticles in a natural rubber matrix *Progress in Polymer Science (Oxford)* **2008**, *33*, 979, 10.1016/j.progpolymsci.2008.06.001.
[91] Tunnicliffe, L. B.; Thomas, A. G.; Busfield, J. J. C. Silica-rubber microstructure visualised in three dimensions by focused ion beam-scanning electron microscopy *Journal of Microscopy* **2012**, *246*, 77, 10.1111/j.1365-2818.2011.03589.x.
[92] Koch, T.; Salaberger, D.; Zankel, A.; Reingruber, H.; Steiger-Thirsfeld, A.; Voronko, Y.; Seidler, S. Methods for Characterizing the 3-D Morphology of Polymer Composites *Macromolecular Symposia* **2012**, *315*, 115, 10.1002/masy.201250515.
[93] Kékicheff, P.; Dabo, M.; Dalongeville, G.; Gauthier, C.; Roland, T. -Polymeric Solid Foams: Mi-crostructure, Topology and Defects Determined by- High Resolution X-Ray Microtomography *Macromolecular Symposia* **2016**, *369*, 56, 10.1002/masy.201600060.
[94] Le Gorju Jago, K. X-Ray Computed Microtomography of Rubber *Rubber Chemistry and Technology* **2013**, *85*, 387, 10.5254/rct.12.87985.
[95] Garcea, S. C.; Wang, Y.; Withers, P. J. X-ray computed tomography of polymer composites *Composites Science and Technology* **2018**, *156*, 305, 10.1016/J.COMPSCITECH.2017.10.023.
[96] Buffière, J.-Y.; Maire, E. *Imagerie 3D en mécanique des matériaux*; Hermes Science Publications, Ed.; Lavosier, **2014**.
[97] Maire, E.; Withers, P. J. Quantitative X-ray tomography *International Materials Reviews* **2014**, *59*, 1, 10.1179/1743280413Y.0000000023.
[98] Salvo, L.; Cloetens, P.; Maire, E.; Zabler, S.; Blandin, J. J.; Buffière, J. Y.; Ludwig, W.; Boller, E.; Bellet, D.; Josserond, C. X-ray micro-tomography an attractive characterisation technique in materials science *Nuclear Instruments and Methods in Physics Research, Section B: Beam Interactions with Materials and Atoms* **2003**, *200*, 273, 10.1016/S0168-583X(02)01689-0.
[99] Tireira, A.; Bornert, M.; Requena, G.; Maire, E.; Sao Jao, S.; Borbely, A.; Klocker, H. Damage in a cast AlSi12Ni alloy: In situ tomography, 2D and 3D image correlation *Materialia* **2019**, *8*, 100475, 10.1016/j.mtla.2019.100475.
[100] Landron, C.; Maire, E.; Bouaziz, O.; Adrien, J.; Lecarme, L.; Bareggi, A. Validation of void growth models using X-ray microtomography characterization of damage in dual phase steels *Acta Materialia* **2011**, *59*, 7564, 10.1016/J.ACTAMAT.2011.08.046.
[101] Marrow, J.; Reinhard, C.; Vertyagina, Y.; Saucedo-Mora, L.; Collins, D.; Mostafavi, M. 3D Studies of Damage by Combined X-ray Tomography and Digital Volume Correlation *Procedia Materials Science* **2014**, 10.1016/j.mspro.2014.06.251.
[102] Buffiere, J. Y. Fatigue Crack Initiation and Propagation from Defects in Metals: Is 3D Characterization Important?; In *Procedia Structural Integrity*; **2017**; 10.1016/j.prostr.2017.11.056.
[103] Liu, R.; Sancaktar, E. Identification of crack progression in filled rubber by micro X-ray CT-scan *International Journal of Fatigue* **2018**, *111*, 144, 10.1016/j.ijfatigue.2018.01.033.
[104] Glanowski, T.; Huneau, B.; Marco, Y.; Le Saux, V.; Champy, C.; Charrier, P. Fatigue initiation mechanisms in elastomers: a microtomography-based analysis *MATEC Web of Conferences* **2018**, *165*, 08005, 10.1051/matecconf/201816508005.
[105] Glanowski, T.; Marco, Y.; Le Saux, V.; Huneau, B.; Champy, C.; Charrier, P. Fatigue

crack initiation around inclusions for a carbon black filled natural rubber: an analysis based on micro-tomography; In *Constitutive Models for Rubber XI*; Huneau, B.; Le Cam, J.-B.; Marco, Y.; Verron, E., Eds.; CRC Press, **2019**; pp 368; 10.1201/9780429324710-64.

[106] Zhou, W.; Chen, L.; Lu, J.; Qi, Z.; Huang, N.; Li, L.; Huang, W. Imaging the strain induced carbon black filler network structure breakage with nano X-ray tomography *RSC Advances* **2014**, *4*, 54500, 10.1039/c4ra09095k.

[107] Nusser, K.; Mosbauer, T.; Schneider, G. J.; Brandt, K.; Weidemann, G.; Goebbels, J.; Riesemeier, H.; Göritz, D. Silica dispersion in styrene butadiene rubber composites studied by synchrotron tomography *Journal of Non-Crystalline Solids* **2012**, *358*, 557, 10.1016/J.JNONCRYSOL.2011.10.009.

[108] Song, L.; Wang, Z.; Tang, X.; Chen, L.; Chen, P.; Yuan, Q.; Li, L. Visualizing the Toughening Mechanism of Nanofiller with 3D X-ray Nano-CT: Stress-Induced Phase Separation of Silica Nanofiller and Silicone Polymer Double Networks *Macromolecules* **2017**, *50*, 7249, 10.1021/acs.macromol.7b00539.

[109] Chen, L.; Song, L.; Li, J.; Chen, P.; Huang, N.; Li, L. From the Volume-Filling Effect to the Stress-Bearing Network: The Reinforcement Mechanisms of Carbon Black Filler in Natural Rubber *Macromolecular Materials and Engineering* **2016**, *301*, 1390, 10.1002/mame.201600235.

[110] Toda, H.; Maire, E.; Aoki, Y.; Kobayashi, M. Three-dimensional strain mapping using in situ X-ray synchrotron microtomography *Journal of Strain Analysis for Engineering Design* **2011**, *46*, 549, 10.1177/0309324711408975.

[111] Limodin, N.; Réthoré, J.; Buffière, J. Y.; Hild, F.; Roux, S.; Ludwig, W.; Rannou, J.; Gravouil, A. Influence of closure on the 3D propagation of fatigue cracks in a nodular cast iron investigated by X-ray tomography and 3D volume correlation *Acta Materialia* **2010**, 10.1016/j.actamat.2010.01.024.

[112] Maire, E.; Le Bourlot, C.; Adrien, J.; Mortensen, A.; Mokso, R. 20 Hz X-ray tomography during an in situ tensile test *International Journal of Fracture* **2016**, *200*, 3, 10.1007/s10704-016-0077-y.

[113] Wu, S. C.; Xiao, T. Q.; Withers, P. J. The imaging of failure in structural materials by synchrotron radiation X-ray microtomography *Engineering Fracture Mechanics* **2017**, *182*, 127, 10.1016/j.engfracmech.2017.07.027.

[114] Khor, K. H.; Buffiérre, J. Y.; Ludwig, W.; Toda, H.; Ubhi, H. S.; Gregson, P. J.; Sinclair, I. In situ high resolution synchrotron x-ray tomography of fatigue crack closure micromechanisms *Journal of Physics Condensed Matter* **2004**, *16*, 10.1088/0953-8984/16/33/012.

[115] Corté, L.; Leibler, L. Analysis of polymer blend morphologies from transmission electron micrographs *Polymer* **2005**, *46*, 6360, 10.1016/j.polymer.2005.05.109.

CHAPTER 2

Materials and protocols

TABLE OF CONTENTS

1 INTRODUCTION

Many applications such as tyres, sealants, and anti-vibration mounts use elastomer. This requires to add various ingredients into the elastomer to optimize its properties. Reinforcing fillers such as carbon black, silica nanoparticles, clay talc or carbon nanotubes are added to the elastomers to modify their ultimate[1], fatigue[2] and visco-elastic[3] properties. Carbon black is predominantly used for various applications. It is available in different grades in the market, varying based on its structure and fineness[4–6]. There also exist different types of elastomer such as Natural Rubber, Isoprene rubber, Styrene butadiene rubber, Butadiene rubber, and Ethylene propylene diene monomer rubber, which can modify the properties of the materials. In this thesis work, we evaluated two types of material composition on their mechanical properties and the defect population inside them. A model material containing just elastomer and carbon black (CB) filler was used to study the analytical effect of concentration of defect on crack initiation and propagation mechanism. The elastomer used is EPDM matrix as it is known to possess good resistance to heat, ozone, oxidation, weathering etc.[7] This material was processed in the laboratory equipment at INSA-Lyon. We tested an industrial compound processed in pilot-scale mixers at LRCCP in Vitry-sur-Seine in order to validate the observed crack mechanism in a material that is used for industrial applications.

2 MATERIALS

2.1 Composition

2.1.1 Elastomer

The elastomer utilized is Ethylene Propylene Diene Monomer (EPDM Keltan 4450)(Figure 1a) from Lanxess. This commercial elastomer contains 52% of polyethylene (PE) and 4.3% of Ethylidene Norbornene (ENB). Depending on the percentage of PE in EPDM, the material can be either crystalline (PE>65%) or amorphous[8]. The composition and Differential Scanning Calorimeter analysis (Method described later) suggest that the elastomer used is a non-crystallizing elastomer[8]. Indeed, this is important to study the influence of carbon black agglomerates on the mechanical properties (crystallinity in the materials can influence the material properties[9]). The glass transition temperature of this EPDM is -52°C (midpoint) (Figure 1b).

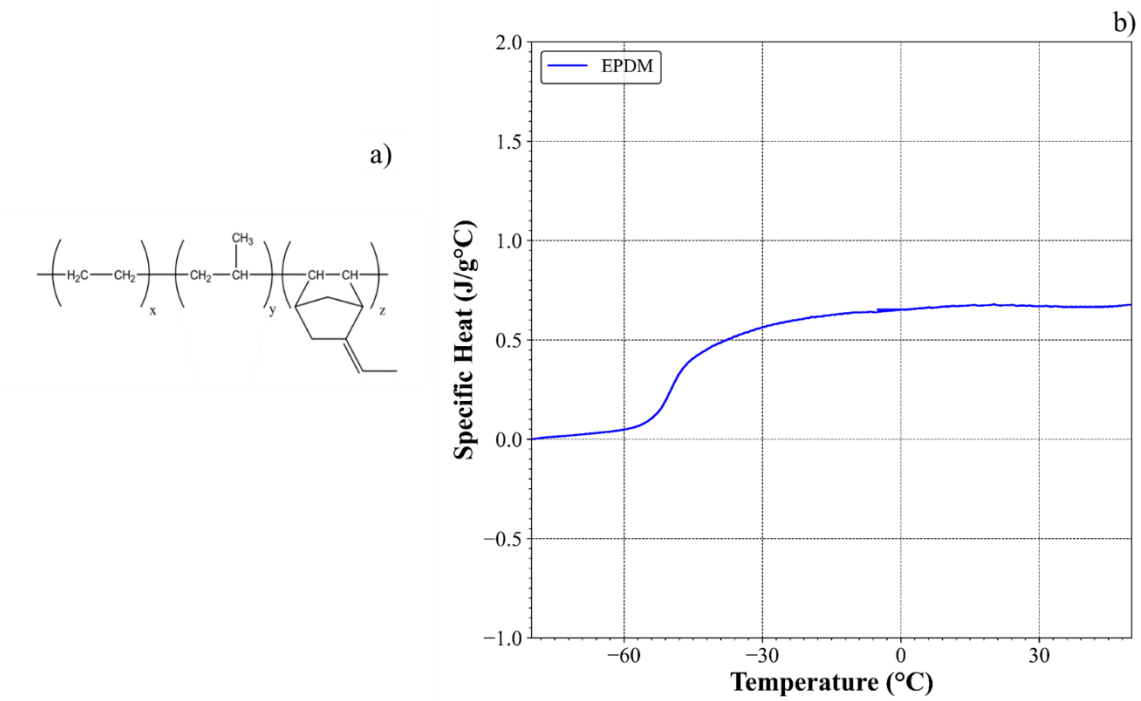

Figure 1: a) Chemical structure for EPDM elastomer, b) DSC heating curve for EPDM Keltan 4450.

2.1.2 Filler

The reinforcing filler in the materials is a high furnace carbon black (N326). N326 carbon black has a surface area of 78m^2/g (BET, Brunauer, Emmett and Teller). Its structure is characterized by a criterion based on oil absorption. The structure indicator is 72 cm^3/100g for this CB. N326 has a low structure with an intermediate specific surface area carbon black (~80m^2/g). The choice of this specific filler is dictated by the objective of generating agglomerates. N326 is known to have bad dispersion in the elastomer. Our studies[10] showed that it is difficult to have a sufficient concentration of carbon black agglomerates, if the material is formulated with higher structure carbon black (N550) (ECCMR Article 1 attached in the Supporting Information).

2.1.3 Curing agents

As mentioned above, we studied two kinds of composition in this thesis. The model materials require a simple composition for characterizing the defects and their impact on crack mechanism. The crosslinking agent used for curing the model materials is unsupported dicumyl peroxide: Bis(α,α-dimethylbenzyl) peroxide (Figure 2). In general, peroxides are supported on filler like $CaCO_3$ for better processability. This has not been chosen in our material formulation as it would introduce unwanted inclusions in the matrix[10]. Sulphur based curing is used in

the industrial material to be more representative of the materials used for various applications. This requires addition of other additives such as ZnO, Stearic acid etc. for cure activation. The complete recipes of both series of materials are given in Table 1 below. Details about the mixing process are given in the following section.

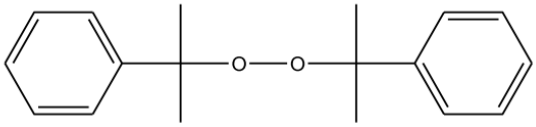

Figure 2: Chemical structure of Bis(α,α-dimethylbenzyl) peroxide

Table1:Materials formulation and mixing process details.

Ingredients	F1 (Phr)	F2 (Phr)	F3 (Phr)	LRCCP (Phr)
EPDM	100	100	100	100
Carbon Black	50	50	50	100
Paraffinique Torilis 6200				40
Zinc Stearate				4.5
MBTS 80				1.5
TBzTD 70				2
Soufre				1.5
ZBEC 70				1
Peroxide	3.2	3.2	3.2	
Rotor Speed (tr/min)	30	60	60	60
Mixing Time (min)	2	4	10	5
Approach	TD 1.EPDM 2.CB	USD 1.CB 2. EPDM	TD 1.EPDM 2.CB	USD 1.CB+Oil 2.EPDM
Filler Volume Fraction	19.3%	19.3%	19.3%	24.8%

2.2 Material processing

The internal mixer used for processing model materials is a Haake Rheomix 600 OS Mixer with a chamber volume of 120cm^3 (Figure 3) equipped with Banbury rotors. The

available volume is then 72 cm^3, which allows to process around 55 g of blend. All the ingredients except curing agents are introduced into the internal mixer for a specific time. The rotor speed of the internal mixer is specified for each material in Table 1. The sequence of introducing the ingredients was varied to study its influence on the occurrence of defects such as agglomerates. USD method refers to “upside down”, i.e. the carbon black is added first, and the elastomer second (1-CB_2-EPDM). TD method refers to “top down”, i.e. the elastomer is introduced first in the internal mixer (1-EPDM_2-CB). The piston that closes the mixing chamber is retracted for few seconds and then the chamber is sealed again at 60s after the start of the mixing process.

Thermo mechanical characterization of the mixing process is presented in Figure 4. The torque attains maximum value in the initial period of mixing which corresponds to the incorporation of the filler inside the elastomer. Torque decreases and eventually stabilizes around 35 Nm. The temperature during mixing increases steadily and reaches a maximum value between 85-90°C at around 120 rotations of banbury rotor. After unloading, the blend undergoes 10 passes in the two-roll mill machine where the curing agent is added. After complete mixing of the material, samples are cured and molded to a square sheet of thickness of 2 mm at 170°C under 190 MPa for 12 min. The samples for mechanical tests are die cut from this sheet by pneumatic punching tool. The pure shear geometry samples (Mini-PS) are prepared using a specific mold under similar curing conditions. The details of the geometries of the samples used for various tests are described in section 3.3.1.

In the processing of industrial materials at LRCCP, the main difference from the laboratory internal mixer used at IMP was the chamber volume (Banbury rotors with 2 liters of chamber volume). USD protocols are commonly used in the industry compared to TD protocol. Here, all the ingredients are introduced at the beginning of the mixing process in the following order: Carbon black along with oil, then elastomer and followed by other additives. The piston that closes the mixing chamber is retracted for few seconds and then the chamber is sealed again at 90s and 240s after the start of the mixing process. This is a standard procedure in industry to improve the re-homogenization of the ingredients. After 300 seconds of mixing, the material is transferred from the internal mixer to the two-roll mill (kept at 30°C) where the curing agents are added. The rest of the procedure is similar to that of model materials.

The cured samples are stocked in a refrigerator, which is at a temperature of -21°C. The samples are taken out only for the experiments.

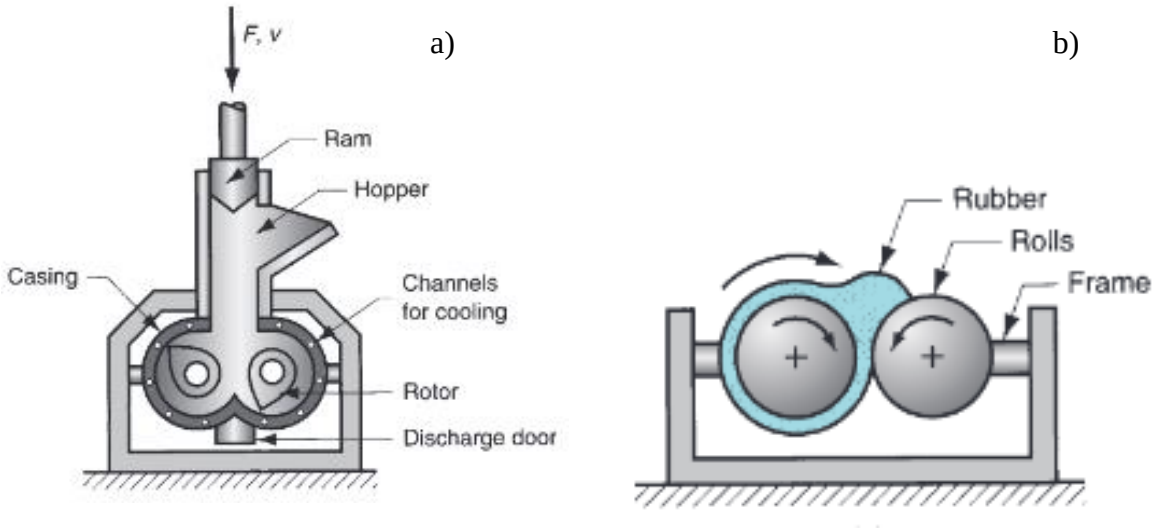

Figure 3: a) Internal mixer, b) 2 roll mill machine [11]

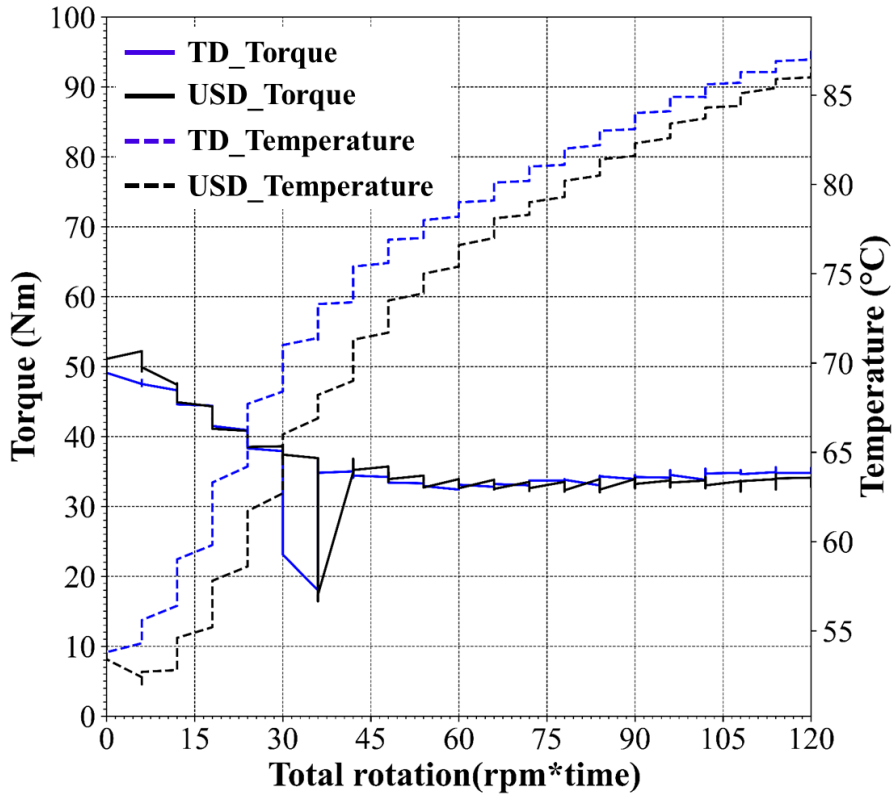

Figure 4: Thermo mechanical characterization of the mixing process.

3 CHARACTERISATIONS OF PHYSICAL PROPERTIES

3.1 Swelling: estimation of crosslinking density

Measurement of swelling of a crosslinked material in a good solvent is a useful technique to obtain the network active chain density, the degree of crosslinking and the fraction of chains that do not belong to the elastomer network (soluble fraction). The degree of swelling depends on the affinity of the solvent and the polymer as well as the average length of polymer chains between the crosslinking nodes.

The solvent used for swelling is Xylene which is very suitable for EPDM elastomers[8]. The protocol for swelling experiment is as follows: a sample (3-4 samples for repeatability) with initial weight M_i is introduced into Xylene at an ambient temperature and let for swelling until it reaches a swelling equilibrium, i.e. constant mass (Figure 5). After weighing the swollen sample (mass M_s), it is dried in a chamber for 24hrs for the evaporation of the solvent. The partially dry sample is completely dried in a vacuum oven at 60°C for another 24hrs, to obtain the final dry mass M_d.

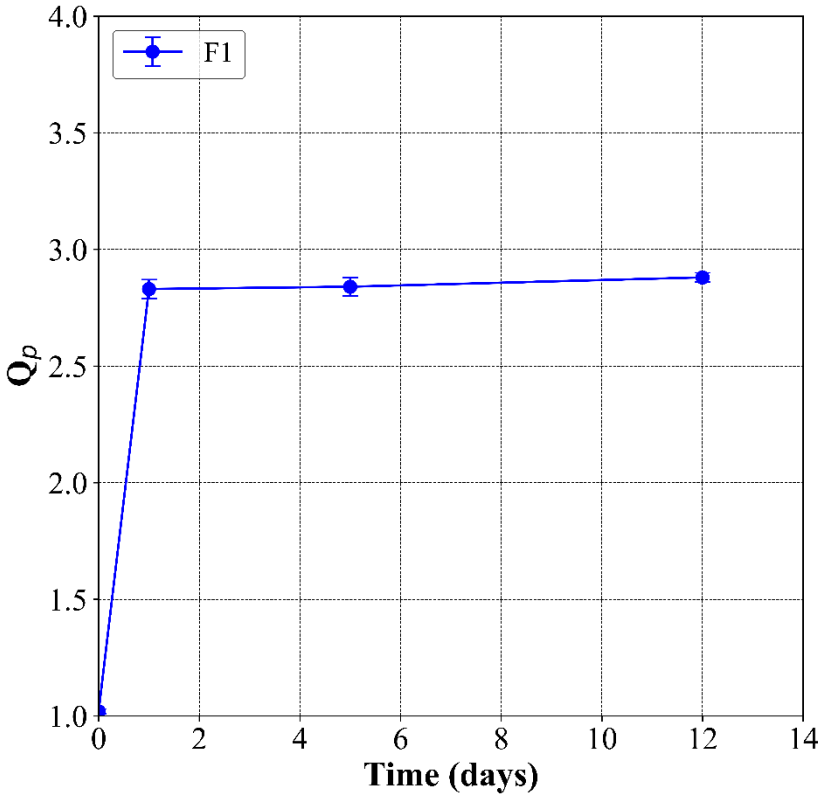

Figure 5: Swelling ratio (Q_p) for the model material F1 as a function of time (days).

The swelling ratio Q and soluble fraction F_s are obtained using:

$$Q = \frac{1}{V_2} = 1 + \frac{\rho_{polymer}}{\rho_{xylene}} . \frac{(M_s - M_d)}{M_d} \quad (1)$$

$$F_s = 100. \frac{M_i - M_d}{M_i} \quad (2)$$

Where, $\rho_{polymer}$, and ρ_{xylene} are the densities of the elastomer and the solvent respectively ($\rho_{polymer}$ = 0.86 g/cm^3, ρ_{xylene} = 0.73g/cm^3). When the elastomer is reinforced with carbon black, it introduces a phase in the materials which cannot be swelled. If we consider that the interaction between the filler and elastomer is perfect, the swelling ratio of the elastomer matrix is given by

$$Q_p = \frac{Q_{composite} - \phi}{1 - \phi} \quad (3)$$

Where ϕ corresponds to the volume fraction of carbon black in the materials and $Q_{composite}$ is the swelling ratio of the material.

One can determine the number of elastically active chains from equilibrium swelling data thanks to the Flory and Rehner equation.

$$\nu_{swelling} = -\frac{[\ln(1 - V_2) + V_2 + \chi * V_2^2]}{V_1 * (V_2^{1/3} - 0.5 * V_2)} \quad (4)$$

Where $\nu_{swelling}$ is the number of active network chain segments expressed in mol.cm^{-3}, V_1 is the molar volume of the solvent (123.4 cm^3/mol for xylene), χ is elastomer-solvent interaction parameter[8] ($\chi_{Xylene-EPDM}$ = 0.49) and V_2 is the volume fraction of elastomer network in the swollen material given by equation 1.

3.2 Differential scanning calorimetry (DSC) analysis

Pyris Diamond Calorimeter (Perkin Elmer, U.S.A) is used for the analysis of phase transitions in the material. This technique measure the amount of heat required to vary the temperature of the sample following a controlled heating/cooling program. From heatflux measurements, one can derive the glass transition temperature of the material (Tg) and the temperatures at which there is crystalline formation (Tc) and melting (Tm). In our protocol, the sample is heated from -80^{0}C to 50°C and cooled back to -80°C at a temperature rate of 10°C/min. To ensure the

thermal equilibrium along the experiments, samples are kept for 5 min at the starting temperature of each step.

3.3 Mechanical testing

3.3.1 Sample geometries for mechanical tests

To understand the macroscopic properties such as tensile, rupture or fatigue, 3 kinds of geometries were used (Figure 6). The sample geometry in Figure 6a is a miniature version of dogbone geometry (used for tensile test and fatigue test) which is adapted for monitoring within the field of view of X-ray Tomography and could then be used for in-situ crack propagation study. The sample geometry in Figure 6b was used for crack initiation study, as it localizes the rupture of the sample at its center and can therefore be studied by X-ray Tomography also. Crack propagation studies have been performed using a pure shear test piece (mini PS) as shown in Figure 6c.

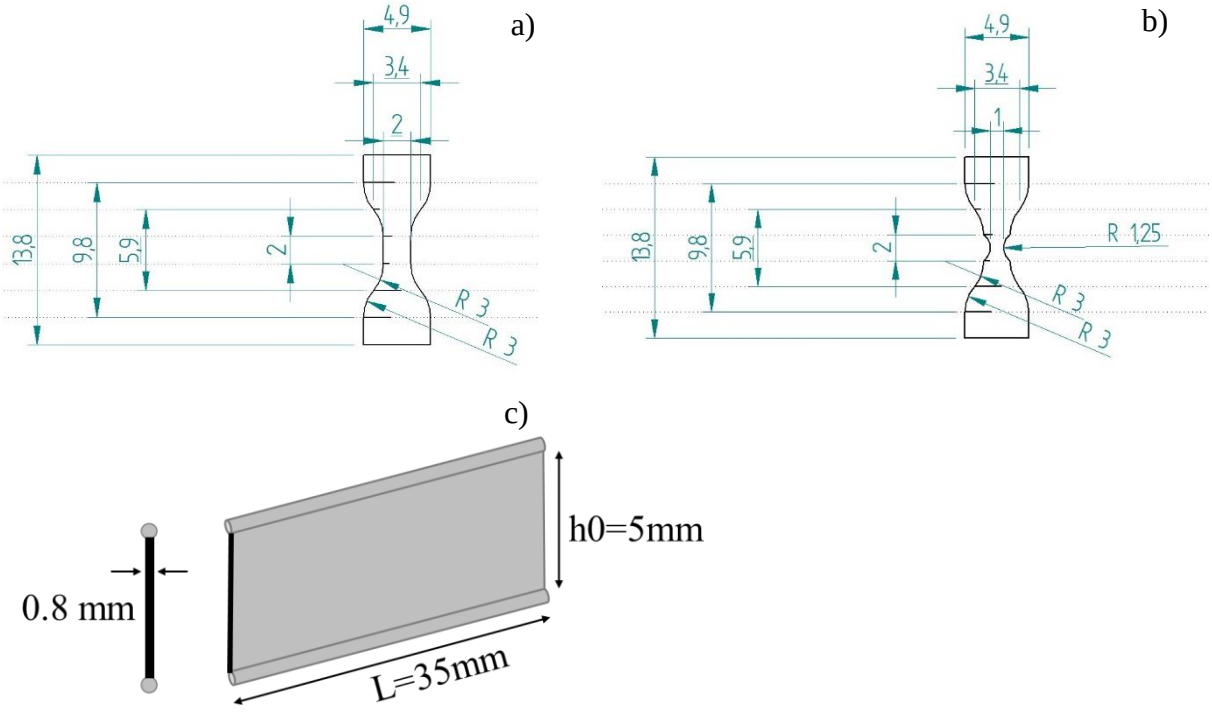

Figure 6: a) Sample geometry used for tensile and fatigue tests. b) Sample geometry used for characterizing the evolution of damage mechanism and rupture properties using in situ tomographic analysis. c) Pure shear specimen geometry used for crack propagation studies.

3.3.2 Uniaxial testing

Tensile testing was performed and the stress-strain curves were analyzed. The nominal stress is defined as $\sigma_n = F(t)/S_0$, where F is the force and S_0 is the initial section of the sample. In most cases, true stress is used, which is defined as $\sigma(t) = F(t)/S(t)$ where *S(t)* is the current

section area of the sample. In elastomeric materials, whose deformation is isochoric, the true stress can be defined as $\sigma_n(1+\epsilon_n)$, where σ_n is the nominal stress and ϵ_n is the nominal strain defined as $\epsilon_n = \frac{\Delta L}{L_0}$ (Figure 7). In the case of homogeneous deformation, the true strain is given by $\epsilon_t = \ln(1+\epsilon_n)$ .The accurate information on nominal and true strains requires specific means for measuring the displacement ΔL, namely mechanical or optical extensometers or, as presented in section 3.4.1, digital image correlation.

Uniaxial tests were conducted on an MTS 1/ME machine equipped with 100N or 1kN load cell depending on the sample geometries used. 100N load cell is suitable for the tensile test on a miniature dogbone sample (Figure 6a, b). For pure shear geometry sample, the force can rise beyond 100N for which 1kN load cell is required. The strain rate is around 0.0065 s^{-1}. In addition, a homemade tensile rig having 5kN load cell has been used for in-situ experiments at synchrotron facilities (section 4.2.2).

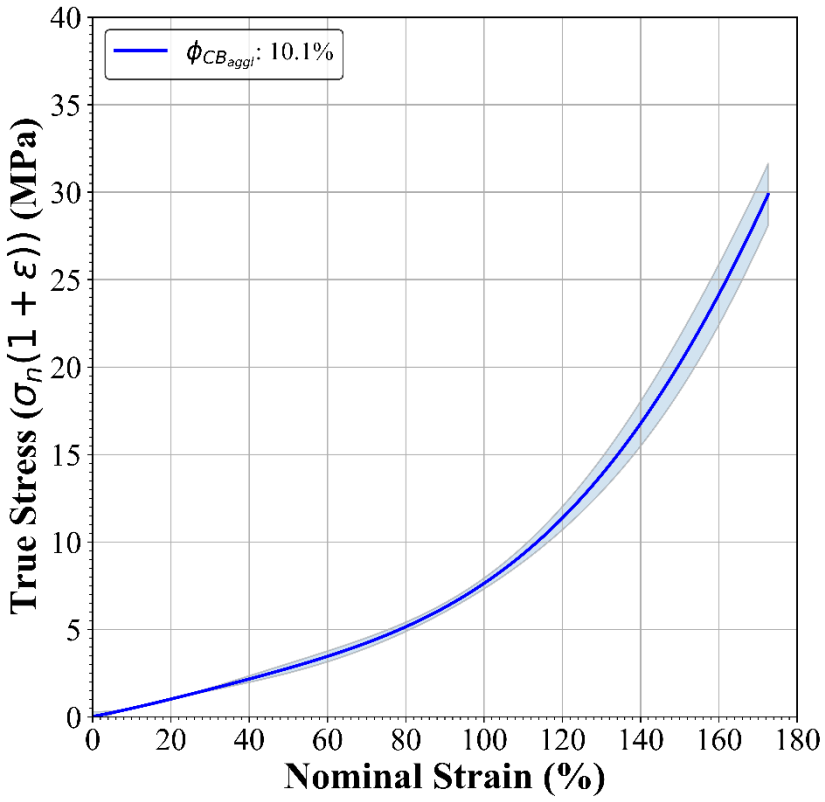

Figure 7: True stress vs nominal strain curves for a model material. The standard deviation in the measurements is given as the shaded region around the main curve.

3.3.3 Fatigue Test

The machine used for fatigue test is Bose Electroforce from TA Instruments. The 22N load cell is used for this experiment. Sample geometry in Figure 6a is used for the test. The frequency of

solicitation is maintained at 2Hz to avoid any self-heating of the samples[12]. All the tests are performed at an ambient temperature. The nominal length of the sample is calculated at a force of 0.1N. The nominal length is calculated after the sample has undergone 100 cycles of accommodation. In addition, the minimum nominal strain is kept at 5% strain in order to avoid any buckling of the sample due to residual deformation. The fatigue life duration of the sample is obtained at various maximum nominal strains. The evolution of crack initiation and further crack propagation is observed through an ex-situ characterization using X-ray Tomography.

3.3.4 Dynamic mechanical analysis (DMA)

DMA is used to study the viscoelastic behavior of materials by measuring its dynamic modulus. One applies a sinusoidal stress (or deformation) to the sample and measures the sinusoidal strain (or stress) response which has a phase shift of an angle δ with the applied solicitation. The dynamic modulus G^* is expressed as $G^* = G' + G''$, where G' is the elastic modulus that measures the stored energy (representing the elastic component of the complex modulus) and G" is the loss modulus which measures the energy dissipated as heat (representing the viscous component). The experiment is performed in the linear viscoelastic domain either in a temperature sweep mode (typically between -150 ° C and 300 ° C, where frequency is constant) or in a frequency sweep mode (typically 0.001 to 1000 Hz, where temperature is constant), or in a strain sweep mode (typically between 0.01% and 50%, where frequency and temperature are constant) to analyze the nonlinear behavior.

We performed dynamic strain sweeps tests at 30°C and 1 Hz in the shear strain range of 0.01% - 10%, using a shear sandwich mode in this thesis. The machine used for the experiment is DMA Q800 (TA Instruments).

3.4 Optical monitoring of mechanical tests

3.4.1 Digital image correlation (DIC)

Digital image correlation is used to understand the true surface deformation profile in the sample during a tensile test. White speckle is sprayed on the sample surface for the purpose of correlation. A high resolution camera of 2Mpixels (1624pixelsx1234pixels) is fixed using a tripod, and is placed at a certain distance of 20 - 50cm from the sample surface. The area around the sample is illuminated using artificial light source. After the calibration of the camera, the images are captured using the software Vic-snap at a frequency of 1Hz - 1000Hz depending on the requirement. After such capture, the images are analyzed using VIC-2D software from Correlated Solutions. The software enables the definition of Region of Interest (ROI) to

calculate the deformation. The coefficient of correlation ($C = \int \left(f(\vec{X}) - g\left[\vec{X} + \vec{U}(\vec{X})\right]\right)^2 d\vec{X}$) is minimized to determine the displacement field $\vec{U}$. $f(\vec{X})$ is the reference configuration of the image and $g\left[\vec{X} + \vec{U}(\vec{X})\right]$ is the deformed configuration. The true nominal strain is calculated based on the successive images rather than using the first image as reference. The mesh size is defined within the region of interest and is provided manually for each sample. The choice depends on the quality of the speckle pattern on the surface. If the speckle pattern is fine and randomly distributed throughout the surface, lower mesh size can be used. This can provide a better spatial resolution of displacement. Otherwise, it can generate errors in the local displacement calculation. In such scenario, a larger mesh size is preferred. For most of the experiments, a mesh size of 15 pixels was kept for correlation. Figure 8 presents differences between the nominal strain ($\frac{\Delta L}{L_0}$) and the nominal strain obtained using DIC on samples tested in the MTS instrument.

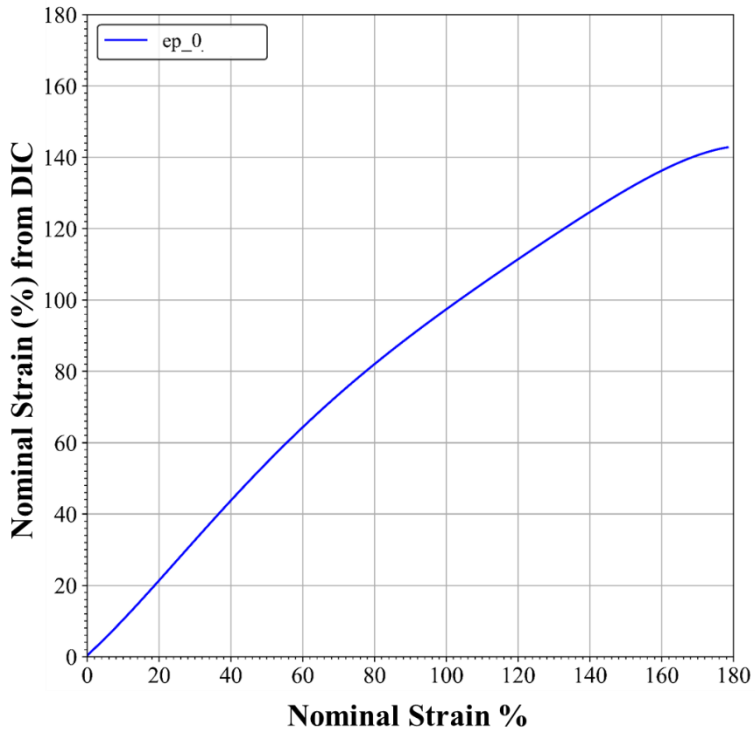

Figure 8 a): Comparison of Nominal strain obtained using DIC vs nominal strain obtained by mechanical extensometer.

3.4.2 Quasi-static crack growth

The study of crack propagation during a quasi-static solicitation requires measurement of crack velocity (Vp), as a function of strain energy release rate (G). G is defined as the energy dissipated during the crack advancement per unit of crack surface area newly formed. The value

of G associated to a crack displacement of c in a mini PS (Figure 9a) with an initial height of h_0 submitted to a stretching of λ, is the product $W(\lambda).h_0$, where $W(\lambda)$ is the strain energy density of the unnotched sample subjected to same elongation. $W(\lambda)$ is calculated from the area under the curve of stress-strain graph. The quasi-static solicitation is performed at a strain rate of 0.0065 s^{-1}. Nominal strain obtained using Digital Image Correlation (DIC) is used for the calculation of G.

3.4.3 Crack propagation speed (V_p)

The samples were not accommodated prior to the crack propagation test. Initial notch of 10mm is made on one side of the test piece with a thin razor blade. Crack displacement up to 5 mm was considered for the analysis of V_p, to ensure the conditions required by Yeoh *et al.* [13], i.e., $1.25< c/h_0 <3$ (c=10mm, h_0=5mm). Crack images were captured using a high-speed camera with a varying temporal resolution of 10ms-100ms. Crack contour (Figures 9a, b, c) and displacement (Figure 9d) on every image were obtained using ImageJ © free software and python modules [14]. Vp was calculated for every 0.2 kJ/m^2 increment of G using the relation: $Vp = (c_{G+0.2} - c_G)/\Delta t$. Finally, the averaged Vp of 3 samples of the same material was used for plotting Vp(G) curves. In addition, instantaneous crack speed (V_{pi}) was calculated from the displacement of the crack between two consecutive images.

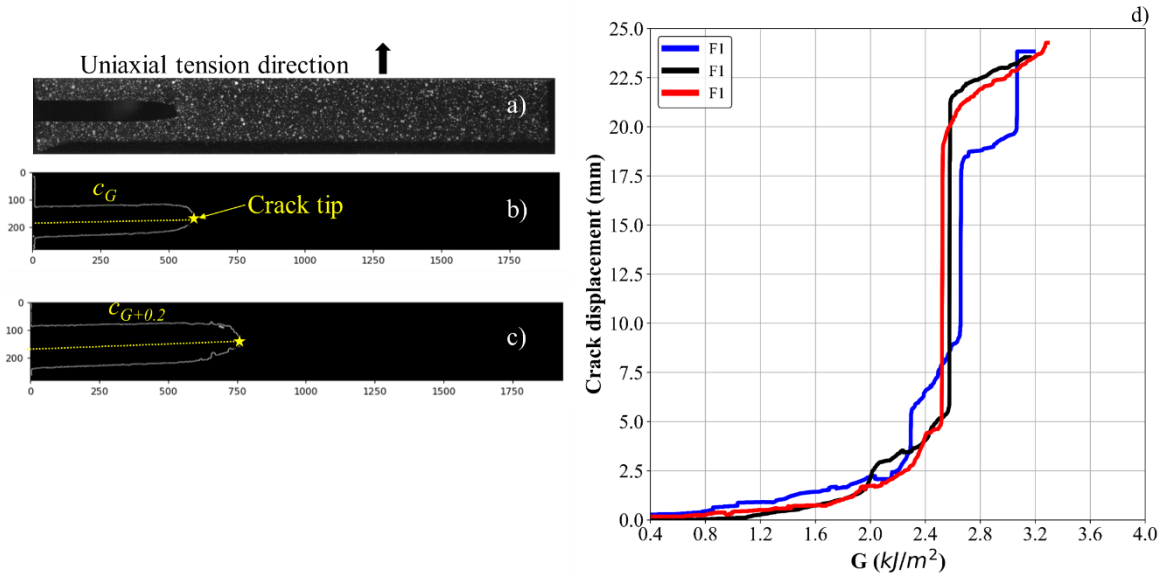

Figure 9: a) Stretched PS notched sample with speckled pattern. b) Crack contour of image presented in the sample in (a) at a given G. The yellow star denotes the crack tip c) Image of the crack propagated after increasing G by 0.2kJ/m^2. d) Crack displacement measured with three samples of the same model material F1 as a function of G.

4 MICROSTRUCTURAL CHARACTERIZATION

4.1 Scanning electron microscopy (SEM)

SEM from Zeiss Supra SEM (Germany) has been used for the observation of rupture surface and dispersion of carbon black in EPDM. All the observations have been made under vacuum without metallizing the surface to avoid any closure of fissure or coating of carbon black agglomerates. The observation of non-metallized sample requires low acceleration voltage to avoid any accumulation of charges on the surface. We have used 1kV and a small working distance (2-6mm) along with secondary electron detector (SE) for characterization. Figure 10 presents the surface of model material F2 that ruptured during a tensile test. In addition, to identify the material composition of the defects at the crack initiation sites, Energy Dispersive X-Ray (EDX) detector has been used along with SE detector. In this combination, acceleration voltage is increased to 10kV to attain a higher emission of characteristic X-ray from the surface of the material.

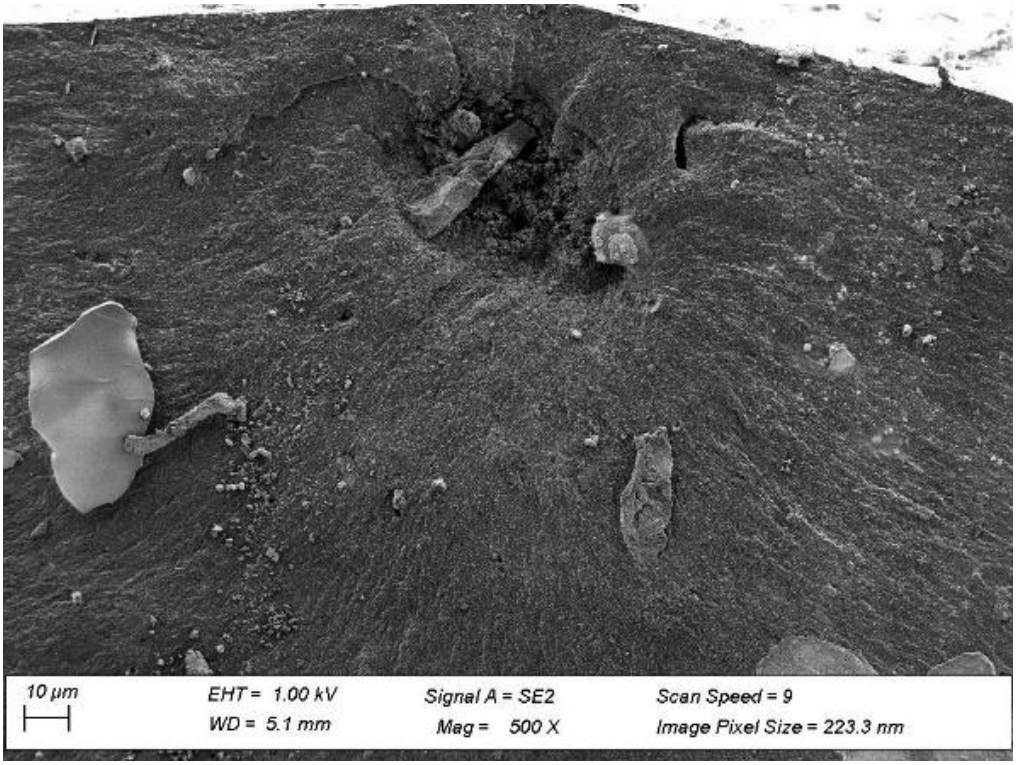

Figure 10: SEM image of model material F2 after rupture

4.2 X-ray tomography

Laboratory sourced and Synchrotron radiation X-ray Tomography have been used extensively in this thesis for various observations.

4.2.1 Laboratory X-ray tomography source (Lab tomography)

The X-ray tomography device is EasyTom Nano from RX solutions (Figure 11a) with a Tungsten target and X-ray sourcing from a LaB_6 cathode filament. CCD detector is used, since it is suitable for X-rays with low energies. The volume analyzed is in the order of 4-6mm^3 with a voxel resolution of 1-2μm^3 depending on the testing requirements. The sample is rotated over 360 degrees in front of the X-ray beam (Figure 11b). Image acquisition is performed at every 0.09° (4000 projections). The tube voltage is kept at 40kV to have an optimised attenuation contrast between the elastomer and agglomerates[10]. A higher tube tension reduces the attenuation contrast of the agglomerates. Lab tomography is used to quantify the morphology and spatial distribution of agglomerates in our model materials. The image processing workflow and protocols related to quantifying morphology and spatial distribution are presented in Chapter 3. Various other measurements such as post mortem analysis of pure shear samples after fracture due to crack propagation, ex-situ measurements during fatigue experiments etc. have been obtained using lab tomography.

a) b)

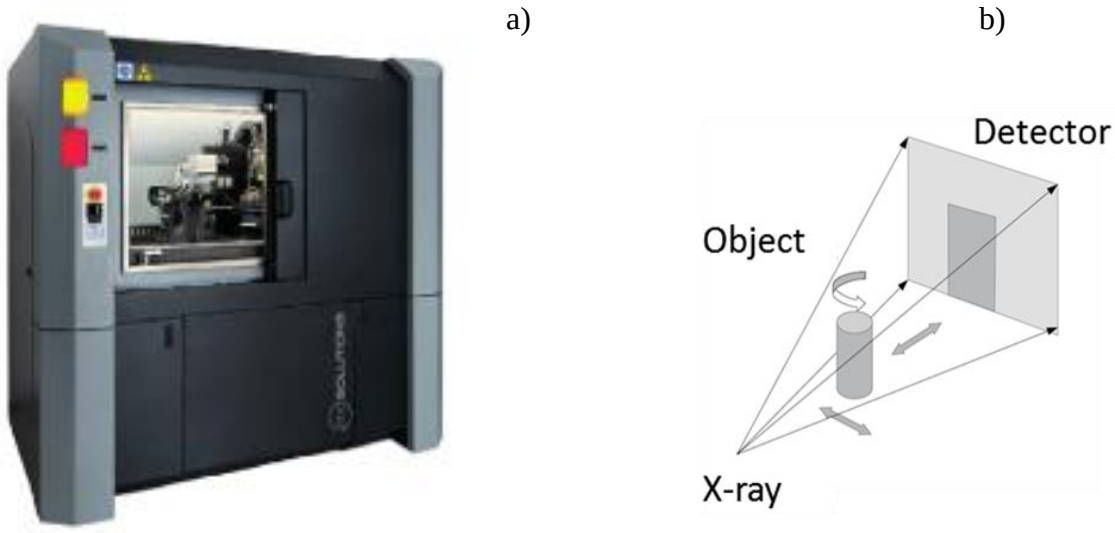

Figure 11: a) EasyTom Nano from RX solution used for X-ray tomography measurements, b) illustration of imaging in X-ray tomography.

4.2.1.1 Ex-situ fatigue test

We conducted an ex-situ test using laboratory sourced X-ray Tomography to characterize the damage evolution in the materials during a fatigue test. Here, we took the tomo scans of the samples by interrupting the fatigue test at pre-determined cycles, i.e. 0 cycle (initial state), 1000 cycles, 2000 cycles etc. These cycles are determined based on the end of life of the material at a given deformation. To obtain the scan, the sample is kept inside the tensile rig as shown in

the Figure 12 and stretched to 15% nominal strain. The sample is kept at this strain to open the cavities or voids inside. The tensile rig consists of plexi-glass® tube. The diameter of the plexi-glass® tube is reduced from 1mm to 0.5mm at the centre, so that there is low transmission loss of photons. The spatial resolution for the experiment is 2µm.

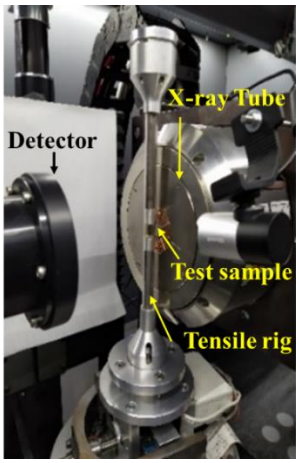

Figure 12: Tensile rig kept inside an X-ray Tomography machine.

4.2.2 Synchrotron radiation computed tomography (SRCT)

Synchrotron radiation has micro resolution and parallel monochromatic X-rays with high spatial coherence. This facilitates phase contrast imaging and precise quantification of the spatial distribution of micro-structural defects in the model materials. Various in-situ characterizations can be performed using this technique due to the fast acquisition capability of synchrotron radiation. Thus, this technique can precisely quantify the microstructure, microstructural evolution of the defects and their impact on the cavitation and crack mechanisms. Experiments have been conducted in two facilities: Anatomix at Soleil, France and P05 imaging beamline at PETRA III, Germany.

4.2.2.1 Characteristics of the synchrotron beamlines

P05 beamline: The energy of monochromatic X-rays was 15keV. The detector for the imaging was a 12 bit CMOS camera (Ximea CB120X8G3) with 4096 x 3072 pixels. We kept the spatial resolution at 2.19µm and applied a binning factor of 2 during the reconstruction, to reduce the file size of the 3D images.

Anatomix beamline: We conducted the experiments using a filtered white beam with a mean energy of 20keV and a 16 bit CMOS camera (Hamamatsu Orca Flash 4.0 V2) with 2048x2048 pixels as a detector. The spatial resolution for the experiment was 1.3µm^3. There was no binning of the images.

4.2.2.2 In-situ mechanical tests using synchrotron X-ray tomography

We studied damage and crack initiation mechanism in our model materials during a tensile test using P05 imaging beamline. The sample is kept inside a load frame for tensile experiments. The load frame consists of polycarbonate tube which has a low impact on the transmission of photons during the imaging (Figure 13a). The load frame is fully integrated into the beamline control system and can be controlled straight from the console. It has a 1 kN load cell. The displacement precision is in microns. The sample undergoes a step displacement of 40µm after every scan, until rupture. The sample is rotated for 360° in steps of 0.225° with 30ms per projection and the total time per scan is 50s. We tested 2 model materials with different concentrations of CB_{aggl}. Each sample had 200 scans taken during the tensile test.

Anatomix beamline is used for crack initiation and propagation studies. To conduct in-situ studies, we installed our own homemade tensile rig on to the rotation stage (Figure 13b). The tensile rig contains a plexi-glass tube. Similar to polycarbonate tube, plexi-glass has low effect on the transmission of photons. The tensile rig has 5kN load cell and displacement precision of 1µm. Using P05 imaging beamline, only 2 samples were tested for crack initiation. Therefore, we conducted further studies at Anatomix to have more statistical points regarding the critical morphology of the defects on the crack initiation. Here sample were scanned at its initial state, at 100% deformed state, and after rupture. The sample geometry used is presented in Figure 7b. Crack propagation studies were carried out using a single-edge notched tensile sample. The sample dimension is 2mm x1 mm (width x thickness), which fits within the field of view (2.3mm x 2.3mm x 2.3mm). The notch length is around 300µm. The notched sample is stretched up to a certain strain (10%, 20% 30% etc.) and kept at the same deformation for 20 min during which the crack can propagate. To stop the crack propagation and the material movements during the tomographic scan, the sample deformation is decreased by 2.5% before launching the scan. The sample is rotated for 360° in steps of 0.18° with 150ms per projection. Each scan took around 8 minutes. The Pagnanin algorithm was applied to reconstruct the phase inside the sample[15].

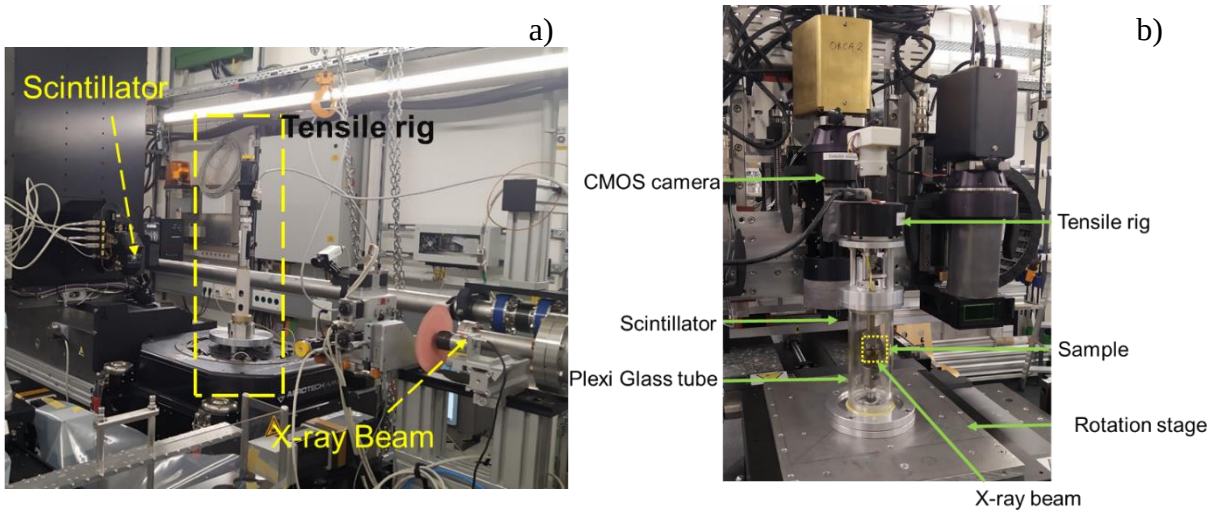

Figure 13: a) Hutch photo with the position of X-ray beam, tensile rig and scintillator at P05, Petra 3, b) hutch photo with the position of X-ray beam, tensile rig, scintillator and homemade tensile rig from MATEIS lab at Anatomix, Soleil.

5 CONCLUSION

This chapter has described the various models and industrial materials studied in this thesis and the methods and protocols related to all the techniques implemented to characterize the properties and microstructures of these materials.

Among these techniques, X-ray tomography will be used extensively for the analysis of microstructural defects and their evolution during a mechanical test. For this purpose, a specific method was designed for the characterization of structural defects. Chapter 3 will be dedicated to the description of this method and of the protocols developed for characterizing the morphology and spatial distribution of the defects using X-ray tomography. Other chapters (Chapters 4, 5, 6) will rely on the use of X-ray tomography for conducting various in-situ experiments to observe the impact of the defects on various mechanical properties. SEM characterization of rupture surface of the materials will be complementary analysis to X-ray tomography analysis.

6 REFERENCES

[1] Medalia, A. I. Effect of Carbon Black on Ultimate Proper.Pdf *Rubber Division, Americal Chemical Society* **1986**, *60*, 45.

[2] Huneau, B.; Masquelier, I.; Marco, Y.; Le Saux, V.; Noizet, S.; Schiel, C.; Charrier, P. Fatigue crack initiation in a carbon black-filled natural rubber *Rubber Chemistry and Technology* **2016**, *89*, 126, 10.5254/rct.15.84809.

[3] *Designing of Elastomer Nanocomposites: From Theory to Applications*; Stöckelhuber,

K. W.; Das, A.; Klüppel, M., Eds.; Advances in Polymer Science; Springer International Publishing: Cham, **2017**; Volume 275; 10.1007/978-3-319-47696-4.

[4] Medalia, A. I. Morphology of aggregates. I. Calculation of shape and bulkiness factors; application to computer-simulated random flocs *Journal of Colloid And Interface Science* **1967**, *24*, 393, 10.1016/0021-9797(67)90267-6.

[5] Medalia, A. I.; Heckman, F. A. Morphology of aggregates—II. Size and shape factors of carbon black aggregates from electron microscopy *Carbon* **1969**, *7*, 567, 10.1016/0008-6223(69)90029-3.

[6] Medalia, A. I. Morphology of aggregates. VI. Effective volume of aggregates of carbon black from electron microscopy; Application to vehicle absorption and to die swell of filled rubber *Journal of Colloid And Interface Science* **1970**, *32*, 115, 10.1016/0021-9797(70)90108-6.

[7] Allen, R. D. Fundamentals of Compounding Epdm for Cost/Performance *Journal of Elastomers & Plastics* **1983**, *15*, 19, 10.1177/009524438301500103.

[8] André, D. A. Propriétés mécaniques et dégradation des élastomères EPDM chargés ATH **2014**, 237.

[9] Rublon, P.; Huneau, B.; Verron, E.; Saintier, N.; Beurrot, S.; Leygue, A.; Mocuta, C.; Thiaudière, D.; Berghezan, D. Multiaxial deformation and strain-induced crystallization around a fatigue crack in natural rubber *Engineering Fracture Mechanics* **2014**, *123*, 59, 10.1016/j.engfracmech.2014.04.003.

[10] Kallungal, J.; Chazeau, L.; Chenal, J.-M.; Adrien, J.; Maire, E.; Barres, C.; Cantaloube, B.; Heuillet, P. Methodology for 3D characterization of microstructural defects in filled polymer using X-ray Tomography; In *Constitutive Models for Rubber XI*; CRC Press, **2019**; pp 77; 10.1201/9780429324710-14.

[11] Groover, M. P. *Fundamentals of modern manufacturing : materials, processes, and systems*; Hoboken, N., Ed.; John Wiley & Sons, Inc., **2020**.

[12] Ostoja-Kuczynski, E.; Charrier, P.; Verron, E.; Marckmann, G.; Gornet, L.; Chagnon, G. Crack initiation in filled natural rubber: experimental database and macroscopic observations *Constitutive Models For Rubber III* **2003**, 41.

[13] Yeoh, O. H. Fracture mechanics of bond failure in the "pure shear" test piece *Rubber Chemistry and Technology* **2003**, *76*, 483, 10.5254/1.3547755.

[14] van der Walt, S.; Schönberger, J. L.; Nunez-Iglesias, J.; Boulogne, F.; Warner, J. D.; Yager, N.; Gouillart, E.; Yu, T. scikit-image: image processing in Python *PeerJ* **2014**, *2*, e453, 10.7717/peerj.453.

[15] Paganin, D.; Mayo, S. C.; Gureyev, T. E.; Miller, P. R.; Wilkins, S. W. Simultaneous phase and amplitude extraction from a single defocused image of a homogeneous object *Journal of Microscopy* **2002**, *206*, 33, 10.1046/j.1365-2818.2002.01010.x.

7 SUPPORTING INFORMATION: "METHODOLOGY FOR 3D CHARACTERIZATION OF MICROSTRUCTURAL DEFECTS IN FILLED POLYMER USING X-RAY TOMOGRAPHY"

J. Kallungal[*,x,†], L. Chazeau, J-M. Chenal, J. Adrien, E. Maire

[*]*Univ Lyon, INSA Lyon, CNRS, MATEIS UMR5510, F-69621, Lyon, France*

C. Barres

[x]*Univ Lyon, INSA Lyon, CNRS, IMP UMR5223, F-69621, Lyon, France*

B. Cantaloube, P. Heuillet

[†]*LRCCP Vitry-sur-Seine, France*

ABSTRACT: Microstructural defects (more precisely their size, their distribution, and their intrinsic characteristics) are known to have a strong impact on crack initiation and propagation and therefore on the material durability. Ultimately, X-Ray tomography represents a relevant experimental tool to provide a 3D characterization of these material defects descriptors. However, the interest of this technique still needs to be evaluated when using non-synchrotron X-ray source. Moreover, the methodology to extract the pertinent data from the 3D scan need to be optimized, especially when phase contrast in the materials is small, as it is the case between carbon black filler and the polymer matrix. In this work, an EPDM matrix is filled with ZnO, Carbon Blacks and Calcium carbonates so that different possible source of structural defects can be evaluated. Several model materials with controlled defects concentration and distribution are then processed. In details, various statistical information such as the distributions of the size and of the inter-particle distance for these defects are computed based on laboratory X-ray Tomography measurements. The discussion then focuses on methodology to determine these crucial microstructural parameters.

7.1 Introduction

Elastomers, due to their specific properties have many applications, the most emblematic being pneumatic and anti-vibration ones. Yet, the optimisation of these properties needs the addition of many ingredients in the pristine polymers: crosslinking agents, fillers, processing aids etc. The incorporation of these ingredients to form a homogeneous mix is achieved through an internal mixer and rolling mill. A typical inorganic filler like carbon black exists as pellets of the size 100µm-2mm. Depending on the processing parameters [1–3]*, a certain fraction of agglomerates is not dispersed and remains as agglomerates. Another typical ingredient used in rubber compounding is ZnO that helps in the activation of the sulphur vulcanization. The existence of unreacted ZnO inclusions in the rubber*

compound after curing was proven through SEM or X-ray Tomography measurements [4,5]. *Moreover regions with over-concentration of fillers (poorly dispersed) can be found as well as micro-bubbles introduced during the mixing step or due to improper wetting of carbon black by matrix. In this paper, the inclusions or agglomerates will be further referred as microstructural defects.*

Early studies demonstrated the importance of considering these defects on the mechanical properties through the physical model developed by Gent and Lake [6–8]. *The modelling effort showed that the intrinsic defects size required for an unfilled non-crystallizing vulcanized rubber to break is 56µm. Similarly, for the rubber compounds reinforced with carbon black, the defect size was found out to be in between 3 to 52µm depending on the characteristics of the filler. Gent et al.* [9] *put forward more evidence on the relevance of these defects by showing the dependence of spatial distribution and surface characteristics of inclusion on the failures of polymer, due to the nucleation of voids to form cavities at critical stress. This result was confirmed using the cavitation model* [10,11] *for multiaxial loading* [4] *which predicts the void location near a defect and the minimum local stress at which a void is created and nucleated to form a cavity. Investigation on a filled polymer compounds* [4,12,13] *under fatigue loading, after its failure or at pre-determined fatigue cycles, showed the existence of defects at the initiation sites of cracks, using high resolution microscopy tools such as SEM. It was observed that* [12], *the minimum size required to initiate the debonding around an agglomerate is 5.1µm in a fatigue test using 100% strain cycle. Under similar condition, the size of the agglomerate for which a cavity around it could become a crack is 41µm, and this could happen as early as 20% of the life cycle. These studies also showed that defects such as ZnO inclusions initiate debonding at the pole with the polymer matrix. Apart from these experimental approaches, numerical studies modelled the defects to predict the fatigue properties* [14], *demonstrating the importance of understanding their spatial distribution.*

All these studies bring-forth the importance of defects in the rubber compounds and hence their precise characterization is required. To this end, most of the literature studies have used SEM, due to its high resolution capability. However, one of the SEM technique drawback is that it can only provide surface information and since it is a destructive method, it does not enable to observe in-situ crack initiation mechanism. Another characterization technique which has been widely used is X-ray Tomography [15,16] *with advantage of obtaining 3D information on the sample at the micron scale. Numerous works have shown the capability of this technique to obtain information on the morphology of voids, inclusions of metallic oxides, and silica filler in the polymer. Nevertheless, few studies reported the detection and distribution of agglomerates of carbon black in the polymer such as SBR, EPDM etc. using non-synchroton sourcing X-ray tomography. Due to the fact that the contrast between the polymer and carbon black is very small, X-ray Tomography using synchroton sourcing is indeed preferred* [17], *because of its phase contrast imaging technique with high intensity flux of photons. With laboratory X-ray Tomograph, optimization of 3D scan acquisition methodology is still required to better characterize these microstructural defects. The aim of this paper is to discuss this optimisation, using model materials*

having controlled concentration and distribution of defects. In addition, we demonstrate the application of X-ray tomography for determining various spatial parameters of the defects.

7.2 Materials and Testing

7.2.1 Materials and Specimen

Formulations of the three model materials chosen for this study are given in Table 1. A non-crystallizing EPDM elastomer has been chosen as the polymer matrix for all the model materials. The curative "Peroxide" used is bis (α, α-dimethylbenzyl) peroxide (~40% weight fraction) sorbed on $CaCO_3$ fillers (~60% weight fraction). HF carbon black was chosen as the reinforcing filler for the model materials 2 and 3. The fabrication of the samples was realized in a Haake Rheomix 600 OS mixer (Volume chamber: 120cm^3) using a Banbury rotor (42 cm^3) for 1 and 2, whereas model material 3 is an industrial grade rubber compound, fabricated using 2kg Banbury internal mixer. Two versions of model 2 were fabricated. They differ by the incorporation time of the carbon black in the matrix, denoted by 2' and 2''. 2' and 2''correspond to the model materials with so-called "bad" and "good" dispersion of the carbon black respectively.

Table 1. Model materials compositions

Ingredients	1 (Phr)	2 (Phr)	3 (Phr)
EPDM	100	100	100
Carbon Black		50	50
Plastiziers			20
ZnO			3
Peroxide	8		8

Table 2. X-ray Tomography parameters

X-ray tube voltage	*40kV-60kV*
Target tube current	*45µA*
Number of projections	*4000-8000*
Resolution	*1 pixel =700nm*

7.2.2 X-ray Tomography

The X-ray Tomography device is from RX solutions with a target of Tungsten and X-ray sourcing from a cathode filament of LaB_6 along with a CCD detector. Volume analyzed is in the order of 10^9 µm^3 with a resolution of 700 nm. The sample is rotated over 360 degrees in front of the X-ray beam, the angle at which each rotation is performed depends on the number

of projections, which could also improves the precision of the image acquisition. All the parameters used in this paper are given in Table 2.

7.2.3 Images processing

ImageJ © free software is used for image processing of the 3D reconstructed volume. Various functions such as geometry offset, ring filter, and phase contrast have been applied to the image stacks to reduce artefacts and to improve the contrast between the matrix and the "fillers". Additionally, 3D median filter function is further used on the image stacks to reduce the overall noise. The segmentation depending on greyscale level, used to differentiate the defects, is performed manually and further manual operation is required to remove the remaining artefacts from the 3D volume reconstruction. It is worth noting that defects with diameters below 2µm are not considered to avoid possible noise artefacts even though data acquisition down to hundreds of nanometres is possible with this apparatus.

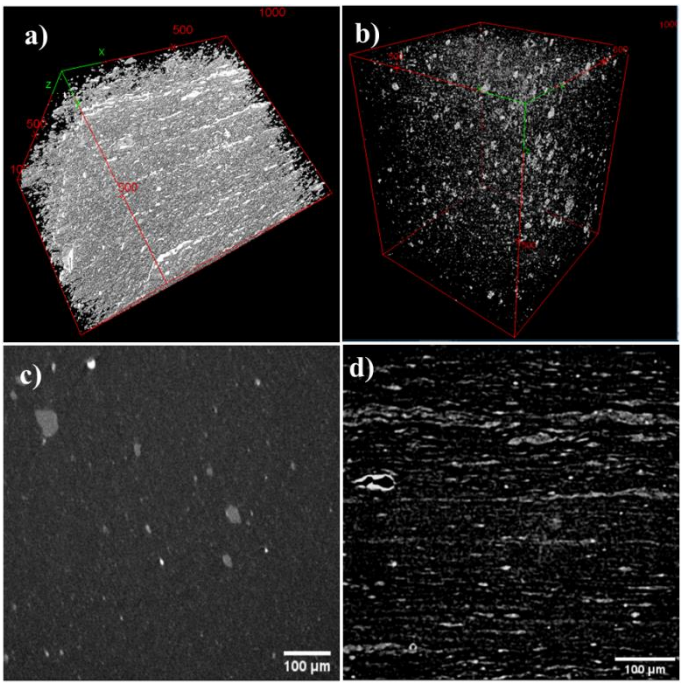

Figure 1: 3D rendering of the 3 model materials highlighting specific defects in them (scale in pixel with 1pixel = 700nm).a) Model 2' with agglomerates of carbon black badly dispersed. b) Model 2''; agglomerates of carbon black well dispersed. c) Grey scale image for $CaCO_3$ filler in model material 1 d) Grey scale image for Carbon black filler in Model 2'

7.3 Results & Discussion

7.3.1 Acquisition parameters

The variation of phase contrast between the defects and the matrix in grey scale images is due to their different linear attenuation coefficient. The corresponding equation for linear attenuation coefficient μ is given by $\mu = K\rho Z^4/E^3$ where K is a constant, ρ is the material density (g/cm^3), Z the atomic number of the material and E is the energy of the incident photon (keV) at the point of interest [18]. This equation indicates that the parameter that could be optimized for improving the linear attenuation coefficient is the energy of the incident photon. In general, changing the tube current increases the number of photons for all the energy spectrum proportionally, while tube voltage changes the energy spectrum (both energy distribution of the photons and quantity). Even though in the laboratory X-ray tomography changing tube voltage from 60kV to 40kV has a low effect on the energy of photon, we observed a significant difference in the contrast for the defects in the model material (Fig 2a). At 60 kV, the total volume fraction of agglomerates (both $CaCO_3$ and Carbon black) obtained is 0.94% whereas at 40kV it has increased to 2.4%. This increase is mainly due to the detection of small defects with size distribution from 2µm to 10µm (Fig 2a). The observed difference in the volume fraction for the same model materials at different tube voltage should come from the better detection of agglomerates of Carbon black. Indeed, the maximum theoretical volume fraction of $CaCO_3$ filler introduced in the material is 1%. To better differentiate $CaCO_3$ and Carbon black, these defects were analysed in a polymer matrix, which only contain either the one or the other (Model materials 1 and 2). The greyscale images for model materials 1 and 2 (Fig 2c-d) show that the contrast between the agglomerates of carbon black or of $CaCO_3$ with the matrix is very similar. Therefore, when both ingredients co-exist in a material (e.g. model material 3), differentiation between them is difficult during segmentation. The proposed optimization of tube voltage is necessary when the phase contrast between defects and matrix is small, whereas for ZnO, since its linear attenuation coefficient is sufficiently high (Z= 30 for Zn), the information obtained at different tube voltage does not vary as shown in Figure 2b. Model material 3 was evaluated at different number of projection (4000 and 8000) to improve the acquisition of defect details. The volume fraction of agglomerates obtained for both cases at 60kV tube voltage, were very similar: 0.94% (4000 projection) vs 0.73% (8000 projections). At 8000 projection we observed higher number of artefacts created by the defects of higher μ, in our case, it's ZnO inclusion. These artefacts can reduce the detection of defects with less contrast in the nearby region, thereby difference in the statistical information.

7.3.2 Processing effect on occurrence of defects

As discussed in section 7.3.1, the minimum volume fraction for the agglomerates that could be obtained is 1.4% even though theoretical total volume fraction of carbon black in the model material 4 is 15.7%. The effect of processing efficiency on the occurrence of the defect is qualitatively and quantitatively verified through Figure 1a-b and Figure 2c. Layers of agglomerates of carbon black are observed in Figure 1c due to the insufficient time given for wetting and dispersion during the mixing process, whereas Figure 1d shows more homogeneously dispersed carbon black in the polymer matrix which corresponds to model 2''. At the same time, the volume fraction of agglomerates in the matrix observed for the model 2' is 4.91% and 0.23 %, for model 2'' (Table 3) which also demonstrates that depending on the dispersion of agglomerates volume fraction detected varies.

7.3.3 Statistical information

A 3D rendering of the defects for each models generated using ImageJ© is shown in Figure 1. Application of X-ray tomography to obtain various statistical information as mentioned in section 2.2 for all the possible defects are given in Figure 2 in detail. The summary of all these parameters are given in the Table 3. The equivalent diameter and inter-particle distance presented in the Table 3 are the median of their distribution. These information are critical to understand initiation and propagation mechanism of cracks. It is interesting to see that statistical distribution for size and inter-particle distance (Fig 2c-d and Table 3) for model materials 1 and 2'' are very similar. At this point one could raise the question of the impact of these 2 types of defects whose the only difference is in their surface characteristics?

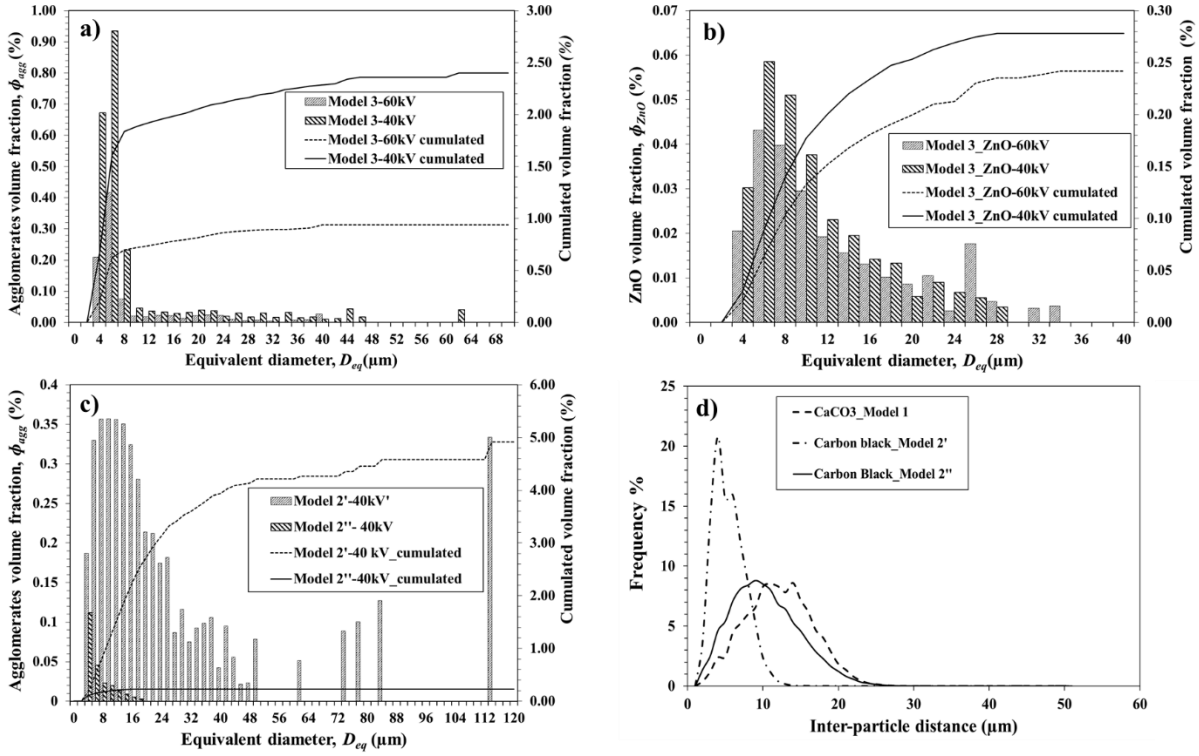

Figure 2. a) ϕ_{agg} of $CaCO_3$ and Carbon black for model 3 at a tube voltage of 60kV and 40kV vs D_{eq}. b) ϕ_{ZnO} for model 3 at different tube voltage 60kV and 40kV vs D_{eq}. c) ϕ_{agg} in model 2' and 2'' vs D_{eq}. d) Frequency distribution of inter-particle distance between the defects for all the model mixes.

Table 3. Summary of the statistical information about defects

Parameters	$CaCO_3$	Carbon Black		ZnO	Agglomerates
	1	2'	2''	3	3
Median Diameter Equivalent (µm)	2.94	3.56	2.69	3.28	2.35
Inter-particle distance (µm)	14.67	7.24	16.8	27.46	27.47
Volume fraction %	0.89	4.91	0.23	0.28	2.4
Theoretical volume fraction %	1.4	18,7	18,7	0.3	16.7

7.4 Conclusion and perspective

The proposed methodology for X-ray Tomography helps us to 3D characterize the defects in the polymer matrix more precisely at the micron scales. It is advisable to use a low tube voltage

in X-ray Tomography, to improve the phase contrast between the defects like agglomerates of carbon black and the polymer matrix. Still X-ray tomography has its own limits, e.g when the linear attenuation coefficient of the defects are very close; it becomes very difficult to differentiate them. Also, methodology presented in this paper does not ensure detection of all the agglomerates with smaller size distribution, which is due to the limitation of the X-ray Tomography with non-synchrotron sourcing. Various statistical information can be obtained from the 3D images analysis using the optimized methodology, such as the distribution of sizes and inter-particle distance. These information are of prime importance when one want to understand the mechanisms of crack initiation and propagation. To do so, the next step of our work will be to conduct in-situ fatigue experiments and to observe the nucleation of voids and crack growth, still using X-Ray tomography.

7.5 References

[1] Cotten, G. R. Mixing of Carbon Black with Rubber I. Measurement of Dispersion Rate by Changes in Mixing Torque *Rubber Chemistry and Technology* **1984**, *57*, 118, 10.5254/1.3535988.

[2] Astruc, M. Thesis,. Étude rhéo-optique des mécanismes de dispersion de mélanges sous cisaillement simple . 1 Mélanges concentrés de polymères immiscibles . 2 Mélanges polymères-charges poreuse, l'École des Mines de Paris, **2008**.

[3] Dizon, E. S. Processing in an Internal Mixer as Affected by Carbon Black Properties. *Rubber Chem. Technol.* **1976**, *49*, 12–27.

[4] Saintier, N. Thesis,. Fatigue multiaxiale dans un élastomère de type NR chargé : mécanismes d'endommagment et critère local d'amorçage de fissure, Ecole Nationale Supérieure d'Arts et Métiers, **2001**.

[5] Marco, Y.; Le Saux, V.; Calloch, S.; Charrier, P. X-ray computed μ-tomography: A tool for the characterization of fatigue defect population in a polychloroprene rubber *Procedia Engineering* **2010**, *2*, 2131, 10.1016/j.proeng.2010.03.229.

[6] Gent, A. N.; Lindley, P. B.; Thomas, A. G. Cut growth and fatigue of rubbers. I. The relationship between cut growth and fatigue *Journal of Applied Polymer Science* **1964**, *8*, 455, 10.1002/app.1964.070080129.

[7] Lake, G. J.; Lindley, P. B. Cut growth and fatigue of rubbers. II. Experiments on a noncrystallizing rubber *Journal of Applied Polymer Science* **1964**, *8*, 707, 10.1002/app.1964.070080212.

[8] Lake, G. J.; Lindley, P. B. The mechanical fatigue limit for rubber *Journal of Applied Polymer Science* **1965**, *9*, 1233, 10.1002/app.1965.070090405.

[9] Gent, A. N.; Park, B. Failure processes in elastomers at or near a rigid spherical inclusion *Journal of Materials Science* **1984**, *19*, 1947, 10.1007/BF00550265.

[10] Hang-Sheng, H.; Abeyaratne, R. Cavitation in elastic and elastic-plastic solids *Journal of the Mechanics and Physics of Solids* **1992**, *40*, 571, 10.1016/0022-5096(92)80004-A.

[11] Fond, C. Cavitation criterion for rubber materials: A review of void-growth models *Journal of Polymer Science, Part B: Polymer Physics* **2001**, 10.1002/polb.1183.

[12] Masquelier, I. Thesis,. Influence de la formulation sur les propriétés en fatigue d'élastomères industriels, Université De Bretagne Occidentale, **2014**.

[13] Le Cam, J. B.; Huneau, B.; Verron, E.; Gornet, L. Mechanism of fatigue crack growth in

carbon black filled natural rubber *Macromolecules* **2004**, *37*, 5011, 10.1021/ma0495386.
[14] Abraham, F. Definition and use of an effective flaw size for the simulation of elastomer fatigue; In *Constitutive models for rubber VII*; Jerrams, S.; Murphy, N., Eds.; CRC Press Inc, London, **2012**; pp 331.
[15] Le Gorju Jago, K. X-Ray Computed Microtomography of Rubber *Rubber Chemistry and Technology* **2013**, *85*, 387, 10.5254/rct.12.87985.
[16] Buffière, J.-Y.; Maire, E. *Imagerie 3D en mécanique des matériaux*; Hermes Science Publications, Ed.; Lavosier, **2014**.
[17] Zhou, W.; Chen, L.; Lu, J.; Qi, Z.; Huang, N.; Li, L.; Huang, W. Imaging the strain induced carbon black filler network structure breakage with nano X-ray tomography *RSC Advances* **2014**, *4*, 54500, 10.1039/c4ra09095k.
[18] Garcea, S. C.; Wang, Y.; Withers, P. J. X-ray computed tomography of polymer composites *Composites Science and Technology* **2018**, *156*, 305, 10.1016/J.COMPSCITECH.2017.10.023.

CHAPTER 3

Novel methodology for quantitative analysis of agglomerates morphology in elastomer composites based on X-ray Tomography

Jesbeer. Kallungal[1,2,3,*], Laurent. Chazeau[1,*], Jean-Marc. Chenal[1], Jérôme. Adrien[1], Eric. Maire[1]

[1]*Univ Lyon, INSA Lyon, CNRS, MATEIS UMR5510, F-69621, Lyon, France*

Claire. Barrès

[2]*Univ Lyon, INSA Lyon, CNRS, IMP UMR5223, F-69621, Lyon, France*

Bernard. Cantaloube, Patrick. Heuillet

[3]*LRCCP Vitry-sur-Seine, France*

Corresponding authors: *jesbeer.kallungal@insa-lyon.fr* *and* *laurent.chazeau@insa-lyon.fr*

Keywords: defects, x-ray tomography, elastomers, microstructural analysis, carbon black agglomerates.

(Article submitted)

TABLE OF CONTENTS

ABSTRACT

In this paper, a novel methodology for characterizing the morphology distribution of filler agglomerates in Elastomer composites is presented, based on laboratory sourced X-ray Tomography. This characterization is mandatory to understand and optimize the fatigue and the rupture properties of this material. Various feature extraction methods (via e.g. Image processing filters, segmentation) and selection tools (Spearman's rank correlation coefficient) combined with K-means unsupervised clustering algorithm were developed for identifying the distinct morphological classes in model materials (carbon filled ethylene propylene diene monomer rubber). The interest of this methodology was demonstrated by precisely differentiating the materials compounded with different processing parameters. For instance, in this example, thanks to this analysis, it was found that introducing the filler before the elastomer in internal mixer tends to favor more structured agglomerates.

1 INTRODUCTION

Elastomers are used in many applications such as load-bearing components, anti-vibration mounts, seals etc… The optimisation of properties for these applications requires the addition of many ingredients in the pristine polymers. The ingredients used are fillers (Carbon black CB, Silica), processing aids (paraffin wax), crosslinking agents (Sulphur, Peroxide), cure activators (zinc Oxide ZnO, Stearic Acid) and accelerators (to control the cure rate). A good dispersion of these ingredients, especially CB, is achieved through their mixing, in an internal mixer and a two roll mill machine. Studies have shown that the choice of processing parameters such as filling ratio, shear rate, ram pressure applied in the internal mixer, mixing energy etc… impacts the morphology (e.g size, shape factor), the spatial distribution and the volume fraction of the CB agglomerates (hereafter referred as CB_{aggl})[1–5]. Apart from them, other microstructural heterogeneities can also exist in the rubber compounds such as unreacted ZnO inclusions, voids etc..[6] Studies have demonstrated the potential impact of all these so called “flaws” or “defects” on crack mechanisms during monotonic and dynamic solicitation of the material[7–16]. Different research works emphasize the importance of quantifying their morphology. For instance, Gent *et al*. proved the dependence of the initiation of cavities in silicone elastomer on the size and spatial distribution of model flaws (using spherical glass beads)[17]. In addition, Chow *et al*. have shown theoretically the importance of the aspect ratio of rigid flaws on these mechanisms, as it impacts the stress concentration at their poles[18].

In literature, the characteristics of carbon black agglomerates (CB_{aggl}) in an elastomer are obtained from the roughness measurement of their micro-tomed sections, or from the light reflexion analysis of a freshly cut sample surface with a Dispergrader technique or from high resolution electron microscopy such as SEM or TEM[10,19]. However, the main drawback of these techniques is that they can only provide 2D information and therefore a full description of the morphology or spatial distribution of CB_{aggl} cannot be drawn up. X-ray Tomography can be used to obtain 3D information on the polymer at the micron scale[20,21]. Due to the similar attenuation contrast of carbon black agglomerates (CB_{aggl}) and elastomer matrix, to the authors' knowledge, only one paper reports their detection and morphological characterization using non-synchrotron sourcing X-ray tomography in an EPDM matrix[22]. To do so, the authors had to adapt the laboratory Tomography parameters. However, a methodology is missing to extract, from the obtained data, the pertinent descriptive features, which can help in relating the agglomerates morphology and spatial dispersion to the material mechanical properties. This is the motivation of the work presented here.

Such methodology could use different tools that have been developed for the classification of filler aggregates. Medalia *et al.*[23–26], through a series of publications, used various Euclidean geometric features, such as bulkiness factor, anisometry, area and structuring factor, to analyse TEM images. Differently, Bourrat *et al*. [27] proposed to use mass fractal analysis, which also applied to the same type of images. This mass fractal approach was extended later by Rieker *et al.* [28] for N330 carbon black dispersed in a polymer matrix, characterized by small-angle X-ray scattering (SAXS) which provides information in the bulk. It was also used by Baeza *et al*. [29] for analyzing the morphology of silica aggregates in an elastomer. Herd *et al.* [30] have shown, when analyzing the morphology of nineteen different carbon blacks dispersed in an elastomer, that the results of both approaches, Fractal *vs* Euclidean geometry, are correlated. However, Euclidean geometry approach appears to be the most pertinent for specific shape classification and for this reason, will be preferred in this paper.

The outline of this article is as follows. The proposed methodology for analyzing filler agglomerates in elastomers is developed using experimental data obtained from model materials. After the description of the model materials and testing methods in section 2, feature extraction and selection techniques are presented (section 3). Following the review of clustering techniques for morphological clustering (section 4), the results and discussion on the classifications are then presented in section 5 and 6 respectively. Such classification is performed for the agglomerates morphology in the different model materials. Our methodology enables to differentiate two materials with identical composition, not only by the volume

fraction of CB_{aggl}, but also through various morphological features. It also provides a valuable tool to understand the impact of operating parameters during the compounding process on the morphology of CB_{aggl}.

2 MATERIALS AND METHODS

2.1 Composition and materials processing

Model elastomers have been fabricated using a non-crystallizing Ethylene Propylene Diene Monomer Rubber (EPDM), and High Furnace carbon black (N326) as reinforcing filler. Table 1 presents the compound composition, which was kept constant, and the compounding process conditions, which were varied. The crosslinking agent is unsupported Bis(α,α-dimethylbenzyl) peroxide. The processing of the samples was performed in a Haake Rheomix 600 OS mixer (chamber volume: 120cm^3) using Banbury rotors (42 cm^3). All the components, except peroxide, were mixed in the internal mixer (IM) for 2 min, and then passed 10 times in the 2 roll mill machine where the peroxide was added. The rotor speed of the internal mixer is specified for each material in Table 1, as well as the sequence for introducing the ingredients. USD protocol refers to "upside down", i.e. the elastomer was added after carbon black. The resulting model materials from this procedure are referenced as 30_rpm_usd and 60_rpm_usd. TD protocol refers to "top down", i.e. carbon black was introduced after the elastomer in the internal mixer, and the resulting model materials are referenced as 30_rpm_td and 60_rpm_td. After the mixing steps, the samples were molded as 2mm thick films by hot pressing at 170°C under 190 MPa for 12 min. Cure time was estimated from the torque measurements, performed using a Monsanto rheometer analyzer.

Table 1: Model materials compositions and compounding process conditions

Ingredients	30_rpm_usd	60_rpm_usd	30_rpm_td	60_rpm_td
	(Phr)	(Phr)	(Phr)	(Phr)
EPDM Keltan 4450	100	100	100	100
Carbon Black N326	50	50	50	50
Peroxide	3.2	3.2	3.2	3.2
Rotor Speed (tr/min)	30	60	30	60
Approach	USD 1. CB 2.EPDM		TD 1.EPDM 2.CB	
Filler Volume Fraction	19.3%	19.3%	19.3%	19.3%

2.2 *X-ray tomography*

The X-ray Tomography device is EasyTom from RX solutions. The Tungsten target current is 45 µA. LaB_6 cathode filament is used, along with a CCD detector. The volume analyzed is in the order of 4-6mm^3. The sample is rotated over 360 degrees in front of the X-ray beam. Image acquisition is performed every 0.09° (4000 projections in total). The voxel resolution in these experiments is 1µm^3. Imaging was performed at a tube voltage of 40kV for an optimised attenuation contrast between the elastomer and agglomerates as discussed in a previous paper[22] .

3 FEATURE EXTRACTION

3D images obtained from X-ray Tomography show different flaws like carbon black agglomerates, voids, etc... The feature extraction methodology involves applying different algorithms of image processing to selectively display CB_{aggl} from the acquired tomography scans. Thereby, various statistical information related to their morphology can be obtained. A methodology to extract the CB_{aggl} spatial distribution was also applied on the same samples. It is described in SI along with the obtained results (Description A1).

3.1 Image processing

Various functions such as geometry offset, ring filter, and phase contrast are applied to the raw images to reduce artefacts and to improve the contrast between the matrix and the filler particles. Image stacks are then built using a filtered back projection reconstruction algorithm. Several Python modules are then used for image processing on the 3D reconstructed volume. The general approach of feature segmentation by segregating the greyscale cannot be applied in our case, since there is no significant difference in the attenuation contrast between the matrix and the CB_{aggl}. Therefore, various image filters are applied again on the image stack (Figure 1a) to optimise the contrast and to remove additional noise. Typical denoising filters such as the median filter are not effective. For this reason, a different workflow of image processing is devised, which is inspired from the works of Emmanuelle Gouillart [31,32] . After intensity rescaling (to improve the brightness and contrast) (Figure 1b), bilateral (Figure 1c) and non-local means (Figure 1d) filters are applied on the image stack. In bilateral filter, the intensity of each pixel in the image is replaced with a weighted average intensity of nearby pixels for noise reduction and edge preservation. In non-local means filter (effective for images with fine-grained texture), each target pixel value is replaced by an average of all the neighbourhood pixels value, weighted by how similar these pixels are to the target pixel [33]. Subsequently,

segmentation of the image is carried out, which is a crucial step for obtaining pertinent information. Here we are using a supervised segmentation algorithm called Random Walker which was developed by Grady to reduce manual intervention and user bias[33,34]. The different image treatments have been implemented through the scikit-image module in Python[35]. The output of the image processing and segmentation is presented in Figure 1e. The final process of removal of the particles touching the edges of the stack, as these may intervene in the morphological classification of CB_{aggl}, is performed using ImageJ © free software. A sample sub volume of the reconstructed 3D image is shown in Figure 2.

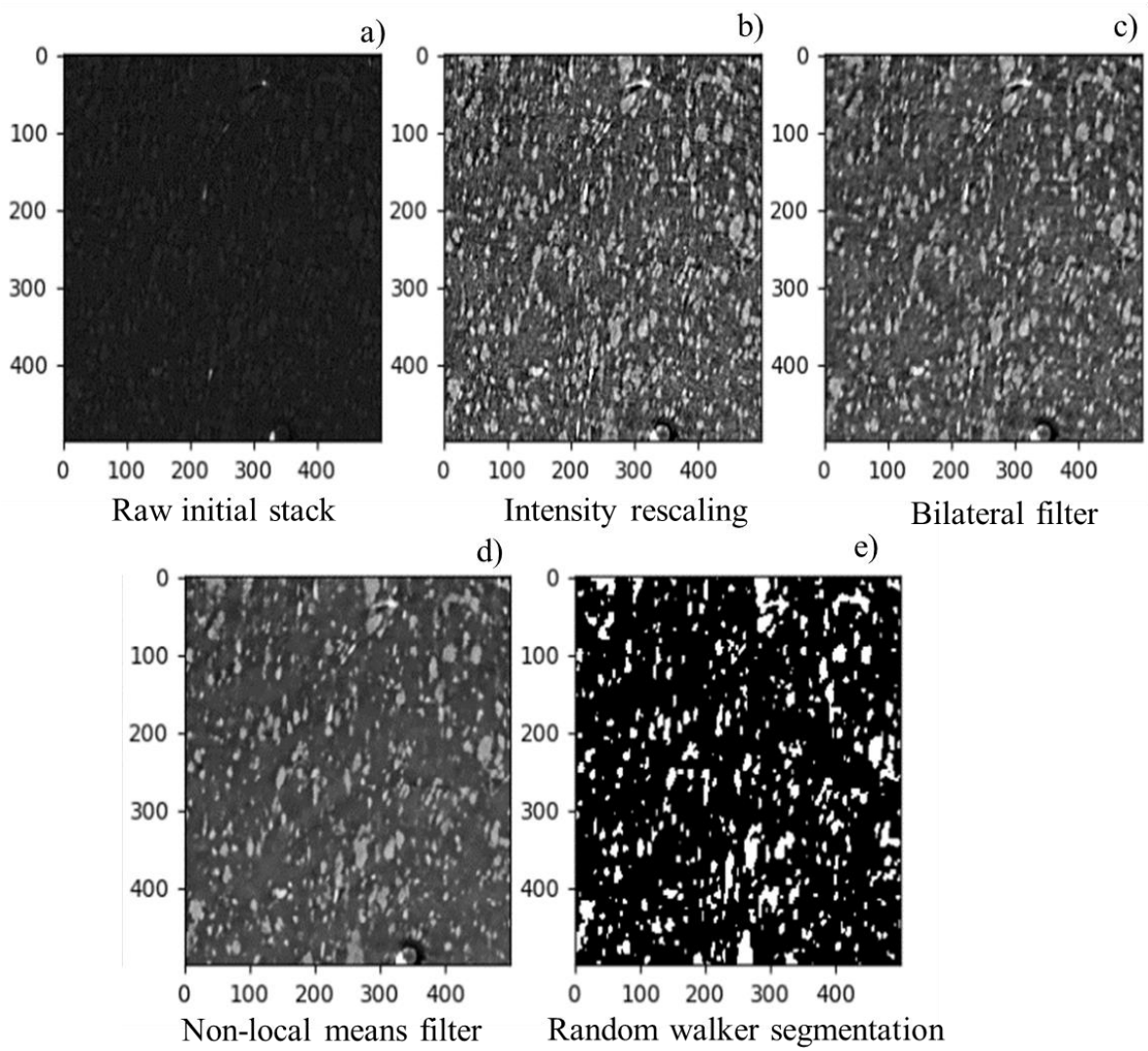

Figure 1: Image processing flowchart

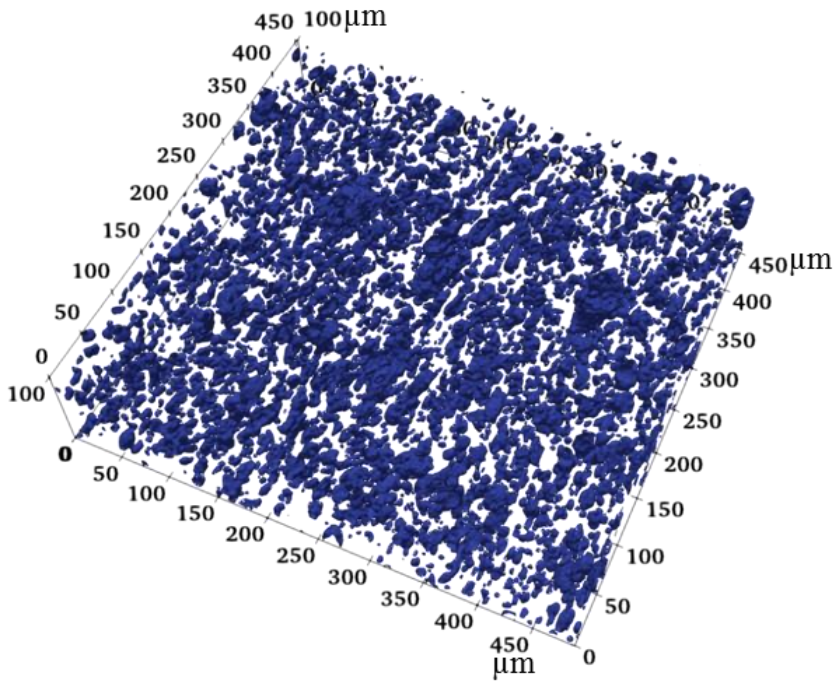

Figure 2: Sub-section volume of the model material 60_rpm_usd obtained using 3D Tomography visualized using ParaView © software. Sub-section volume of the model material 30_rpm_usd is given in SI (Figure A4)

3.2 Morphological features extracted

Each agglomerate is labelled in the binary image after its segmentation from the matrix. Agglomerates with volume below 125 voxels have not been considered. Geometric features such as Eccentricity E, Anisometry Q, Bulk factor B, Volume V, Equivalent Diameter Eq_{diam}, Length of major principle axis a, and Length of minor principle axis b of each CB_{aggl} are extracted using the *regionprops* module in Python[35].

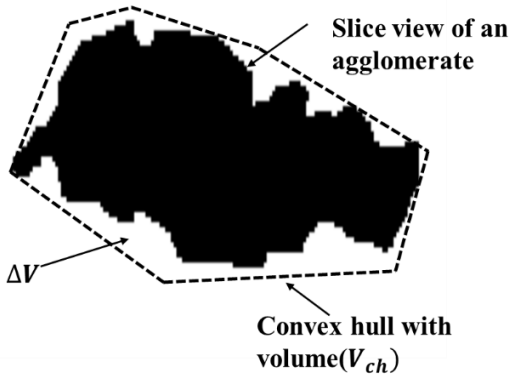

Figure 3: Bounding of convex hull around an agglomerate to calculate the bulk factor

The volume V of a CB_{aggl} is calculated by counting the number of voxels it contains. The Equivalent diameter (Eq_{diam}) represents a diameter of a fictive spherical inclusion having the

same volume as the analyzed CB_{aggl}. Length of major (a) and minor principal axis (b) are those of an *ellipsoid* that has similar normalized 2nd central moment [36] as the CB_{aggl}. Eccentricity (E) of an ellipse is defined as the ratio between its distance of two foci and the major principal axis length. Here, E is the eccentricity of the centered elliptic section of the ellipsoid, perpendicular to the c axis (with $a > c > b$):

$$E = \sqrt{1 - b^2/a^2} \quad (1)$$

For E=0, the morphology is a sphere and for E close to 1 the morphology get closer to that of a 1D or 2D object. Anisometry (Q) is the ratio of radii of gyration and corresponds to anisometry of the agglomerates as calculated by Medalia *et al.* [23]:

$$Q = b/a \quad (2)$$

Bulk factor (B) corresponds to the ratio of the free space (volume in this case) between the agglomerates and the convex hull constructed around the agglomerate (ΔV) to the total volume of the convex hull (V_{ch}), as shown in Figure 3:

$$B = 1 - V/V_{ch} \quad (3)$$

This definition is slightly different from the approach used by Medalia *et al*. [23] who proposed to express bulkiness as a ratio of the area of radius-equivalent ellipse drawn around the object to its projected area.

3.3 Feature selection

Using all the features V, Eq_{diam}, B, E, b, a, and Q for clustering presents some disadvantages. Firstly, if the two relevant features chosen are strongly correlated to each other, they add more weight to the classification process and thereby generate biased clusters. Secondly, the computation complexity of clustering increases as the number of features increases. Therefore, feature selection techniques have to be applied to evaluate the relevance of each one. Such step is very critical when defining the morphology classes by unsupervised pattern recognition, since we lack prior knowledge of each morphology class features. First, the relevance of each feature was checked using Laplacian Score technique (described in SI: Description A2). Then Spearman's rank correlation coefficient (ρ) has been used to discard the redundant feature. ρ characterises the monotonic relations (linear or not) between two features. It varies between -1 to 1. A value close to |1| implies that they are correlated. Here, if two features have a coefficient value below |0.7|, they will be considered distinct. All the calculated ρ values are reported in Figure 4 along with their distribution. All data from all studied materials have been used for the analysis. They show that a, b, and Eq_{diam} are correlated to each other and also to V. As expected, E is negatively correlated to Q (aspect ratio). B is only correlated to a and feature a is correlated

to other features (V, Eq_{diam} and b). Feature B has been retained because it can provide information on the fact whether the agglomerates are structured or not and the two other relevant retained features are V (size) and E (Eccentricity).

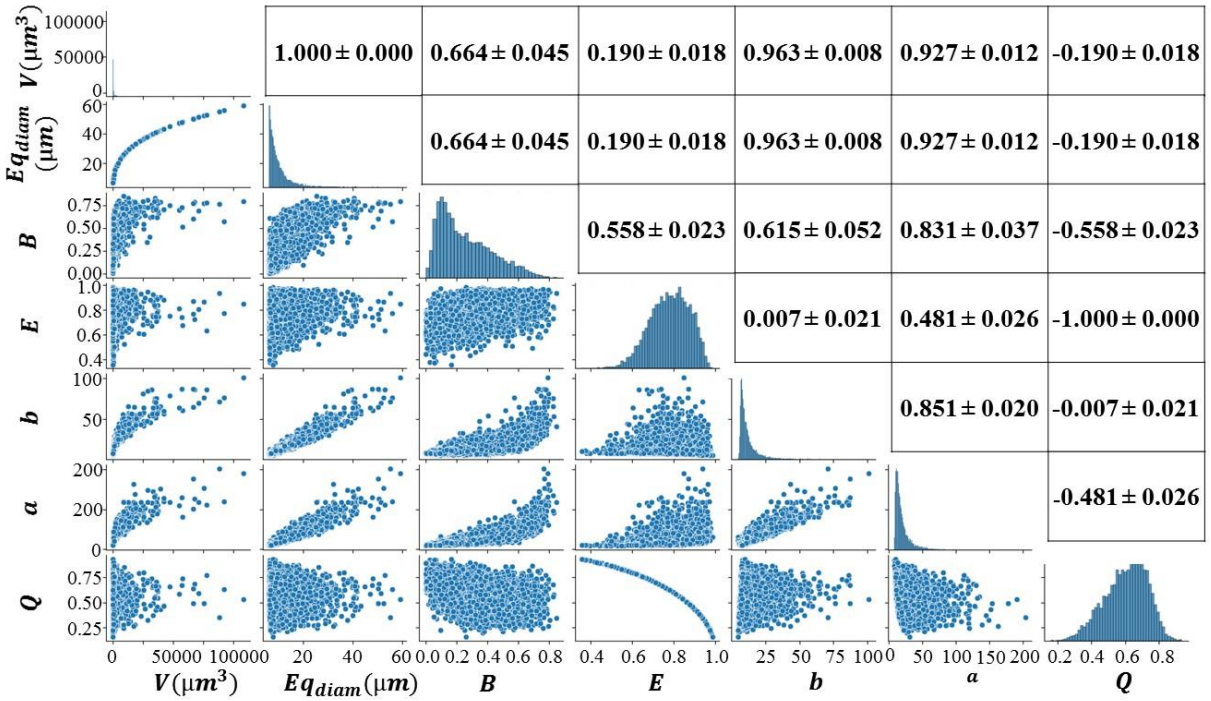

Figure 4: Lower half of diagonal: Correlation plot for feature pairs, Diagonal: relative frequency distribution of each feature. Upper half of diagonal: Spearman's rank correlation coefficient between features.

The distributions of V, E and B for the 4 model materials are plotted in Figure 5. V distribution is similar for all the materials, with a slight difference in the domain $1.25*10^3$-$2.25*10^3$ µm^3. The relative frequency is lower for the materials processed with the upside-down protocol (USD) in this domain (cf Figure 5a, b). The distribution curves of B (structure factor) have a similar shape for all the materials (Figure 5c). The curves also indicate that the agglomerates of the 60_rpm_td are the less structured, and those in the 30_rpm_usd are the most structured. The E distributions of the 4 materials (cf Figure 5d) have similar Gaussian shape with mean values around 0.75 for all the materials, indicating that their agglomerates are not spherical.

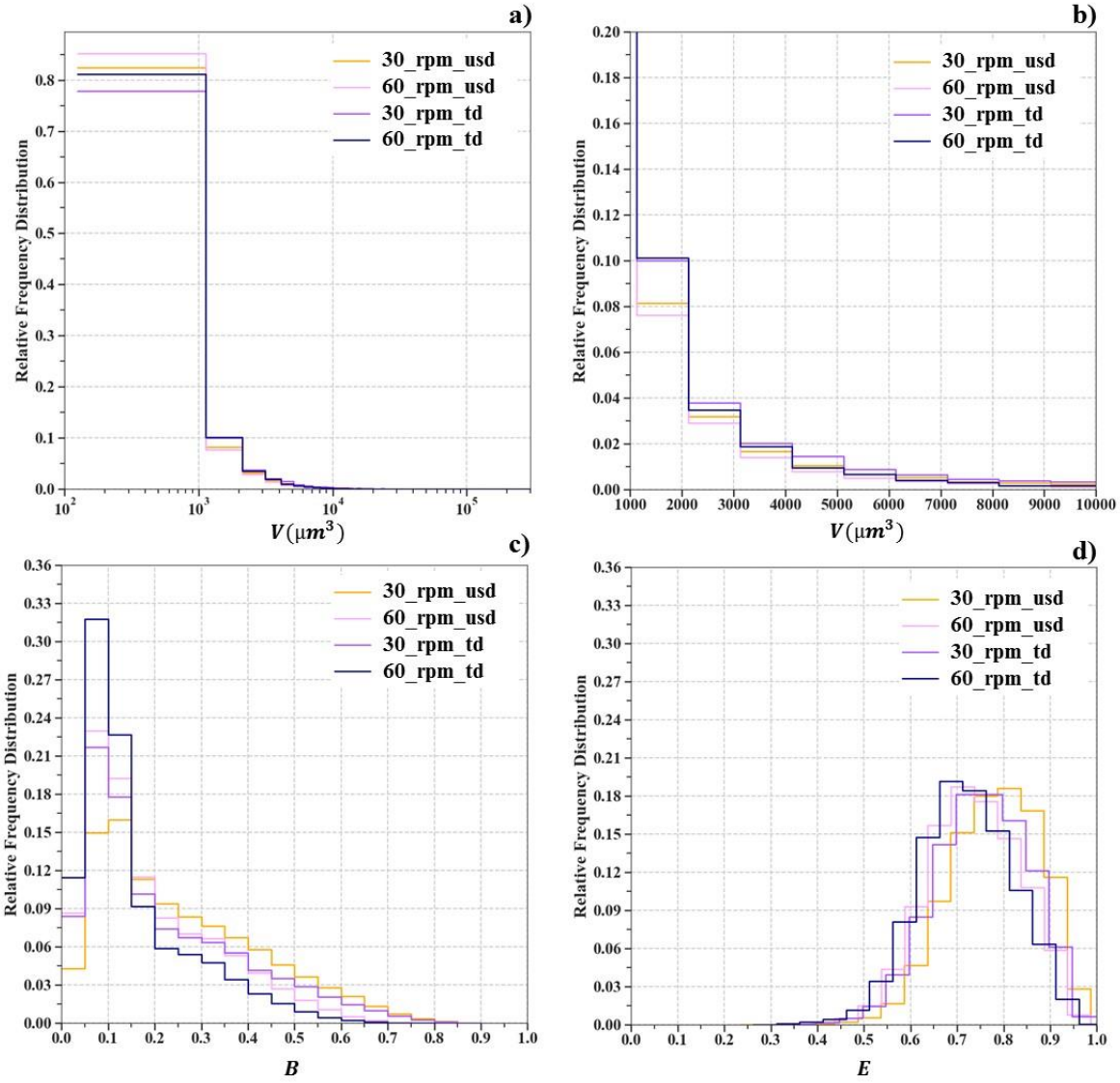

Figure 5: Statistics on each geometric features of the morphology of CB_{aggl} for all the model mixes (30_rpm_usd, 60_rpm_usd, 30_rpm_td, 60_rpm_td) : a) volume V ; b) zoom on V values in the 10^3-10^4 decade ; c) bulk factor B ; d) eccentricity E.

To sum up, there are only slight differences between the 4 materials, regarding their *E*, *B*, and *V* distributions. Moreover, as they can only be discussed separately, it is impossible to know for instance, if the largest number fraction of agglomerates with a low structure factor in the 60 rpm_td is related to the smallest or the biggest agglomerates. In other words, these distributions do not provide a clear picture of the differences in the agglomerates morphology. This motivates the use of the clustering methodology described in the following.

4 CLUSTERING

Manual clustering of all agglomerates using all the relevant features is a cumbersome task. Some authors have recently used unsupervised clustering techniques (Machine learning algorithms) such as hierarchical clustering, or principle component analysis [36] to solve this problem[36–38] . For practical reasons, we chose K-means unsupervised clustering algorithm. This was implemented using scikit-learn machine learning module in Python[39] .

4.1 K-means unsupervised clustering

K-means clustering algorithm attributes a set of data points x_i (x_i is defined by p coordinates) describing n agglomerates $(1 \leq i \leq n)$ by p features (*V, B, E*)) into k clusters C= $\{C_1, C_2,..,C_k\}$. Each cluster can be described by the mean μ_j of the observations in the cluster, commonly called as cluster centroid. The algorithm tries to find a centroid that minimizes the inertia or the variance of the squared Euclidean distance within the cluster, $||x_i-\mu_j||^2$

$$\sum_{j=1}^{k} \sum_{x \in C_j} \left\| x_i - \mu_j \right\|^2 \qquad (4)$$

As the number of clusters *k* is not known *a priori*, 2 validation criteria were used to determine the optimal number of clusters.

- Calinski Harabasz (*CAH*): this ratio is sometimes called variance ratio criterion.

  $$CAH = (SS_B/SS_W) \times (N - k) / (k - 1) \qquad (5)$$

  Where SS_B is the overall "between-cluster" variance, SS_w is the overall "within cluster" variance, *k* is the number of clusters and N is the total number of data points (i.e. agglomerates). *CAH* metric works very well for clustering algorithm based on squared Euclidean distances such as K-means[40] . The ideal number of clusters corresponds to the highest *CAH* score.

- The Davies and Bouldin index (*DBI*) can be used to infer the average similarity of a cluster with its most similar cluster[41]. In this context, it is given by the equation as follows:

  $$DBI = \frac{1}{k} \sum_{i=1}^{k} \max_{j \neq i} \left(\frac{s_i + s_j}{d_{ij}} \right) \qquad (6)$$

  s_i is the average distance between each data points in cluster i and its centroid (similarly for s_j) , d_{ij} is the average distance between the clusters centroids i and j. *DBI* index is the lowest for the ideal number of clusters.

The workflow deployed in this article to have a generalized morphological cluster analysis is schematized in Figure 6. Across-over sampling between model materials 30_rpm_usd, 60_rpm_usd, 30_rpm_td and 60_rpm_td has been applied. 30% of the overall data points

(163907 data points) have been randomly chosen to train the clustering algorithm. This step is repeated 10 times to remove the effect of sampling on the determination of the number of clusters. The trained model is later on applied to all the data of each material to build their final clustering.

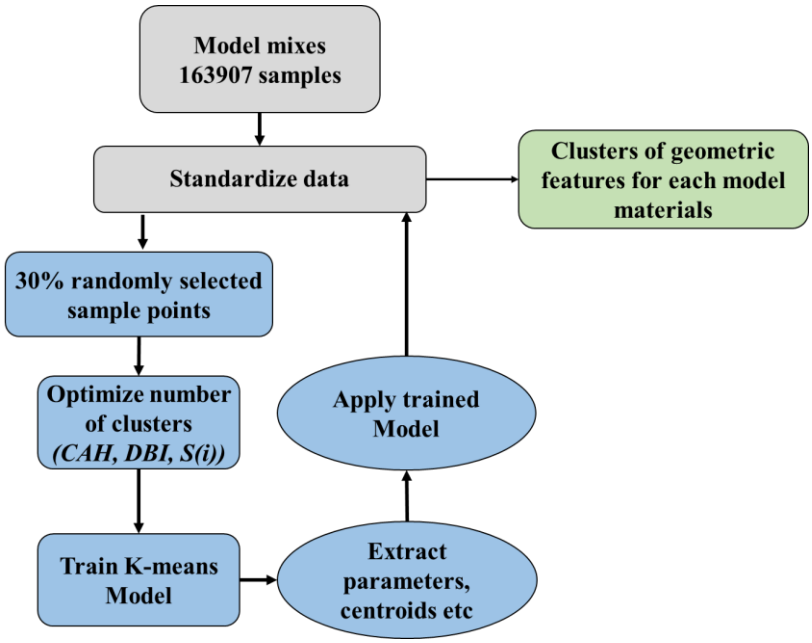

Figure 6: Illustration of the sampling of data and training of the K-means model

4.2 Statistical analysis of geometric features

As shown in the relative frequency distribution of V (cf. Figure 5), the 75% quartile and mean values indicate that most of the data lie close to the lower side of the distribution. In the case of *B* and *E*, they are more uniformly distributed. Since these features have a different order of magnitude, clustering on the raw data of *V* might bring biased clusters. For this reason, we applied standardization calculation to each feature *f* as follows:

$$f_{standard} = \frac{f(x) - f_{mean}}{\sigma} \quad (8)$$

which scales the data to unit variance and 0 mean. f_{mean} and σ are the mean and standard deviation of the distribution of the observations of the feature *f*. Other standardization techniques exist, such as rescaling the data to [0, 1], scaling the data according to the quantile range, or transforming data from various distributions to a normal distribution. These techniques were discarded as it was found that they do not provide relevant results. The normalized distribution for each feature is presented in SI (Figure A5).

4.3 Number of clusters

The number of clusters is chosen from the calculations of the metrics *DBI* and *CAH*. As said previously, they have been calculated from 10 random samplings of data. These samplings have a very small influence on the found metric values. Their average is given in Table 2 for *DBI*, and reported in Figure 7 for *CAH*. Note that a third criteria, Silhouette coefficient (S_{avg}) has also been used to determine the optimal number of clusters[42] . However, this metric does not seems relevant for the choice of the cluster number (Description A3 and Table A3 in SI). For a cluster number of 9, *DBI* and CAH metrics show a local minimum and maximum respectively, suggesting that 9 is the optimal number of clusters.

Table 2: DBI Metric evaluation for each number of clusters, deduced from 10 random samplings

k number of clusters	*DBI*
2	0.932±0.01
3	0.800±0.05
4	0.836±0.00
5	0.853±0.08
6	0.859±0.03
7	0.811±0.02
8	0.801±0.02
9	**0.797±0.02**
10	0.829±0.02
11	0.849±0.02
12	0.852±0.01
13	0.852±0.01
14	0.846±0.02

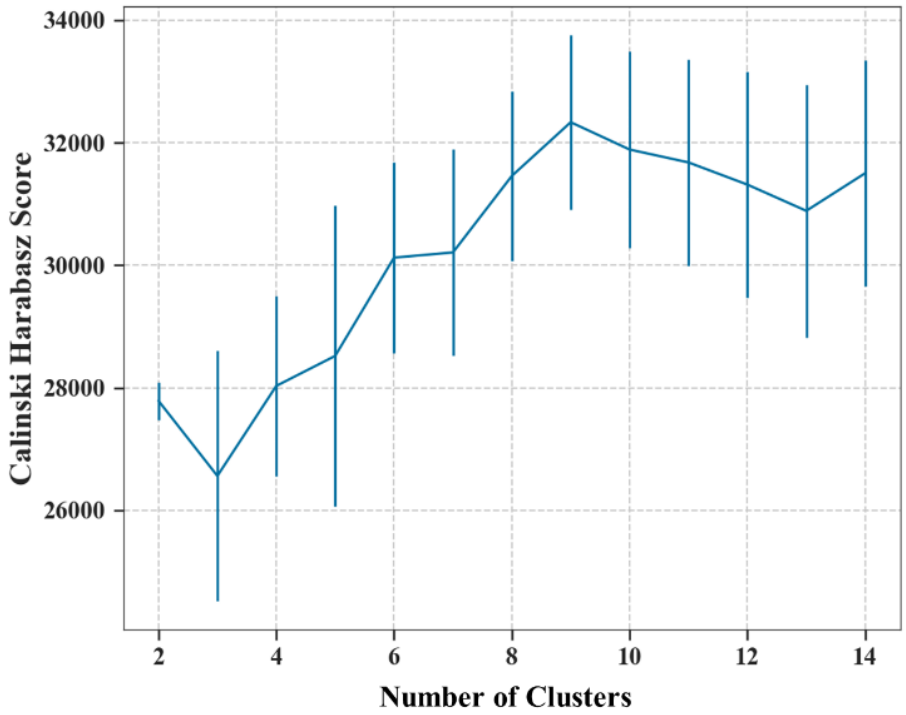

Figure 7: CAH score evolution with the number of clusters (with the standard deviation)

5 RESULTS

5.1 Classification of the agglomerates

Morphology features of the centroids (V_C, E_C, B_C) of the 9 classes are presented in Table 3. They can also be visualised in (V, B) or (E, B) plots (cf. Figure 8).

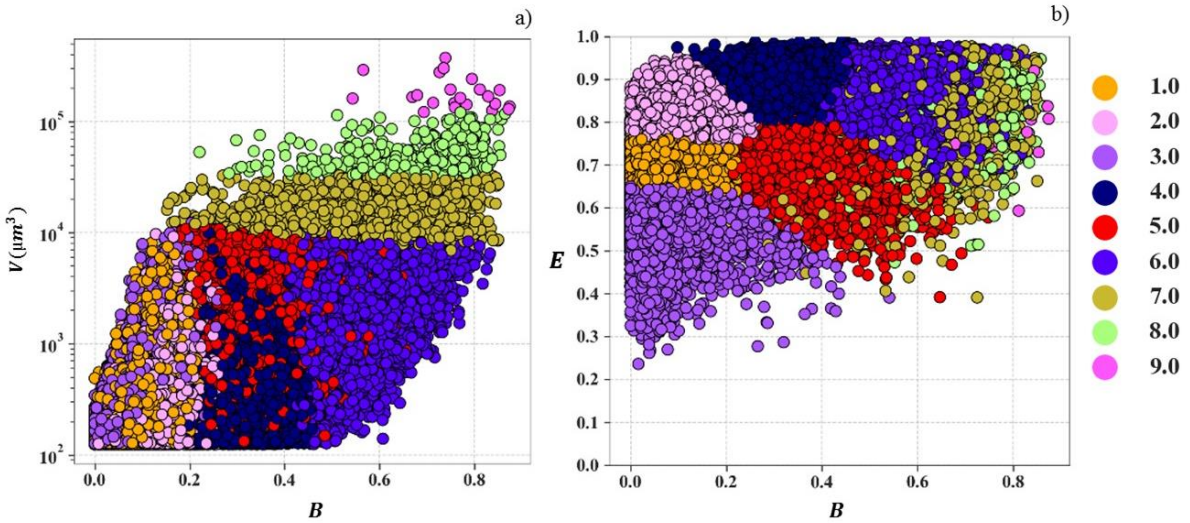

Figure 8: Visualisation of the agglomerate clusters (considering the agglomerates from all the model materials), presented in a) (V, B) plot and b) (E, B) plot

Table 3: Features of centroid of each morphological class

Class label	V_c (μm^3)	B_c	E_c
1	411	0.102	0.702
2	415	0.145	0.804
3	421	0.082	0.591
4	662	0.317	0.873
5	1662	0.341	0.721
6	2381	0.526	0.849
7	14631	0.589	0.783
8	50979	0.667	0.804
9	190991	0.730	0.806

The agglomerates in classes #1, #2, #3 are the smallest and most similar in size (Figure A6a in SI and Figure 8a). They differ from each other by their E_C values and E distributions (Figure 9a). These distributions are well separated from each other with small overlap. The class #3 agglomerates have the lowest eccentricity (most spherical) and structure (lowest bulk factor), whereas class #2 has the highest eccentricity (E_C = 0.804). The representative B_C and B distributions (Figure A6b in SI and Figure 8b) for the 3 first classes suggest that they contain low structured agglomerates (low B_C values). Class #1 and #3 have similar B distribution, whereas B values for class #2 is higher (meaning its CB_{aggl} are more structured).

The agglomerates belonging to classes #2, #4 and #6 have an intermediate size (even though the class #6 agglomerates are significantly bigger than those from classes #2 and #4) (Figure A7 a in SI). Their eccentricity is the largest suggesting that they are the most elongated in one or both directions (cf Table 3, Figure A7b in SI). The main difference between these three classes lies in their structure factor B, as shown in Figure 9b, the class #6 agglomerates are the most structured, followed by the class #4 agglomerates.

The agglomerates belonging to the #7, #8 and #9 classes are the biggest of all agglomerates. The differentiating parameter between these classes is the size of the agglomerates: the higher the class, the bigger the agglomerates. Their eccentricity distribution is very similar. Moreover, the bigger the agglomerates, the more structured they are, as shown on Figure 8a. Finally, the class #5 agglomerates have an intermediate size and a B distribution

close to that of class #4 agglomerates (cf. Figure 9b), and an *E* distribution close to that of agglomerates in class #1 (cf. Figure A7c).

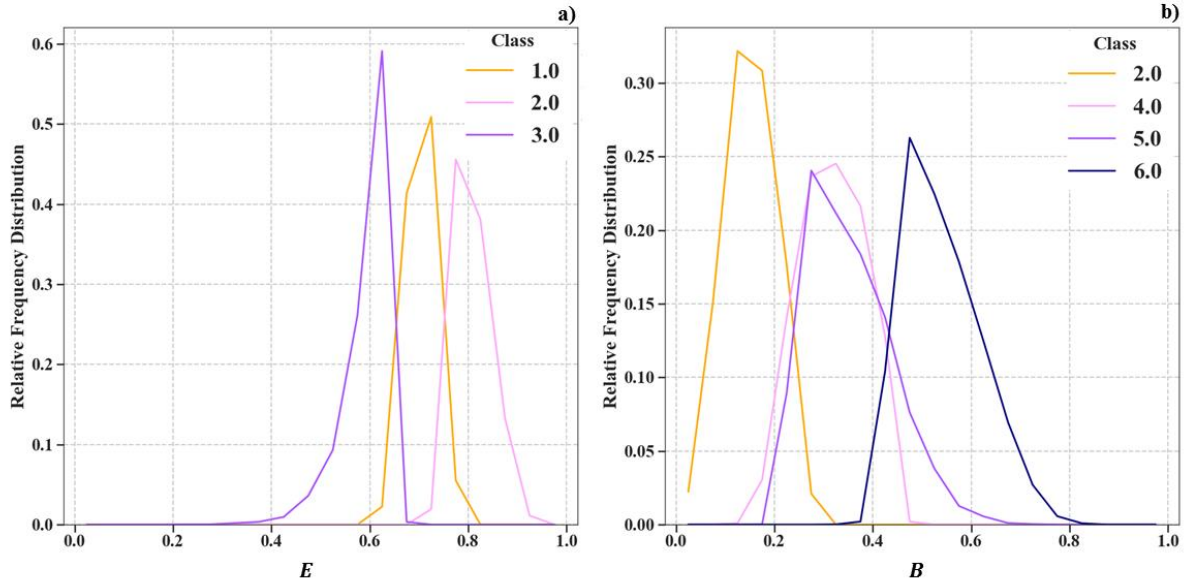

Figure 9: a) Relative frequency distribution plots of *E* for model material 30_rpm_usd corresponding to morphological classes #1, #2 and #3, b) relative frequency distribution plots of *B* for model material 30_rpm_usd corresponding to morphological classes #2, #4, #5 and #6

5.2 Application of the methodology to the model materials

Model materials presented in Materials and testing section have been processed differently. Two rotor speeds (30 rpm vs 60 rpm) along with 2 ways of introducing the fillers and rubber into the internal mixer (Upside-down and Top-down approach) have been tested. Cumulated volume fraction ϕ_{cumul} of CB_{aggl} in the model mixes is clearly correlated to the rotor speed (30_rpm_usd: 10.4%, 30_rpm_td: 11.6%, 60_rpm_usd: 6.0%, 60_rpm_td: 5.6%). Note that the cumulated volume fraction of the agglomerates of size below 125 voxels, which have not been taken into account in the morphological analysis, is around 0.4% for all the materials. A deeper analysis of the agglomerates morphology and spatial distribution is required to understand the differences induced by the USD and TD approaches. Actually, as described in SI (Description A1), the consequences of changing from TD to USD protocol on the CB_{aggl} spatial distribution is small. An analysis of the morphology classes of the agglomerates appears to be much more insightful and is presented in the following.

5.2.1 Differentiation of model mixes using CB_{aggl} morphology clustering

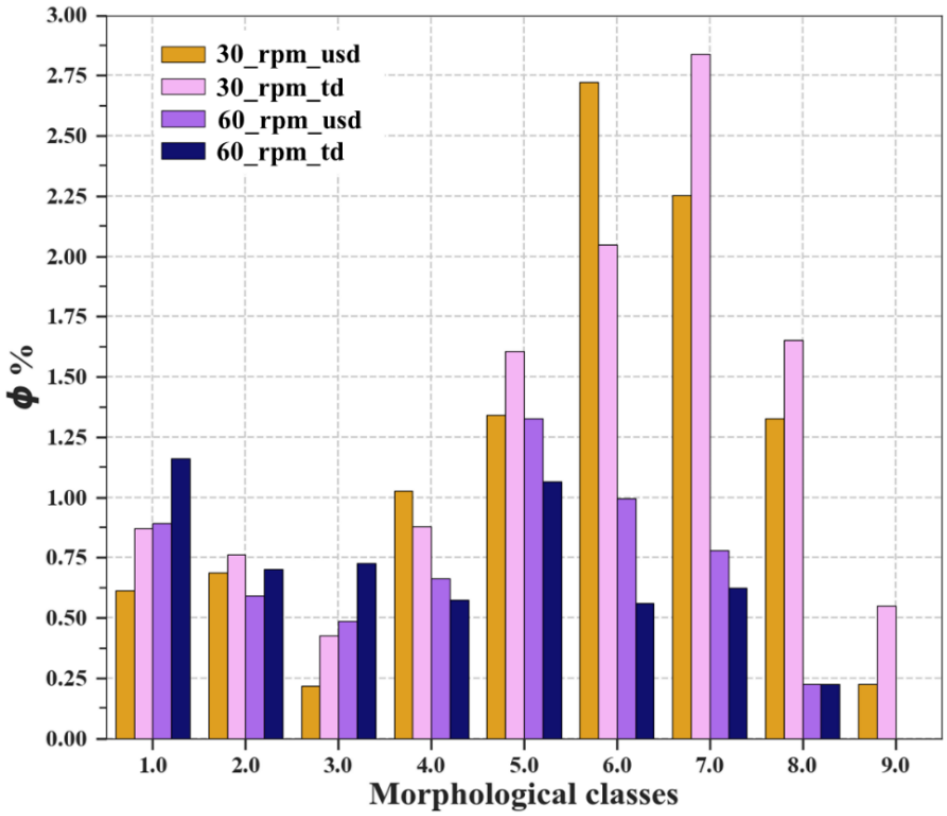

Figure 10: CB_{aggl} volume fraction in the different classes, for the 4 model materials.

CB_{aggl} volume fraction in each morphological class for the 4 model mixes is presented in Figure 10. For a given filler addition protocol, in most of the classes, the agglomerate volume fraction decreases when the rotor speed is increased, especially for classes with the biggest agglomerates and/or the most structured ones. Interestingly, the contrary is found for classes #1 and #3, which correspond to relatively small and low structured agglomerates (that have a larger eccentricity than in class #2).

As mentioned earlier, ϕ_{cumul} of CB_{aggl} in the model mixes is not significantly changed when the filler addition protocol changes. Compared to TD protocol, Upside Down protocol on model mixes processed at 30_rpm leads to larger volume fractions of agglomerates in the classes #4 and #6, which correspond to the agglomerates with the largest eccentricity. In the other morphological classes, the agglomerates volume fraction is lower when the USD protocol was applied. The impact of changing from USD to TD protocol is different for the materials processed at 60_rpm. With this rotor speed, the USD protocol leads to a higher volume fraction of CB_{aggl} in the classes #4 and above, corresponding to agglomerates with *V* and *B* distribution which spread over a domain of values larger than in classes #1, #2 and #3.

Knowing the distribution of each feature in each morphological class, the differentiation between the model mixes can be analyzed even more accurately. One can use for instance, the cumulative frequency distribution of the features *B* and *E*, shown in Figure 11. Increasing the rotor speed produces agglomerates with lower structure (with a shift in the cumulative probability distribution of B towards the lowest values). This effect is prominent for the morphological classes #7 and #8 (Figure 11a, b) (as seen in SI Figure A8, this effect is negligible for the other classes), which were the classes for which the differentiating parameter was the size. Similarly, there is a decrease in *E* of the agglomerates in class #8 (which corresponds to the biggest agglomerates) due to an increase in the rotor speed, as shown in Figure 11c.

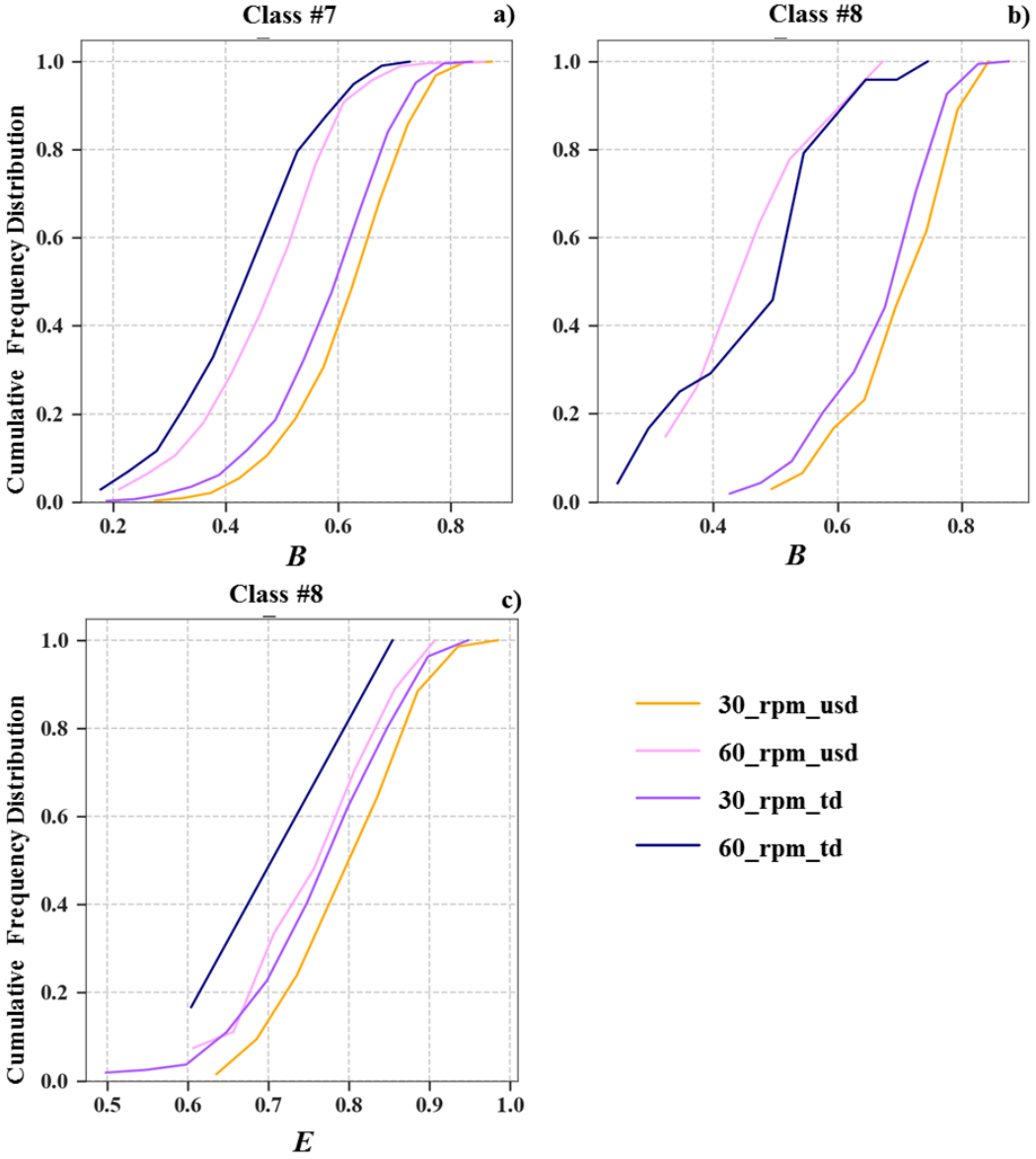

Figure 11: a) and b) Cumulative probability distribution of *B* for agglomerates of classes #7 and #8, for all the model materials, c) cumulative probability distribution of *E* for agglomerates of class #8, for all the model materials.

6 DISCUSSION

As shown above, the methodology we developed, provides insightful information (and because of the use of only 3 features, they were easy to visualize, in Figure 8) to evaluate the influence of the processing parameters on the morphology of the CB_{aggl}. By doubling the rotor speed, the total shear deformation undergone by the compound in the internal mixer was also doubled. This promotes more rupture and erosion of agglomerates[43,44]. As expected, this leads to a lower cumulative volume fraction of agglomerates with B parameter above 0.2 (10.4% vs 6.0%), corresponding to the classes #4 and above, i.e. this decreases the volume of the large and more structured agglomerates. Moreover, the increase in the volume fraction of the less structured small agglomerates (classes #1 and #3) with the smallest eccentricity (compared to class #2) suggests that the increase in the rotor speed promotes the creation of more spherical agglomerates from the erosion of the big ones. This is confirmed by the evolution of the *E* and *B* distributions within the classes #7 and #8.

In the comparison of TD vs USD protocol, interesting differences can be found through the clustering methodology. The consequences of the carbon black addition protocol seems to depend on the rotor speed. At 30 rpm, when changing from TD to USD protocol, one observes in particular that the volume fraction of the big agglomerates (classes #7, #8 and #9) decreases. These agglomerates seem to be broken down to lower size agglomerates with large eccentricity corresponding to an increase in the CB volume fraction in the classes #4 to #6. At 60 rpm, the trend seems different with a slight increase in the volume fraction of the biggest agglomerates (classes #7 and #8). In general, TD protocol leads to a more rapid incorporation of CB in comparison to USD approach, as shown by the higher fraction of remaining CB, not incorporated after the IM step (SI Table A4), i.e. prior to the roll mill step. This is actually in contradiction with the previous observations for the model materials mixed at 30 rpm. This means that the final CB agglomerates dispersion and morphology are the result of a very complex interplay between the CB dispersion at the end of the IM step with the following roll mill step. Only supplementary studies, including a precise CB dispersion characterization as a function of time during the different mixing steps may help to understand our model material microstructure. For this, the use of the methodology developed in this paper is required.

7 CONCLUSION

Very few studies have focused on the morphologies of carbon black agglomerates in industrial rubber compounds. This is mainly due to the limitations in the characterization

techniques available at laboratory scale. Here, we demonstrated that even when using laboratory sourced X-ray Tomography, a good attenuation contrast between agglomerates and matrix is attainable provided that a LaB_6 X ray source operated at 40 kV is used. The attenuation contrast between phases can also be increased with the help of various image processing algorithms, thereby the extraction of various features becomes efficient. Like with carbon black aggregates, various morphological features can be used to characterize CB_{aggl}. Out of the 7 features extracted from image analysis, only 3 were retained using feature selection technique (Spearman's rank correlation coefficient). The relevant features appeared to be the volume, the bulk factor and the eccentricity. Morphological classification based on these features was performed using K-means unsupervised clustering algorithm.

Thus, we developed a complete methodology to obtain a morphological classification on CB_{aggl}. This provides many insights on the peculiarity of the morphology of agglomerates in the studied model materials, and enables to distinguish samples with the same measured agglomerates volume fraction. The main advantage of our approach is that it enables to understand the impact of small changes in the materials processing protocol. Notably in the current study, the impact of two processing parameters, (influence of rotor speed and filler addition protocol) can be precisely characterized. This paves the way for a better understanding of the incorporation and desagglomeration mechanisms of carbon blacks during the process. This can also provide useful information to identify in the final materials, the critical morphology of carbon black agglomerates for crack initiation and propagation.

8 ACKNOWLEDGEMENTS

This work was supported by LRCCP and ANRT (CIFRE N° 2018 /0429)

9 SUPPORTING INFORMATION

1. Description A1: spatial distribution:

In addition to the agglomerates morphologies, the spatial distribution of agglomerates in a mix is another important information to characterise the quality of the filler dispersion. To understand the aggregation of agglomerates at the micron level, it is interesting to calculate the distances to the nearest neighbours of each CB_{aggl}. In order to do it, a matrix with the distances between each agglomerate and all other agglomerates in the model material has to be evaluated, based on their position. Since the number of agglomerates in each model material is very high, it requires huge computation power and memory storage. To reduce this computation and the memory requirement, spatial clustering was performed on each model material using the same

K-means algorithm applied for morphological clustering, except that the data points are the spatial coordinates of the agglomerates. All the agglomerates that are close to each other (centroids of the agglomerates) in the model material are clustered into one spatial class. Here 8 classes have been identified as the optimal number, which translates to around 12% of the volume fraction for each spatial class in the stack (Figure A1 in appendix). The distribution of the spatial distance of each agglomerate in each class to the class centroid $D_{centroid}$ ($D_{centroid} = (x_i\text{-}\mu_k)^{0.5}$, where x_i is the spatial coordinates of agglomerate center and μ_k is the centroid of the k^{th} spatial class ($1 \leq k \leq 8$)) gives insight on the agglomerates spatial distribution. The distributions found for the 8 spatial classes are very close to each other (Figure A2a) indicating that each class can be considered as a representative volume of the model mix. As mentioned earlier, we are more interested in the dispersion at lower scale. The clustering (equivalent to a reduction of the sample size) being completed, the distances between the 20 nearest neighbours for each agglomerate in one class can therefore be calculated. 20 has been arbitrarly chosen, knowing that a parallelepiped in which an agglomerate can be bounded, counts 26 neighbors (in contact through the faces, vertices and edges). These distances *d* are the minimal ones between the surfaces of 2 agglomerates, as depicted in figure A2b, and are calculated as follows:

$$d_i = \sqrt[2]{(x_i - x_j)^2 + (y_i - y_j)^2 + (z_i - z_j)^2} - \left(r_i + r_j\right) \quad (1 \leq j \leq 20)(1 \leq i \leq M) \quad (9)$$

Where *x, y, z* are the spatial coordinates of the agglomerate centre, *r* its radius calculated from its Eq_{diam}, the index *i* is for the agglomerate considered, *j* for one of its 20 closest neighbours and M is the total number of agglomerates in the spatial class considered for the analysis . In Figure A3, we have chosen the spatial class n°1 for all the model materials.

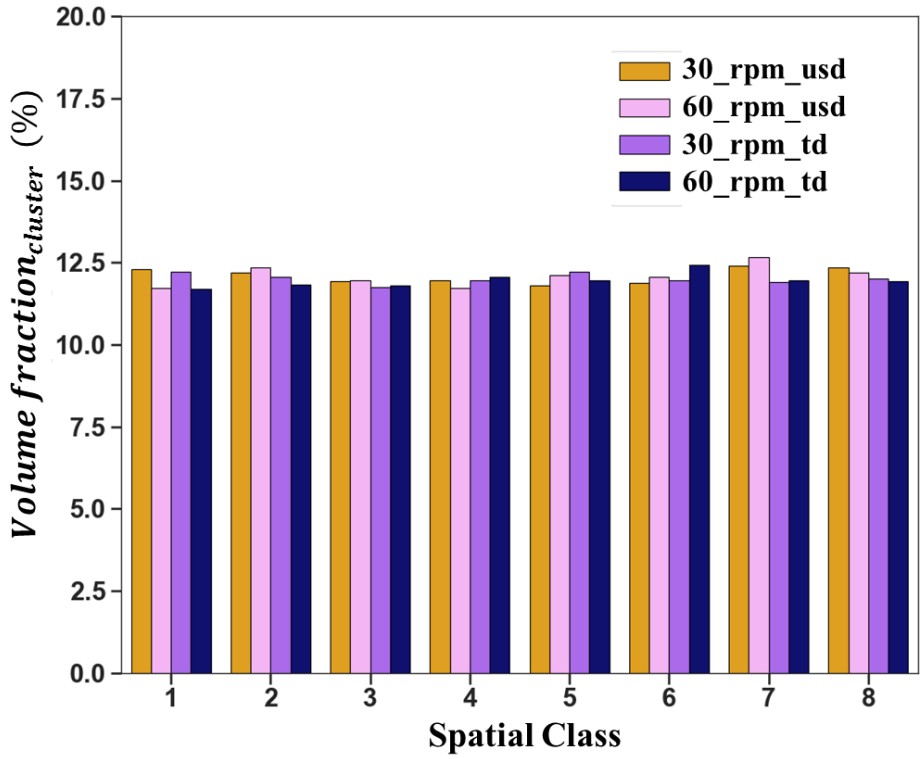

Figure A1: Volume fraction of each spatial class for 4 model materials.

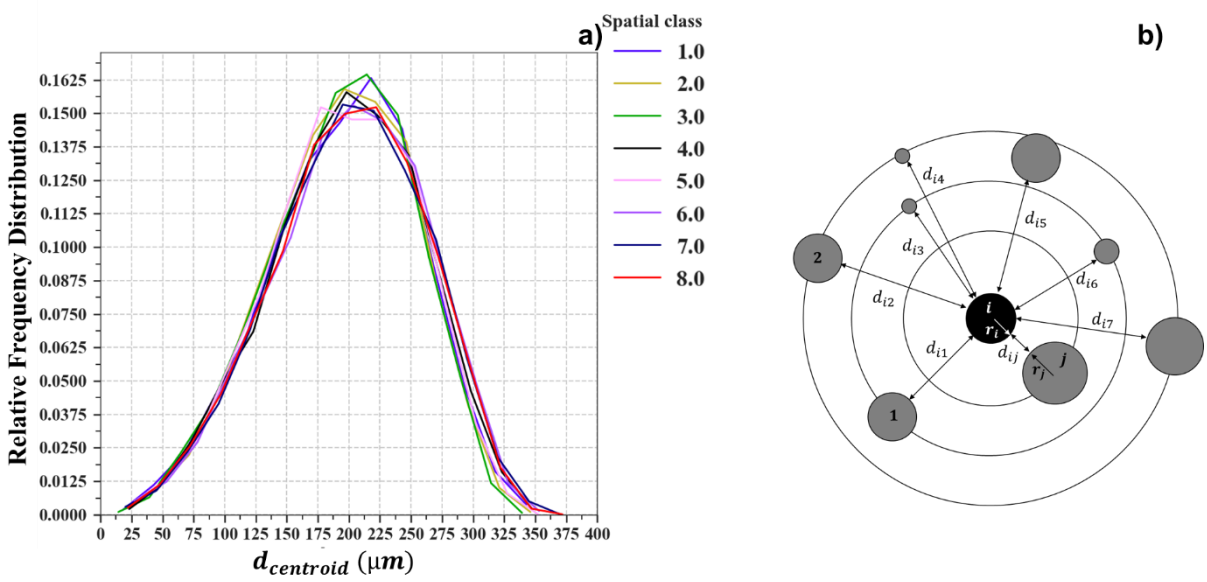

Figure A2: a) Distribution of the distances of each agglomerate to its class centroid. b) Illustration of the nearest-neighbour distance

Result: Spatial Distribution of CB_{aggl}

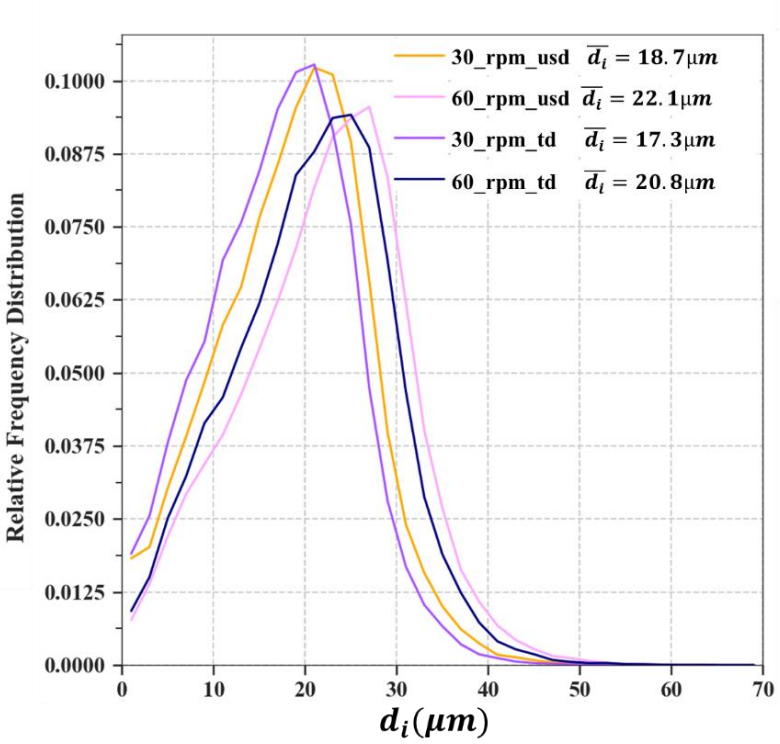

Figure A3: Distribution of nearest-neighbour distance for various model mixes along with the mean value for each mix. $\overline{d_i}$ corresponds to the mean of the distribution

Model mixes	WMH (µm)
30_rpm_usd	18.9
60_rpm_usd	20.9
30_rpm_td	18.1
60_rpm_td	20.1

Table A1 : Value of the Width at MidHeight of the peak of the nearest neighbor distance distribution for the model mixes

The distributions of the distances to the nearest neighbours are presented in figure A3 for all the model mixes. There are slight differences between the different materials. Increasing the rotor speed leads to a shift in the distribution towards larger values. The Width of the peak distribution at its MidHeight (cf Table A1) is also slightly increased. In addition, we know that the agglomerates volume fraction is reduced. Thus, the increase in the rotor speed improves the CB deagglomeration, reduces the size and volume fraction of the agglomerates, and logically increases the distance between them.

2. Description A2: laplacian score

Laplacian Score (LS) works on the principle that data from the same class tend to be close to each other and each feature is evaluated based on its "locality preserving power". LS ranges from 0 to 1, where score value close to 1 corresponds to a relevant parameter. The algorithm developed by He *et al.* [45] has been used to calculate the Laplacian score for each feature (Table A2). Laplacian score shows that each feature can be used to distinguish different clusters in the data as all the features have a LS above 0.9, except *B* (0.85).

V	***Eq$_{diam}$***	***B***	***E***	***b***	***a***	***Q***
1.000	1.000	0.851±0.034	0.920±0.009	0.972±0.004	0.970±0.003	0.925±0.010

Table A2: Laplacian score for each feature

3. Figure A4

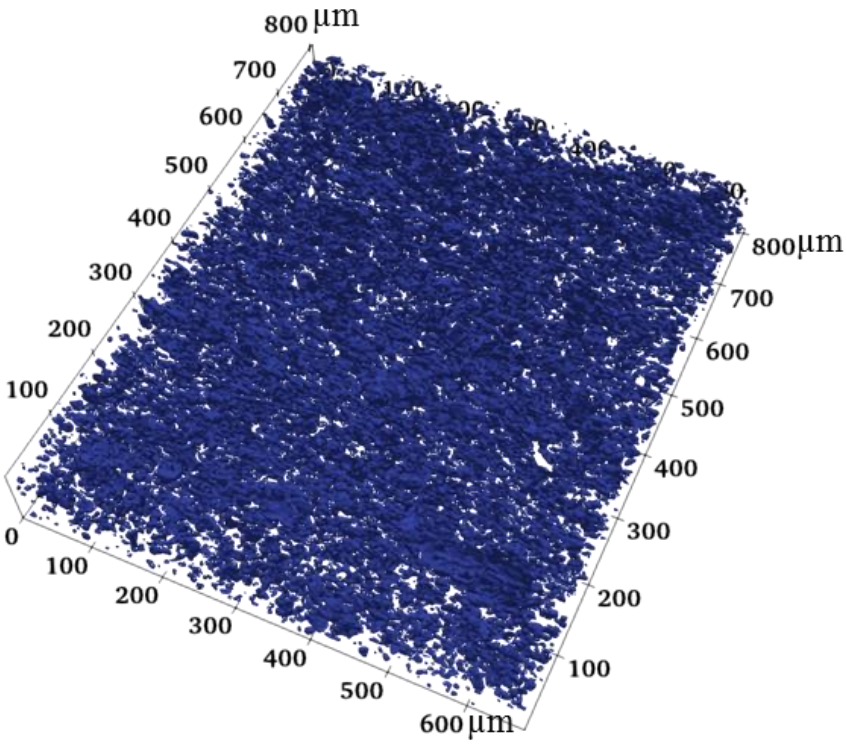

Figure A4: Sub-section volume of the model material 30_rpm_usd obtained using 3D Tomography visualized using ParaView © software

4. Figure A5

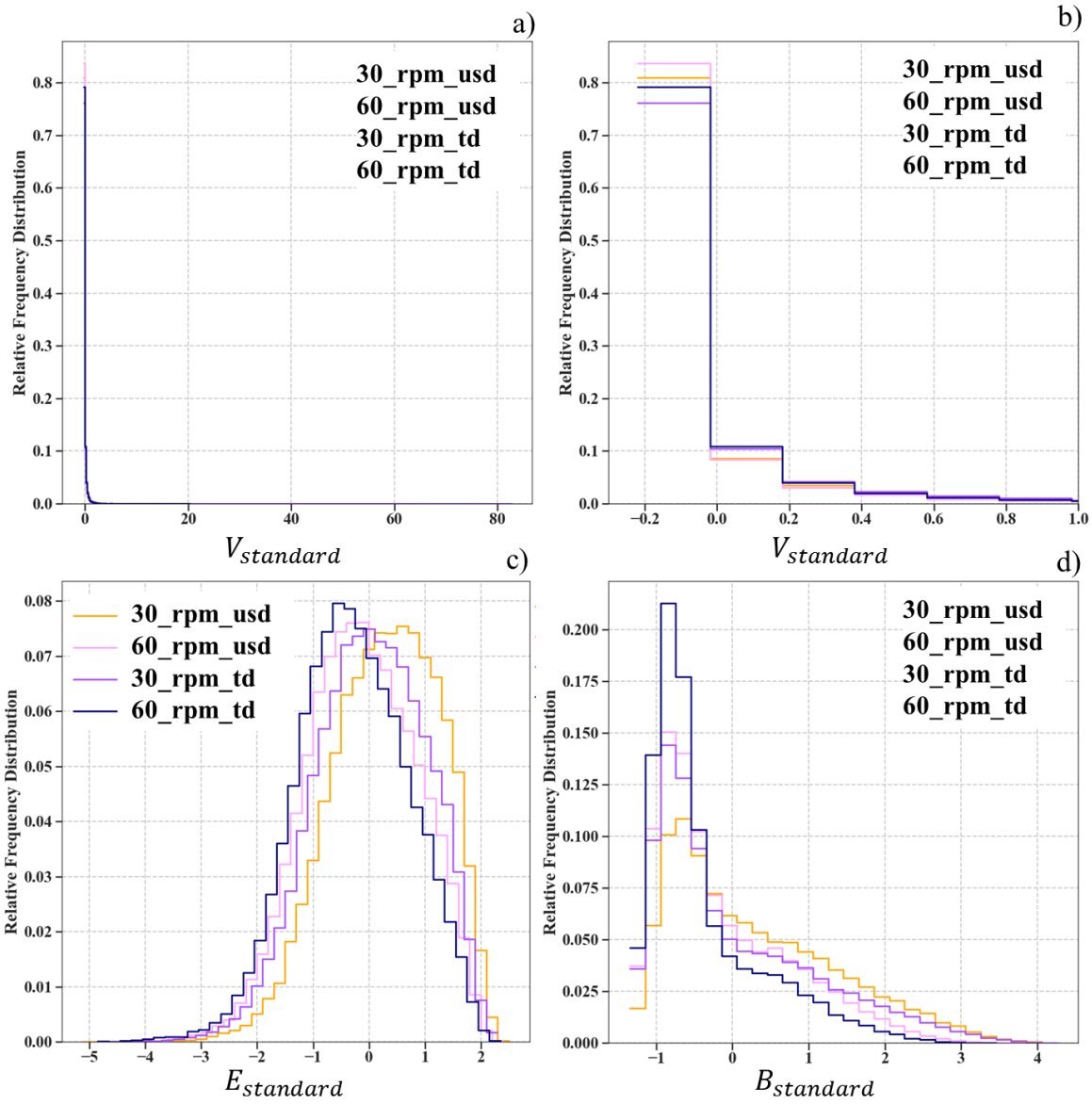

Figure A5: Statistics on each standardized geometric features(using equation 8), $V_{standard}$ ((a), (b)), $E_{standard}$ (c) and $B_{standard}$ (d)- which have been retained as descriptors of the morphology of CB_{aggl} for all the model mixes (30_rpm_usd, 60_rpm_usd, 30_rpm_td, 60_rpm_td) - is presented

5. Description A3: silhouette coefficient

The Silhouette coefficient (S) [42] is a validation metric to check the consistency within clusters of data. It calculates the cohesion of an observation to its own cluster compared to other clusters using the following equation.

$$S(i) = \frac{b(i)-a(i)}{max\{a(i),b(i)\}} \quad (7)$$

Where *b(i)* is the mean distance of i^{th} data point to all other data points in the closest neighboring cluster to which *i* is not linked, i.e. between an agglomerate and agglomerates from other clusters (mean nearest-cluster distance) and *a(i)* is the average distance of i^{th} observation to all other observations in the same cluster (mean intra-cluster distance). *S(i)* varies between -1 and 1, where 1 corresponds to a good partition of a cluster, score near 0 indicates overlapping of clusters space and negative value signifies that observations have been partitioned wrongly. We will use S_{avg} which is the average of all the *S(i)* values.

k number of clusters	S_{avg}
2	0.448±0
3	0.450±0
4	0.371±0
5	0.365±0
6	0.347±0
7	0.358±0
8	0.351±0
9	0.344±0
10	0.327±0
11	0.322±0
12	0.326±0
13	0.323±0
14	0.315±0

Table A3: S_{avg} metric evaluation for each number of clusters, deduced from 10 random samplings

6. Figure A6

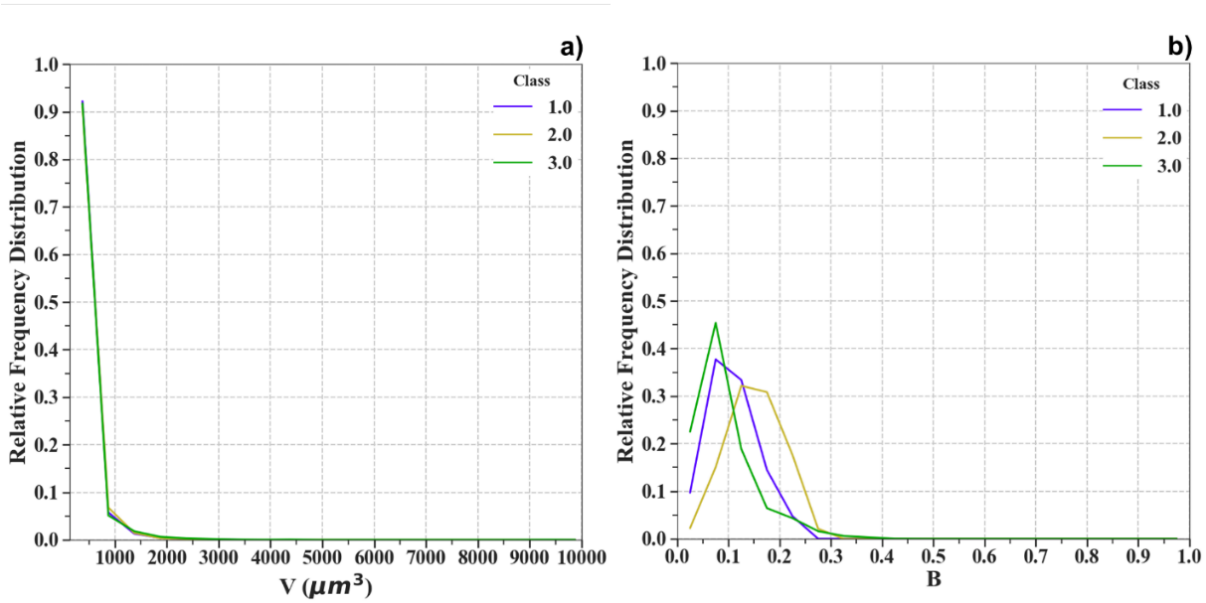

Figure A6: a) and b) Show the relative frequency distribution plot of V and B for model material 30_rpm_usd corresponding to morphological classes #1, #2 and #3.

7. Figure A7

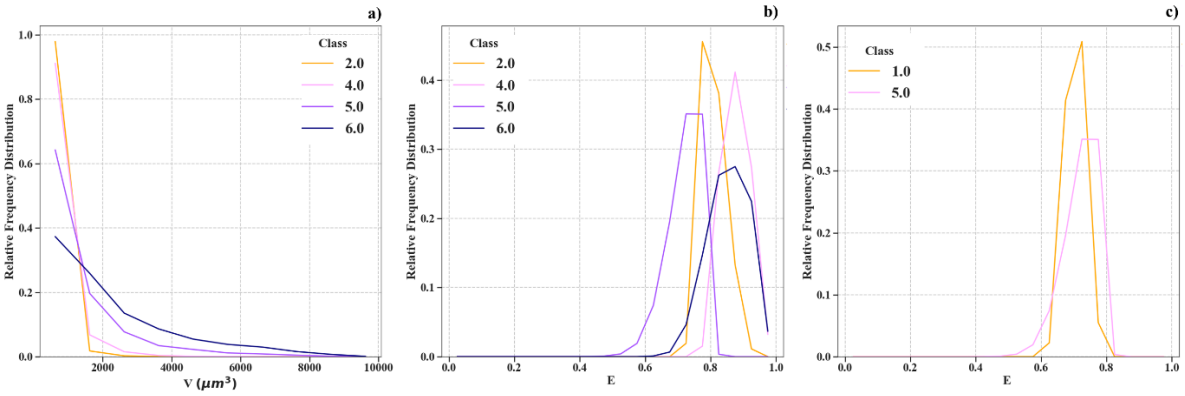

Figure A7: a) and b) Show the relative frequency distribution plot of V and E respectively corresponding to morphological classes #2, #4, #5 and #6, c) shows the relative frequency distribution plot of E corresponding to morphological classes #1 and #5 . The agglomerates considered for plotting is from model material 30_rpm_usd

8. Figure A8

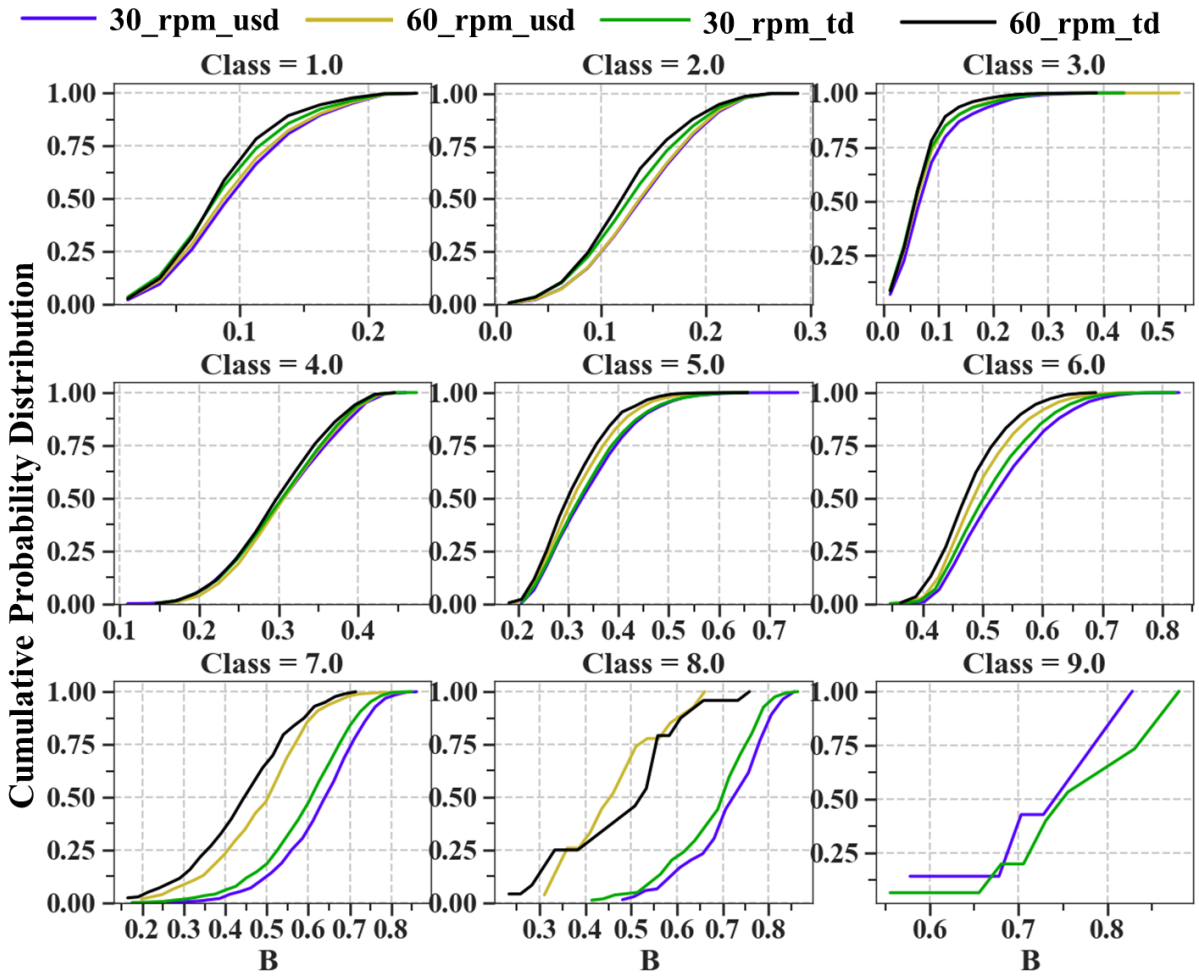

Figure A8: Cumulative probability distribution of B within each morphological class corresponding to each model material.

9. Table A4

Protocol	Time (min)	Total rotation (rad)	Cohesive (gm)	Loose Carbon Black (gm)	Total mass (gm)	% of Carbon Black loose
USD @ 60 rpm	2	753.6	53.1	1.8	54.9	3.3
TD @ 60 rpm	2	753.6	54.4	0.2	54.6	0.4
USD @ 30 rpm	2	376.8	52	2.392	54.392	4.4
TD @ 30 rpm	2	376.8	51	1.761	52.76	3.3

Table A4: Amount of Carbon Black incorporated depending on the filler addition protocol and rotor speed of the internal mixer. (This information was obtained for a mix fabricated using the filler addition protocol suggested in Materials and Testing). This table demonstrates the differences in the CB incorporation in the mix depending on the time spent in the internal mixer.

10 REFERENCES

[1] Cotten, G. R. Mixing of Carbon Black with Rubber I. Measurement of Dispersion Rate by Changes in Mixing Torque *Rubber Chemistry and Technology* **1984**, *57*, 118, 10.5254/1.3535988.

[2] Astruc, M. Thesis,. Étude rhéo-optique des mécanismes de dispersion de mélanges sous cisaillement simple . 1 Mélanges concentrés de polymères immiscibles . 2 Mélanges polymères-charges poreuse, l'École des Mines de Paris, **2008**.

[3] Dizon, E. S. Processing in an Internal Mixer as Affected by Carbon Black Properties. *Rubber Chem. Technol.* **1976**, *49*, 12–27.

[4] Hess, W. M.; Swor, R. A.; Micek, E. J. The Influence of Carbon Black, Mixing, and Compounding Variables on Dispersion *Rubber Chemistry and Technology* **1984**, *57*, 959, 10.5254/1.3536052.

[5] Collin, V.; Boudimbou, I.; Peuvrel-Disdier, E. New insights in dispersion mechanisms of carbon black in a polymer matrix under shear by rheo-optics *Journal of Applied Polymer Science* **2013**, *127*, 2121, 10.1002/app.37769.

[6] Horiuchi, S.; Dohi, H. Nanoimaging and spectroscopic analysis of rubber/ZnO interfaces by energy-filtering transmission electron microscopy *Langmuir* **2006**, *22*, 4607, 10.1021/la052308f.

[7] Huneau, B.; Masquelier, I.; Marco, Y.; Le Saux, V.; Noizet, S.; Schiel, C.; Charrier, P. Fatigue crack initiation in a carbon black-filled natural rubber *Rubber Chemistry and Technology* **2016**, *89*, 126, 10.5254/rct.15.84809.

[8] Weng, G.; Huang, G.; Lei, H.; Qu, L.; Nie, Y.; Wu, J. Crack initiation and evolution in vulcanized natural rubber under high temperature fatigue *Polymer Degradation and*

Stability **2011**, *96*, 2221, 10.1016/j.polymdegradstab.2011.09.004.
[9] Liu, R.; Sancaktar, E. Identification of crack progression in filled rubber by micro X-ray CT-scan *International Journal of Fatigue* **2018**, *111*, 144, 10.1016/j.ijfatigue.2018.01.033.
[10] Dizon, E. S.; Hicks, A. E.; Chirico, V. E. The Effect of Carbon Black Parameters on the Fatigue Life of Filled Rubber Compounds. *Rubber Chem. Technol.* **1974**, *47*, 231–249.
[11] Lake, G. J.; Lindley, P. B. Cut growth and fatigue of rubbers. II. Experiments on a noncrystallizing rubber *Journal of Applied Polymer Science* **1964**, *8*, 707, 10.1002/app.1964.070080212.
[12] Abraham, F. Definition and use of an effective flaw size for the simulation of elastomer fatigue; In *Constitutive models for rubber VII*; Jerrams, S.; Murphy, N., Eds.; CRC Press Inc, London, **2012**; pp 331.
[13] Le Cam, J.-B.; Huneau, B.; Verron, E. Fatigue damage in carbon black filled natural rubber under uni- and multiaxial loading conditions *International Journal of Fatigue* **2013**, *52*, 82, 10.1016/j.ijfatigue.2013.02.022.
[14] Gent, A. N.; Lindley, P. B. Internal Rupture of Bonded Rubber Cylinders in Tension *Proceedings of the Royal Society A: Mathematical, Physical and Engineering Sciences* **1959**, *249*, 195, 10.1098/rspa.1959.0016.
[15] Gent, A. N.; Lindley, P. B.; Thomas, A. G. Cut growth and fatigue of rubbers. I. The relationship between cut growth and fatigue *Journal of Applied Polymer Science* **1964**, *8*, 455, 10.1002/app.1964.070080129.
[16] Lake, G. J.; Lindley, P. B. The mechanical fatigue limit for rubber *Journal of Applied Polymer Science* **1965**, *9*, 1233, 10.1002/app.1965.070090405.
[17] Gent, A. N.; Park, B. Failure processes in elastomers at or near a rigid spherical inclusion *Journal of Materials Science* **1984**, *19*, 1947, 10.1007/BF00550265.
[18] Chow, T. S. The effect of particle shape on the mechanical properties of filled polymers *Journal of Materials Science* **1980**, *15*, 1873, 10.1007/BF00550613.
[19] Otto, S.; Randl, O.; Goncalves, O.; Cantaloube, B. New reference value for the description of filler dispersion with the dispergrader 1000 NT *KGK Kautschuk Gummi Kunststoffe* **2005**, *58*, 390.
[20] Garcea, S. C.; Wang, Y.; Withers, P. J. X-ray computed tomography of polymer composites *Composites Science and Technology* **2018**, *156*, 305, 10.1016/j.compscitech.2017.10.023.
[21] Maire, E.; Withers, P. J. Quantitative X-ray tomography *International Materials Reviews* **2014**, *59*, 1, 10.1179/1743280413Y.0000000023.
[22] Kallungal, J.; Chazeau, L.; Chenal, J.-M.; Adrien, J.; Maire, E.; Barres, C.; Cantaloube, B.; Heuillet, P. Methodology for 3D characterization of microstructural defects in filled polymer using X-ray Tomography; In *Constitutive Models for Rubber XI*; CRC Press, **2019**; pp 77; 10.1201/9780429324710-14.
[23] Medalia, A. I.; Heckman, F. A. Morphology of aggregates—II. Size and shape factors of carbon black aggregates from electron microscopy *Carbon* **1969**, *7*, 567, 10.1016/0008-6223(69)90029-3.
[24] Medalia, A. I.; Heckman, F. A. Morphology of aggregates. VII. Comparison chart method for electron microscopic determination of carbon black aggregate morphology *Journal of Colloid And Interface Science* **1971**, *36*, 173, 10.1016/0021-9797(71)90162-7.
[25] Medalia, A. I. Morphology of aggregates. VI. Effective volume of aggregates of carbon black from electron microscopy; Application to vehicle absorption and to die swell of filled rubber *Journal of Colloid And Interface Science* **1970**, *32*, 115, 10.1016/0021-9797(70)90108-6.

[26] Medalia, A. I. Morphology of aggregates. I. Calculation of shape and bulkiness factors; application to computer-simulated random flocs *Journal of Colloid And Interface Science* **1967**, *24*, 393, 10.1016/0021-9797(67)90267-6.
[27] Bourrat, X.; Oberlin, A.; Van Damme, H.; Gateau, C.; Bachelar, R. Mass fractal analysis of conducting carbon black morphology *Carbon* **1988**, *26*, 100, 10.1016/0008-6223(88)90016-4.
[28] Rieker, T. P.; Hindermann-Bischoff, M.; Ehrburger-Dolle, F. Small-angle X-ray scattering study of the morphology of carbon black mass fractal aggregates in polymeric composites *Langmuir* **2000**, *16*, 5588, 10.1021/la991636a.
[29] Baeza, G. P.; Genix, A.-C.; Degrandcourt, C.; Petitjean, L.; Gummel, J.; Couty, M.; Oberdisse, J. Multiscale Filler Structure in Simplified Industrial Nanocomposite Silica/SBR Systems Studied by SAXS and TEM *Macromolecules* **2013**, *46*, 317, 10.1021/ma302248p.
[30] Herd, C. R.; McDonald, G. C.; Hess, W. M. Morphology of Carbon-Black Aggregates: Fractal Versus Euclidean Geometry *Rubber Chemistry and Technology* **1992**, *65*, 107, 10.5254/1.3538594.
[31] Gouillart, E.; Nunez-Iglesias, J.; van der Walt, S. Analyzing microtomography data with Python and the scikit-image library *Advanced Structural and Chemical Imaging* **2017**, *2*, 10.1186/s40679-016-0031-0.
[32] Gouillart, E. Processing X-ray tomography images with Python. *Github*. https://github.com/emmanuelle/image-processing-tutorials/blob/master/tomo_segmentation.ipynb.
[33] Gouillart, E.; Toplis, M. J.; Grynberg, J.; Chopinet, M.-H.; Sondergard, E.; Salvo, L.; Suéry, M.; Di Michiel, M.; Varoquaux, G. In Situ Synchrotron Microtomography Reveals Multiple Reaction Pathways During Soda-Lime Glass Synthesis *Journal of the American Ceramic Society* **2012**, *95*, 1504, 10.1111/j.1551-2916.2012.05151.x.
[34] Grady, L. Random walks for image segmentation *IEEE Transactions on Pattern Analysis and Machine Intelligence* **2006**, 10.1109/TPAMI.2006.233.
[35] van der Walt, S.; Schönberger, J. L.; Nunez-Iglesias, J.; Boulogne, F.; Warner, J. D.; Yager, N.; Gouillart, E.; Yu, T. scikit-image: image processing in Python *PeerJ* **2014**, *2*, e453, 10.7717/peerj.453.
[36] Denis, E. P.; Barat, C.; Jeulin, D.; Ducottet, C. 3D complex shape characterization by statistical analysis: Application to aluminium alloys *Materials Characterization* **2008**, *59*, 338, 10.1016/j.matchar.2007.01.012.
[37] Fernández-Arjona, M. del M.; Grondona, J. M.; Granados-Durán, P.; Fernández-Llebrez, P.; López-Ávalos, M. D. Microglia morphological categorization in a rat model of neuroinflammation by hierarchical cluster and principal components analysis *Frontiers in Cellular Neuroscience* **2017**, *11*, 10.3389/fncel.2017.00235.
[38] Madra, A.; Adrien, J.; Breitkopf, P.; Maire, E.; Trochu, F. A clustering method for analysis of morphology of short natural fibers in composites based on X-ray microtomography *Composites Part A: Applied Science and Manufacturing* **2017**, *102*, 184, 10.1016/j.compositesa.2017.07.028.
[39] Pedregosa, F.; Varoquaux, G.; Gramfort, A.; Michel, V.; Thirion, B.; Grisel, O.; Blondel, M.; Prettenhofer, P.; Weiss, R.; Dubourg, V.; Vanderplas, J.; Passos, A.; Cournapeau, D.; Brucher, M.; Perrot, M.; Duchesnay, É. Scikit-learn: Machine Learning in Python *Journal of Machine Learning Research* **2011**, *12*, 2825.
[40] Hämäläinen, J.; Jauhiainen, S.; Kärkkäinen, T. Comparison of internal clustering validation indices for prototype-based clustering *Algorithms* **2017**, *10*, 10.3390/a10030105.
[41] Davies, D. L.; Bouldin, D. W. A Cluster Separation Measure *IEEE Transactions on*

Pattern Analysis and Machine Intelligence **1979**, *PAMI-1*, 224, 10.1109/TPAMI.1979.4766909.

[42] Rousseeuw, P. J. Silhouettes: A graphical aid to the interpretation and validation of cluster analysis *Journal of Computational and Applied Mathematics* **1987**, *20*, 53, 10.1016/0377-0427(87)90125-7.

[43] Rwei, S. P.; Manas-Zloczower, I.; Feke, D. L. Characterization of agglomerate dispersion by erosion in simple shear flows *Polymer Engineering & Science* **1991**, *31*, 558, 10.1002/pen.760310804.

[44] Collin, V. Thesis,. Étude rhéo-optique des mécanismes de dispersion du noir de carbone dans des élastomères, **2009**.

[45] He, X.; Cai, D.; Niyogi, P. Laplacian Score for feature selection *Advances in Neural Information Processing Systems* **2005**, 507.

CHAPTER 4

Crack propagation in filled elastomers: 3D study of mechanisms involving the filler agglomerates

Jesbeer. Kallungal[1,2,3,*], Laurent. Chazeau[1,*], Jean-Marc. Chenal[1], Jérôme. Adrien[1], Eric. Maire[1], Claire. Barrès[2], Bernard. Cantaloube[3], Patrick. Heuillet[3], Fabien Wilde[4], Julian Moosmann[4], Timm Weitkamp[5]

[1]*Univ Lyon, INSA Lyon, CNRS, MATEIS UMR5510, F-69621, Lyon, France*

[2]*Univ Lyon, INSA Lyon, CNRS, IMP UMR5223, F-69621, Lyon, France*

[3]*LRCCP Vitry-sur-Seine, France*

[4]*PETRA III, Helmholtz-Zentrum Hereon, Hamburg, Germany*

[5]*Synchrotron SOLEIL, Gif-sur-Yvette, France*

Corresponding authors: laurent.chazeau@insa-lyon.fr

(Article submitted)

TABLE OF CONTENTS

ABSTRACT

This paper presents the impact of Carbon Blacks agglomerates, at different concentrations, on crack propagation mechanisms in a CB filled Ethylene Propylene Diene Monomer (EPDM) elastomer. As shown by Transmission electron microscopy, these CB_{aggl} consist of aggregates clusters with interpenetrating elastomer, and for this reason, are soft and deformable. Crack tip observation using X-ray tomography demonstrates that these CB_{aggl} can either undergo fracture (Abstract figure) or arrest/ deviate a crack during propagation. This causes higher energy dissipation at the crack tip, which contributes to the dissipative component of the strain energy release rate G. For this reason, it is found that among the two materials tested with a significant amount of CB_{aggl} (more than 3%), the material with the highest concentration has a slower crack propagation speed at high G.

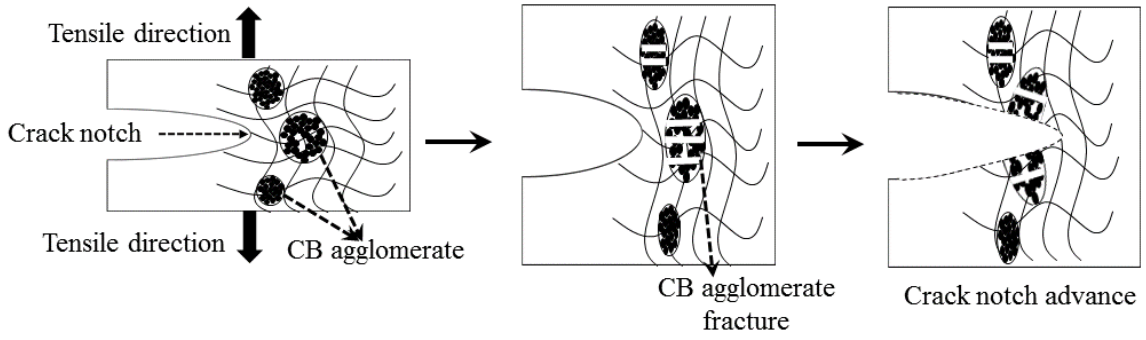

Abstract figure: Illustration of crack propagation mechanism in the presence of carbon black agglomerates at the crack tip vicinity.

1. INTRODUCTION

Many applications such as pneumatics, sealants, and anti-vibration device uses elastomer based materials. In these applications, these materials undergo static or dynamic strain solicitations which reduce their durability. They contain reinforcing fillers such as carbon black (CB), silica nanoparticles, clay, talc or carbon nanotubes to improve their ultimate, fatigue and/or visco-elastic properties[1,2]. These fillers can form agglomerates in the processed materials, in spite of the efforts made to avoid what is considered as defects or flaws[3,4]. Other defects can also be found like metallic oxides inclusions, micro-bubbles or voids. Unfortunately, all these defects are known to influence the rupture properties[5,6].

Since 1950s, many researchers extensively studied these properties in rubber materials. Rupture is the consequence of the initiation and propagation of a crack or multiple cracks through the entire section of the material during its solicitation[6]. In some cases, crack propagation mostly dictates the durability of the material. Hence, many studies characterized the material evolution in the vicinity of the crack tip during the crack growth[7,8]. Postmortem analysis using electron microscopy showed the presence of defects like ZnO, carbon black agglomerates (CB_{aggl}), and cavities in the crack vicinity[7–11]. Cavities participate in the crack propagation which occurs by successive breaking of the ligaments between them and the crack tip[8,12]. The high hydrostatic stress beyond the crack tip promotes the formation of cavities at the poles of the defects made of rigid inclusions[7,13,14]. On the other hand, in the case of filled elastomer, improvement of resistance to crack propagation is ascribed to the ability of the filler to deviate or arrest the crack[15]. Crack can follow the contours of the fillers, and are therefore deviated, increasing the crack path length[16]. Same mechanisms are also suspected for filler agglomerates, but they have not been explored. The crack can also be arrested by the reinforced anisotropic structures (fibrillary structure) formed at the crack tip where the material is submitted to very large strain[17]. Even though all these mechanisms are often discussed in literature, their experimental observation is much less reported, especially using in situ techniques.

Various tools such as Scanning electron microscopy (SEM), Transmission electron microscopy (TEM), Atomic Force Microscopy, Small Angle X-ray Scattering, and X-ray Tomography are available to precisely characterize the defects in elastomer materials. Although techniques like SEM[11,18,19], TEM[20] and AFM[21] provide a better resolution, use of these techniques for in-situ characterization is limited due to small observable area, small size of the sample, or to the material degradation during the observation. SAXS is a non-destructive characterization technique that provides spatially averaged information at sub-micron scale such as the average particle size, shape, distribution of defects or cavities[22]. It is however difficult to visualize or quantify the local dissipative mechanism occurring in the crack tip vicinity using this technique. Recent studies showed that X-ray tomography using laboratory or synchrotron sources is a powerful technique which can provide 3 dimensional information of the microstructures inside the sample at the micron-scale[23–25]. This technique is also suitable to conduct in-situ analysis[26] on the crack propagation and to characterize the materials, crack surface and material evolution in the vicinity of the crack notch.

This paper aims at understanding the impact of defects, specifically CB_{aggl} on the crack propagation in elastomer materials. The influence of the defects concentration will be explored, thanks to the study of model materials with different CB_{aggl} concentrations. It will be shown that the difference in the crack propagation resistance correlates with the energy dissipation inside the material, which is related to the defects concentration. In-situ tensile and crack propagation tests using X-ray Tomography enable to understand the various dissipative mechanisms associated to CB_{aggl} at the origin of this dissipation energy.

2. MATERIALS AND TESTING

2.1 Composition and materials processing

Model materials used for the current study are based on a non-crystallizing Ethylene Propylene Diene Monomer Rubber (EPDM Keltan 4450) reinforced with high furnace carbon black (N326 from Cabbot) and cross-linked using unsupported Bis (α,α-dimethylbenzyl) peroxide. The composition of the model materials (Table 1) was kept constant whereas compounding process conditions were varied in order to generate more or less flaws inside the materials. All the ingredients except the peroxide were mixed in a Haake Rheomix 600 OS mixer (chamber volume: 120cm^3) using Banbury rotors (42 cm^3) at a certain rotor speed and mixing time (Table 1), and were then passed 10 times in a two-roll mill where the peroxide was added. The sequence of ingredients addition is detailed in Table 1. USD method refers to "upside down", i.e., the elastomer was added after carbon black and TD method refers to "top down", i.e., carbon black was introduced after the elastomer in the internal mixer. After the mixing steps, the samples were molded into pure shear geometry specimens (Length=35mm, height =5mm, width =0.8mm) by hot pressing at 170°C under 190 MPa for 12 min. Curing time was estimated from torque measurements performed using a Monsanto rheometer analyzer.

Table 1: Composition of the model materials

Ingredients	*F1*	*F2*	*F3*
	(Phr)	*(Phr)*	*(Phr)*
EPDM Keltan 4450	*100*	*100*	*100*
Carbon Black N326	*50*	*50*	*50*
Peroxide	*3.2*	*3.2*	*3.2*
Rotor Speed (tr/min)	*30*	*60*	*60*
Mixing Time (min)	*2*	*4*	*10*

Introduction Protocol	*TD* *1.EPDM* *2.CB*	*USD* *1.CB* *2.EPDM*	*TD* *1.EPDM* *2.CB*
Filler Volume Fraction	*19.3%*	*19.3%*	*19.3%*

2.2 Multiscale characterization of materials

Microstructural analysis was performed using X-ray Tomography (laboratory source and synchrotron radiation source). The internal structure of carbon black agglomerates or aggregates was characterized by TEM.

2.2.1 X-ray tomography laboratory source (Lab Tomography):

The laboratory X-ray tomography device used for postmortem analysis of the crack propagation path and to understand the fracture surface is the EasyTom apparatus from RX Solutions. The Tungsten target current is 45 µA. LaB_6 cathode filament is used, along with a CCD detector. The volume analyzed is ca. 4-8mm^3 with a voxel resolution chosen in the range of 1-2µm^3 depending on the requirements. The sample was rotated over 360 degrees by steps of 0.09° in front of the X-ray beam. The tube voltage was kept at 40kV to have an optimised attenuation contrast between the elastomer and the agglomerates[27].

2.2.2 Synchrotron radiation computed tomography (SRCT)

SRCT experiments were performed at the PETRA III P05 beamline at DESY, Germany (operated by Helmholtz-Zentrum Hereon), and the Anatomix beamline at SOLEIL , France. The P05 beamline was used to study the local damage mechanisms inside the material during a tensile test. The monochromatic X-rays energy was fixed at 15keV with a spatial resolution of 2.19µm. The sample was mounted in a tensile rig (Figure 1a). Its specific geometry (Figure 1b) was designed to create higher stress in the region of interest (ROI). The sample was rotated over 360° by steps of 0.225°. Each projection step lasted 30ms per projection resulting in a total time per scan of 50s. Experiments performed at Anatomix @SOLEIL focused on the phenomena occurring beyond the crack tip during quasi-static uniaxial extension. The filtered white beam used had a mean energy of 20keV. The experimental setup is shown in Figure 1c. The spatial resolution was 1.3µm. The sample was rotated over 360° by steps of 0.18°. Each projection required 150 ms. The Pagnanin algorithm was applied to reconstruct the phase inside the sample[28]. Similar filter was not used with the data obtained at P05 beamline, as 3D reconstruction was performed from attenuation contrast.

2.2.3 Transmission electron microscopy (TEM)

Nanoscale characterization was performed using TEM (CM120 Philips microscope) on a section with 90nm thickness prepared by cryo-ultra-microtomy (Leica Ultra cut UCT microtome). This section is placed on a 400-mesh copper grid. The accelerating voltage was set to 120kV and the CCD detector used is an Orius CCD camera from Gatan.

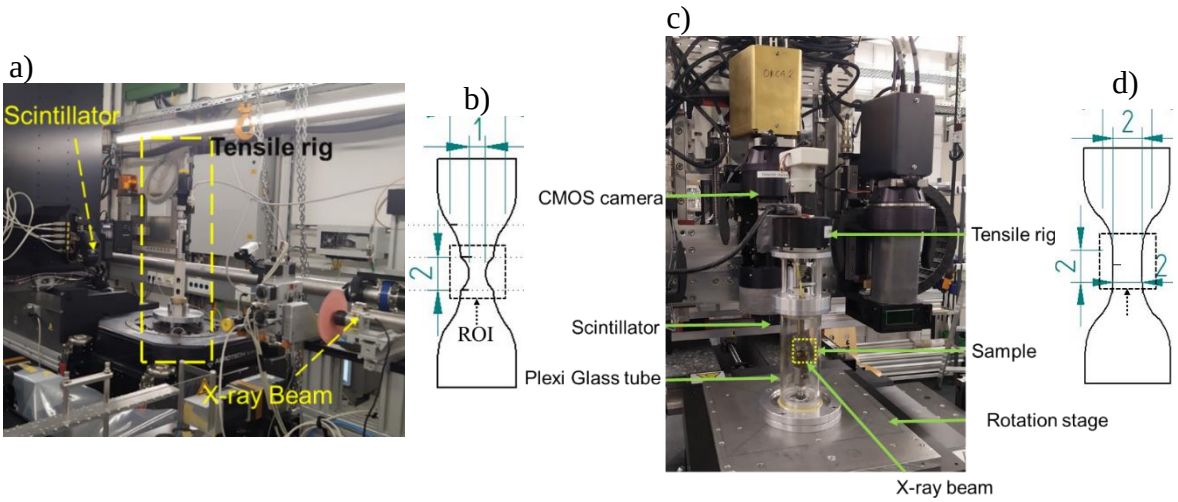

Figure 1: P05 beamline experiments: a) general view of the setup with the position of X-ray beam, tensile rig and scintillator, b) sample geometry used for in-situ tensile test. Anatomix beamline: c) homemade tensile rig from MATEIS lab, d) Single edged notched sample geometry used for in-situ crack propagation test.

2.3 Crack growth measurement technique

2.3.1 Strain energy release rate versus crack propagation speed

Crack propagation speed (Vp) was characterized as a function of the strain energy release rate. G is the product of W(λ) by h_0 for a pure shear geometry specimen with a crack displacement length c, where W(λ) is the strain energy density of the unnotched sample submitted to a stretching of λ with an initial height of h_0 [29]. W(λ) is calculated from the area under the curve of the stress-strain plot. This one is deduced from the nominal stress strain curve obtained from the tensile test of unnotched PS specimen, using Digital Image Correlation (High speed camera combined with the CORELI software, the image acquisition frequency was 1Hz). The DIC resolution is estimated to be 34 μm.

We applied a modified version of the static-growth test introduced by Lake etal. [30] involving the continuous deformation of a notched test piece (PS) at a constant strain rate (0.0065 s^{-1}). This allows to characterize Vp over a broad range of strain energy release rate. Note that the

samples were not accommodated prior to the crack propagation test. An initial notch (c_0) of 10mm was made on one side of the test piece with a thin razor blade. Crack displacement up to 5 mm was considered for the analysis of Vp, to ensure conditions required by Yeoh et al. [31], i.e., 1.25< c/h_0 <3 (c=10mm, h_0=5mm). The acquisition of the crack images during the first 90s of crack propagation test was performed every 100ms (crack propagation is slow), the time intervals was reduced to 10ms for the rest of the experiment.

Crack contour (Figure 2a, b, c)) and displacement (Figure 2d)) were derived from every image using ImageJ © free software and python modules [32]. Vp was calculated for every 0.2 kJ/m^2 G variation from the equation $Vp = c_{G+0.2} - c_G / \Delta t$, where c refers to crack tip position (Figure 2b). Finally, the averaged Vp of 3 specimens of the same material was used for plotting the Vp(G) curves. In addition, "instantaneous" crack speed (V_{pi}) was calculated from the crack displacement between two consecutive images.

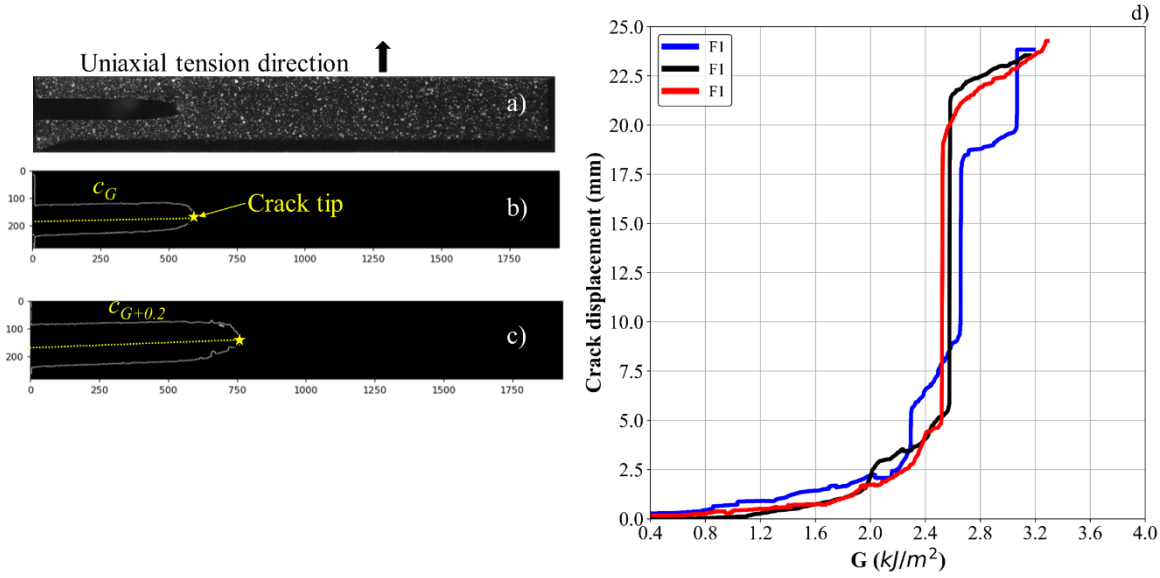

Figure 2: a) Stretched notched PS specimen with speckled pattern. b) Crack contour plotted derived from the picture (a) at a given G. The yellow star denotes the crack tip c) evolution of the crack contour after the increase of G by 0.2kJ/m^2. d) Crack displacement measured with three specimens of the same model material F1 as a function of G. The same plots for F2 and F3 materials are reported in SI (Figure A1).

2.3.2 In-situ crack propagation test using X-ray tomography (Anatomix)

For the in-situ tomography study of the crack propagation, single edge notched geometry (SENT) (Figure 1d) was used instead of PS geometry due to field of view limitations (2.3mm x

2.3mm x 2.3mm). The notched sample was stretched up to a given strain (10%, 20% 30% etc.) and maintained at this stretching level for 20 min during which the crack can propagate. To stop the crack propagation and the material movements during the tomographic scan, the sample deformation was decreased by 2.5% before launching the 8 min scan. This protocol enables to obtain images with good quality.

3. RESULTS

3.1 Multiscale CB_{aggl} analysis

Lab Tomography was used for the characterization of the CB_{aggl} existing in the different model materials[27]. The cumulative volume fraction (ϕ_{cumul}) of CB_{aggl} whose volume is above 125µm^3 is 10.1%, 3.0% and <0.2% in F1, F2, and F3, respectively. Similar characterization of agglomerates using synchrotron radiation computed Tomography (SRCT) leads to slightly higher values (11.5%, 4.3% and <0.85% in F1, F2, and F3 respectively), due to a better detection of CB_{aggl} . Since good correlation is observed between both methods and more data are available from lab tomography, ϕ_{cumul} calculated from this technique will be quoted throughout this paper. F1 has a higher percentage of agglomerates with intermediate and big size (Figure A2 in SI). Eq_{diam} represents the diameter of a fictive inclusion having the same volume as the analyzed CB_{aggl}. The mean size (i.e. mean Eq_{diam} value) of the CB_{aggl} in F1, F2 and F3 is 10.8µm, 11.µm and 9.7µm respectively. Based on the ϕ_{cumul}, F2 can be considered as more representative of industrial grade rubber compounds and F3 as a special case which rarely exists in the industry.

As shown in the TEM image in Figure 3, CB_{aggl} detected by tomography are actually made of local over concentration of aggregates inter-penetrated by elastomer. At 200nm resolution, we can observe the dispersion of aggregates either in CB_{aggl} or in the matrix of F1 (Figure 3b). Thus, the detected agglomerates appear as soft deformable clusters in which concentration of aggregates varies locally.

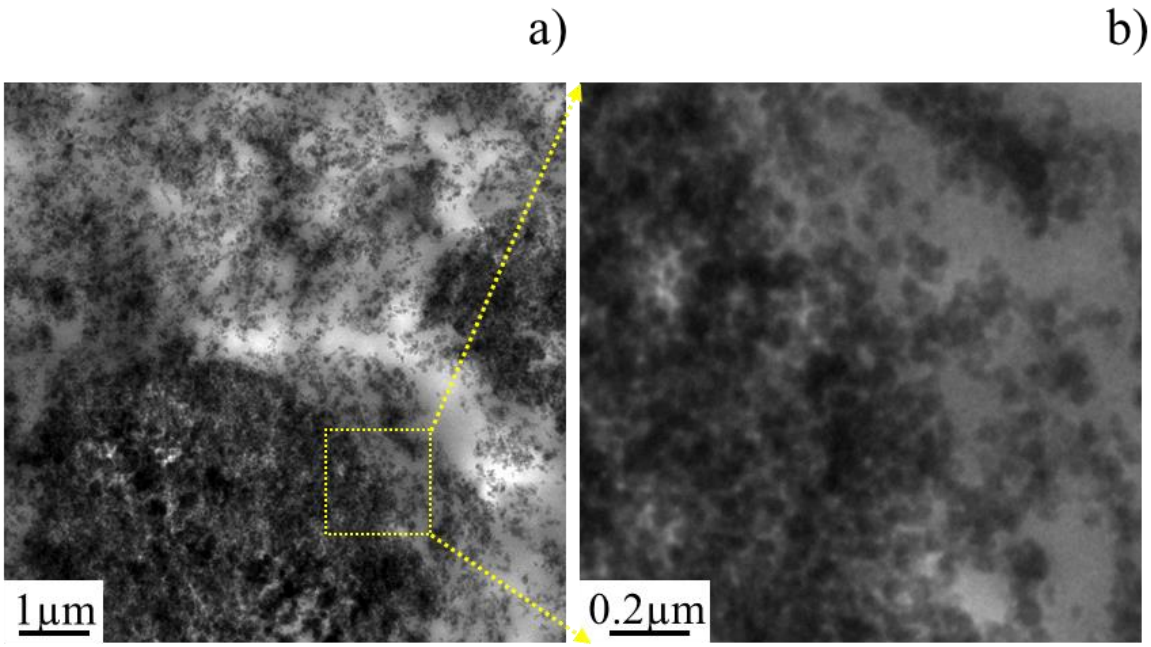

Figure 3: a) TEM image of a slice of CB_{aggl} in F1 at a resolution of 1µm, b) zoomed portion of the yellow square in 'a)' at a resolution of 200nm.

3.2 Macroscopic properties

3.2.1 Dynamic and mechanical properties

The viscoelastic properties of the materials are governed by the size of the filler aggregates, their volume fraction, and the polymer-filler interactions. The dynamic mechanical analysis (at 1Hz & 30°C) shows that all the model materials have similar dynamic properties for deformation below 8%, which is consistent with the agglomerates structure obtained using TEM, i.e. aggregates in CB_{aggl} have interactions with polymer chains . The consequence of this can also be seen in the monotonic uniaxial loading test of the materials (Pure shear geometry: Figure 4b). All the materials have similar mechanical behavior at high nominal strain up to 100% with PS geometry (it was also checked for dogbone geometry).

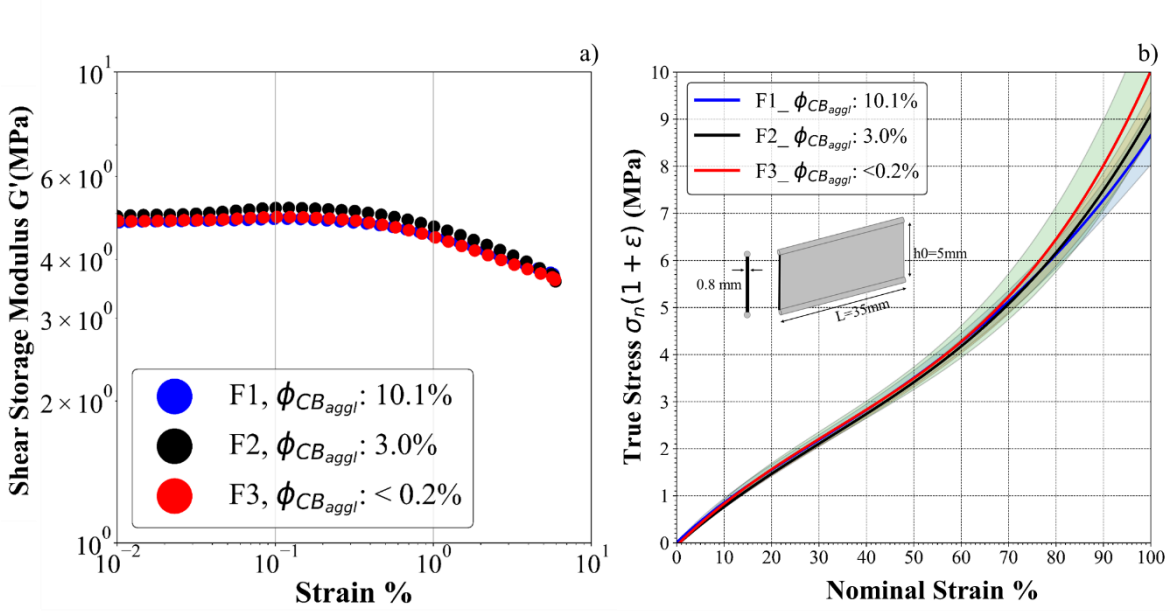

Figure 4 a) Shear storage modulus vs strain sweep for 3 model materials, b) true stress vs nominal strain properties up to 100% strain of model materials using unnotched pure shear geometry. The shaded region along each curve represents the standard deviation. True Stress vs nominal strain properties up to rupture are given in SI (Figure A3).

The materials have been cyclically strained three times up to a fixed nominal strain (25%, 50%, and 75%) using a dogbone sample geometry (Figure 1d). For a given maximum nominal strain, the unloading curves of the three cycles superimpose while the loading curves for the 2nd and 3rd cycle coincide with each other and are below the 1st loading curve (Figure A4 in SI). Such behavior is observed with filled elastomer and is characteristic of the so-called Mullins effect. The energy dissipated only during the first cycle[33] is deduced from: $\Delta U^n_{hyst} = \int_{0\ cycle\ 1}^{\epsilon_{\max\_mullins}} \sigma_N d\epsilon - \int_{0\ mean(cycle\ 2\ \&3)}^{\epsilon_{\max\_mullins}} \sigma_N d\epsilon$, where σ_N and ϵ are the nominal stress and strain and $\epsilon_{\max\_mullins}$ is the maximum nominal strain applied during the cycle. The hysteresis loss (ΔU^n_{hyst}) at high strain is higher for F1 (Figure 5) compared to F2 and F3.

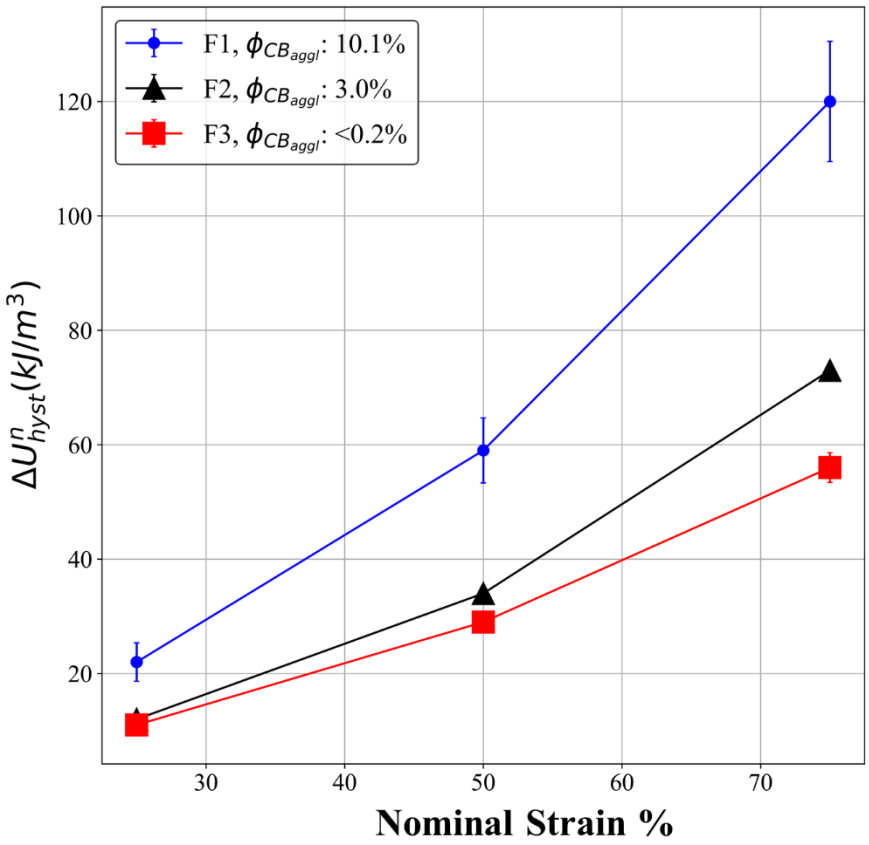

Figure 5: Irreversible hysteresis loss (ΔU^n_{hyst}) for F1, F2 and F3.

3.2.2 Crack propagation regime

Figure 6 presents the "*instantaneous*" crack speed measured during a continuous uniaxial deformation of a notched PS sample. In F1 and F2 materials, it suggests that the crack propagates by several cycles of crack growth and arrest, rather than a continuous propagation, for G value below 1.2kJ/m^2 for F1 and ca. 0.8-1.2 kJ/m^2 for F2. For F3, the results indicates a rather continuous crack propagation for all the G measurement domain (Figure 6c). This is consistent with observations of the crack surface of the ruptured materials. Figures 6 d-f presents the crack surface projection on a 2D projection plane. The color coding is the height variation of crack surface (Z profile) with respect to the Z value at the origin of the crack. The typical characteristics of stick slip crack surface shape such as saw tooth[17], wavy[34], etc. can be observed in Figures 6 d-f. This appears as a linear or triangle-shape wave front. All these results confirm that Vp is in the domain of the Vp(G) curve where stick slip occurs [12,17,34,35]. Occurrence of crack arrest is more frequent in F1 (higher number of triangle

wave front). The number of crack arrests for F2 is intermediate between F1 and F3. In F3, the crack propagation has a rather smooth profile.

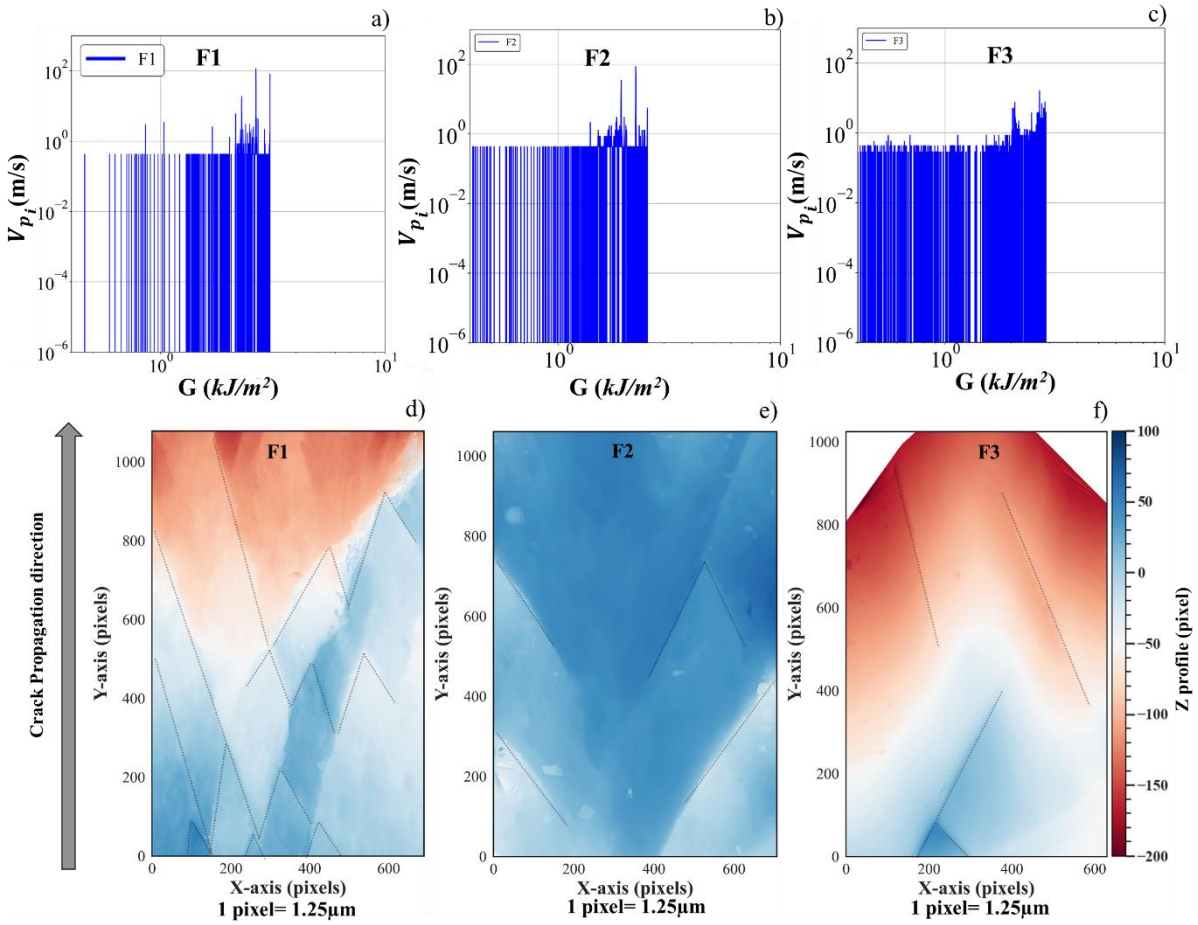

Figure 6 a), b), and c): Examples of Vp based on subsequent images for one specimen of the model materials F1, F2, and F3, respectively. d), e) and f) crack surface for the model materials F1, F2, and F3, respectively. The color range indicates the height variation with respect to the height of the crack origin. The pixel resolution is 1.25µm

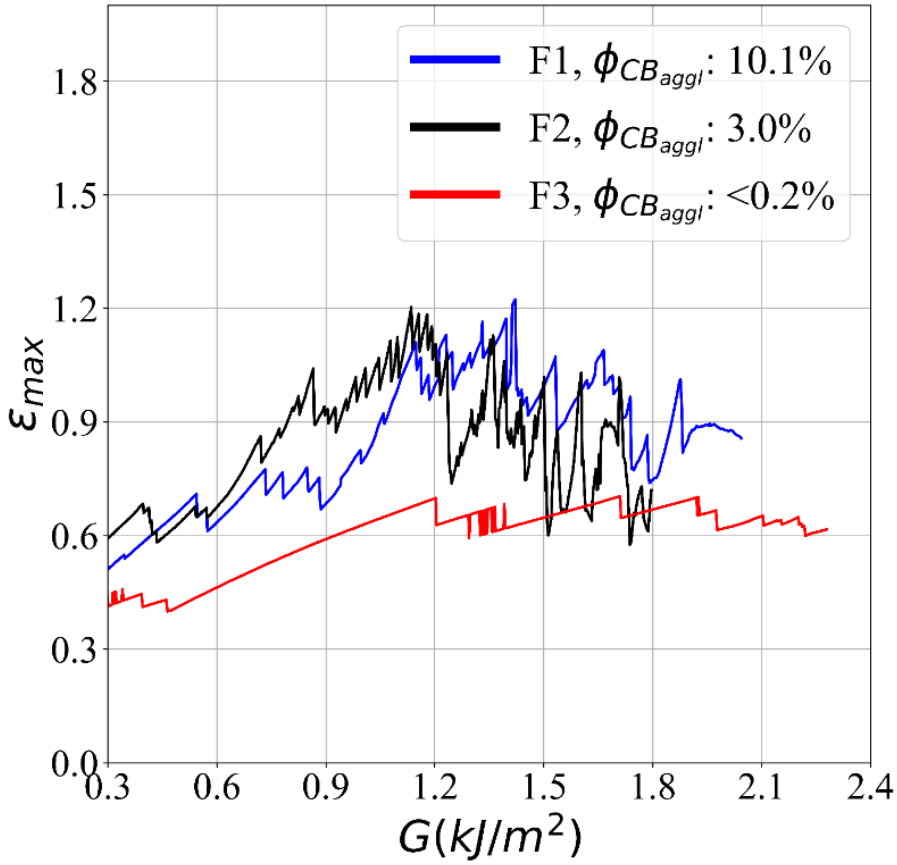

Figure 7: a) ϵ_{max} observed next to crack tip as a function of G for F1, F2 and F3,

The displacement field was deduced from the images acquired during the crack propagation (cf. SI Figure A5). From this, the nominal strain in the tensile direction was calculated as a function of the distance to the crack tip, for different G. The nominal strain at the crack tip is maximal and noted ϵ_{max}. As shown in Figure 7, ϵ_{max} is above 50% for F1 and F2 for any given G. The zig-zag pattern in the maximum nominal strain curve confirms the existence of cycles of crack growth and arrest during the crack propagation. As expected, the ϵ_{max} profile for F3 is much smoother compared to the one of F1 and F2 (Figure 6 d, e).

3.2.3 Vp(G)

Vp(G) curves of 3 tests are presented in Figure 8. Following the literature, in the identified domain of the Vp(G) curve, the crack growth rate obeys a power law dependency on G as follows: $V_p = A.G^{\beta}$ [36–38]. A and β are materials constants which depend on the material properties, and therefore on their formulation and thermomechanical history [36–40]. β is found equal to 2.6, 3.3, and 3.7 for F1, F2, and F3, respectively. These values are consistent with the ones found in the literature for EPDM [16,41–44]. Vp varies from 10^{-6} m/s to 10^{-3} m/s for G

values ranging from 0.4 kJ/m^2 to 2.5kJ/m^2. For practical purpose, the domain of Vp above 8.10^{-5} m/s is called hereafter high Vp or high G domain whereas the one with Vp below 8.10^{-5} m/s, low Vp or low G domain. The observed crack growth begins at low G (<0.4kJ/m^2) for both F1 and F2, whereas it is at around 0.8kJ/m^2 for F3. The high value of G for F3 may be associated to the very good dispersion of carbon black, without agglomerates. More interestingly, at the highest Vp values, G is higher for F1 than for F2.

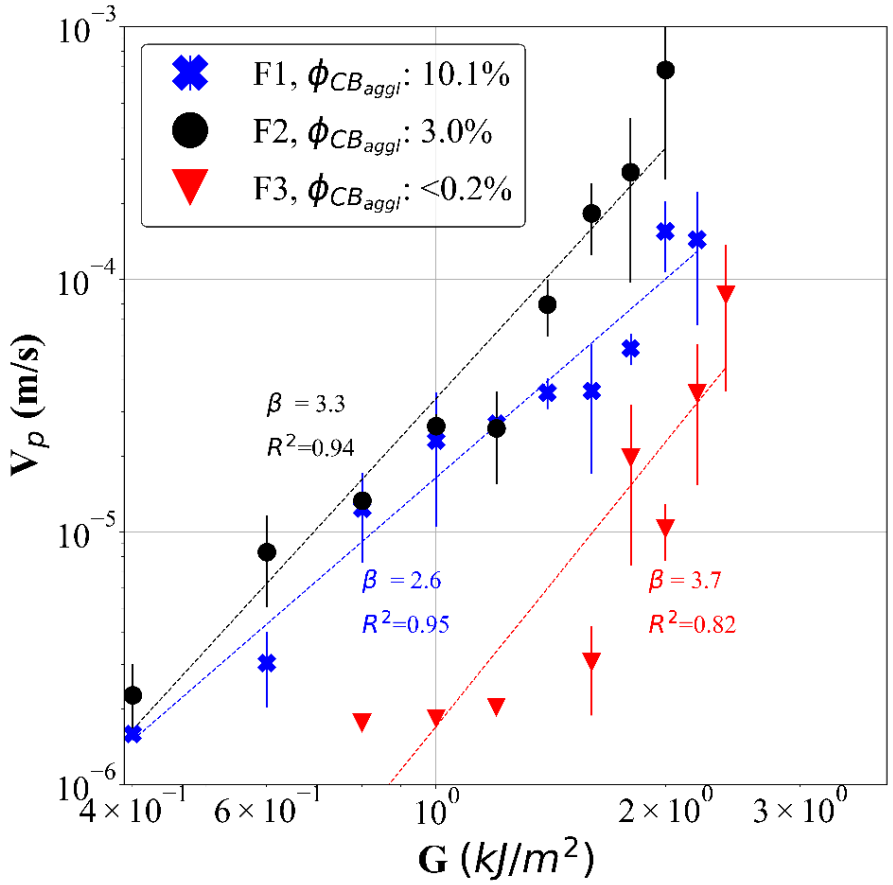

Figure 8: Vp(G) curve for F1, F2 and F3.

3.3 Microscopic analysis

3.3.1 CB_{aggl} damage mechanisms

An in-situ tensile test using SRCT (P05 imaging beamline) is used to identify local damage mechanisms at microscale. The results from F2 material are presented in Figure 9. The slice view of a CB_{aggl} at different nominal strains (Figure 9a) shows that agglomerates undergo multiple fractures. Between 40% and 50% nominal strains, we only observed the breakage of the biggest CB_{aggl} (with Eq_{diam} above ca. 78µm). For higher nominal strain, more CB_{aggl} undergo internal fracture. The higher the nominal strain, the smaller the minimum size of the CB_{aggl}

broken. For instance, the minimum Eq_{diam} of CB_{aggl} that undergoes fracture at 60% and 70% nominal strain is 33µm and 20µm respectively (Figure A6 in SI). A slice view from the 3D volume of F2 (Figure 9b) at 100% nominal strain shows that most of the agglomerates in the sample have been fractured (some are marked by a yellow circle). Moreover, the number of fractures inside a CB_{aggl} increases with the strain, as shown with the biggest observed CB_{aggl} (cf Figures 9a-b). The same phenomenon of CB_{aggl} fracture is evidenced at the crack tip in notched sample (cf. Figures 10a-d). The greyscale intensity profiles throughout the observed agglomerates at 0% and 37% nominal strain are plotted in Figure 10c and Figure 10d respectively. The dips in the profile are a clear indication of these fractures (marked by a circle in Figure 10*c*).

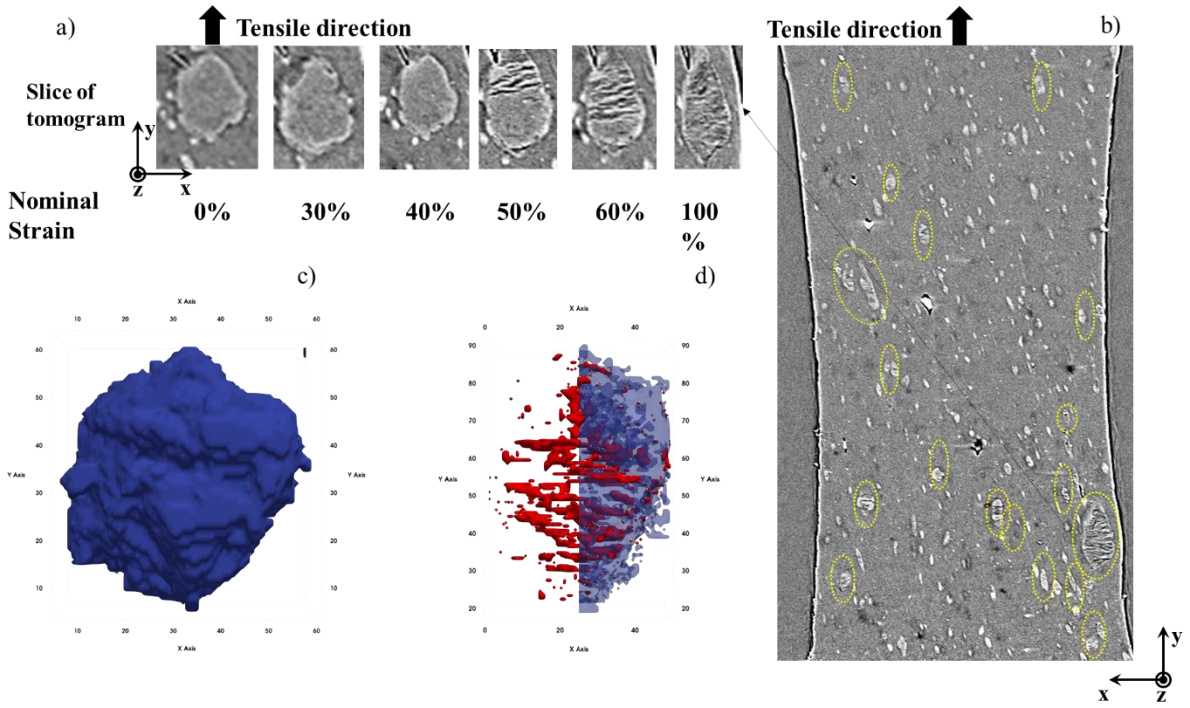

Figure 9 a) Slice view of the evolution of damage of CB_{aggl} upon stretching. b) The circles in the slice view of the sample volume at 100% nominal strain indicates the fractured agglomerates. c) and d) 3D view of the agglomerate at 0% and 100% nominal strain respectively. The red layers correspond to cavities created between the layers of fractured CB_{aggl}.

3.3.2 Other mechanisms observed at the crack tip

Figures 10 e)-f) and Figures 10 g)-h) present a slice view of a crack tip for F1 in two different planes, at 0% and 36% nominal strain. In the image of the first plane at 36% nominal strain (Figure 10 f), one can see that the crack has been stopped by an agglomerate. However, in the

second observation plane, for the same nominal strain, the crack has also propagated through another agglomerate (Figures 10 g)-h)). In addition, it was also observed that during crack propagation, the crack path can be sometimes deviated towards a CB_{aggl}, which was not in the initial notch plane (Figure A7 in SI). The existence of all the above mechanisms is not specific to the geometry used for SRCT, and was also confirmed with the pure shear geometry samples (cf. SI for further information, Figure A8).

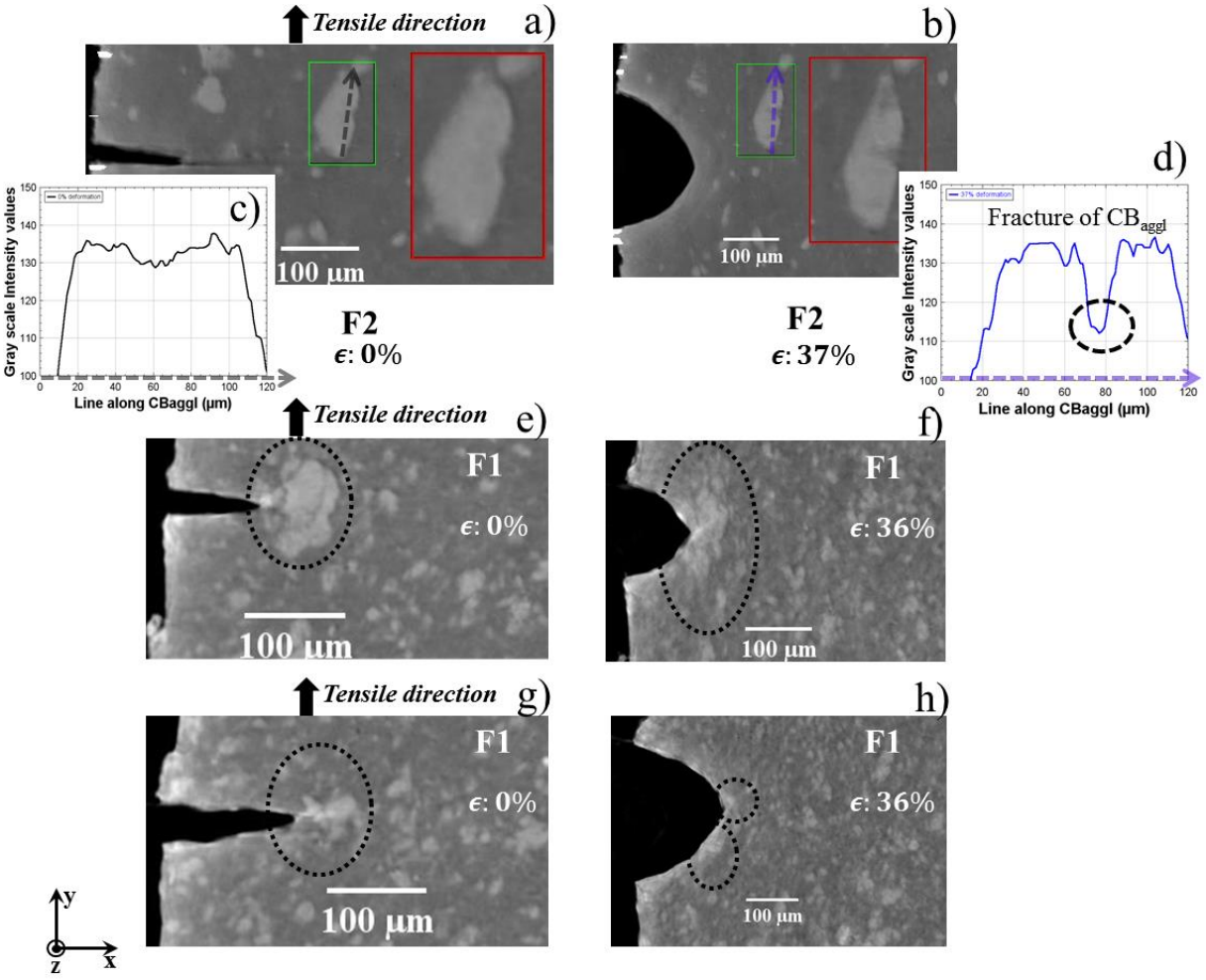

Figure 10: a)-b) Fracture of an agglomerate near a crack tip for F2 sample. c) - d) grey scale intensity values along the black and blue line drawn on the CB_{aggl} from a) and b) images respectively. e) & f) F1 material strained at 0% and 36% respectively (same observation plane). g)-h) crack propagation through a fractured agglomerate in F1 sample in another observation plane. In g) CB_{aggl} are identified by dotted circle at the crack tip. In h) the fractured CB_{aggl} is identified by 2 circles at the crack tip.

4. DISCUSSION

Micron size agglomerates exist in industrial products, usually in non-negligible concentration. To understand their role on the crack propagation mechanisms, three model filled EPDM samples have been processed with a low CB_{aggl} concentration, a CB_{aggl} concentration representative of the one found commonly in industrial products, and an abnormally high one. We measured their crack propagation resistance and observed the local damage mechanisms occurring at the micron-scale during this propagation. Compared to a material with quasi absence of agglomerates (F3), increasing the agglomerates concentration ato 3.0% (F2) or 10.1% (F1) does not significantly change the mechanical properties, i.e. the viscoelastic modulus and tensile stress strain curve at large strain (cf. Figure 4). Nevertheless, the crack propagation is made faster whatever the G value tested. This is consistent with the larger curvature radius of the crack tip (SI Figure A9) and the smaller maximum strain seen by the F3 materials at the crack tip (Figure 7). Our assumption is that in F1 and F2, the significant agglomerates concentration locally perturbs the material deformation at the crack tip, hence increasing the local stress concentration. More interestingly, the increase in the agglomerates concentration from 3.0% to 10.1% decreases the crack propagation velocity as G increases.

Past studies correlated the energy dissipation during high strain loading to the crack propagation resistance[17,33,45]. Thus, the better resistance to crack propagation for filled elastomers vs unfilled one was partially attributed to an increase in the strain energy release rate brought by the energy dissipated by the Mullins effect [12,34,45,46]. Similarly, the studies by Ducrot *et al.*[33] and Slootman[47] showed that mechanisms involving sacrificial bonds, by dissipating more energy in the crack tip vicinity, also improve the fracture toughness of the material.

When CB_{aggl} are present, they can influence the crack propagation resistance through different mechanisms. Like in the work of Kailash *et al.*[51], we have shown that CB agglomerates can deviate the crack from its original path (SI Figure A7) , and therefore increase the total crack path. In addition, they can also lead to a crack arrest as shown in Figures 10 e)-f).Thus, the crack tip is momentarily reinforced and increases the stored energy available for the crack advance. Note that such mechanisms are however temporary which explains the better properties of F3 which has very few CB_{aggl}.

Moreover, we have clearly evidenced that CB_{aggl} are also the source of dissipative mechanisms. Figures 3 shows that in the 3 materials, they contain soft layers of polymer. For this reason, instead of relaxing stress concentration by cavitation at their poles, one observes, at sufficiently

large deformation, their internal fracture relaxes the stress concentrations [22] (Figure 9). This is consistent with the higher Mullins effect of the F1 material (shown by its higher ΔU_{hyst}^{n} , Figure 5) since it contains more agglomerates. Moreover, the higher the strain, the higher the energy dissipated in the big agglomerates, since those can be multi-fractured (cf. Figure 9). These mechanisms should lead to more dissipated energy in F1 than in F2 (as it has a larger CB_{aggl} content), and therefore a larger strain energy release rate at a given crack propagation speed.

Nevertheless, this does not explain the convergence of the Vp(G) curves of F1 and F2 at low G values. The size of the zone where the strain is amplified ahead of the crack tip must also be considered. Strain as a function of the distance to the crack tip, in the notch plane, is reported in Figure 11 for F1 material at low G value(0.6 kJ/m^2) and high G value (1.6 kJ/m^2) (see Figure A10 in SI for F2). From these figures, the distance to the crack tip below which the strain is larger than 50%, 60% and 70% can be estimated. 50% is the minimum nominal strain to observe CB_{aggl} fracture. We also know the dependence of this minimum strain with the CB_{aggl} size. One can then roughly estimate the corresponding volumes in the crack tip vicinity (assuming a tube or cylindrical zone). They are reported in table A1 in SI. They indicate that a significant number of agglomerates are submitted to strain larger than the strain at which they can be fractured, confirming that a lot of agglomerates fracture are occurring ahead of the crack tip for the G domain considered. Much more agglomerates are concerned in F1 than in F2 (with a ratio around 5). Their numbers are however largely reduced when G is decreased from 1.6kJ/m^2 to 0.6kJ/m^2. Thus, we can assume that at 0.6kJ/m^2, the energy dissipated at the crack tip by the agglomerate fracture is too low in both the materials to lead to a differences in the Vp(G) curves. By increasing the G value, the dissipated energies in both the materials during crack propagation are increased as well as their difference in absolute value, hence explaining the divergence of their Vp(G) curves.

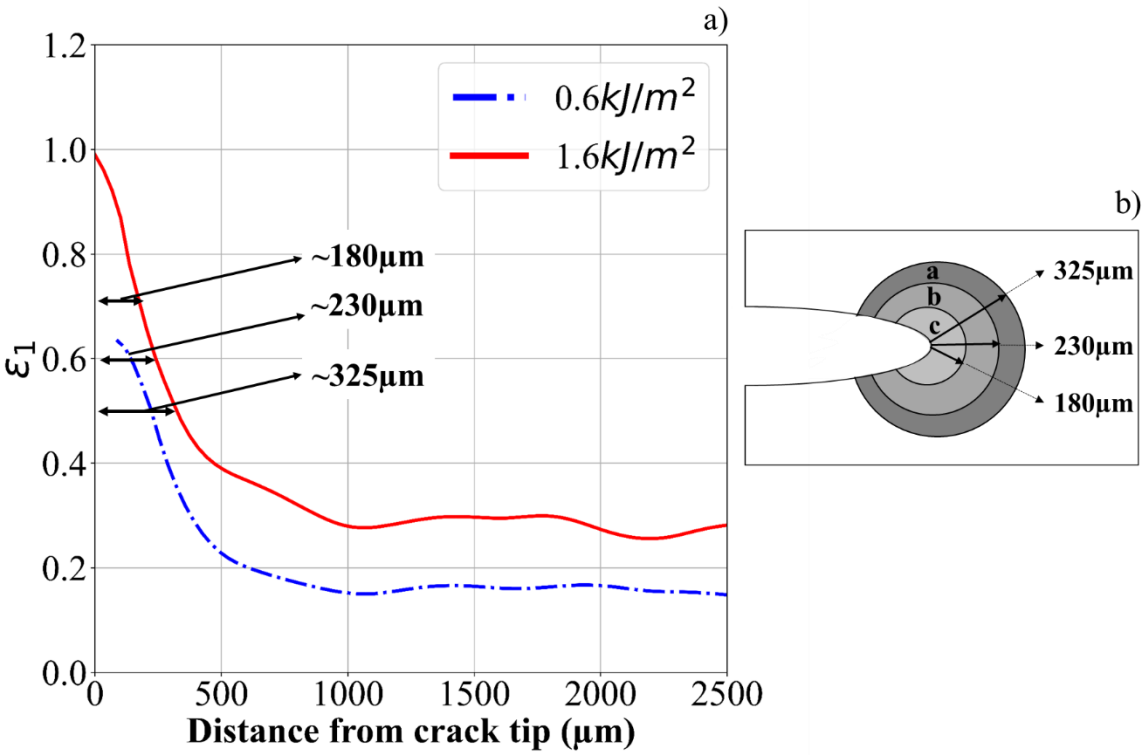

Figure 11: a) Nominal strain profile ahead of the crack tip for F1 at 2 G values (0.6 kJ/m^2, 1.6kJ/m^2). The arrow indicates the size of the zone for which the nominal strain is above 50%, 60%, and 70%. The plot for F2 is presented in SI (Figure A10). b) Scheme of the influence zone in F1: cylinder of radius "a" for strain between 50% and 60%, "b" for strain between 60% and 70% deformation, and "c" for strain above 70%.

5. CONCLUSION

An ideal reinforced elastomer always contains defects such as filler agglomerates especially during industrial production. These agglomerates are likely formed of overconcentration of filler aggregates and are therefore soft and deformable. Our original investigation by in-situ Synchrotron source X-ray tomography has showed that these agglomerates can fracture at high strain, depending on their size. Thus, they provide dissipative mechanisms around the crack tip which can be particularly significant at high strain energy release rate.

6. ACKNOWLEDGEMENTS

This work was supported by LRCCP and ANRT (CIFRE N° 2018 /0429). We thank Florent Dalmas from MATEIS, INSA Lyon who performed the TEM characterizations.

7. SUPPORTING INFORMATION

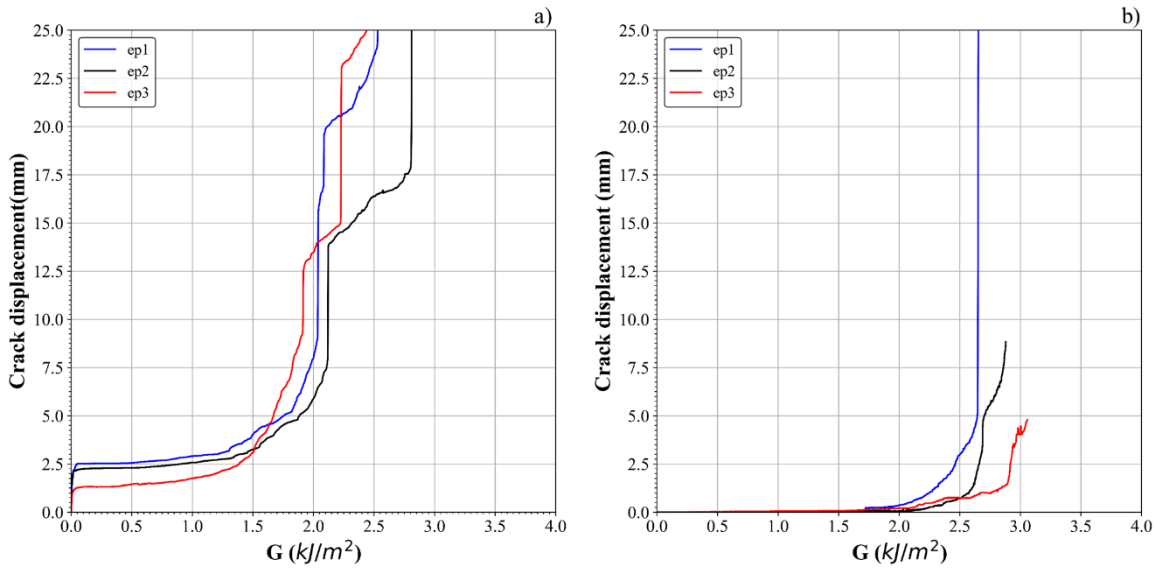

Figure A1: Crack displacement as a function of G for a) F2 and b) F3.

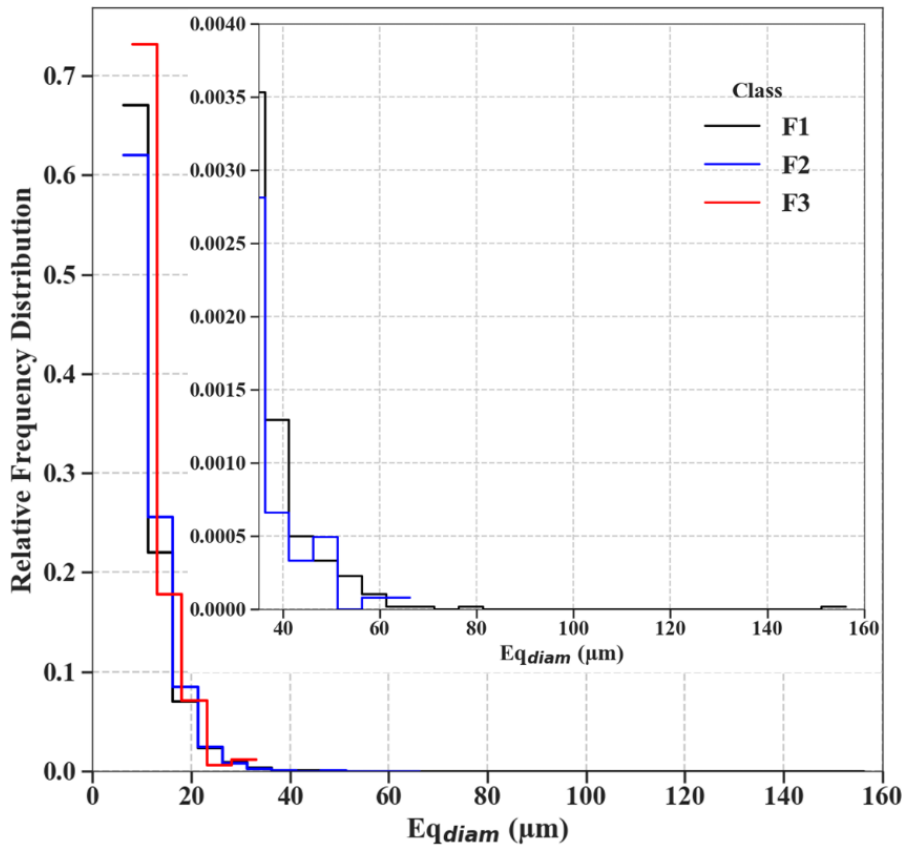

Figure A2: Distribution of the equivalent diameters of the agglomerates (Eq_{diam}) for the materials F1, F2 and F3.

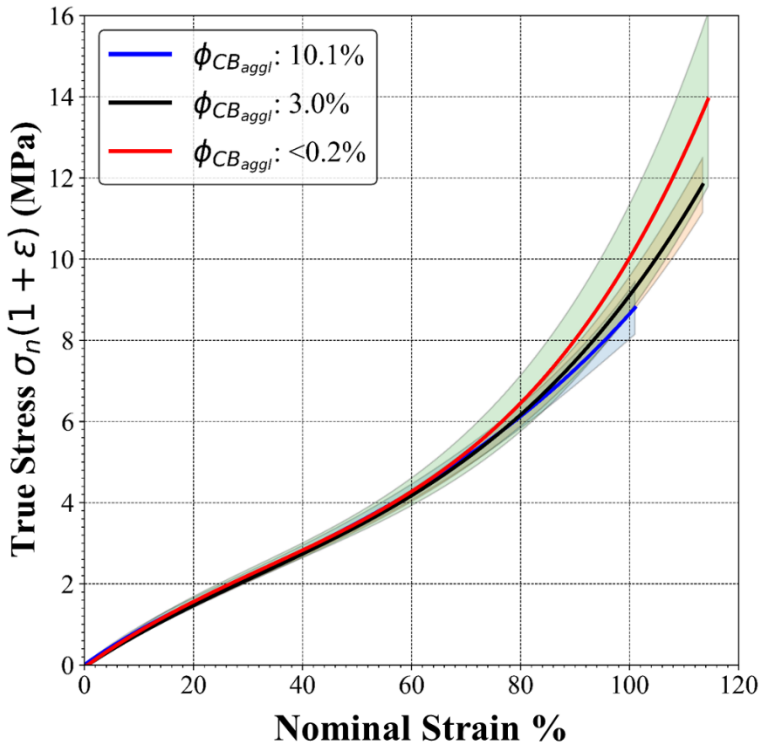

Figure A3: True Stress vs nominal strain plots of model materials using unnotched pure shear specimen geometry. The shaded region along each curves represents the standard deviation.

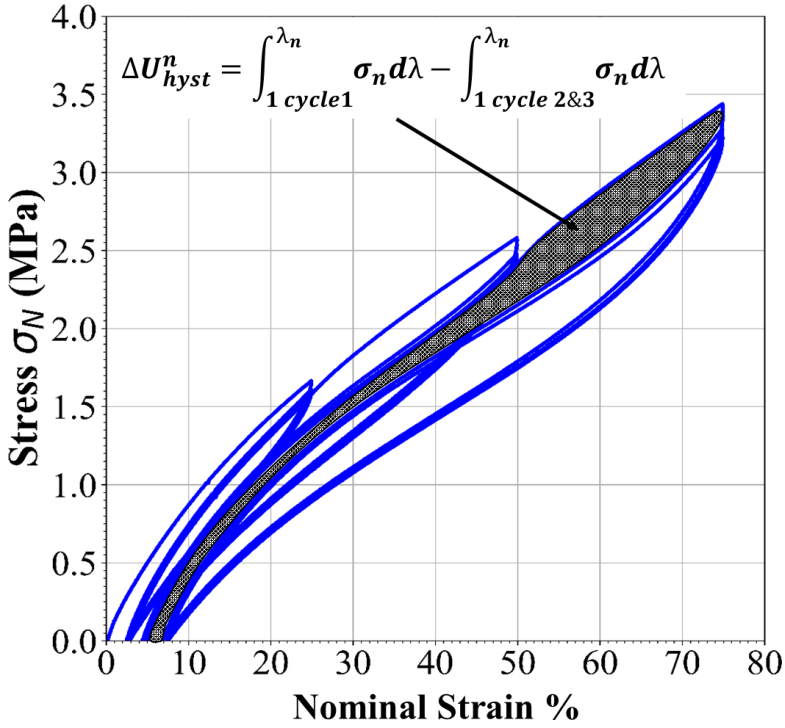

Figure A4: Materials have been cyclically deformed three times up to a fixed nominal strain (25%, 50%, and 75%) using a dogbone sample geometry. Shaded area is the irreversible energy lost at 75% nominal strain.

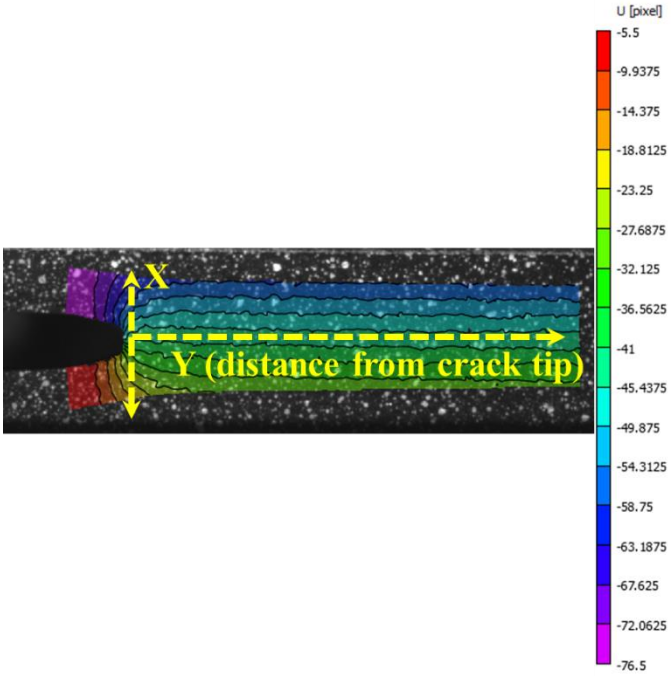

Figure A5: Example of displacement field (U_x) along the tensile direction deduced from DIC measurement during crack propagation.

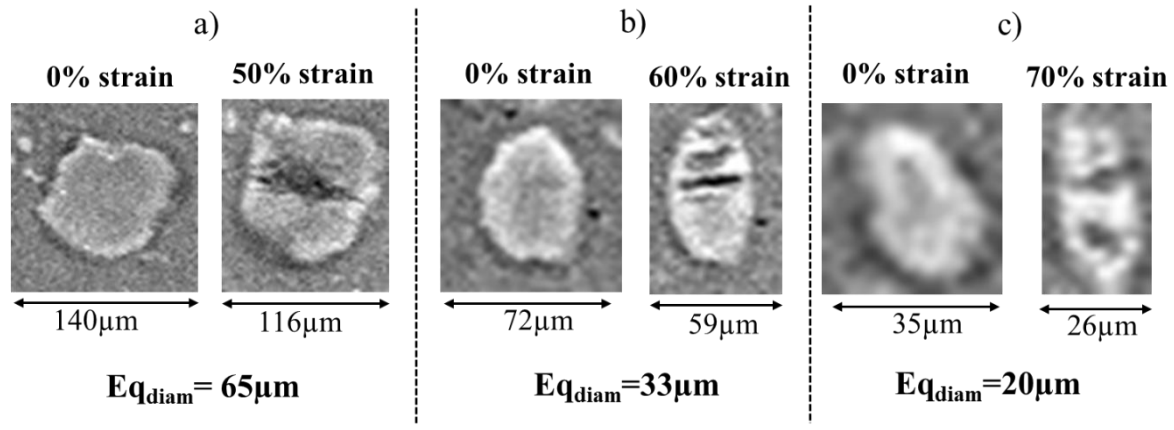

Figure A6: The smallest CB_{aggl} that undergo fracture at a given strain. a) CB_{aggl} with Eq_{diam} = 65µm undergo fracture at 50% nominal strain. b) CB_{aggl} with Eq_{diam} = 33µm undergo fracture at 50% nominal strain. c) CB_{aggl} with Eq_{diam} = 20µm undergo fracture at 50% nominal strain.

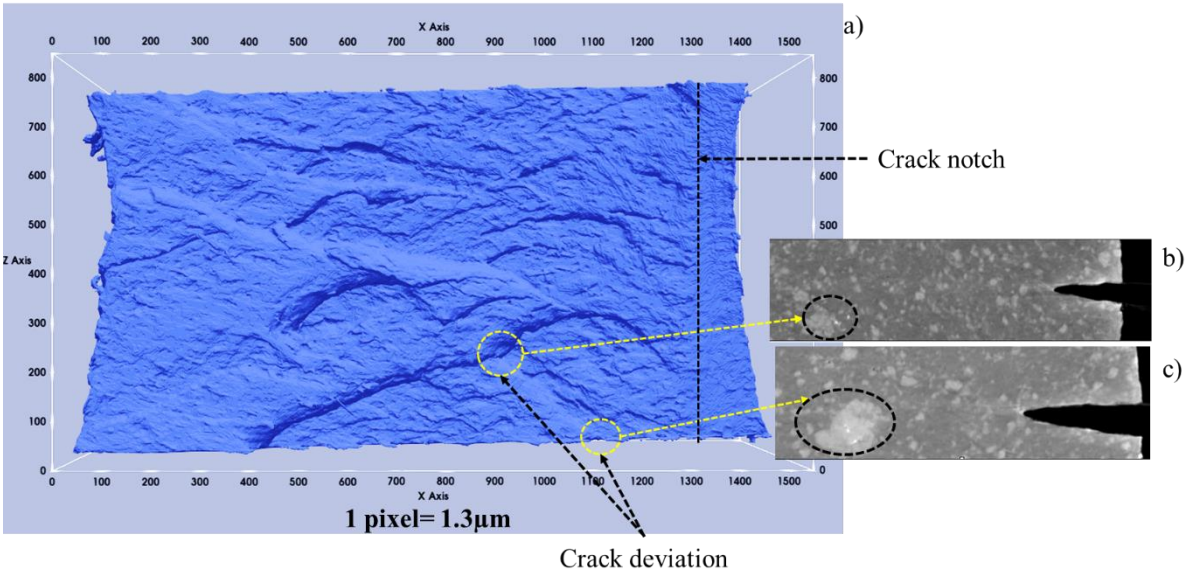

Figure A7: a) Crack surface of F1 visualized using SRCT. Crack arrests are identified by yellow circles. There is a change in the direction of crack and the crack front forms triangle waves. Post mortem analysis revealed that at each of these circled points, there was a CB_{aggl} which had stopped the propagation or deviated the crack from its original path. b)-c) The corresponding slice views of these agglomerates are presented alongside the picture (a).

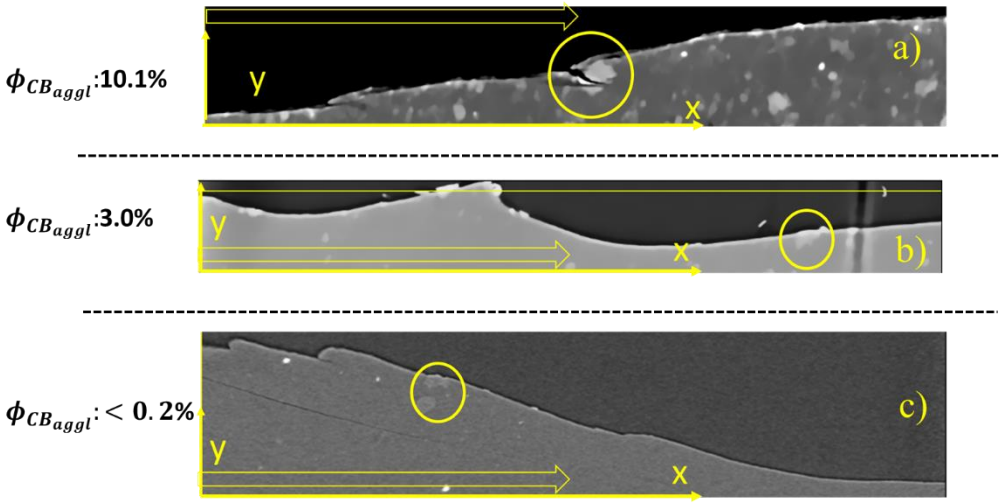

Figure A8: a)-c), slice view obtained from lab tomography of fractured surfaces for the 3 model materials. When crack approaches a CB_{aggl}, it breaks it (yellow circle) and propagates through it, rather than undergoing deviation along the agglomerate's contour, which is contrary to the mechanism often proposed in the literature[16,48]. Crack arrest is visible in F1 (yellow circle in Figure A8a) due to the presence of CB_{aggl} and a secondary crack initiation which originates from this point changes the direction of crack. Initiations of secondary crack are less observed in F2 (Figure A8b and Figure 6e). The contour of the propagation path looks similar to a saw

tooth profile[17]. In F3, crack deviation is observed (visually less significant compared to F2 in Figure 6f), although it is not induced by the presence of agglomerates (Figure A8c). The crack propagation direction is modified in the very beginning, maybe due to the notch geometry. This can also be confirmed in the graph of ϵ_{max} at the crack tip for F3, as it is generally smooth throughout the crack propagation (no crack arrest).

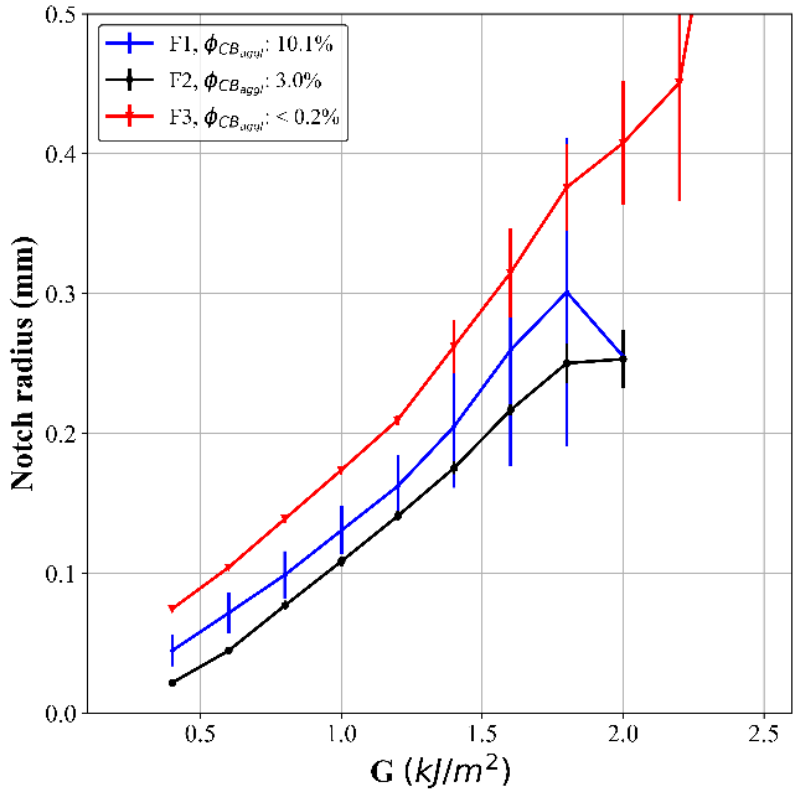

Figure A9: Evolution of notch radius as a function of G during a crack propagation in a pure shear geometry.

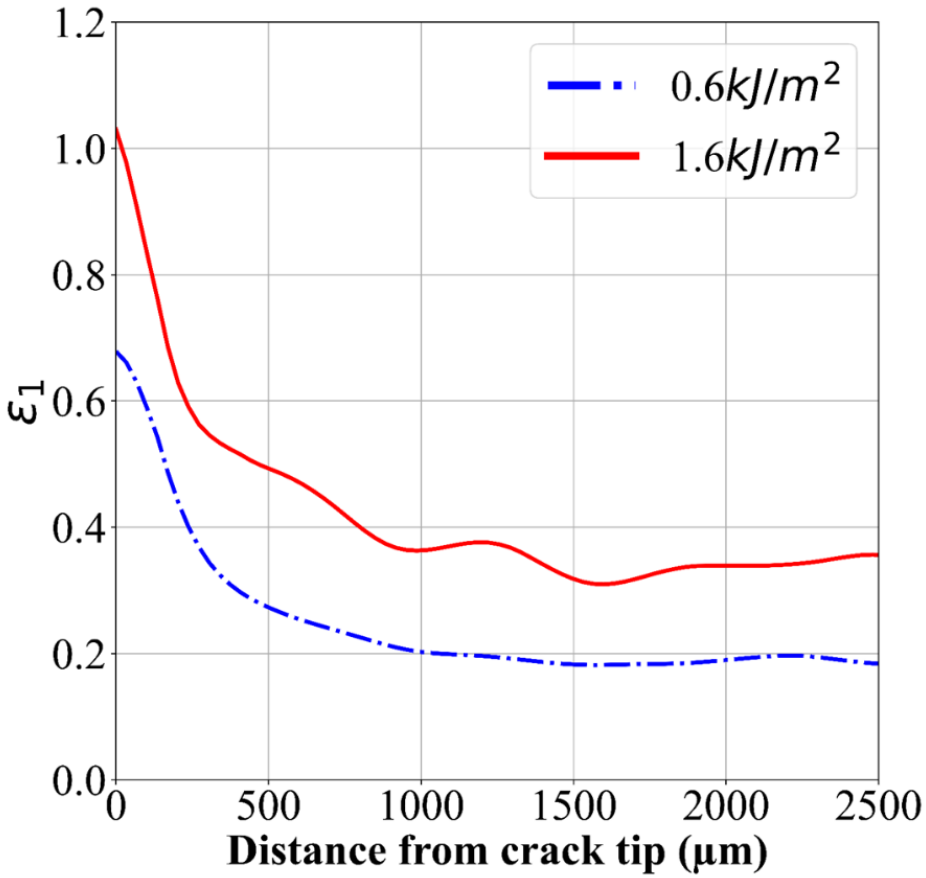

Figure A10: Nominal strain profile ahead of the crack tip in the notch plane for F2 at 2 G values (0.6 kJ/m^2, 1.6kJ/m^2)

Calculation of Number of CB$_{aggl}$ highly deformed in the crack tip vicinity:

At 1.6 kJ/m^2 (high G), the distance from the crack tip with nominal strain greater than 50%, 60% and 70% is around 325µm, 230µm and 180µm respectively for F1. Similarly for F2, it is around 440µm, 200µm and 160µm respectively. At 0.6 kJ/m^2 (low G), size of the zone with strain above 50% and 60% for F1 is 220µm and 130µm respectively and for F2, it is 170µm and 100µm respectively. There is no zone next to the crack tip with strain greater than 70%.

Number of CB$_{aggl}$ in a zone= Volume of the zone (e.g. *a* or *b* or *c*)*volume fraction of CB$_{aggl}$/ Volume of one CB$_{aggl}$ with median Eq_{diam}

G (kJ/m^2)	Material	Zone	Length of the zone	Volume of the zone ($10^8 \mu m^3$)	Minimum size of CB_{aggl} which fracture	Median size of CB_{aggl}	Vol fraction of CB_{aggl} above the minimum size (%)	N
1.6/0.6	F1	a	325/220	1.4/0.9	65	79	0.4	2/1
		b	230/130	0.6/0.5	33	39	1.6	30/25
		c	180/-	0.9/-	20	23	4.5/0	647/0
	Total Number of CB_{aggl}							**~680/25**
	F2	a	440/170	4.3/0.3	65		0.01	0/0
		b	200/130	0.4/0.5	33	36	0.3	5/6
		c	160/-	0.3/-	20	23	1.2/-	135/0
	Total Number of CB_{aggl}							**~140/6**

Table A1: Calculation of Number of CB_{aggl} for each material in the dissipative zones

8. REFERENCES

[1] Medalia, A. I. Effect of Carbon Black on Ultimate Proper.Pdf *Rubber Division, Americal Chemical Society* **1986**, *60*, 45.

[2] Nusser, K.; Mosbauer, T.; Schneider, G. J.; Brandt, K.; Weidemann, G.; Goebbels, J.; Riesemeier, H.; Göritz, D. Silica dispersion in styrene butadiene rubber composites studied by synchrotron tomography *Journal of Non-Crystalline Solids* **2012**, *358*, 557, 10.1016/J.JNONCRYSOL.2011.10.009.

[3] Astruc, M. Thesis,. Étude rhéo-optique des mécanismes de dispersion de mélanges sous cisaillement simple . 1 Mélanges concentrés de polymères immiscibles . 2 Mélanges polymères-charges poreuse, l'École des Mines de Paris, **2008**.

[4] Collin, V.; Boudimbou, I.; Peuvrel-Disdier, E. New insights in dispersion mechanisms of carbon black in a polymer matrix under shear by rheo-optics *Journal of Applied Polymer Science* **2013**, *127*, 2121, 10.1002/app.37769.

[5] Dizon, E. S.; Hicks, A. E.; Chirico, V. E. The Effect of Carbon Black Parameters on the Fatigue Life of Filled Rubber Compounds *Rubber Chemistry and Technology* **1974**, *47*, 231, 10.5254/1.3540429.

[6] Huneau, B.; Masquelier, I.; Marco, Y.; Le Saux, V.; Noizet, S.; Schiel, C.; Charrier, P. Fatigue crack initiation in a carbon black-filled natural rubber *Rubber Chemistry and Technology* **2016**, *89*, 126, 10.5254/rct.15.84809.

[7] Beurrot, S.; Huneau, B.; Verron, E. In situ SEM study of fatigue crack growth mechanism in carbon black-filled natural rubber *Journal of Applied Polymer Science* **2010**, *43*, NA, 10.1002/app.31707.
[8] Le Cam, J. B.; Huneau, B.; Verron, E.; Gornet, L. Mechanism of fatigue crack growth in carbon black filled natural rubber *Macromolecules* **2004**, *37*, 5011, 10.1021/ma0495386.
[9] Roland, C. M.; Smith, C. R. Defect Accumulation in Rubber. *Rubber Chem. Technol.* **1985**, *58*, 806–814.
[10] Aglan, H.; Chudnovsky, A.; Moet, A.; Fleischman, T.; Stalnaker, D. Crack layer analysis of fatigue crack propagation in rubber compounds *International Journal of Fracture* **1990**, *44*, 167, https://doi.org/10.1007/BF00035514.
[11] Saintier, N. Thesis,. Fatigue multiaxiale dans un élastomère de type NR chargé : mécanismes d'endommagment et critère local d'amorçage de fissure, Ecole Nationale Supérieure d'Arts et Métiers, **2001**.
[12] Fukahori, Y.; Sakulkaew, K.; Busfield, J. J. C. Elastic-viscous transition in tear fracture of rubbers *Polymer* **2013**, *54*, 1905, 10.1016/j.polymer.2013.01.019.
[13] Gent, A. N.; Park, B. Failure processes in elastomers at or near a rigid spherical inclusion *Journal of Materials Science* **1984**, *19*, 1947, 10.1007/BF00550265.
[14] Oberth, A. E.; Bruenner, R. S. Tear Phenomena around Solid Inclusions in Castable Elastomers *Transactions of the Society of Rheology* **1965**, *9*, 165, 10.1122/1.548997.
[15] Kraus, G. Reinforcement of elastomers by carbon black; In *Fortschritte der Hochpolymeren-Forschung*; Springer Berlin Heidelberg: Berlin, Heidelberg; pp 155; 10.1007/3-540-05483-9_12.
[16] Lorenz, H.; Steinhauser, D.; Klüppel, M. Morphology and Micro-mechanics of Filled Elastomer Blends: Impact on Dynamic Crack Propagation; **2013**; pp 81; 10.1007/978-3-642-37910-9_3.
[17] Stacer, R. G.; Yanyo, L. C.; Kelley, F. N. Observations on the Tearing of Elastomers. *Rubber Chem. Technol.* **1985**, *58*, 421–435.
[18] Le Cam, J.-B.; Huneau, B.; Verron, E. Fatigue damage in carbon black filled natural rubber under uni- and multiaxial loading conditions *International Journal of Fatigue* **2013**, *52*, 82, 10.1016/j.ijfatigue.2013.02.022.
[19] Pal, P. K.; Bhowmick, A. K.; De, S. K. Scanning Electron Microscopy Studies on Failure of Natural Rubber. *Int. J. Polym. Mater. Polym. Biomater.* **1982**, *9*, 139–149.
[20] Zhang, F.; Chen, Y.; Sun, C.; Wen, S.; Liu, L. Network evolutions in both pure and silica-filled natural rubbers during cyclic shear loading *RSC Advances* **2014**, *4*, 26706, 10.1039/c4ra02003k.
[21] Mdarhri, A.; Elies, P.; Brosseau, C. Stress induced cracks in carbon black filled elastomers probed by atomic force microscopy *Journal of Applied Physics* **2008**, *104*, 10.1063/1.3042218.
[22] Cao, X.; Zhou, X.; Weng, G. Nanocavitation in silica filled styrene-butadiene rubber regulated by varying silica-rubber interfacial bonding *Polymers for Advanced Technologies* **2018**, *29*, 1779, 10.1002/pat.4284.
[23] Maire, E.; Withers, P. J. Quantitative X-ray tomography *International Materials Reviews* **2014**, *59*, 1, 10.1179/1743280413Y.0000000023.
[24] Withers, P. J. Fracture mechanics by three-dimensional crack-tip synchrotron X-ray microscopy *Philosophical Transactions of the Royal Society A: Mathematical, Physical and Engineering Sciences* **2015**, *373*, 10.1098/rsta.2013.0157.
[25] Buffière, J.-Y.; Maire, E. *Imagerie 3D en mécanique des matériaux*; Hermes Science Publications, Ed.; Lavosier, **2014**.
[26] Maire, E.; Le Bourlot, C.; Adrien, J.; Mortensen, A.; Mokso, R. 20 Hz X-ray tomography during an in situ tensile test *International Journal of Fracture* **2016**, *200*, 3,

10.1007/s10704-016-0077-y.
[27] Kallungal, J.; Chazeau, L.; Chenal, J.-M.; Adrien, J.; Maire, E.; Barres, C.; Cantaloube, B.; Heuillet, P. Methodology for 3D characterization of microstructural defects in filled polymer using X-ray Tomography; In *Constitutive Models for Rubber XI*; CRC Press, **2019**; pp 77; 10.1201/9780429324710-14.
[28] Paganin, D.; Mayo, S. C.; Gureyev, T. E.; Miller, P. R.; Wilkins, S. W. Simultaneous phase and amplitude extraction from a single defocused image of a homogeneous object *Journal of Microscopy* **2002**, *206*, 33, 10.1046/j.1365-2818.2002.01010.x.
[29] Rivlin, R. S.; Thomas, A. G. Rupture of rubber. I. Characteristic energy for tearing *Journal of Polymer Science* **1953**, *10*, 291, 10.1002/pol.1953.120100303.
[30] Lake, G. J.; Lawrence, C. C.; Thomas, A. G. High-speed fracture of elastomers: Part I *Rubber Chemistry and Technology* **2000**, *73*, 801, 10.5254/1.3547620.
[31] Yeoh, O. H. Fracture mechanics of bond failure in the "pure shear" test piece *Rubber Chemistry and Technology* **2003**, *76*, 483, 10.5254/1.3547755.
[32] van der Walt, S.; Schönberger, J. L.; Nunez-Iglesias, J.; Boulogne, F.; Warner, J. D.; Yager, N.; Gouillart, E.; Yu, T. scikit-image: image processing in Python *PeerJ* **2014**, *2*, e453, 10.7717/peerj.453.
[33] Ducrot, E.; Chen, Y.; Bulters, M.; Sijbesma, R. P.; Creton, C. Toughening Elastomers with Sacrificial Bonds and Watching Them Break *Science* **2014**, *344*, 186, 10.1126/science.1248494.
[34] Tsunoda, K.; Busfield, J. J. C.; Davies, C. K. L.; Thomas, A. G. Effect of materials variables on the tear behaviour of a non-crystallizing elastomer *Journal of Materials Science* **2000**, *35*, 5187, 10.1023/A:1004860522186.
[35] Papadopoulos, I. C.; Thomas, A. G.; Busfield, J. J. C. Rate transitions in the fatigue crack growth of elastomers *Journal of Applied Polymer Science* **2008**, *109*, 1900, 10.1002/app.28086.
[36] Kaang, S.; Jin, Y. W.; Huh, Y. il; Lee, W. J.; Im, W. Bin A test method to measure fatigue crack growth rate of rubbery materials *Polymer Testing* **2006**, *25*, 347, 10.1016/j.polymertesting.2005.12.005.
[37] Gent, A. N.; Lindley, P. B.; Thomas, A. G. Cut growth and fatigue of rubbers. I. The relationship between cut growth and fatigue *Journal of Applied Polymer Science* **1964**, *8*, 455, 10.1002/app.1964.070080129.
[38] Lake, G. J.; Lindley, P. B. Cut growth and fatigue of rubbers. II. Experiments on a noncrystallizing rubber *Journal of Applied Polymer Science* **1964**, *8*, 707, 10.1002/app.1964.070080212.
[39] Grasland, F. Thesis,. Vieillissement du caoutchouc naturel parthermo-oxydation: Etudes de ses conséquences sur lacristallisation sous déformation, la fissuration et larupture, INSA Lyon, **2018**.
[40] Grasland, F.; Chazeau, L.; Chenal, J.-M.; Caillard, J.; Schach, R. About the elongation at break of unfilled natural rubber elastomers *Polymer* **2019**, *169*, 195, 10.1016/j.polymer.2019.02.032.
[41] Stoček, R. Some Revisions of Fatigue Crack Growth Characteristics of Rubber; **2020**; pp 1; 10.1007/12_2020_72.
[42] Klüppel, M. The role of filler networking in fatigue crack propagation of elastomers under high-severity conditions *Macromolecular Materials and Engineering* **2009**, *294*, 130, 10.1002/mame.200800263.
[43] Klüppel, M. Evaluation of viscoelastic master curves of filled elastomers and applications to fracture mechanics *Journal of Physics Condensed Matter* **2009**, *21*, 10.1088/0953-8984/21/3/035104.
[44] Stoček R., Heinrich G., Gehde M., K. R. Analysis of Dynamic Crack Propagation in

Elastomers by Simultaneous Tensile- and Pure-Shear-Mode Testing.; In *Fracture Mechanics and Statistical Mechanics of Reinforced Elastomeric Blends.*; Grellmann W., Heinrich G., Kaliske M., Klüppel M., Schneider K., V. T., Ed.; Springer, Berlin, Heidelberg: vol 70., **2013**; pp 269; https://doi.org/10.1007/978-3-642-37910-9_7.

[45] Lake, G. J.; Thomas, A. G. The strength of highly elastic materials *Proceedings of the Royal Society of London. Series A. Mathematical and Physical Sciences* **1967**, *300*, 108, 10.1098/rspa.1967.0160.

[46] Chazeau, L.; Chenal, J.-M.; Gauthier, C.; Kallungal, J.; Caillard, J. About the Influence of Materials Parameters on the Ultimate and Fatigue Properties of Elastomers; In *Fatigue Crack Growth in Rubber Materials. Advances in Polymer Science*; G., H.; R., K.; R., S., Eds.; Springer, Cham., **2020**; pp 297; 10.1007/12_2020_80.

[47] Slootman, J. Thesis,. Quantitative detection of damage in soft materials using mechano-fluorescence, l'Ecole Supérieure de Physique et de Chimie Industrielles de la ville de Paris (ESPCI Paris), **2019**.

[48] Jajam, K. C.; Tippur, H. V. Role of inclusion stiffness and interfacial strength on dynamic matrix crack growth: An experimental study *International Journal of Solids and Structures* **2012**, *49*, 1127, 10.1016/j.ijsolstr.2012.01.009.

CHAPTER 5

Microscopic damage and crack initiation mechanisms in a filled EPDM observed during tensile testing with in situ synchrotron X-ray tomography

(Proposition for an article)

TABLE OF CONTENTS

ABSTRACT

The paper presents a precise 3D quantification of damage evolution and eventual crack initiation due to metallic oxide inclusions and filler agglomerates during uniaxial solicitation, thanks to synchrotron radiation X-Ray Tomography. An in-situ tensile study using this technique reveals debonding at the poles of all metallic oxide inclusions upon stretching. These cavities caused by debonding do not lead to crack initiation since they grow parallel to the applied stress direction. Conversely, crack always initiates from carbon black agglomerates (CB_{aggl}) in filled elastomers. The crack initiation mechanism is a three step process that begins with the nucleation of cavities inside the CB_{aggl} upon stretching. This is followed by the growth of these cavities which brings about the fracture of the agglomerates. Finally, this fracture can lead to the creation of a matrix crack at the origin of the material rupture. It is also confirmed that CB_{aggl} that initiate the critical crack in the material are the biggest sized CB_{aggl} and are located close to the edges of the sample.

1. INTRODUCTION

Elastomers used in various applications are required to withstand high strain deformation during different types of solicitations. Incorporation of reinforcing fillers is an efficient way to improve their rupture and fatigue properties during such solicitations[1–3]. If the fillers disperse improperly, particularly during industrial production, they will remain as filler agglomerates. The existence of these agglomerates is inevitable in materials[4,5]. They are known to be precursors for crack initiation and are considered as defects in the materials. Apart from these, there are other defects like metallic oxides inclusions, micro-bubbles and voids in materials[6]. The latter appear in the matrix, mostly at the poles of the defects. There is a competition between cavitation and debonding mechanisms, depending on the adhesion strength between the matrix and the inclusions[7–9]. These damage mechanisms have been observed in industrial rubber compounds, e.g. debonding at the poles of ZnO inclusions and cavitation in filler agglomerates[10,11]. Post mortem analysis using electron microscopy reveals agglomerates at the crack initiation sites in a ruptured material [6,10]. Huneau *et al.*[10] have suggested that crack intiation from a filler agglomerate is due to cavity growth from its pole. However, this is contrary to the observations made by Gent *et al.*[7,12] and Lefèvre *et al.*[13], who studied material rupture in the presence of more than one inclusion. They noticed that cavity growth at the midpoint distance between two inclusions leads to rupture rather than cavitation at their poles. Thus, there is no accordance in the literature on the transition phenomena from local

damage associated to a defect to a crack that ruptures the material, especially for carbon black agglomerates (CB_{aggl}) in an industrial rubber compound. Such study requires a precise 3D quantification and visualization of the damage initiation, its evolution and the eventual crack initiation resulting from this damage.

To do so, we studied the rupture properties of 3 model materials containing a fixed concentration of inclusions and varying concentrations of CB_{aggl}. We performed an in-situ tensile study on these materials using Synchrotron Radiation Computed Tomography (SRCT). When performed concomitantly with mechanical testing, tomography enables a direct observation of damage mechanisms associated to defects like metallic oxide inclusion and CB_{aggl}, the damage evolution and crack formation inside the material. This analysis enables to extract various features controlling crack initiation mechanism such as the morphology and the location of the critical defects at the origin of the material rupture.

2. MATERIALS AND TESTING

2.1 Composition and materials processing

Model materials used for the current study are based on a non-crystallizing Ethylene Propylene Diene Monomer rubber (EPDM Keltan 4450) reinforced with high furnace carbon black (N326) and cross-linked using unsupported Bis (α,α-dimethylbenzyl) peroxide. The composition of the model materials (Table 1) was kept constant whereas compounding process conditions were varied in order to generate more or less flaws inside the materials. This specific composition enables the generation of CB_{aggl} defects. All the ingredients except the peroxide were mixed in a Haake Rheomix 600 OS mixer (chamber volume: 120cm^3) using Banbury rotors (42 cm^3) at a certain rotor speed and mixing time (Table 1), and were then passed 10 times in a two-roll mill where the peroxide was added. The sequence of ingredients addition is detailed in Table 1. USD method refers to "upside down", i.e., the elastomer was added after carbon black, TD method refers to "top down", i.e., carbon black was introduced after the elastomer in the internal mixer. After processing the material in the internal mixer and the two-roll mill machine, the samples were molded to a 2 mm thick sheet at 170°C under 190 MPa for 12 min. Curing time (t98) was estimated from torque measurements performed using a Monsanto rheometer analyzer. The samples for mechanical tests were die cut from this sheet using pneumatic punching tool. Hereafter, the samples are named S_X with X corresponding to the volume fraction of CB_{aggl} with a volume larger than 125 µm^3. This volume fraction was calculated from observations by synchrotron source X-ray tomography (and not from

laboratory sourced X-ray tomography like in chapter 4). ***Note that the so called S_11.5 and S_4.3 samples correspond to F1 and F2 presented in Chapter 4.***

Table 1: Composition of the Model Materials and process conditions

Samples	*S_11.5=F1*	*S_4.3=F2*	*S_9.0*
Ingredients	*(Phr)*	*(Phr)*	*(Phr)*
EPDM Keltan 4450	*100*	*100*	*100*
Carbon Black	*50*	*50*	*50*
ZnO			
Peroxide	*3.2*	*3.2*	*3.2*
Rotor Speed (tr/min)	*30*	*60*	*30*
Mixing Time (min)	*2*	*4*	*2*
Introduction Protocol	*TD* *1.EPDM* *2.CB*	*USD* *1.CB* *2.EPDM*	*USD* *1.CB* *2.EPDM*
Filler Volume	*19.3%*	*19.3%*	*19.3%*

2.2 Scanning electron microscopy (SEM)

We characterized the rupture surface of the materials by SEM using Zeiss Supra SEM (Germany). The materials were not metallized to avoid any closing of the crack. Observation of non-metallized surfaces requires low acceleration voltage to avoid any accumulation of charges. Thus, the energy of the electron beam was kept at 1 kV. The detector used is secondary electron detector. The composition of defects was obtained using Energy Dispersive X-Ray (EDX) detector. EDX needs a higher acceleration voltage of 10 kV for a higher emission of characteristic X-ray from the material surface.

2.3 Synchrotron radiation computed tomography (SRCT)

SRCT experiments were performed at the PETRA III P05 beamline at DESY, Germany (operated by Helmholtz-Zentrum Hereon), and the Anatomix beamline at SOLEIL , France. We obtained information regarding the onset of damage and crack initiation mechanism using both beamlines. At P05 imaging beamline, the energy of the monochromatic X-rays was 15keV with a spatial resolution of 2.19µm. The sample was mounted in a tensile rig (Figure A1a, SI). Its specific geometry (Figure 1) was designed to create as high stress as possible in the region of interest (ROI). The sample was rotated over 360° by steps of 0.225°. Each projection step lasted

30ms resulting in a total time per scan of 50s. We reconstructed 3D images with and without phase contrast. Images without phase contrast were used for the detection of damage (CB_{aggl} fracture and cavities) in the materials during the test. Then the CB_{aggl} associated to damage were segmented from the images acquired with phase contrast. This contrast was obtained by applying a phase retrieval algorithm implemented by Mooseman et al. [14]. *Experiments performed at Anatomix @SOLEIL used a filtered white beam with a mean energy of 20keV and a spatial resolution of 1.3µm. The experimental setup is shown in SI (Figure A1b). We used a homemade tensile rig with 5kN load cell for the tensile tests. The sample was rotated over 360° by steps of 0.18°. Each projection required 150 ms. At Anatomix, we improved the phase contrast of the image by applying Pagnanin filter before the 3D volume reconstruction*[15].

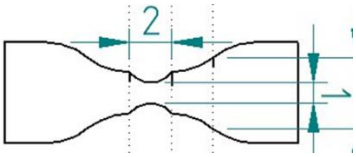

Figure 1: Sample geometry used for in-situ tensile test

After the reconstruction, we performed image analysis to optimize the contrast and to remove additional noise. Chapter 3 contains the details of the protocol. Each agglomerate is labelled in the binary image after its segmentation from the matrix. Its geometric features such as Volume V, Equivalent Diameter Eq_{diam}, Length of major principle axis a, Length of minor principle axis b and Eccentricity E are extracted using the regionprops module[16] *in Python. The volume V of a CB_{aggl} is the number of voxels it contains. The Equivalent diameter (Eq_{diam}) represents the diameter of a fictive inclusion having the same volume as the analyzed CB_{aggl}. Length of major (a) and minor principal axis (b) are those of an ellipsoid that has similar normalized 2nd central moment as the CB_{aggl}. Eccentricity (E) of an ellipse is the ratio between the distance of its two foci and the major principal axis length. Here, E is the eccentricity of the centered elliptic section of the ellipsoid, perpendicular to the c axis (with a > c > b):* $= \sqrt{1 - b^2/a^2}$ *. The bulk factor (B) of an agglomerate corresponds to the ratio of the free space (volume in this case,* ΔV*) between the agglomerate and the convex hull constructed around it to the total volume of the convex hull (V_{ch}), i.e.* $B(\Delta V) = 1 - V/V_{ch}$

2.4 Transmission electron microscopy (TEM)

We performed nanoscale characterization using TEM (CM120 Philips microscope) on a 90nm-thick section prepared by cryo-ultra-microtomy (Leica Ultra cut UCT microtome). The thin

section was placed on a 400-mesh copper grid. The accelerating voltage was set to 120kV and the CCD detector used was Orius CCD camera from Gatan.

2.5 Tensile testing

Tensile tests were conducted on an MTS 1/ME machine equipped with a 100N load cell. The nominal stress is defined as $\sigma_n = F/S_0$*, where F is the force and* S_0 *is the initial section of the sample. In most cases, true stress is used, which is defined as* $\sigma(t) = F(t)/S(t)$ *where S(t) is the current section area of the sample. In elastomeric materials whose deformation is isochoric, the true stress can be defined as* $\sigma_n(1+\epsilon_n)$*, where* σ_n *is the nominal stress and* ϵ_n *is the nominal strain defined as* $\epsilon_n = \frac{\Delta L}{L_0}$ *(*L_o *is the nominal length and* ΔL *is the displacement). The nominal strain is obtained using digital image correlation. The strain rate was around 0.005* s^{-1}*. The geometry of the sample used for tensile tests is presented in Figure 1.*

3. RESULTS

3.1 Microstructural characterization of different defects

Filled EPDM contains mainly 2 kinds of defects, pre-existing inclusions in the polymer and non-dispersed CB_{aggl}. As illustrated in Figure 2, the inclusions have high greyscale values, which indicates that they are made of elements with higher atomic number than carbon. EDX analysis confirms that they are inclusions of metallic oxides (Na_2O or K_2O) (SI 6.2). Their volume fraction is around 0.03-0.05% in the 3 model materials. Their average and largest Eq_{diam} are 7.5µm and 32µm, respectively.

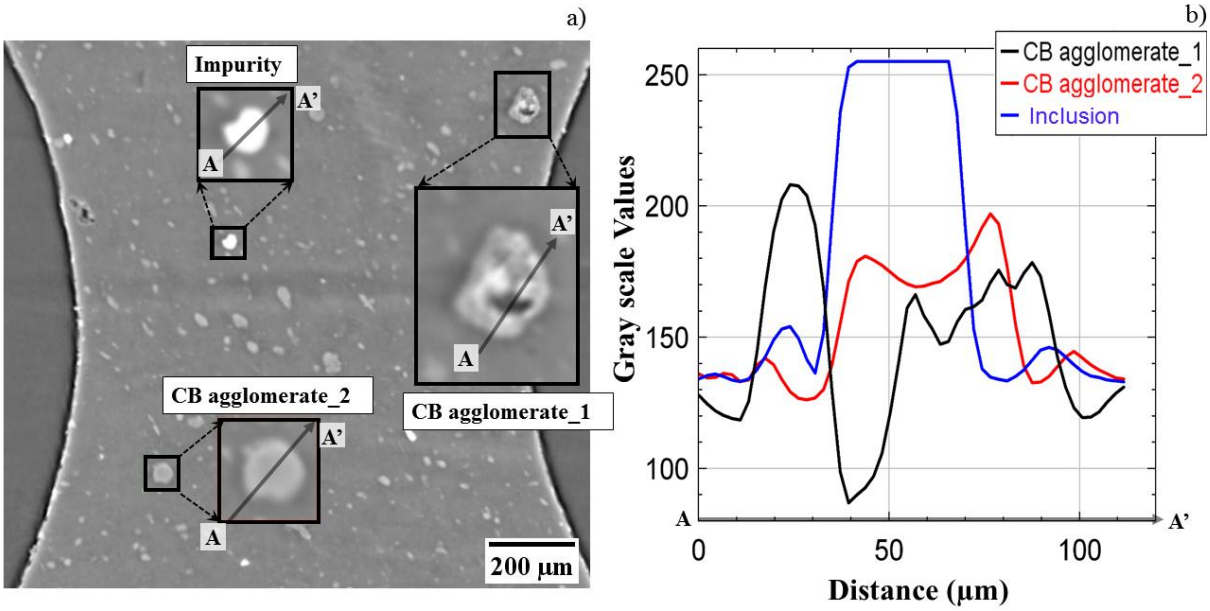

Figure 2: a) slice view of ROI of an S_9.0 test sample. Zoomed areas correspond to an inclusion and two CB_{aggl}. The grey scale intensity values across the lines drawn through these defects are plotted in b).

CB_{aggl} can be clearly distinguished from the matrix owing to the phase contrast imaging techniques implemented at P05 beamline. The two agglomerates presented in Figure 2 have different densities. CB_{aggl_1} has a lower density at the center than CB_{aggl_2} since there is a drop in greyscale values in its center. CB_{aggl_2} is the most frequently observed type of agglomerate in the material. TEM images have shown that these agglomerates are made of local over concentration of aggregates inter penetrated by elastomer (cf Figure 3 in chapter 4). The smaller electronic density of CB_{aggl_1} can be due to a lower concentration of aggregates and the possible presence of voids. In any case, all the detected agglomerates are deformable clusters in which concentration of aggregates varies locally. The volume fractions of CB_{aggl} with a volume above 125µm^3 are 11.5%, 4.3% and 9%, in S_11.5 (*F1 in chapter 4*), S_4.3 (*F2 in chapter 4*) and S_9.0 respectively. The corresponding mean Eq_{diam} of these CB_{aggl} populations are 10.8µm, 11.0µm and 11.1µm respectively. The distribution of their structure factor (SI 6.3) shows that CB_{aggl} in S_11.5 are the most structured and those is S_9.0 are the least structured.

3.2 Tensile properties

Figure 3 shows the stress-strain diagrams obtained for the 3 model materials using the sample geometry in Figure 1. The mechanical properties are not affected by the concentration of CB_{aggl}, similar to the results reported in Chapter 4 for pure shear geometry specimens. An analysis of their rupture properties reveals that they all have similar strain and stress at break (Figure 3b).

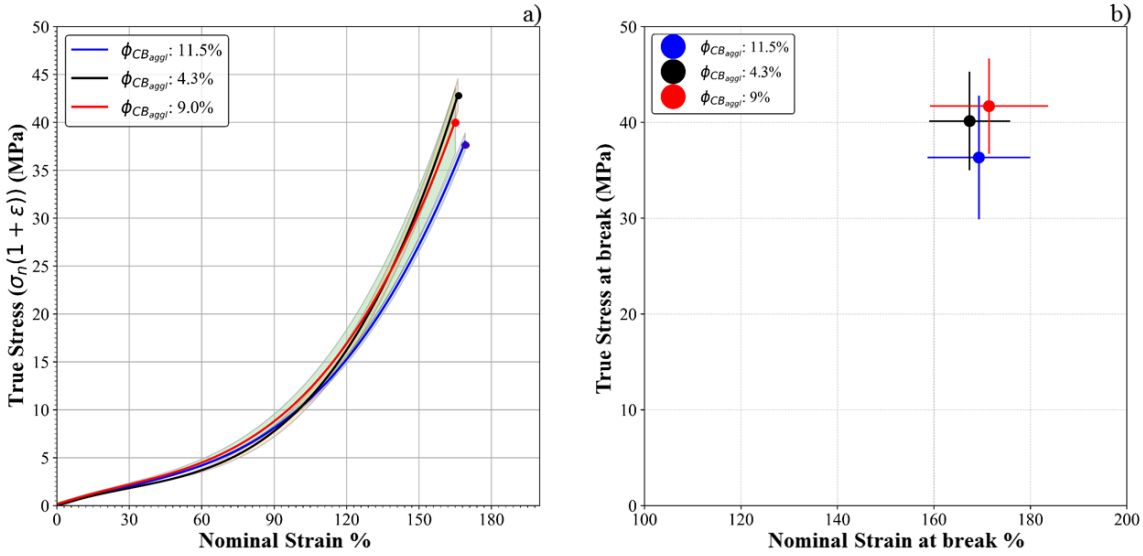

Figure 3: a) true stress vs nominal strain for the 3 materials with different concentrations of CB_{aggl}, b) true stress and nominal strain at break for the 3 materials.

3.3 Damage mechanisms associated to the different types of defects

3.3.1 Visualization of damage mechanism

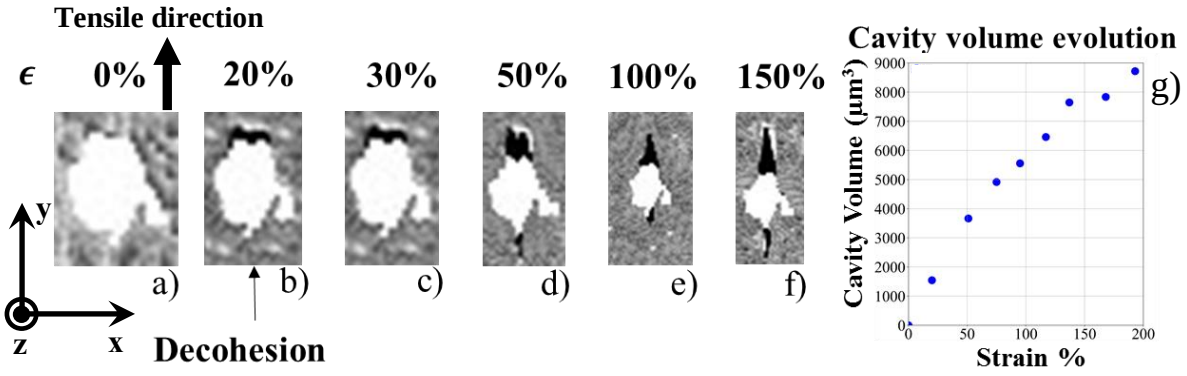

Figure 4: a)-f): damage evolution around an inclusion with V= 18000µm^3 (Eq_{diam} = 32µm) as a function of deformation: b) decohesion, e) and f) cavity growth in the direction of the applied stress, g) cavity volume around this inclusion, as a function of nominal strain.

Figure 4 shows the slice view of an inclusion with V= 18000µm^3 (Eq_{diam} = 32µm) inside the material during its tensile testing. These inclusions are rigid, they do not deform during the experiment and do not fracture like sometimes observed with ZnO inclusions (SI 6.4). As the material deforms, decohesion occurs at the poles of the inclusions since they have a weak adhesion with the matrix. This phenomenon can occur at the early stages of deformation, depending on the size of the inclusion. In the present case, the cavity volume increases with

the strain up to around 135%, then slows down. As shown in SI 6.5, the smaller the inclusion, the sooner the cavity volume slows down: at 90% nominal strain for a V=6700µm^3 (Eq_{diam} of 23µm).

The damage in CB_{aggl} was already described in the previous chapter (Figure 9, Chapter 4): cracks appear inside the agglomerates at a certain applied strain. Upon further stretching, more cracks appear within the agglomerates. Most of the CB_{aggl} undergo this damage sooner or later. Similar damage evolution was also observed in S_9.0 material (see SI 6.6).

3.3.2 Decohesion onset

In addition to the strain at which decohesion occurs, the corresponding stress can be analyzed (Figure 5). The comparisons are made with Eq_{diam} instead of V for an easy understanding.

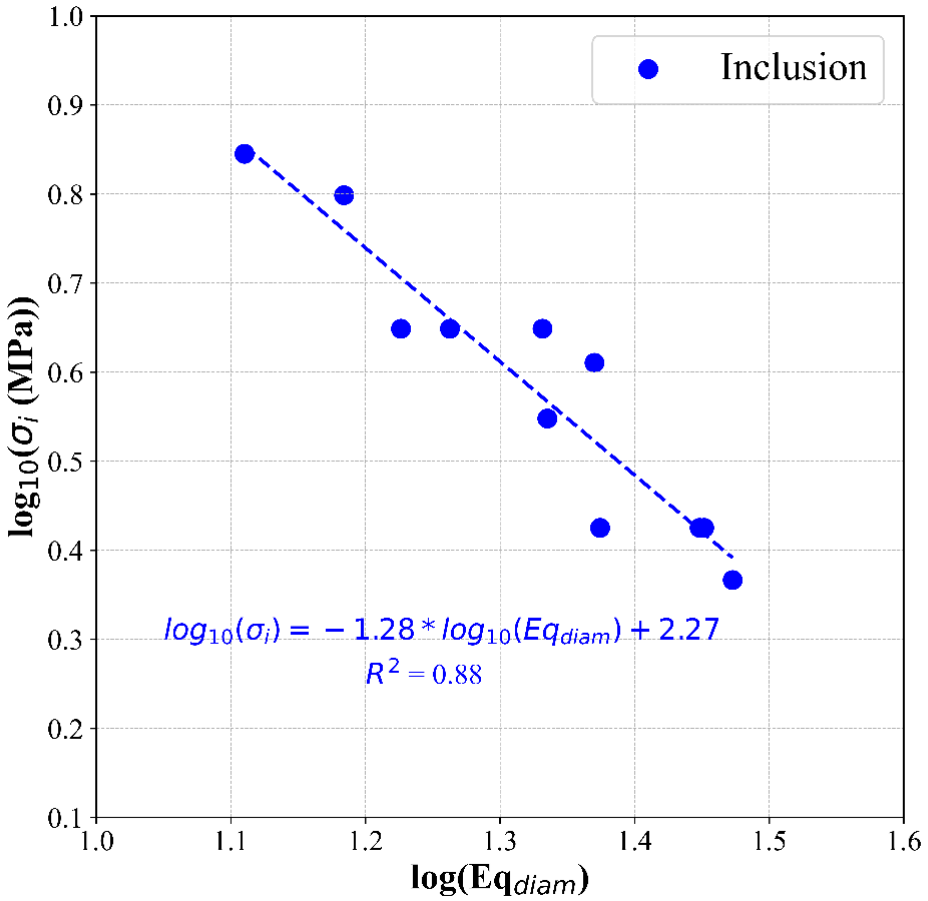

Figure 5: log plot of evolution of stress at the decohesion onset (σ_i) with the Eq_{diam} of the inclusion (S_4.3 material). Dotted line for the linear curve fitting.

The plot of macroscopically applied stress σ_i at the onset of decohesion for inclusions of different Eq_{diam} (Figure 5) clearly shows that smaller inclusions require higher macroscopic

stress for decohesion, as often reported in literature[8,9,17]. The stress at the onset decohesion depends on the size of the debonded zone. If one assumes that the stress depends only on the square root of the diameter of the inclusion and that the bond fracture surface area is independent of the particle size - like Gent *et al.*[9] did for the decohesion from spherical inclusion- then one should find a linear dependence of σ_i with ${Eq_{diam}}^{-0.5}$. As shown in Figure 5, the curve fitting rather indicates a dependence with ${Eq_{diam}}^{-1.28}$. This discrepancy is not so surprising since the model relies on strong assumptions (spherical inclusions) whereas the inclusions observed here are very irregular. Actually, the good quality of the fit is more surprising.

Similarly, the onset of cavitation in agglomerates was correlated to the true macroscopic stress (Figure 6).

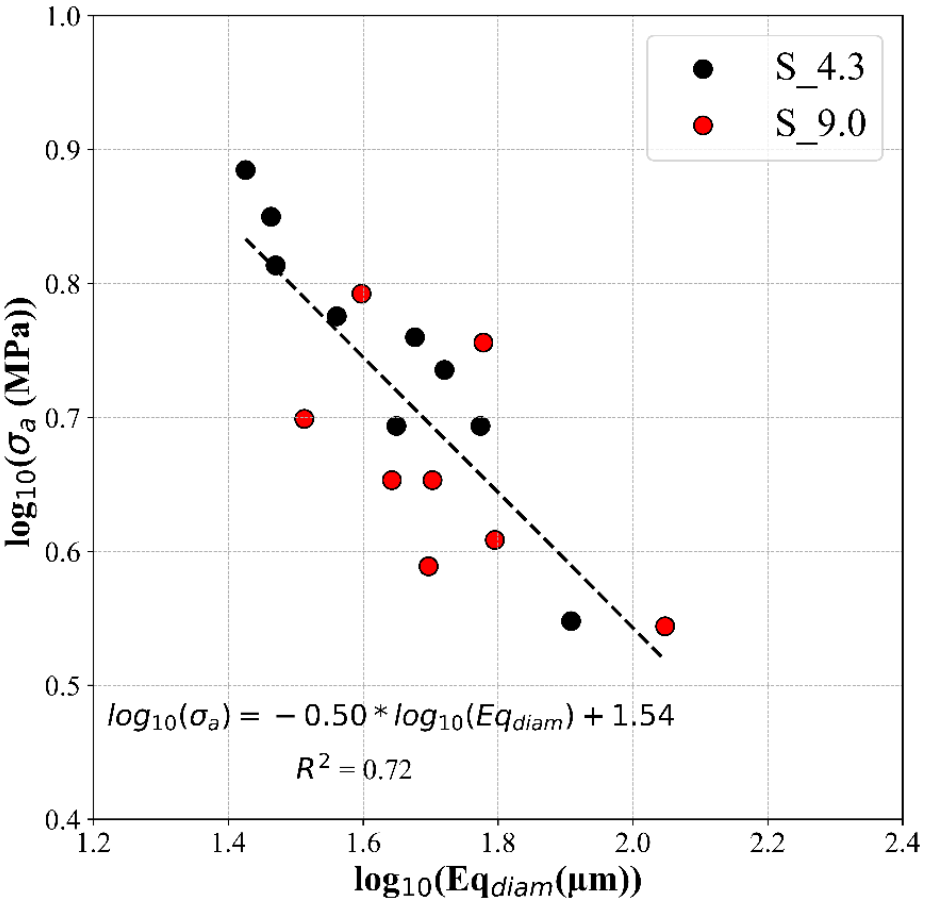

Figure 6: applied stress at the cavitation onset (σ_a) as a function of the Eq_{diam} of the agglomerate in which it occurs (results from S_4.3 and S_9.0 materials). Dotted line for the linear curve fitting.

As shown in Figure 6, the linear curve fitting is satisfactory and suggests a dependence of σ_a on $Eq_{diam}^{-0.5}$. The cavity being created *inside* the agglomerates, the Gent model previously cited seems irrelevant to explain these results. One may rather use the Mossakovskii and Rybka description (which is actually not so far from the Gent description), which derives the stress for the detachment of an elastic half space from a rigid plate when a circular debond of radius a is located at the interface. It predicts a dependence with $a^{-0.5}$. We have indeed observed that the structure of agglomerates is very heterogeneous and may be described like an assembly of strong aggregate layers separated by soft polymer layers. In this description, the largest layers, close to the equator of the agglomerate (the poles indicating the tensile stress direction), are the ones where the cavitation (originating here from debonding) is the easiest[18] and have indeed a circular surface with a radius close/proportional to the radius of the agglomerate. Some similarities can be found with the cavitation observed in a semi crystalline polyamide 6 specimen undergoing tensile deformation[19].

3.4 Visualization of crack initiation

The transition from a fracture within a CB_{aggl} towards a crack inside the matrix has been visualized by tomography. This is illustrated in Figure 7 with the S_9.0 material. Note that the agglomerate shown in Figure 7a is of the same type as CB_{aggl_1} in Figure 2 i.e. it has a lower density compared to most of the observed agglomerates. The greyscale values show that its core is less dense. Nevertheless the observations on this agglomerate are very similar to those performed on other samples, and have been preferred for the quality of the images (see another example in SI 6.7). The onset of the fracture nucleation occurs at around 75% nominal strain for this CB_{aggl} whose Eq_{diam} is 40µm. The fracture inside the agglomerate transforms to a crack in the matrix at around 130% nominal strain. Such crack can then propagate through the material. Figure 7d shows the state of the crack inside the matrix just before material rupture. The evolution of nominal strain with the cavity volume (i.e. the future catastrophic crack) created in the agglomerate has been deduced from the tomography images and is pictured in Figure 7e. Between 70%-120% nominal strain, the volume variation is almost negligible. Then, at higher strain, the cavity rapidly grows radially and its volume increases exponentially. When the cavity becomes a crack propagating in the matrix, its volume grows catastrophically. SEM images (Figures 8a and 8b) confirm the above observation, with evidence of crack initiation from one critical defect (CB_{aggl}). However, a filled EPDM can also break due to multiple initiations as shown in Figure 9. In this case, the SEM image shows that cracks originate and

propagate radially from the two CB_{aggl} observed. The 2 cracks eventually coalesce and this leads to the material rupture.

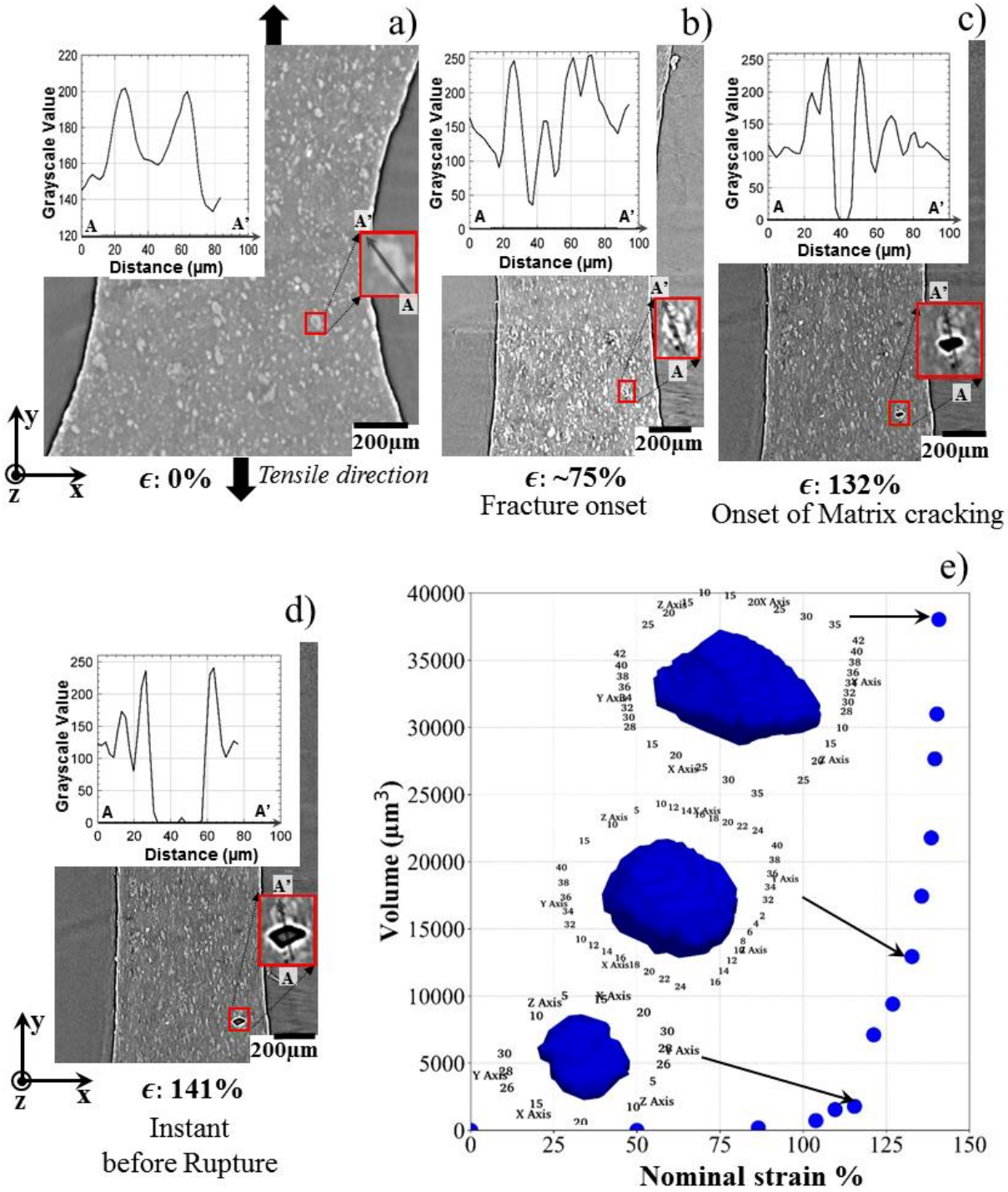

Figure 7: visualization of crack initiation in a filled EPDM, a)-d) microstructural evolution of the critical defect with nominal strain (ϵ). The inset photo in each figure shows a magnified CB_{aggl}..b) onset of the fracture/cavitation inside the CB_{aggl} at 75% nominal strain, c) onset of matrix cracking at 132% nominal strain, d) state of the crack just before sample rupture, e) volume of the cavity inside the agglomerate as a function of the macroscopic deformation.

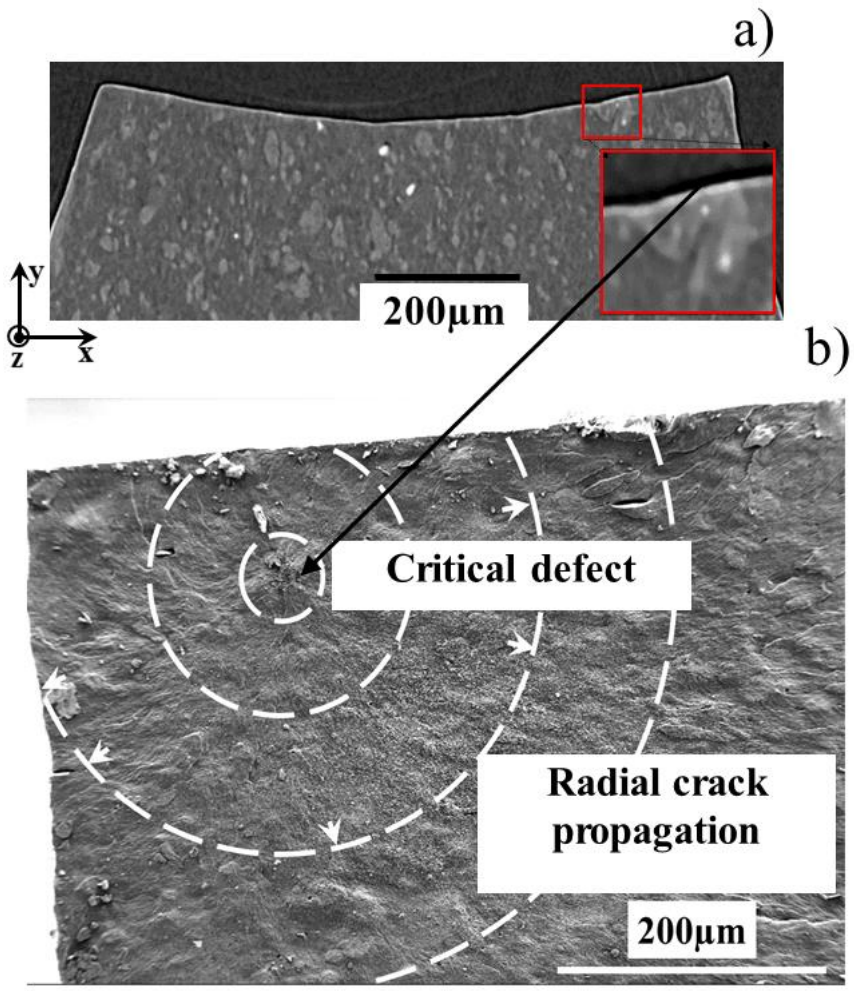

Figure 8: Continuation of Figure 7, a) slice view of the broken sample with the critical defect. The inset photo shows the magnified critical CB_{aggl}. b) SEM observation confirming the crack initiation and further propagation of the crack from the critical defect.

Even though other defects (metallic oxide inclusions) exist in the materials, crack always initiates from CB_{aggl} defect(s). Moreover, we can conclude from our observations that the crack initiation mechanism remains the same whatever the CB_{aggl} concentration in the material is (as shown in SI 6.7 for material with 4.3% of CB_{aggl}). It is worth noting to be complete that, there are exceptions to this when there is a surface defect such as a pre-existing cut at the surface edge due to improper die cutting of the samples (SI 6.8).

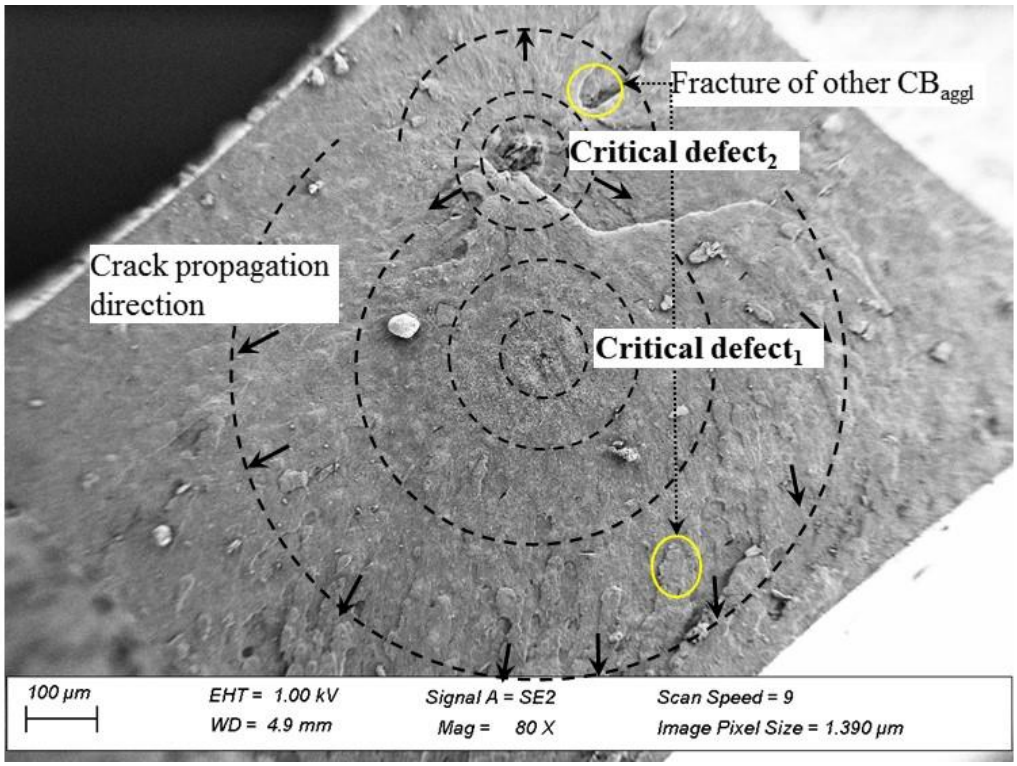

Figure 9: SEM observation of the ruptured surface of S_11.5.

4. DISCUSSION

The filled material presented in this chapter contains two types of defects – metallic oxide inclusions and CB_{aggl}. To understand their role on crack initiation mechanism, model materials with 3 different concentrations of CB_{aggl} have been processed; the 1st material contains very high concentration of CB_{aggl} (S_11.5 with 11.5% volume fraction), the 2nd material has CB_{aggl} concentration representative of those commonly found in industrial production (4.3%) and the last material contains an intermediate CB_{aggl} concentration between the former 2 model materials (9%). It is worth noting that we did not incorporate ZnO particles (commonly used in the industry) to avoid problems related to the non-visibility of CB_{aggl} in their presence, as reported in some recent literature studies. However, the studied EPDM contains low concentrations (less than 0.05%) of pre-existing metallic oxide inclusions in them. The mechanical property characterization shows that despite their different concentrations of CB_{aggl}, all the model materials have similar rupture properties, i.e. strain and stress at break, which is a counterintuitive result. A micron-scale characterization of the material is performed to understand this result.

Crack initiation is due to the nucleation of damage and its final evolution to a matrix crack. Matrix decohesion occurs at the pole of the rigid metallic oxide inclusions when the

material is stretched. This debonding does not lead to crack initiation. For instance, a debonded cavity with Eq_{diam} of 35µm does not rupture the material even when the material is stretched above 135% nominal strain. The created cavities mostly grow in parallel to the applied stress direction as shown in previous studies[7,20]. This might be due to lower tearing energy along the direction of applied stress compared to propagation in the perpendicular direction: in an NR matrix, the fracture strength required for the tear to grow in the direction of applied stress is about 40% less than the strength required for it to grow in the perpendicular direction[21,22]. The study concluded that this crack tends to stop eventually. Thus, defects like metallic oxide inclusions are not critical for crack initiation; we confirmed this through the observation of rupture surfaces of different samples (SI 6.9). This is consistent with the observations made by Huneau *et al*.[23] regarding materials containing ZnO submitted to fatigue solicitation.

Conversely, CB_{aggl} can initiate cracks in the material upon stretching. Cavitation occurs inside the agglomerates. The dependence of the stress needed to observe this cavitation with power -0.5 of the agglomerate diameter suggests that it may originate from some decohesion mechanism at the interface between two of the layers (with different aggregates concentration) which form the agglomerates. In a second step, the cavity grows rapidly inside the CB_{aggl}. Not all CB_{aggl} transform their internal fracture into a crack in the matrix. To do so, their location inside the sample should be in a zone with large stress triaxiality. Moreover, when they undergo multiple internal fractures, this likely delays the propagation of the main internal cavity to the matrix, which triggers a fracture through the matrix. This was verified for all our model materials, using SRCT characterization combined with SEM analysis.

The morphology features of 9 critical CB_{aggl} that initiated crack are presented in Figure 10. Critical agglomerates in S_11.5 have larger structure factor compared to S_4.3 (due to more shearing energy provided to S_4.3 inside the internal mixer, as explained in Chapter 3), and they are more elongated, but this is also the case for all the agglomerates of S_11.5 when compared to those of S_4.3. Actually, the common feature of all the critical agglomerates, without distinction of the materials, is a minimum volume around 40000µm^3 which corresponds to an Eq_{diam} around 40µm. All these critical CB_{aggl} were also found to be closer to the surface edges, where the strain is larger compared to the specimen center (SI 6.10). Now, given the different CB_{aggl} concentration, these results show that in the range of the tested concentrations, the quantity of CB_{aggl} is not important with respect to crack initiation (likely because the probability to find a critical agglomerate is large enough for all the tested materials). This is

indirectly confirmed by results of tensile testing (Figure 3), which do not exhibit significant differences between the 3 compounds.

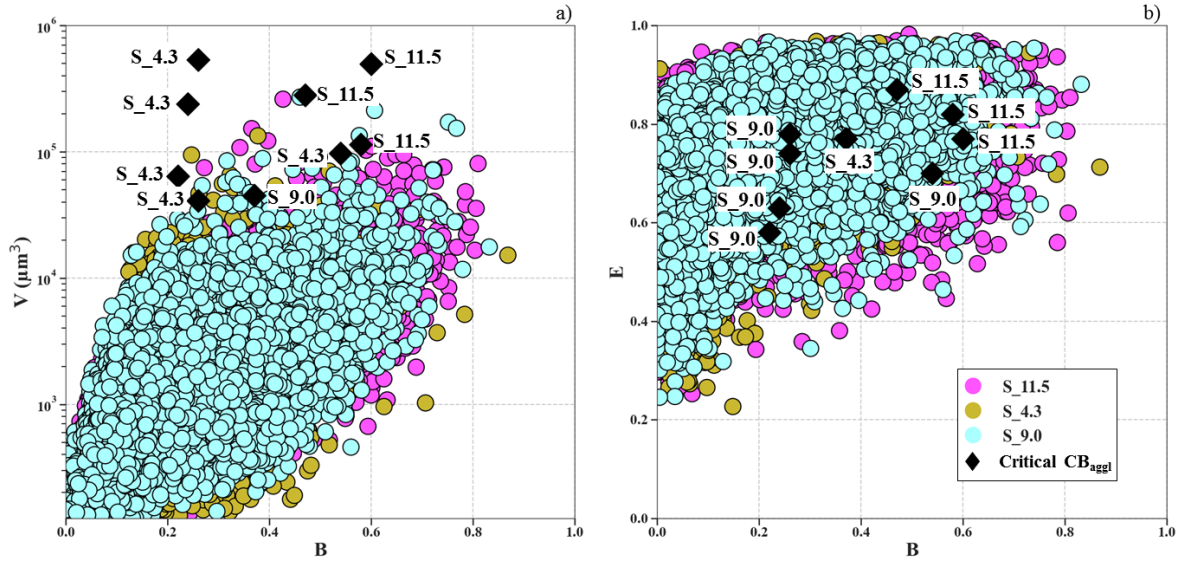

Figure 10: morphology features: a) V vs B and b) E vs B for materials S_11.5, S_4.3 and S_9.0. The black symbols characterize the morphology of the critical defects found in these materials.

After crack initiation, crack propagates and ruptures the material. The previous chapter showed that the crack propagation resistance of S_11.5 (F1) is higher than S_4.3 (F2) at high strain energy release rate (G). However, the ultimate properties of these materials remain the same. This is ascribed to the small cross section dimensions of the tensile specimen (1mm x 1mm) which is not sufficient for crack propagation. At high G (high strain) crack propagation speed is in the order of magnitude of 10^{-4} m/s. Note that G increases with the strain and the crack size. Therefore the sample breaks too fast to see any differentiation in the rupture properties between the materials. Thus, in this geometry during tensile test, rupture properties are governed by the crack initiation mechanism.

5. CONCLUSION

An in-situ tensile study using SRCT on a filled EPDM shows the damage and the crack initiation mechanisms associated to different defects which act differently upon stretching the material. We demonstrated that the damage mechanism associated to defects based on metallic oxide inclusions is debonding and the stress for debonding onset depends on their size. The power law dependence between applied stress and inclusion size requires further studies, which takes into account the debonded area, adhesion energy etc… In any case, the inclusions are not

critical defects in the material and the cavities they bring about grow in the direction of the applied stress rather than perpendicular to it. On the other hand, CB_{aggl} are found to be critical defects for crack initiation. The first step is nucleation of a cavity inside the agglomerate due to debonding of polymer layer from the aggregates layers. However, this needs to be further explored through a nanoscale characterization for understanding cavity nucleation mechanisms inside CB_{aggl}. The nucleated cavity grows as the fractured CB_{aggl} undergoes further deformation, and then propagates into the matrix, which triggers rupture of the material. However, all the CB_{aggl} that fracture do not lead to a crack propagating in the matrix. Only those with size bigger than 40 μm and in the more deformed zone of the specimen (close to the edges of the sample in our test) initiate a crack.

6. SUPPORTING INFORMATION

6.1 SRCT experiments

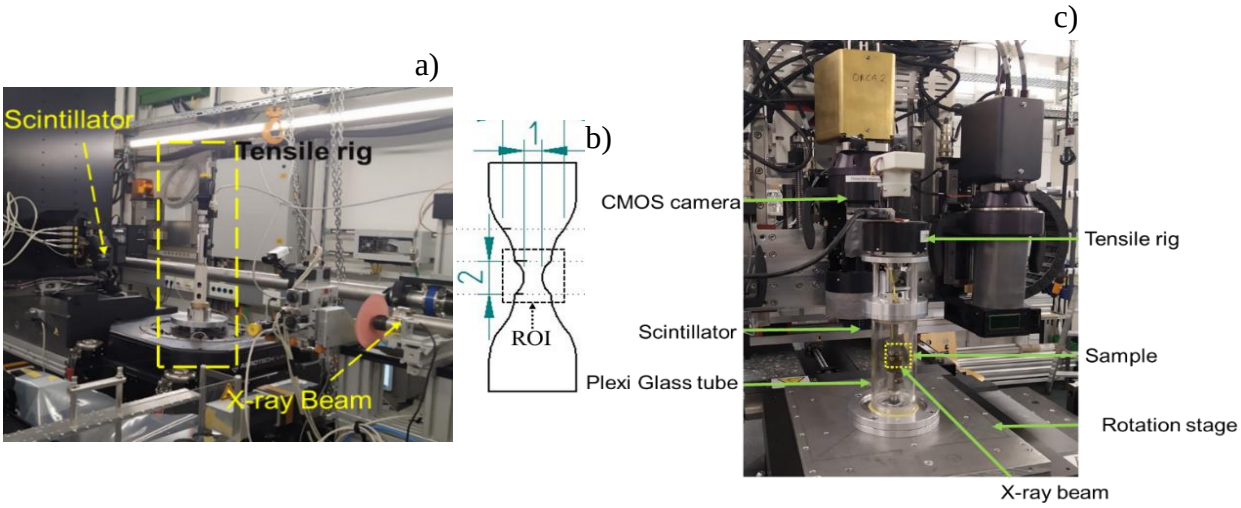

Figure A1: a) P05 beamline experiments: hutch photo with the position of X-ray beam, tensile rig and scintillator, b) sample geometry used for in-situ tensile test, c) Anatomix beamline: homemade tensile rig from MATEIS lab.

6.2 EDX analysis of inclusions

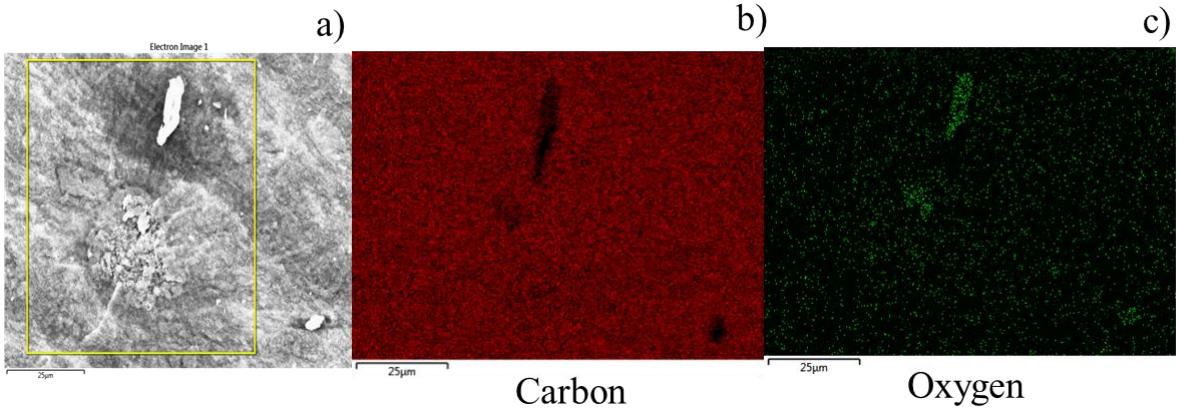

Figure A2: a) SEM image of rupture surface of S_9.0. The critical defect is a carbon black agglomerate. The bright spot is an inclusion. b) EDX analysis for C. c) EDX analysis for O.

Spectrum Label	Map Sum Spectrum
C	94.81
N	0.00
O	4.15
Na	0.27
S	0.28
K	0.26
Ca	0.23
Total	100.00

Table A1: Mass fraction of the elements present on the surface of the ruptured material.

The EDX results show that the inclusion has lower C content and higher O content than the rest of the components.

6.3 Distribution of the structure factor of CB_{aggl}

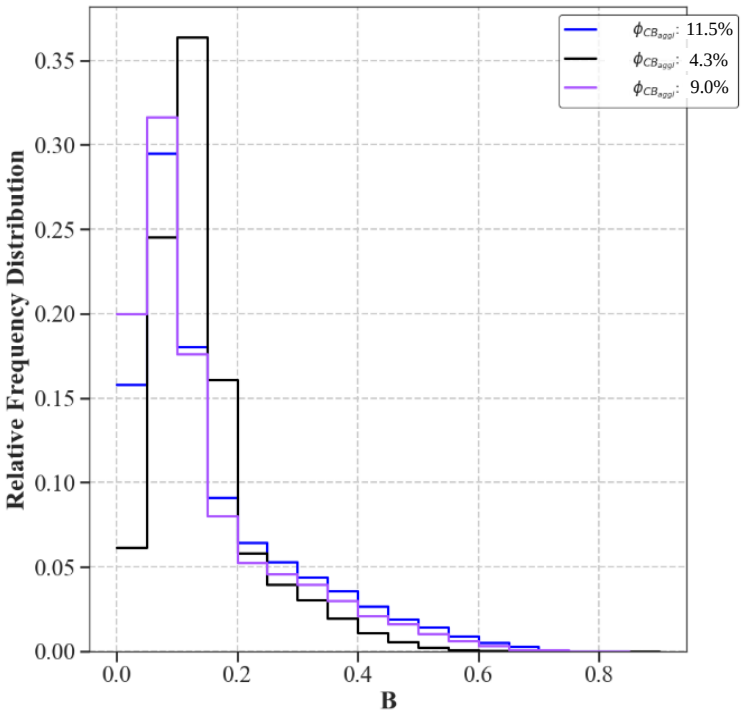

Figure A3: Distribution of the B feature describing the structure of CB_{aggl} in S_11.5, S_4.3 and S_9.0

6.4 Onset of damage mechanism for ZnO

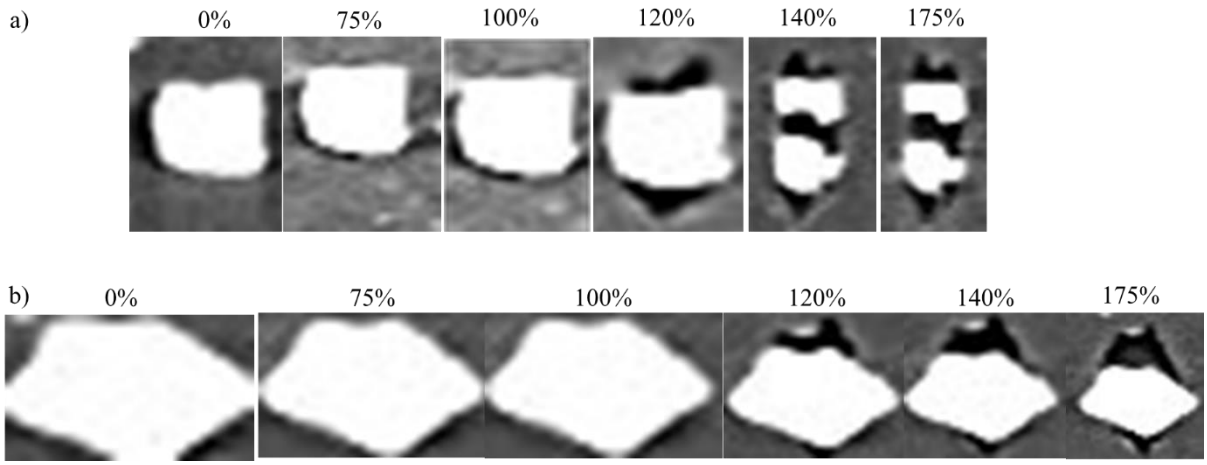

Figure A5: Damage evolution in a material containing 3% volume fraction of ZnO. a) at 120% nominal strain, there is a debonding at the poles followed by fracture of ZnO at 140% nominal strain. b) debonding at the poles of ZnO inclusion at 120% nominal strain, without subsequent fracture of the inclusion.

6.5 Growth of cavity volume for inclusion with size =23µm

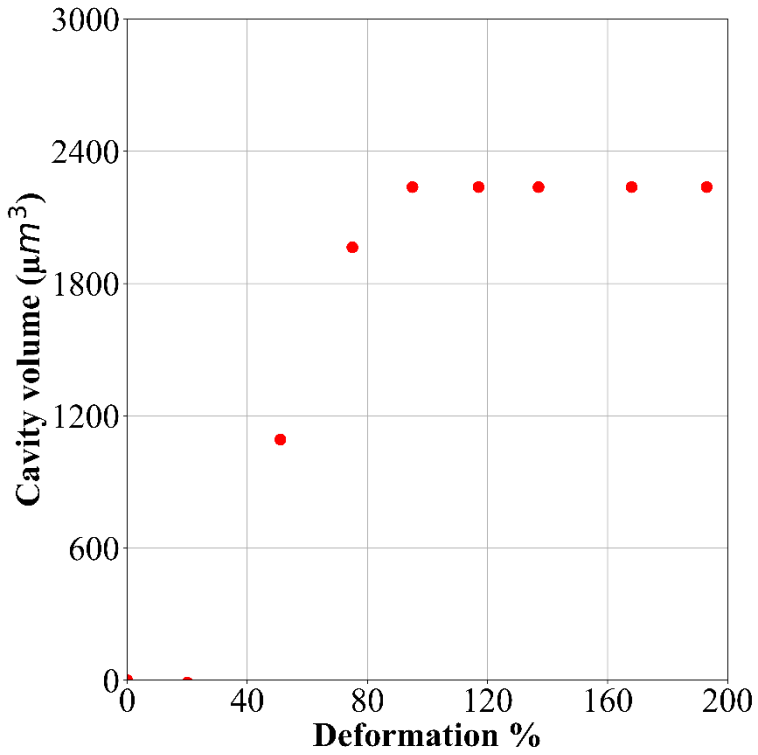

Figure A4: Evolution of cavity associated to a defect with Eq_{diam}= 23µm

6.6 S_9.0 damage mechanism of CB_{aggl}

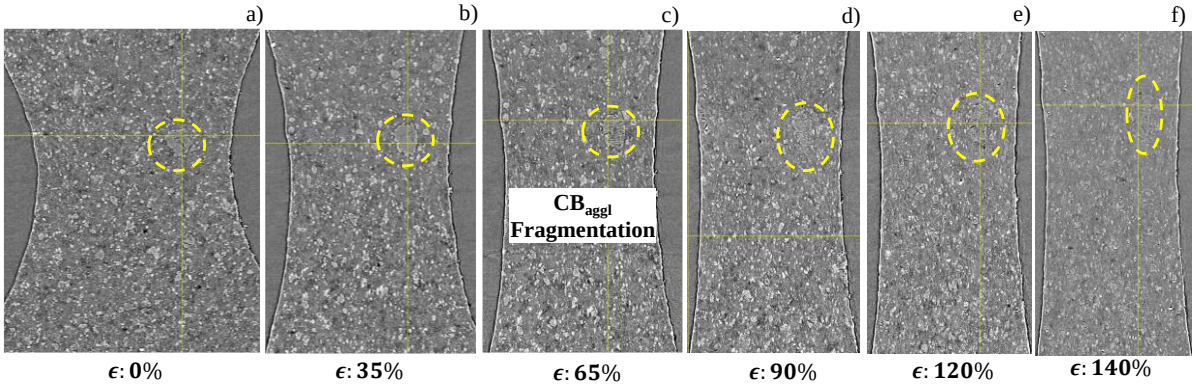

Figure A6: a)-f) evolution of CB_{aggl} during a tensile test of material S_9.0 observed using SRCT. CB_{aggl} are fractured between 35%-65%, to be precise at 40% nominal strain. CB_{aggl} undergo multiple fragmentations as the macroscopic deformation increases.

6.7 S_4.3 damage mechanism

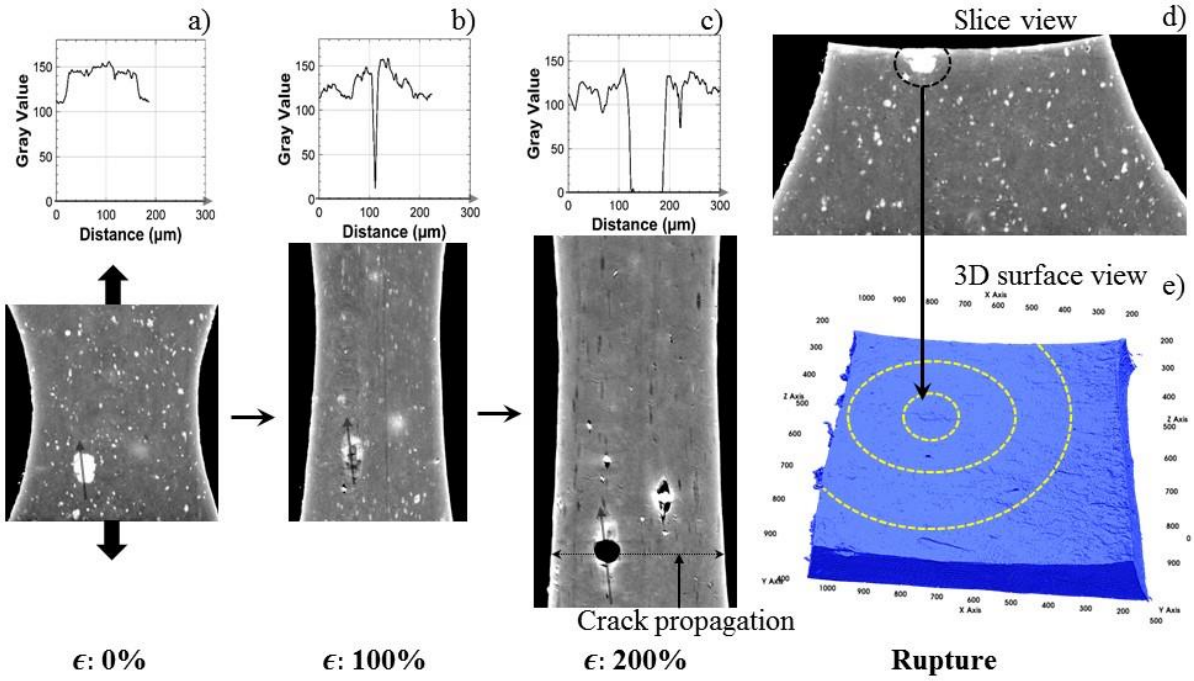

Figure A7: Crack initiation mechanism for S_4.3

6.8 Images of the CB_{aggl} in the edges

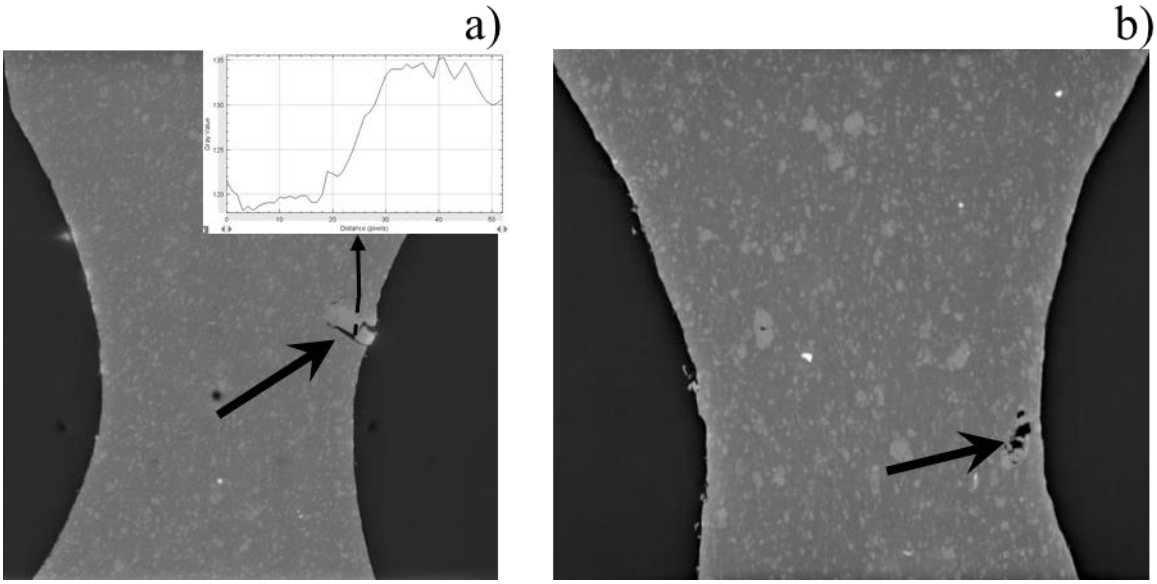

Figure A8: Slice images showing critical defects. The defects pointed in the images are CB_{aggl}

6.9 Material Rupture surfaces

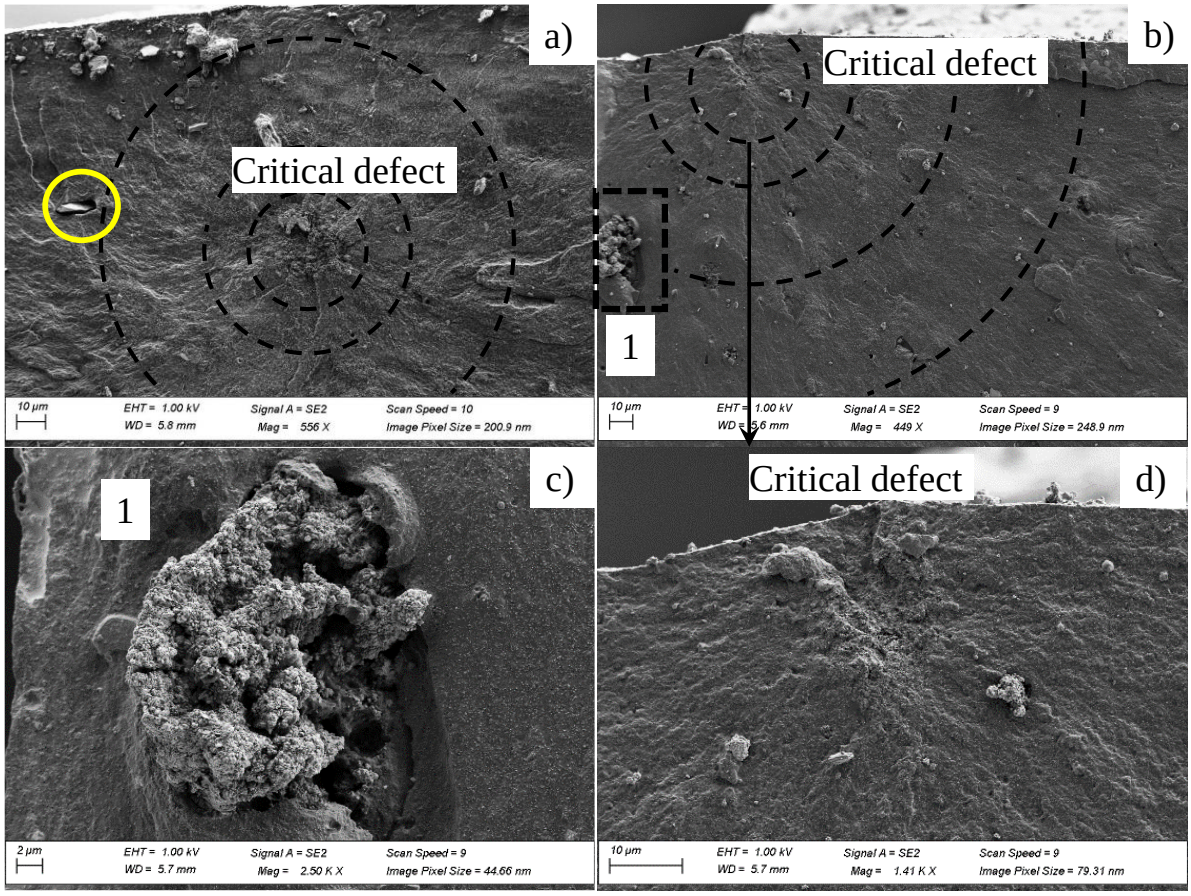

Figure A9: SEM image showing the rupture surface of S_9.0, a) decohesion at the inclusion, marked by a yellow circle next to the critical defect, b) rupture surface and critical defect (CBaggl) in a material containing ZnO. c) and d) enlarged views of a ZnO inclusion (rectangle 1) and of the critical defect from picture b).

6.10 Digital volume correlation

Digital Volume Correlation (DVC) is a correlation methodology to measure the 3-dimensional displacement and strain field inside a material volume during a solicitation (e.g. compression, tension etc.) The principle used in DVC is developed from DIC, where the displacement vector of each voxel in the volume subset is obtained and is used to calculate the strain field. The analysis was performed using a routine developed by Joel Lachambre in his thesis [24]. An ROI of 400*300*200 voxels has been defined within a sample volume of 850*1000*500 voxels. In order to have a good correlation, the step displacement during tensile test is limited to 40 µm The chosen size of the mesh is 16 voxels. The resolution of the voxel is 2.19µm^3.

Figure A10 shows the strain field inside the sample for a 50% applied nominal strain on the sample. The strain field represents the region with strain greater than 0.8*maximum strain. The strain is higher towards the edges. The critical CB_{aggl} is marked in blue color in Figure A10. The CB_{aggl} are closer to the region where there is high strain.

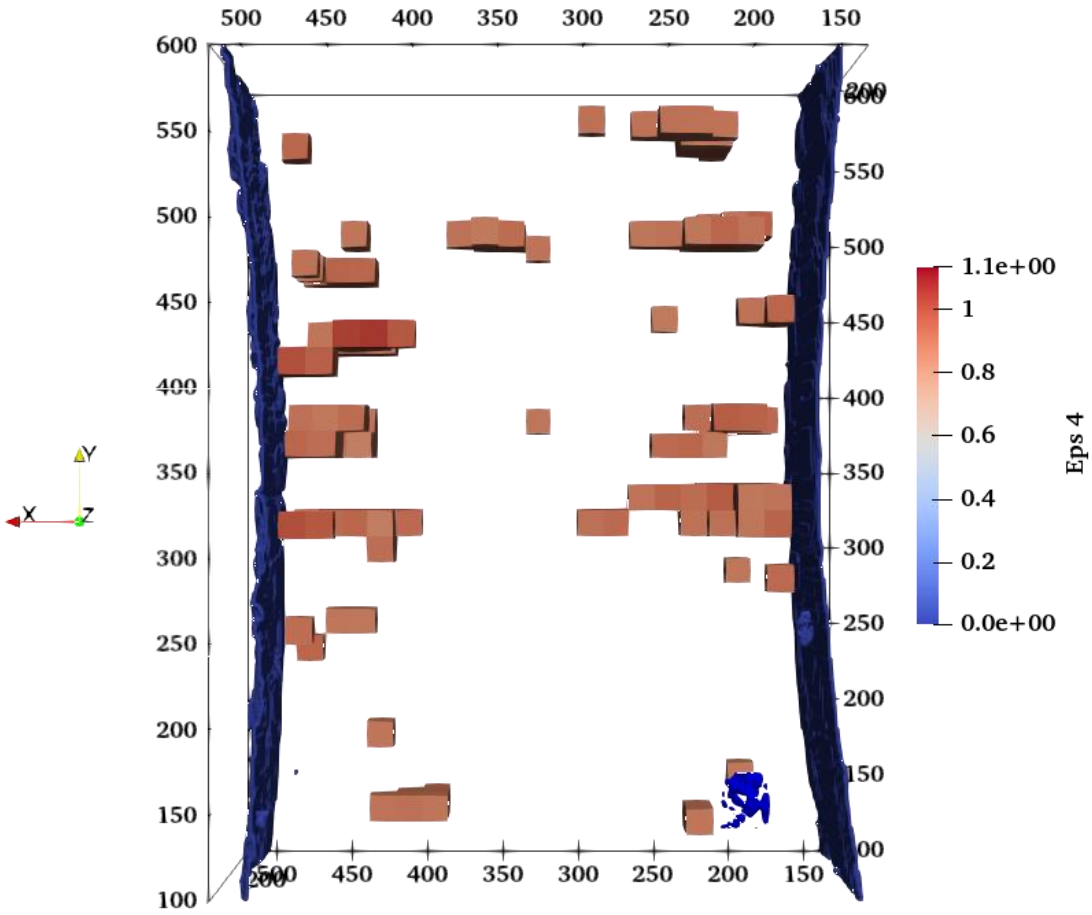

Fig A10: Strain field for model material S_9.0 in the direction of applied stress. The colored areas are those where local strain is greater than 80% of the maximal strain.

7. REFERENCES

[1] Medalia AI, Heckman FA. Morphology of aggregates. VII. Comparison chart method for electron microscopic determination of carbon black aggregate morphology. J Colloid Interface Sci 1971;36:173–90. https://doi.org/10.1016/0021-9797(71)90162-7.

[2] Medalia A. Effect of Carbon Black on Ultimate Properties. Rubber Div Am Chem Soc 1987;60:45–60.

[3] Dizon ES, Hicks AE, Chirico VE. The Effect of Carbon Black Parameters on the Fatigue Life of Filled Rubber Compounds. Rubber Chem Technol 1974;47:231–49. https://doi.org/10.5254/1.3540429.

[4] Astruc M. Étude rhéo-optique des mécanismes de dispersion de mélanges sous cisaillement simple . 1 Mélanges concentrés de polymères immiscibles . 2 Mélanges

polymères-charges poreuse. l'École des Mines de Paris, 2008. https://doi.org/tel-00275370.

[5] Collin V, Boudimbou I, Peuvrel-Disdier E. New insights in dispersion mechanisms of carbon black in a polymer matrix under shear by rheo-optics. J Appl Polym Sci 2013;127:2121–31. https://doi.org/10.1002/app.37769.

[6] Le Cam J-B, Huneau B, Verron E. Fatigue damage in carbon black filled natural rubber under uni- and multiaxial loading conditions. Int J Fatigue 2013;52:82–94. https://doi.org/10.1016/j.ijfatigue.2013.02.022.

[7] Gent AN, Park B. Failure processes in elastomers at or near a rigid spherical inclusion. J Mater Sci 1984;19:1947–56. https://doi.org/10.1007/BF00550265.

[8] Zhuk A V., Knunyants NN, Oshmyan VG, Topolkaraev VA, Berlin AA. Debonding microprocesses and interfacial strength in particle-filled polymer materials. J Mater Sci 1993;28:4595–606. https://doi.org/10.1007/BF00414247.

[9] Gent AN. Detachment of an elastic matrix from a rigid spherical inclusion. J Mater Sci 1980;15:2884–8. https://doi.org/10.1007/BF00550559.

[10] Huneau B, Masquelier I, Marco Y, Le Saux V, Noizet S, Schiel C, et al. Fatigue crack initiation in a carbon black-filled natural rubber. Rubber Chem Technol 2016;89:126–41. https://doi.org/10.5254/rct.15.84809.

[11] Glanowski T, Marco Y, Le Saux V, Huneau B, Champy C, Charrier P. Fatigue crack initiation around inclusions for a carbon black filled natural rubber: An analysis based on micro-tomography. Const Model Rubber XI - Proc 11th Eur Conf Const Model Rubber, 2019 2019:368–73. https://doi.org/10.1201/9780429324710-64.

[12] Gent AN, Hwang YC. Internal failures in model elastomeric composites. J Mater Sci 1990;25:4981–6. https://doi.org/10.1007/BF00580117.

[13] Lefèvre V, Ravi-Chandar K, Lopez-Pamies O. Cavitation in rubber: an elastic instability or a fracture phenomenon? Int J Fract 2015;192:1–23. https://doi.org/10.1007/s10704-014-9982-0.

[14] Moosmann J, Ershov A, Weinhardt V, Baumbach T, Prasad MS, LaBonne C, et al. Time-lapse X-ray phase-contrast microtomography for in vivo imaging and analysis of morphogenesis. Nat Protoc 2014;9:294–304. https://doi.org/10.1038/nprot.2014.033.

[15] Paganin D, Mayo SC, Gureyev TE, Miller PR, Wilkins SW. Simultaneous phase and amplitude extraction from a single defocused image of a homogeneous object. J Microsc 2002;206:33–40. https://doi.org/10.1046/j.1365-2818.2002.01010.x.

[16] van der Walt S, Schönberger JL, Nunez-Iglesias J, Boulogne F, Warner JD, Yager N, et al. scikit-image: image processing in Python. PeerJ 2014;2:e453. https://doi.org/10.7717/peerj.453.

[17] Gent AN, Park B. Failure processes in elastomers at or near a rigid spherical inclusion. J Mater Sci 1984;19:1947–56. https://doi.org/10.1007/BF00550265.

[18] Fond C. Cavitation criterion for rubber materials: A review of void-growth models. J Polym Sci Part B Polym Phys 2001. https://doi.org/10.1002/polb.1183.

[19] Selles N, Cloetens P, Proudhon H, Morgeneyer TF, Klinkova O, Saintier N, et al. Voiding Mechanisms in Deformed Polyamide 6 Observed at the Nanometric Scale. Macromolecules 2017;50:4372–83. https://doi.org/10.1021/acs.macromol.7b00727.

[20] Cho K, Gent AN, Lam PS. Internal fracture in an elastomer containing a rigid inclusion. J Mater Sci 1987;22:2899–905. https://doi.org/10.1007/BF01086488.

[21] Gent AN, Kim HJ. Tear Strength of Stretched Rubber. Rubber Chem Technol 1978;51:35–44. https://doi.org/10.5254/1.3535725.

[22] Gent AN, Razzaghi-Kashani M, Hamed GR. Why do cracks turn sideways? Rubber Chem Technol 2003;76:122–30. https://doi.org/10.5254/1.3547727.

[23] Huneau B, Masquelier I, Marco Y, Le Saux V, Noizet S, Schiel C, et al. Fatigue crack

initiation in a carbon black-filled natural rubber. Rubber Chem Technol 2016;89:126–41. https://doi.org/10.5254/rct.15.84809.

[24] Lachambre J. Développement d'une Méthode de Caractérisation 3D des Fissures de Fatigue à l'aide de la Corrélation d'Images Numériques obtenues par Tomographie X. l'Institut National des Sciences Appliquées de Lyon, 2014.

CHAPTER 6
Tomography observation of crack initiation from CB agglomerates in filled EPDM submitted to fatigue loading

TABLE OF CONTENTS

1. INTRODUCTION

Many studies have shown the existence of cavities and their growth during fatigue solicitation of filled elastomers, especially carbon black-filled ones [1–5]. These cavities are formed mainly at the pole of metallic oxide inclusions (e.g. ZnO particles, which is a cure activator in sulphur based curing system) or between these inclusions. Recent studies have also detected cavities which are not associated to these inclusions and are presumed to be related to CB_{aggl}. Thus, a clear understanding of the mechanism of crack initiation from CB_{aggl} is lacking in the literature. Since CB_{aggl} are not detected easily, the impact of the concentration and the nature of CB_{aggl} on crack initiation is also unknown. Such analysis requires a 3D quantification of the crack initiation process from CB_{aggl} during fatigue.

Thus, this chapter aims at understanding the role of CB_{aggl} on crack initiation mechanism during fatigue solicitation of carbon black filled elastomer. To this end, two model filled EPDM materials have been processed, one with a very high concentration of CB_{aggl} and the other with a CB_{aggl} concentration usually found in manufactured products. These materials were already studied in Chapters 4 and 5 for crack propagation and initiation tests during uniaxial and monotonic solicitations. This chapter also presents results obtained from the same methodology with an industrial material. This one contains oil, and is typically used in many applications such as seals, ant-vibration mounts etc... It also contains a higher concentration of carbon black than the model materials. The results obtained with the model and the industrial materials are presented separately in sections 3 and 4 respectively. Both series of results are discussed comparatively in section 5.

2. MATERIALS AND PROTOCOLS

2.1 Composition and materials processing

Table 1 presents the formulation of both the model and the industrial materials. They were performed at INSA Lyon and LRCCP (Vitry-sur-Seine) respectively. The details of the processing are given in Chapter 2 section 2.2. It is worth noting that we used Zn Stearate complex instead of ZnO in order to avoid the presence of residual ZnO particles in the final material. The presence of ZnO perturbs the detection of carbon black agglomerates.

Ingredients	S_11.5 (Phr)	S_4.3 (Phr)	I (for industrial) (Phr)
EPDM KELTAN 4450	100	100	100
N326	50	50	100
Paraffinic oil Torilis 6200			40
Zn Stearate			4.5
MBTS 80			1.5
TBzTD 70			2
Sulfur			1.5
ZBEC 70			1
Peroxide	3.2	3.2	
Rotor Speed (rpm)	30	60	60
Mixing Time in internal mixer(min)	2	4	5
Introduction protocol	TD 1.EPDM 2.CB	USD 1.CB 2.EPDM	USD 1.CB 2.EPDM
Filler Volume fraction	19.3%	19.3%	24.8%

Table 1: Material formulations and protocols for model and industrial materials.

2.2 Fatigue testing

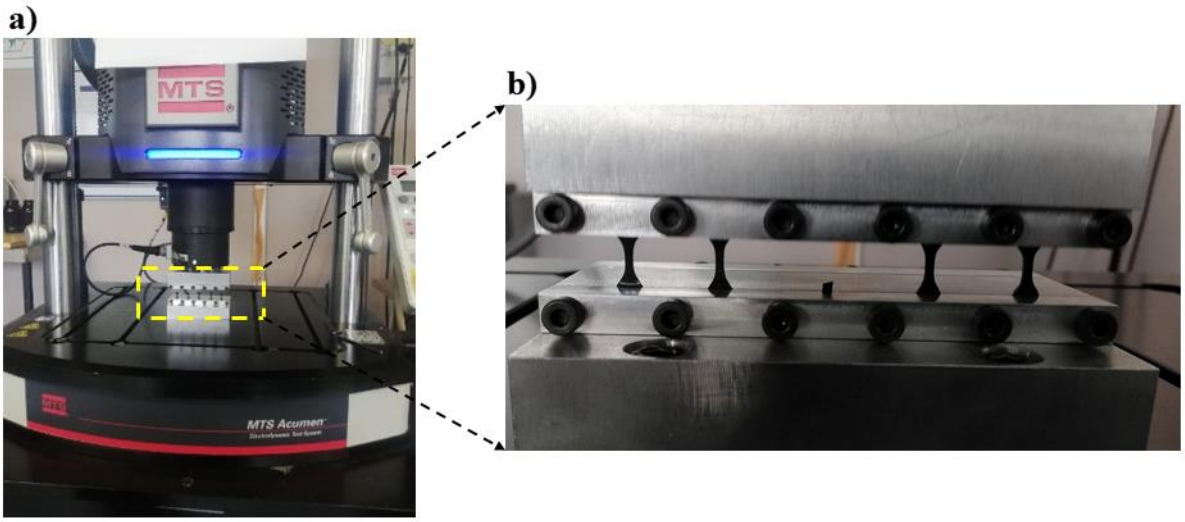

Figure 1: a) MTS Acumen Electrodynamic test systems used for fatigue testing at LRCCP, Vitry-sur-Seine. b) the special clamping jaw enables to test up to 10 samples in parallel

The machine used for the fatigue testing of model materials at the laboratory is Bose Electroforce from TA Instruments equipped with 22N load cell, whereas the machine used for testing the industrial mix is Acumen Electrodynamic test systems from MTS (Figure 1). Sample

geometry is depicted in Figure 2b. The solicitation frequency is maintained at 2Hz to avoid any self heating of the samples[6]. All the tests are performed at ambient temperature. The minimum nominal strain applied is 5% in order to avoid any buckling of the sample (cf. Figure A1 in SI). The nominal length of the samples of model materials is calculated at force of 0.1N, after the sample has undergone 100 cycles of accommodation. However, such calibration was not performed for the industrial materials. The fatigue life duration of the sample is obtained at various maximum nominal strains. Crack initiation and further crack propagation are observed through ex-situ characterization of the fatigued samples using X-ray Tomography.

2.3 Ex situ microstructural characterization using Laboratory X-ray tomography source (Lab tomography)

We conducted ex-situ test using laboratory sourced X-ray Tomography to characterize the damage evolution in the materials during fatigue test. Tomography scans of the samples were performed after interruption of the fatigue test at a pre-determined number of cycles. These cycle numbers were determined from the knowledge of the number of cycles needed for the rupture the material at the chosen strain.

The X-ray tomography device is EasyTom Nano from RX solutions with a Tungsten target and X-ray sourcing from a LaB6 cathode filament. CCD detector is used, since it is suitable for X-rays with low energies. The volume analyzed is ca. 4-6mm^3 with a voxel resolution of 2-2.25µm3 depending on the testing requirements. The resolution chosen for the fatigue studies on model materials is 2µm^3 and for industrial materials is 2.25µm^3. The sample is rotated over 360 degrees in front of the X-ray beam (Figure 2). Image acquisition is performed at every 0.09° (for a total of 4000 projections). The tube voltage is kept at 40kV to obtain an optimised attenuation contrast between the elastomer and agglomerates.

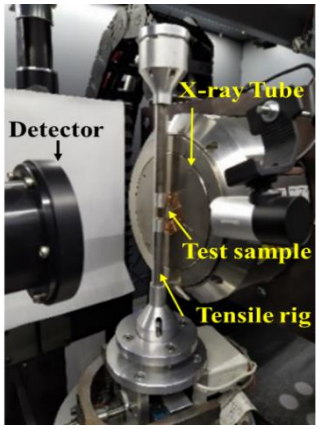

a)

b)

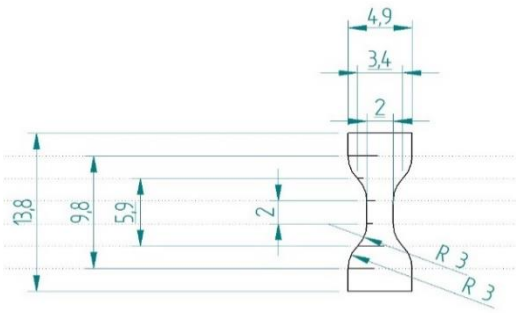

Figure 2: Tensile rig kept installed inside an X-ray Tomography machine, b) sample geometry used for fatigue tests

During the scan, the sample is mounted in the tensile rig as shown in Figure 2a and stretched up to 15% strain to open the cavities or voids inside it. The tensile rig is made of a plexi-glass® (PMMA) tube. The thickness of the plexi-glass® tube is reduced from 1mm to 0.5mm at the centre, so that there is low transmission loss of photons.

3. RESULTS

3.1 Model materials

This section presents the fatigue properties of both model materials, S_11.5 and S_4.3. These are the same materials studied in *chapter 4 (called F1 and F2)* and *chapter 5 (called S_11.5 and S_4.3)*. Their cumulative volume fraction ($\phi_{CB_{aggl}}$) of CB_{aggl} whose volume is above 125µm^3, deduced from lab tomography experiment, is 10.1% and 3.0% in S_11.5 and S_4.3 respectively (cf. Chapter 3).

3.1.1 Fatigue data

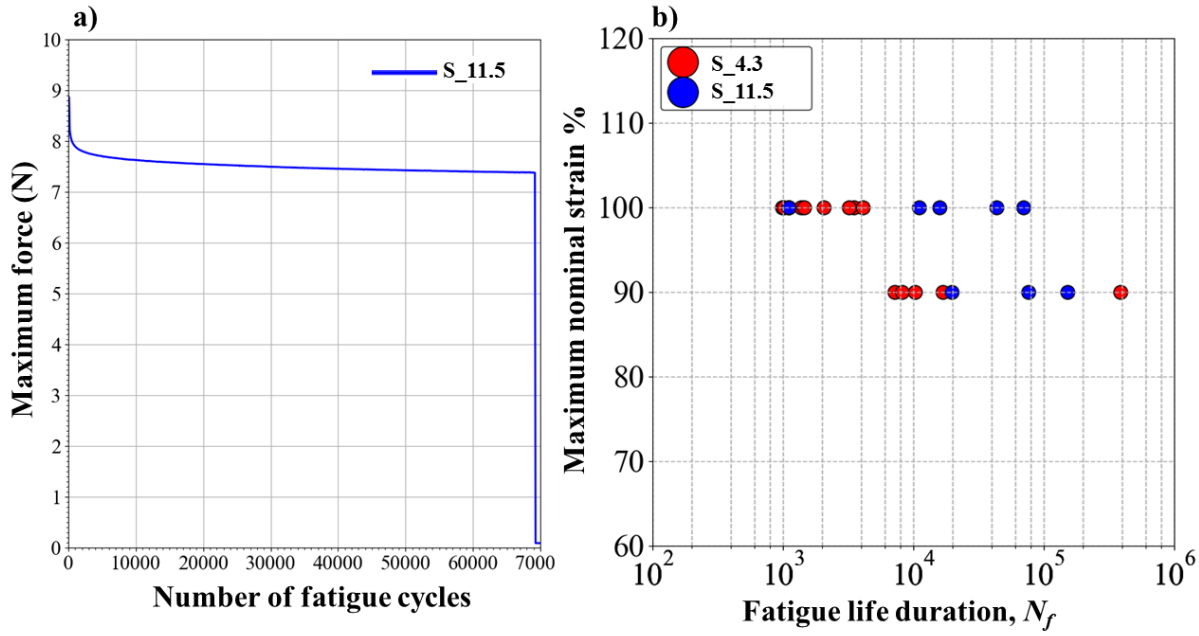

Figure 3: a) Evolution of the maximum force during a fatigue test for model material S_11.5 at 100% maximum nominal strain, b) fatigue life duration of the model materials at a maximum nominal strain of 90 % (3 and 5 specimens tested for S_4.3 and S_11.5 respectively) and 100% (5 specimens tested for each sample).

Figure 3a presents the evolution of the maximum force during the fatigue test of the model material S_11.5 cycled at maximum nominal strain of 100%. There is a drop of around 0.8 N during the first 100 cycles of fatigue. Thereafter, the maximum force gradually decreases

throughout the fatigue test, and abruptly drops at material rupture. The number of cycles required to reach this abrupt decrease is considered as the life duration (N_f). Figure 3a shows Nf of both model materials fatigued at a maximum nominal strain of 90% and 100%. From preliminary fatigue tests performed at different maximum nominal strain ranging from 75% up to 110%, we chose these strains to have a N_f anywhere between 1000 cycles and 10000 cycles. At 100%, the fatigue life duration (N_f) of S_11.5 (28000±25000 cycles) seems to be higher than that of S_4.3 (2200±1100), even though the results for this material are much more dispersed. Better life duration for S_11.5 may be deduced from the fatigue tests at 90% maximum nominal strain. Nevertheless, this conclusion must be taken with caution, one fatigue test with S_4.3 led to an exceptionally high Nf value, 385000, leading to a higher dispersion of the results. Disregarding this result, N_f is found to be equal to 82000±54000 cycles for S_11.5, and 11000±3700 for S_4.3.

The rupture is a consequence of crack(s) initiation and its (their) subsequent propagation through the entire material section. At the macroscale, as seen on Figure 3a only a couple of cycles are required to rupture the material after N_f. Usually, literature studies suggest that crack(s) initiation occurs much before N_f, and that the sudden drop at N_f is only the consequence of a catastrophic propagation of the crack(s)[2]. To understand this sudden rupture, it is therefore necessary to characterize the cracks initiating and propagating in the materials *during* the fatigue test. This was done using ex-situ tomographic analysis of fatigued samples.

3.1.2 Crack initiation during fatigue

Crack initiation was performed on both S_4.3 and S_11.5. We only discuss the results of S_4.3 which are also representative of the observations made on S_11.5. Figure 4a-d shows the evolution of a CB_{aggl} during a fatigue test at 100% maximum nominal strain, particularly the one highlighted with a red square. This CB_{aggl} undergoes fracture between 0 and 1000 fatigue cycles. Such mechanism is similar to what was observed in the previous chapter during tensile tests. After several cycles, the fractured CB_{aggl} can initiate a crack as shown in Figure 4c. The size of this crack then increases radially with the fatigue cycles (cf Figure 4). However, the CB_{aggl} presented in Figure 4a-e is not a critical defect for rupture, as the material finally breaks from a crack initiated in another critical CB_{aggl} at a different location unfortunately not in the initial observation window (cf. Figure 4f). SEM images of rupture surfaces confirmed these observations (SI Figure A2 and A3).

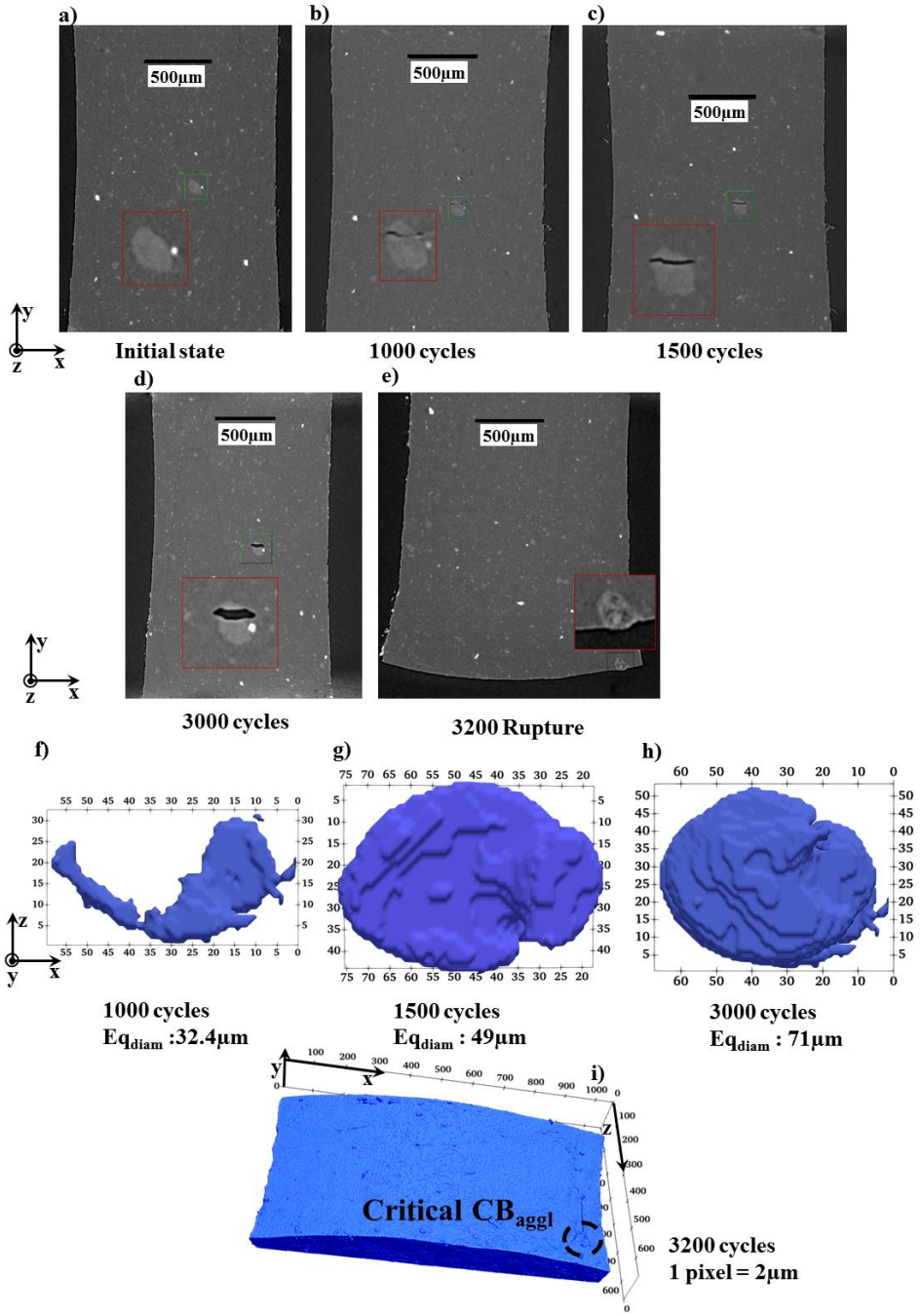

Figure 4: a) slice view of the S_4.3 material at initial state. The inset photo in each figure shows a magnified CB_{aggl}. b) a fracture appears in CB_{aggl} after 1000 cycles of fatigue at a maximum nominal strain of 100%, c)-e) evolution of the cavity inside the CB_{aggl} finally leading to a crack in the material at around 1500 cycles. e) at 3200 cycles, the material is ruptured (bottom of the picture showing the contour of the rupture surface) due to another critical CB_{aggl} shown in the inset photo (unfortunately this one was not in the observation window before rupture). f)-h) evolution with the number of fatigue cycles of the cavity volume inside the CB_{aggl} shown in figures b) - d) (inset photos). i) 3D view of the rupture surface of the material.

3.2 Industrial material

3.2.1 Microstructural analysis

We studied 3 specimens from industrial material *I*. The cumulative volume fraction of CB_{aggl} in these 3 specimens are 3.8%, 2.5%, and 2.7%, respectively, meaning that it is 3.0±0.6% in the compound. The morphology distribution of CB_{aggl} deduced from the analysis of the specimen with $\phi_{CB_{aggl}}$=3.8% is presented along with that in S_4.3 ($\phi_{CB_{aggl}}$=3.0% using X-ray laboratory sourced X-ray Tomography and $\phi_{CB_{aggl}}$= 4.3% using SRCT) in Figure 5. As shown in Figure 5a the agglomerates size in one *I* specimen are distributed over a larger size domain. (Eq_{diam} of CB_{aggl} in *I* ranges from around 14µm to 188µm for an average Eq_{diam} of 24.1µm versus 11.1µm for S_4.3). These agglomerates are also less structured than in the model materials (their structure factor is most likely in the domain [0.0 - 0.15] compared to [0.0-0.25] for S_4.3). Same conclusions could be drawn from the distribution derived from the study of the other two specimens of the industrial material.

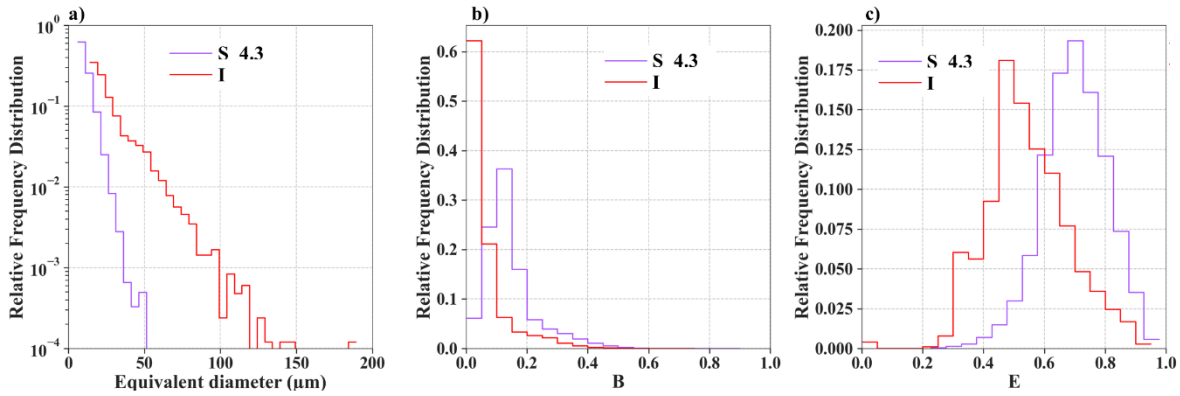

Figure 5: Morphological parameters distribution of CB_{aggl} in the industrial material I_1 and model material S_4.3, a) equivalent diameter. b) structure (B), c) eccentricity (E).

3.2.2 Fatigue Properties

Figure 6 shows the tensile properties of *I* and S_4.3. The industrial material undergoes rupture at 283%±24% nominal strain, whereas S_4.3 rupture is at 167%±8% nominal strain. The tensile properties at large nominal strain of these two materials are significantly different. Strain hardening is much more important in the model materials, which do not contain any oil. The crosslink densities of both materials are also different since they do not have the same crosslinking recipe (the apparent crosslink density derived from swelling experiments was found equal to $1.9*10^{-4}$ mol.cm^{-3} and $3.8*10^{-4}$ mol.cm^{-3} for *I* and S_4.3 respectively).

Figure 7a shows the evolution of the total maximum force for five *I* specimens simultaneously tested in fatigue. The observed trend is similar to that of the model materials. A ca. 15% drop of the force is first observed within the first 100 cycles. Afterwards, the force slowly decreases with the number of cycles until one of the specimens is broken, leading to a drop in the total force. Here, at around 48000 cycles, 3 specimens are broken. The two others broke after 85000 cycles. The life duration (N_f) deduced from these tests at a maximum nominal strain of 115% and 135% is reported in Figure 7. It is worth noting that we chose 115% maximum nominal strain because it enables to perform a sufficient number of fatigue cycles ((i.e. 10000 cycles) between two successive tomographic scans. At 135% nominal strain, N_f is 28500 ±9100 cycles and at 115% nominal strain, N_f is 62500 ±18500 cycles. The standard deviation is large and around 30%, but lower than that of the model materials.

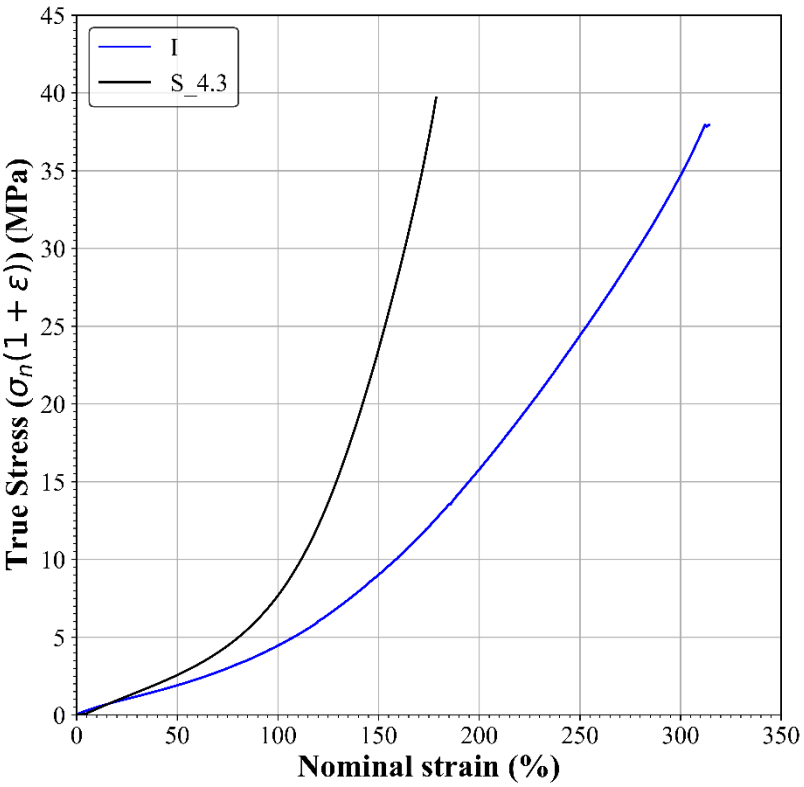

Figure 6: representative true stress-nominal strain curve of the Industrial material and of S_4.3.

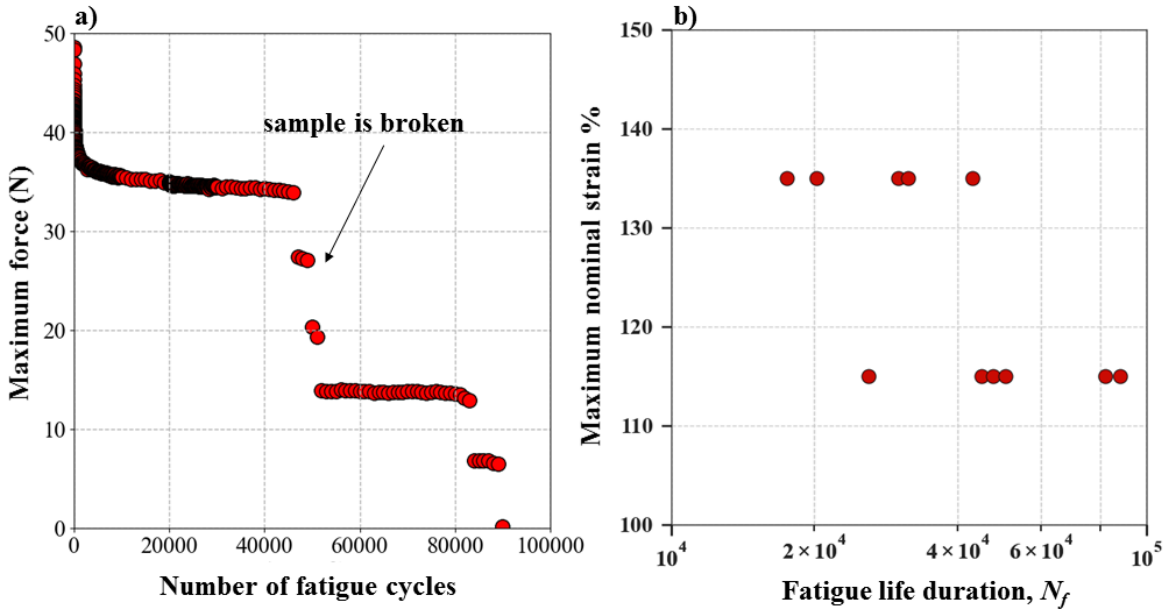

Figure 7: a) total maximum force during the fatigue tests performed simultaneously with 5 samples as a function of the number of fatigue cycles, b) fatigue life duration of the industrial material fatigued with cycle at a maximum nominal strain of 115% and 135%.

3.2.3 Ex-situ observations of crack initiation

Figure 8 shows the microstructural evolution of 3 CB_{aggl} in *I* during a fatigue test, as observed by laboratory Tomography, after 0 cycle (initial state), 10000 cycles, 20000 cycles etc… All the three CB_{aggl} have similar initial sizes (1: 149.0 µm, 2: 153.7µm, 3: 145.0µm). CB_{aggl}1 develops a complete internal fracture within 10000 fatigue cycles. There is nucleation of internal fracture in CB_{aggl} 2 and CB_{aggl} 3 at this stage. As the material still undergoes fatigue cycling, internal fracture grows radially and enters the matrix which leads to crack initiation. A crack is initiated from CB_{aggl} 1 between 10000 - 20000 fatigue cycles whereas for CB_{aggl} 2 and CB_{aggl} 3, it occurs between 20000 – 30000 cycles. In addition to CB_{aggl} fracture mechanism, there is cavitation at the pole of CB_{aggl} 2 at 10000 cycles (inset photo in Figure 8d, f, g & j). This damage mechanism is observed only for few CB_{aggl} in the material. At 40000 cycles, the crack from the fractured CB_{aggl} 1 propagates to the surface and into the bulk of the material. When this occurs, rupture of the material is very fast. Actually, CB_{aggl} 2 is in the same yz plane as CB_{aggl} 1 (not visible on the selected figures of Figure 8). Their crack may have coalesced to rupture the material, but we unfortunately did not confirm it by observation as tomography was not performed on totally broken material. It is also noteworthy that CB_{aggl} with sizes smaller than the aforementioned ones also undergo similar internal fracture mechanisms (cf. Figure A5

in SI). However, the crack initiated remained inside the agglomerate, even though it seemed to reach agglomerate frontier.

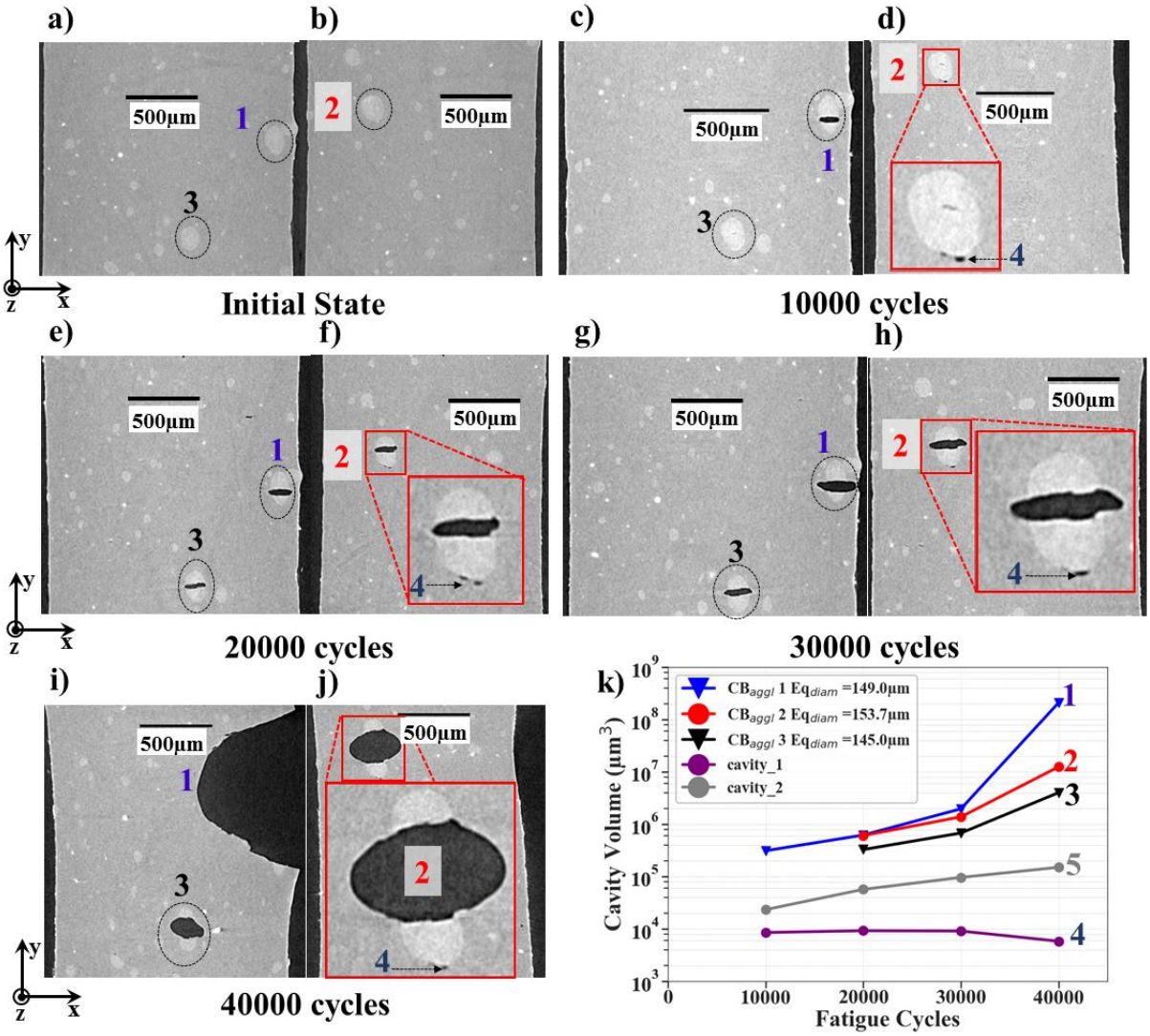

Figure 8: Microstructural evolution of 3 CB_{aggl} in *I* specimen undergoing fatigue tests at a maximum strain of 115%, observed by laboratory source Tomography: a)-b) slice view of the sample at its initial state. 3 CB_{aggl} are observed, labelled 1, 2, and 3. The cavity at the pole of CB_{aggl} 2 is labelled as 4. The inset photo in d), f), h) and j) shows a three time magnified CB_{aggl} 2. c)-d) at 10000 cycles, e-f) at 20000 cycles, g)-h) at 30000 cycles, and i)-j) at 40000 cycles. k) volume of the different observed cavities versus the number of fatigue cycles. Note that the cavity_2 at the pole of CB_{aggl} is not visible in Figures a)-j), because it is in another xy plane (more images of this cavity is presented in SI Figure A4).

The growth of the cavities formed at the CB_{aggl} pole remains slow and these cavities (e.g. cavity_1 # 4) do not transform into a propagating crack. Conversely, the volume of the cavity, created due to CB_{aggl} cracking, increases rapidly with the number of fatigue cycles. Even though the crack inside the agglomerates can be initiated between 10000-20000 cycles, 20000 or more cycles are still necessary for that crack to finally rupture the material (Figure 8k, 9). The total volumes (over the whole volume observed by tomography) of the all cavities (formed from the fracture of CB_{aggl} from cavitation at the CB_{aggl} poles) are plotted in Figure 9. The contribution of the cavities at the agglomerates pole in this total volume is negligible and this curve enables to estimate the importance of the fracture process inside the CB agglomerates.

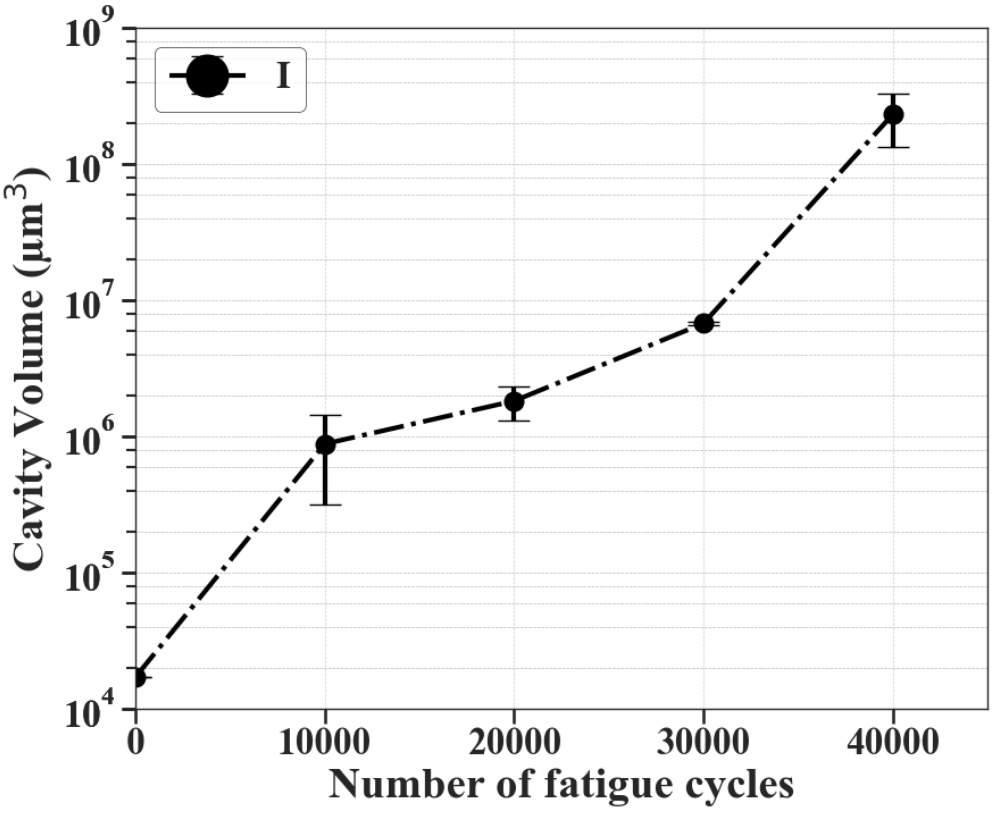

Figure 9: Evolution of the cavity volume as a function of the number fatigue cycles in three specimens of the same industrial material.

3.2.4 Morphology of crack-initiating CB_{aggl}

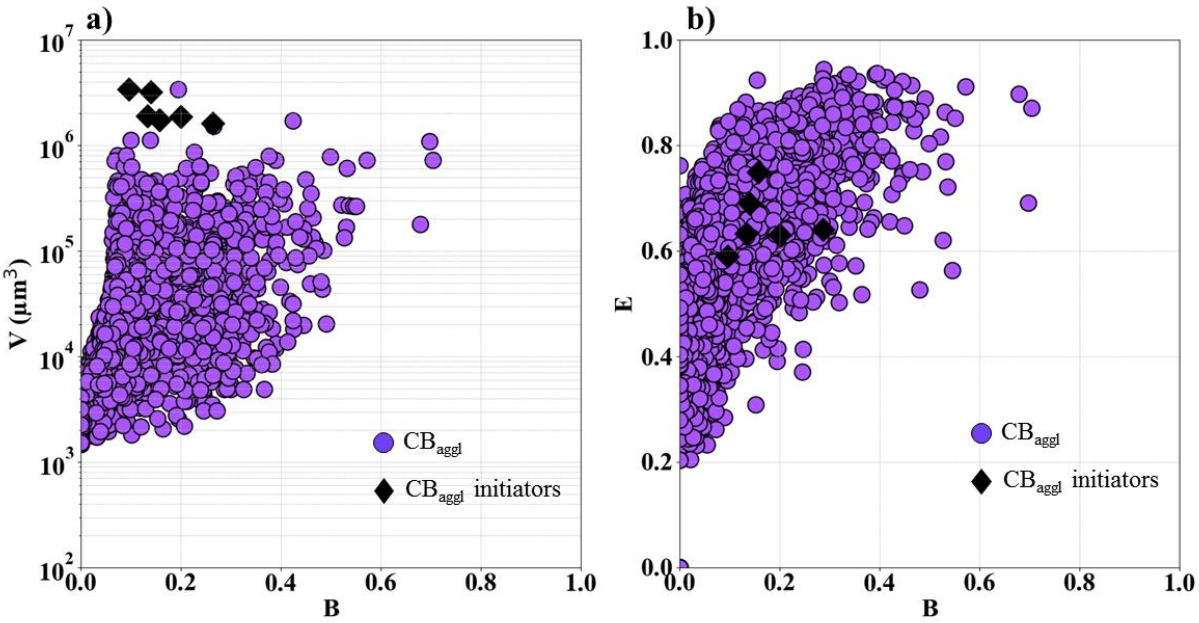

Figure 10: Morphology of CB_{aggl} in I (calculated for the specimen with ϕ_{cumul}: 3.8%): a) V versus B; b) E versus B. Diamonds correspond to the CB_{aggl} that initiated crack propagation in the matrix.

The morphological characteristics (*V* volume, *B* structure, and *E* eccentricity) of some CB_{aggl} that have initiated crack in the industrial matrix are reported in Figure 10. The crack-initiating CB_{aggl} are among the biggest in the material (with diameter above 140µm). The eccentricity of these CB_{aggl} is in the range of 0.6-0.8, i.e. like for most of the agglomerates. In Figure 10a one might conclude that these agglomerates have also a low structure factor (below 0.3). Nevertheless, Figure 10b shows that the (*E, B*) couple values are not specific to these agglomerates. Thus, the volume is a critical parameter compared to *E* and *B*. Unfortunately, we cannot make the same conclusion with the model materials for fatigue tests, but we can recall that this conclusion was made in tensile tests.

4. DISCUSSION

Filled elastomers contain microstructural defects. The concentration and morphology of these defects depend on the processing parameters as well as the chosen formulation. Adding oil along with CB leads to a different morphology of the agglomerates at the end of process when compared to a model material (with similar concentration of CB_{aggl}). They are bigger, their size is more distributed, they are also less structured and have a lower eccentricity. (cf Figure 5). As shown in a seminal work by Hess et.al[7], the addition of oil , depending on the

processing parameters (addition of the oil in the internal mixer with the CB or after, shearing time before this addition, shearing energy etc…) can reduce the dispersion of the carbon blacks and eventually promote the formation of compact agglomerates. The morphology of our agglomerates indeed suggests that the simultaneous addition of the CB and oil in the internal mixer during the processing, has led to a weaker shearing of the blend at the beginning of the mixing step, than with the *S* formulation (the swelling of the polymer by the oil reduced the shearing modulus). This has limited the rupture of the initial agglomerates which have been eroded afterward during the remaining shearing time and hence, forming more spherical shaped agglomerate.

The industrial material has agglomerates with different morphologies and also different mechanical properties than the *S* ones since it contains oil, has a different crosslinking formulation, and a different CB concentration. Despite this, the rupture mechanisms occurring during fatigue test remains the same (Figures 4 and 8) and similar to what was described for tensile tests (Chapter 4); more and more CB_{aggl} are fractured during the test, and some of these fractured CB_{aggl} initiate multiple cracks which propagate into the surrounding material. This is at the origin of the gradual decrease of the maximum force at the beginning of the fatigue test. The rapid decrease of the force and the material rupture happens when one of these propagating cracks reaches the surface, which is more likely when the agglomerates which initiated them are closer to the surface.

The number of cycles at which we observed a crack going out of an agglomerate is between 1000 and 1500 for S_4.3 fatigued at 100 % strain, and between 10000 and 20000 at 115% for *I* material. In both cases this cycle number is around 30% - 40% of N_f. One may rapidly conclude that the formation of a crack from the agglomerate is easier in *S* material. Comparison between both materials is however difficult because in these examples, the maximum macroscopically applied stress is actually lower in the industrial materials (which also leads also to a lower stress applied at the pole of the agglomerates). Fortunately, fatigue tests have also been performed on the *I* material at 135% maximum strain, which leads to a maximum applied stress of 7.5 MPa, i.e. very close to the macroscopically applied stress on the S_4.3 material cycled at 100% maximum strain. N_f for *I* material fatigued at 135% is around 28000 cycles. Tomography scan was not performed for these conditions, but we can reasonably estimate that in this case, initiation (defined as the moment where crack exits from the agglomerates) occurs at more than 8000 cycles (i.e. at more than 30% of N_f). This is significantly higher than the number of cycles required to initiate cracks in the S_4.3 material for the same macroscopic applied stress. All

this suggests that agglomerates fracture process is more difficult for the agglomerates of the industrial materials. This explains why cavitation at the pole was observed for these agglomerates and not for the softer agglomerates of the *S* materials. The reason for the larger strength of these agglomerates is the presence of oil in the formulation and the processing conditions.

After the crack initiation, for the remaining fatigue cycles, crack continues to propagate through the volume of the material during a large number of cycles which represents the majority of the cycle number to rupture the material (around 60% of N_f). Similar observations have been previously reported in the literature. For instance, a study by Le Saux et. al[8] reported that cavities appeared in filled polychloroprene rubber within the first few fatigue cycles, much before the rupture. The growth rate of these cavities is therefore slow until this rupture. Similar remarks were made by Bertrand et.al[3] in a CB filled NR observed using SEM. At the microscale, we also observed that the crack propagation step is longer than the crack initiation step in the model and the industrial materials. This is particularly helpful in explaining the reason as to why S_11.5 has a better N_f compared to S_4.3 (even though the data is highly dispersed) on the basis of the crack propagation resistance observed for these materials under tensile tests (Chapter 3). However, the confirmation of this hypothesis requires further investigation on crack propagation under fatigue solicitation.

At last, the materials presented here (both model and industrial) have a certain concentration of CB_{aggl} that can initiate rupture cracks within the sample. The determining morphological parameter of such CB_{aggl} is their size. In case of industrial and model materials, Eq_{diam} is greater than 150µm and 40µm respectively (information in previous chapter). These agglomerates are distributed at different locations within the sample. Under fatigue test, all these critical CB_{aggl} can initiate a crack, i.e. multiple crack initiations can occur, as shown in Figures 4 and 8. However, the observation of the rupture surface mostly shows a single critical defect at the crack origin. This can be observed in the CB_{aggl} presented in Figure 4b and Figure 8 (CB_{aggl} 3) where the cracks from such CB_{aggl} did not rupture the material. There is therefore a competition between the crack growth from CB_{aggl} that are away from the sample edges and those from CB_{aggl} that are close to the sample edges. The crack that ruptures the material always initiates from the CB_{aggl} close to the sample edges (observation made from 6 samples), e.g. CB_{agg} 1 in Figure 8 and SEM observation in SI Figure A2. This is likely due to the strain field which leads to high strain energy release rate for the surface cracks[9]. All these results corroborate the results from tensile tests (Chapter 5).

5. CONCLUSION

Thanks to X-ray Tomography, we could observe in 3D the damage originating in CB_{aggl} during fatigue test. We have visualized the crack initiation from "non-visible inclusions" which were presumed in the literature to be CB_{aggl}. Through this investigation we found out that the crack initiation mechanism in filled EPDM, i.e. CB_{aggl} fracture, is indifferent to how CB_{aggl} are dispersed (with and without oil), to the concentration of CB_{aggl}, and the type of solicitation (tensile, fatigue) etc (as far as we have agglomerates bigger than 150µm and 40µm in industrial and model material respectively) … We also confirmed that adding oil in the elastomer matrix can lead to stronger CB_{aggl} and therefore delay the crack initiation. In addition, our results indicate that CB_{aggl} size is much more decisive than its structure or eccentricity in the fact that it will initiate a crack in the matrix (in the ranges observed) and similarly location of CB_{aggl} in the specimen is also an important factor. At last, the location, i.e. the strain field of this big agglomerates determine the criticality of the initiated crack.

6. SUPPORTING INFORMATION

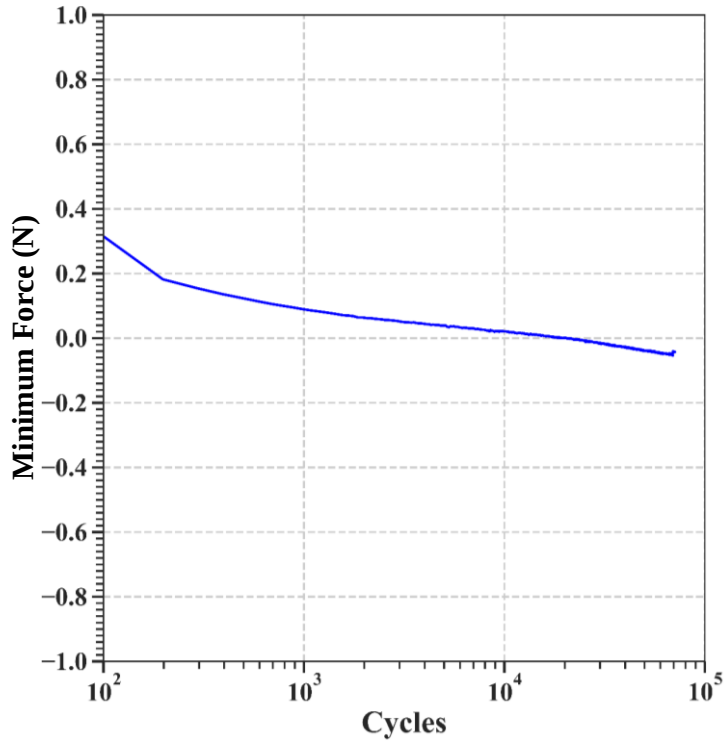

Figure A1: evolution of the minimum force during a fatigue test for model material S_11.5.

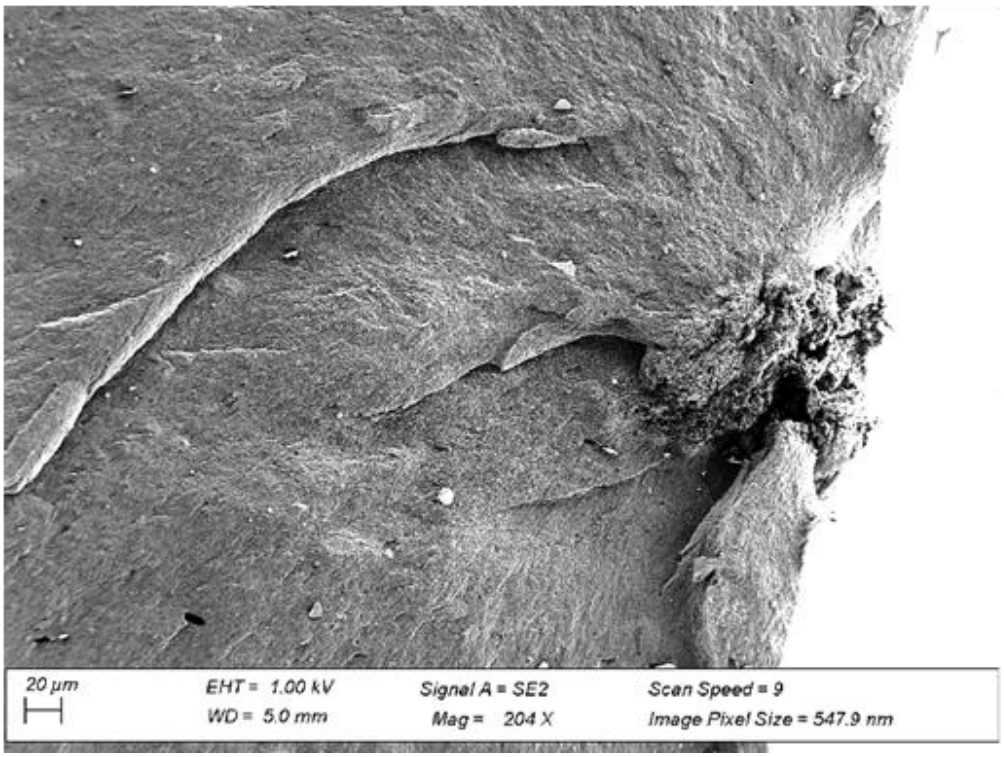

Figure A2: a) a crack is initiated from CB_{aggl} for model material S_11.5.

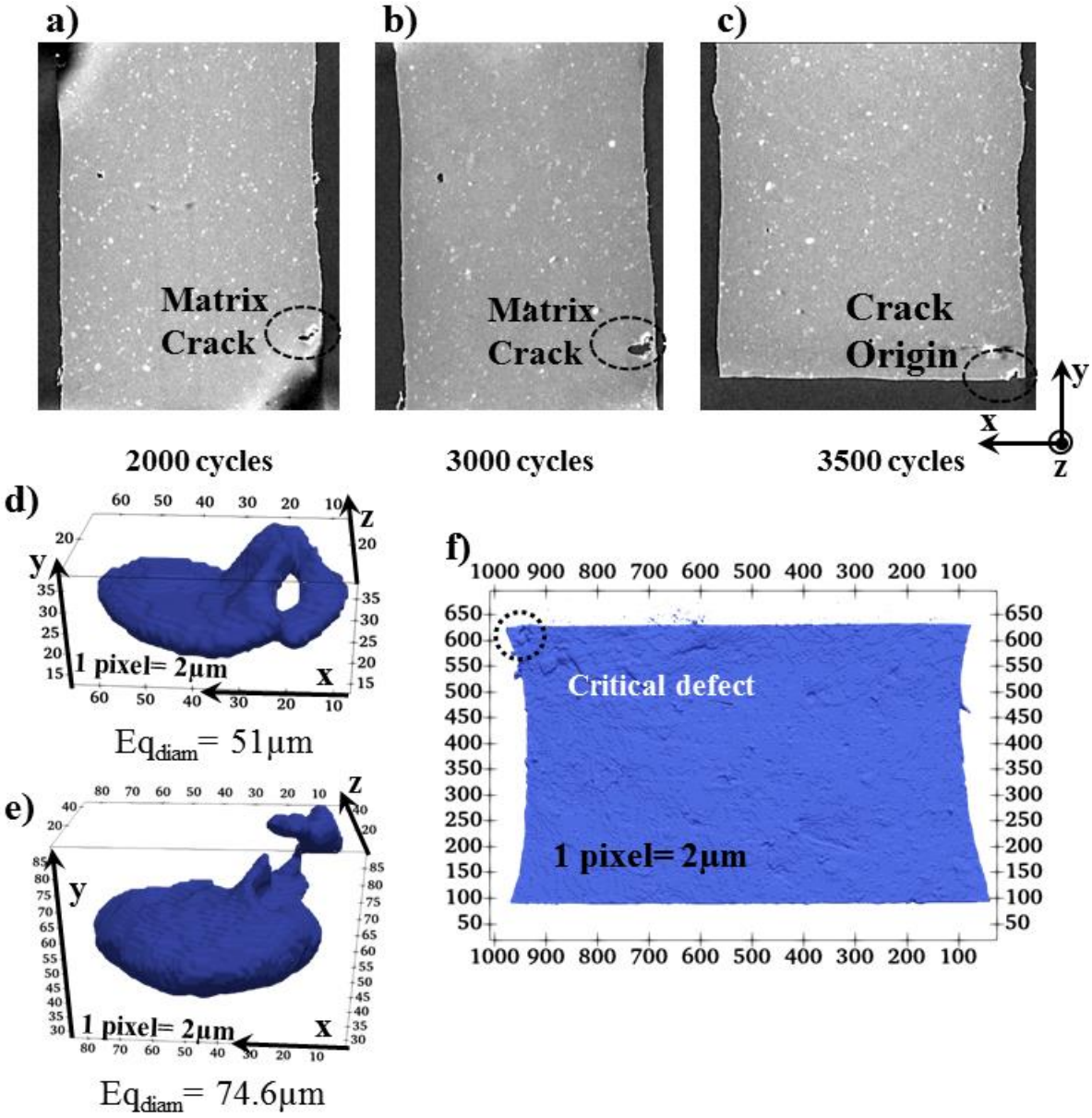

Figure A3: Model material S_4.3 observed using lab tomo during the fatigue test at a) 2000 cycles, b) 3000 cycles, c) after rupture. d) and e) visualization of the crack within the CB_{aggl} corresponding to a) and b) respectively. f) Ruptured surface of S_4.3.

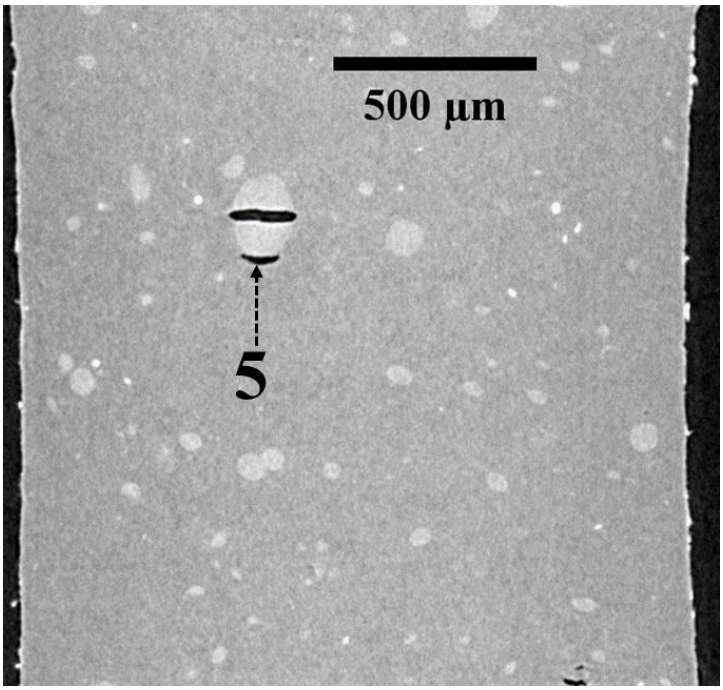

Figure A4: cavity_2 in Figure 8k

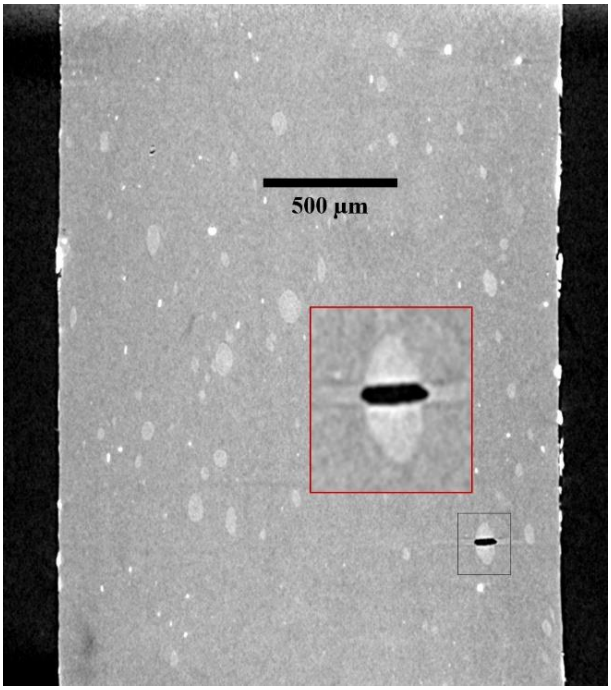

Figure A5: Fracture in CB_{aggl} with Eq_{diam} 44µm

7. REFERENCES

[1] Le Gorju Jago, K. X-Ray Computed Microtomography of Rubber *Rubber Chemistry and Technology* **2013**, *85*, 387, 10.5254/rct.12.87985.

[2] Glanowski, T.; Marco, Y.; Le Saux, V.; Huneau, B.; Champy, C.; Charrier, P. Fatigue crack initiation around inclusions for a carbon black filled natural rubber: an analysis based on micro-tomography; In *Constitutive Models for Rubber XI*; Huneau, B.; Le Cam, J.-B.; Marco, Y.; Verron, E., Eds.; CRC Press, **2019**; pp 368; 10.1201/9780429324710-64.

[3] Huneau, B.; Masquelier, I.; Marco, Y.; Le Saux, V.; Noizet, S.; Schiel, C.; Charrier, P. Fatigue crack initiation in a carbon black-filled natural rubber *Rubber Chemistry and Technology* **2016**, *89*, 126, 10.5254/rct.15.84809.

[4] Masquelier, I. Thesis,. Influence de la formulation sur les propriétés en fatigue d'élastomères industriels, Université De Bretagne Occidentale, **2014**.

[5] Le Saux, V.; Marco, Y.; Calloch, S.; Doudard, C.; Charrier, P. Fast evaluation of the fatigue lifetime of rubber-like materials based on a heat build-up protocol and micro-tomography measurements *International Journal of Fatigue* **2010**, *32*, 1582, 10.1016/j.ijfatigue.2010.02.014.

[6] Ostoja-Kuczynski, E.; Charrier, P.; Verron, E.; Marckmann, G.; Gornet, L.; Chagnon, G. Crack initiation in filled natural rubber: experimental database and macroscopic observations *Constitutive Models For Rubber III* **2003**, 41.

[7] Hess, W. M.; Swor, R. A.; Micek, E. J. The Influence of Carbon Black, Mixing, and Compounding Variables on Dispersion *Rubber Chemistry and Technology* **1984**, *57*, 959, 10.5254/1.3536052.

[8] Le Saux, V.; Marco, Y.; Calloch, S.; Charrier, P. Evaluation of the fatigue defect population in an elastomer using X-ray computed micro-tomography *Polymer Engineering & Science* **2011**, *51*, 1253, 10.1002/pen.21872.

[9] Le Cam, J.-B.; Huneau, B.; Verron, E. Fatigue damage in carbon black filled natural rubber under uni- and multiaxial loading conditions *International Journal of Fatigue* **2013**, *52*, 82, 10.1016/j.ijfatigue.2013.02.022.

General conclusion

CONCLUSION

The main goal of this thesis was to understand the role of defects on the durability of rubber products and thereby deduce the relevant defects characteristics that are required for the development of appropriate quality control benchmarks for these products. To this end, the first objective was to develop a robust methodology to quantify the dispersion and the morphological features of defects that are present in a CB filled EPDM matrix using synchrotron sourced and laboratory sourced X-ray Tomography. The 2nd objective was to understand the influence of microstructural defects on the rupture and fatigue properties with the help of the X-ray Tomography.

In order to achieve the first objective, we initially optimized the operating parameters of laboratory sourced X-ray Tomography for image acquisition to study the CB filled EPDM effectively. It is advisable to use a lower tube tension in laboratory sourced X-ray Tomography (40 kV) to improve the attenuation contrast of defects like CB_{aggl}. The contrast can be further improved by applying various image processing algorithms presented in chapter 3. Various morphological features can be easily extracted from 3D images, but some of those features can be redundant. In such cases, feature selection tools are necessary to identify them. With the studied materials, we found that Volume, Structure and Eccentricity (related to aspect ratio or elongation) can adequately describe CB_{aggl}. Nevertheless, a simple analysis of their distribution does not provide clear information on the differences between different materials. For this reason, we developed a classification method of the CB_{aggl} based on their three morphological features. This classification proved to be effective in distinguishing our materials. In the studied case, it can provide insights on the influence of processing parameters such as rotor speed, CB addition protocol etc. on the final CB_{aggl} morphology. The potential application of such methodology is in the analysis of conformity of rubber products. For instance, it can be used to identify the undesirable defects and ensure that the ones present in the products are within acceptable levels.

Rupture is a consequence of the initiation and propagation of crack(s) through the entire section of the materials. The crack initiation process during tensile tests is discussed in Chapter 5. We studied materials with different concentrations of CB_{aggl}; one with abnormally high CB_{aggl} concentration and another one with a CB_{aggl} concentration representative of those commonly found in industrial production. In X-ray Tomography images, CB_{aggl} are almost invisible in the presence of high attenuation contrast particles like ZnO (hence, the term non-

visible inclusions used in some recent literature studies refers to CB_{aggl}). To mitigate such problems, ZnO was not incorporated in our model materials. Despite this, the studied elastomers contain low concentrations (less than 0.05%) of pre-existing metallic oxide inclusions in them. We evidenced that CB_{aggl} are the only precursors of crack initiation and that decohesion at the metallic oxide inclusion pole does not initiate a crack. Moreover, the rupture properties (using tensile specimen geometry) are independent of the CB_{aggl} concentration in the materials we studied. Observation during an in-situ tensile testing under synchrotron sourced X-ray Tomography showed cavitation inside CB_{aggl} upon stretching. An interesting power law dependence was found between the true macroscopic stress at the cavitation onset and the equivalent diameter of CB_{aggl}. This correlation suggests that these cavities might have originated due to decohesion at the interface between the polymer and aggregates layers which constitute the agglomerates. These cavities grow to become an internal fracture inside CB_{aggl}. As observed in many agglomerates, as long as the fracture remains within them, there is no crack initiation in the sample. To observe this initiation, the fractured CB_{aggl} must be in or near a zone of high triaxial stress. In addition, the CB_{aggl} should have a critical size greater than 40µm. The other morphological features of CB_{aggl} like structure and eccentricity, are not as critical when compared to the size. Moreover, the transition of the internal CB_{aggl} fracture to a crack appears to be delayed if CB_{aggl} undergo multiple fractures. All the studied materials with varying concentrations of CB_{aggl} contain these critical CB_{aggl}; this explains their similar rupture properties. Thus, during the processing of the material, to improve rupture properties, more efforts should be made to remove agglomerates with this critical size rather than reducing the overall concentration of agglomerates in the material.

The specificity of crack initiation during fatigue solicitation is presented in chapter 6. As expected, the crack initiation mechanism during fatigue test remains the same as that in tensile studies, i.e. the origin of crack initiation is CB_{aggl} fracture. We extended our study by comparing CB_{aggl} in the model materials with that of an industrial material whose formulation also contains oil. The presence of this oil changes the morphology of the CB_{aggl}; they are bigger, less structured and more spherical (lower eccentricity). Certainly, this is the consequence of reduced shear rate at the beginning of the mixing due to lower shear modulus of the oil-swelled polymer. Although there is a difference between the morphology and mechanical properties of the industrial materials and the model materials, their crack initiation mechanism still remains the same (crack/cavitation growth in the agglomerate which transforms into a crack in the

matrix). However, CB_{aggl} in industrial material appear to be stronger than those in the model materials, and require more fatigue cycles to fracture.

The crack propagation which leads to material rupture is discussed in Chapter 4. The presence of CB_{aggl} influences the crack propagation. This was observed during a classic crack propagation test, i.e. measuring the crack propagation speed as a function of strain energy release rate (G) in a pure shear geometry specimen. In the presence of CB_{aggl}, the strain at the crack tip vicinity is higher. In the crack tip vicinity subjected to high strain, CB_{aggl} undergo internal fracture (as previously discussed). These dissipative mechanisms reduce the crack propagation rate at a given macroscopic G. They are obviously more important in materials with high CB_{aggl} concentration, and have a significant impact only at high G when the highly strained volume becomes very large. Furthermore, we observed other mechanisms such as crack deviation/arrest by agglomerates (fractured or not) which also increase the energy required to rupture the material.

PERPECTIVES

Although this thesis has deepened our understanding of the influence of CB_{aggl} on the rupture and fatigue properties, the presented methodology and the results bring out new questions and perspectives for further works.

The methodology in chapter 3 evidenced a difference in the volume fraction of CB_{aggl} belonging to morphology classes 7, 8 and 9 for the materials processed with TD and USD addition protocols. Their difference is however reversed when the rotor speed of the internal mixer is changed. Understanding this complex behavior requires the characterization of the impact of some influential parameters such as temperature, shear stress inside the internal mixer etc. on the CB dispersion during the mixing. Similarly, the effect of roll mill process on CB dispersion should also be characterized to derive meaningful insights. Indeed, the proposed methodology is useful for such study. Currently, it was applied for classification of CB_{aggl} in the model materials. One can extend its application to the industry by training the classification algorithm using the CB_{aggl} morphology data from the industrial materials. Methodology can also be made better/efficient by using other image processing algorithms in the feature extraction technique such as Total variation filter instead of non-local means for faster computation, un-supervised segmentation algorithm etc.. Apart from the abovementioned

prospective works, we have not explored the influence of processing parameters on the orientation of CB_{aggl} and the consequence of this orientation on the mechanical properties.

Chapter 5 presented a crack initiation chronology starting with cavity nucleation inside CB_{aggl} up to the material rupture during a tensile test. Based on the power law dependence between true macroscopic stress at the cavitation and Eq_{diam}, we assume that the origin of cavitation is due to decohesion at the interface between the polymer and aggregates layers. Even though this proposition is coherent with the literature, we cannot confirm if there is a nonoccurrence of cavitation inside the confined polymer due to high hydrostatic stress inside CB_{aggl}. This requires further nanoscale characterization of CB_{aggl} during material stretching using nano X-ray Tomography (for instance, holotomography technique at the ESRF beamline ID22NI). Moreover, such studies can also reveal why some of the internal fractures inside CB_{aggl} get arrested within. Such studies will facilitate the development of a more precise model for CB_{aggl} in materials for future numerical studies. It is worth noting that above mentioned study was limited to a specific type of CB_{aggl}, made of one type of CB (N326) with one formulation. These choices control the intrinsic properties of these agglomerates. Thus, it could be interesting to extent this study to other formulations, and in particular, to other types of carbon black like N234, N550 etc…

Another aspect that requires further work is related to the debonding mechanism at the poles of metallic oxide inclusion. It is interesting to observe that we do not have the same exponent value (-1.2) in the power law relationship between true macroscopic stress at decohesion and Eq_{diam} when compared to the literature studies (-0.5). This might be due to the non-consideration of various important parameters such as initial debonded area at the poles (or debonding angle), shape factor and orientation of the inclusion in the model. Integrating all these factor can devise a better model for the decohesion mechanism. Currently, the inclusion size (Eq_{diam}) in the elastomer is less than 40µm; therefore, to derive a generalized conclusion, one may study the same phenomena by introducing big sized metallic oxide inclusions and also different kinds of metallic oxide inclusions, e.g. ZnO.

One common characteristic in the crack initiation mechanism observed in both fatigue and tensile studies is that the crack mostly originated from critical agglomerates close to the edges. The study could not establish any one factor (size or location) as more significant than the other since all the materials studied had high probability of finding these critical agglomerates close to the edges. 2 strategies can be used to study this. The first one is through a numerical study to compare the crack propagation caused by a crack at the edge and a crack

away from the edge subjected to similar strain energy release rate. The second strategy would be carefully selecting the samples with and without critical CB_{aggl} at the edges using the methodology proposed in chapter 3 and thereby conducting tensile or fatigue tests. Finally, although we have information on the types of agglomerates to be avoided, we can further extend our study to deduce a statistical relationship between the CB_{aggl} and the rupture/fatigue properties.

The discussion of crack propagation presented in this thesis is based on the dissipative mechanism of CB_{aggl}. Mullins test results have evidenced such dissipation due to CB_{aggl}. Nevertheless, it is difficult to estimate the local strain energy release rate available at the crack tip for crack propagation. Literature studies have shown methodologies to calculate local G based on the 2D measurements of strain using DIC. Such analysis can give an approximate information; however, it is not sufficient since there are occurrences of multiple mechanisms such as CB_{aggl} fracture and crack deviation/arrest at the crack tip. A methodology has to be devised to calculate the local strain energy release rate from 3D strain field at the crack tip. One can use digital volume correlation to obtain 3D strain field around the crack tip with respect to the macroscopic strain applied to the material.

The current crack propagation study is valid for uniaxial solicitation only. In real world applications, materials are subjected mostly to cyclic loadings. Therefore, it would be interesting to study the influence of CB_{aggl} on crack propagation during fatigue tests. Similar to the prospective work proposed for crack initiation, one can also compare the influence of different kinds of CB fillers, on the CB_{aggl} characteristics and the crack propagation during tensile and fatigue tests.

APPENDIX 1

About the influence of materials parameters on the ultimate and fatigue properties of elastomers

L. Chazeau[1], J.-M. Chenal[1], C. Gauthier[2], J.Kallungal[1] and J. Caillard[2]

[1] Univ Lyon, INSA Lyon, CNRS, MATEIS UMR5510, F-69621, Lyon, France.
[2] Centre de technologies, Manufacture Française des Pneumatiques Michelin, 63040 Clermont Ferrand Cedex 9, France.

Keywords. Cyclic/static crack growth • Filled polymers • Viscoelasticity • Mullins effect • Rupture properties • Dissipation.

TABLE OF CONTENTS

ABSTRACT
The aim of this chapter is to revisit the historical works, mechanisms and modeling approaches available in the field of fatigue crack growth resistance and rupture properties. After introducing the methodology developed to evaluate these properties, the impact of testing parameters such as temperature, loading speed and pre-deformation will be highlighted. We will then review the influence of some material characteristics on rupture and crack propagation and the local mechanisms involved. Finally, a theoretical framework primarily dedicated to the description of crack propagation under static load will be discussed, that aims to underline the connection between resistance to crack growth and the ability of a material to dissipate energy.

1 INTRODUCTION

Optimizing life duration of pneumatics, seismic isolators, mechanical membranes, seals etc. requires a good understanding of the capability of elastomers they are made of, to withstand mechanical loading and resist to crack initiation/propagation. The mechanisms of crack initiation and propagation in elastomers have been of continuous interest to the scientific community, as shown by the numerous reviews on this topic [1–6]. In addition, many recent works have been dedicated to a fine characterization of the material in the close vicinity of cracks. More recently, new fields of applications have emerged in connection with soft robotics, stretchable electronics and bio-medical applications [7]. New ideas for the architecture of biomimetic materials with improved performance ermerged [8, 9]. Recent years have thus seen the synthesis of novel elastomeric networks, such as 'double networks', which appear to provide remarkable fracture properties [10]. This contributed to a renewed interest in understanding and modelling the damage and rupture of elastomeric and filled elastomeric networks [11, 12].

2 EXPERIMENTAL METHODS AND KEY FEATURES RELATED TO VISCOELASTICITY

From a very general point of view, rupture appears as the consequence of the initiation and eventual propagation of one or more cracks over the entire section of the material. It can occur under a constant, monotonic, or cyclic loading or a combination of these three. Understanding crack mechanisms requires the use of microstructural characterization tools that allow to observe the process of crack appearance from the very beginning. Several studies focused on the links between the processing conditions and the presence of defects, such as cavities, aggregates or agglomerates, from which cracks can nucleate. They are generally extended to the study of the number of cracks created under a given load scenario (monotonic or cyclic). The geometries that allow stress localization and consequently the control of the zone where cracks will appear are generally preferred (e.g diabolo or hourglass type) [13, 14], in order to limit the observation region. Many studies use optical or electron microscopy (SEM) to observe the surface of the specimen. The fast development of tomography now allows to access a 3-dimensional information inside the object. This one can be correlated with the strain energy necessary for the crack´s nucleation and subsequent propagation that can be calculated at a macroscopic scale or locally through the characterization of strain fields inside the material (using necessarily a modeling step). It is thus possible to better understand the initiation mechanism and its link with local stress or existing flaws in the material (their morphology or their spatial distribution) [15–17]. Nevertheless, note that the estimated strain energy, or the local or macroscopic critical stresses / strains to which crack initiation is related, depend very much on observation tools and their resolution.

In many cases, cracks initiation is not considered as the mechanism which dictates the lifetime. Thus, many works have been rather devoted to crack propagation. Different experimental protocols and specimen geometries can be used (the most commonly used geometries are pure shear, trouser, and tensile test-pieces). This can make difficult comparison and generalisation

of the results. The test-piece can be strained, at a constant load force and one then measures the crack propagation velocity Vp(t). The trouser test-piece is the most suitable for this so-called crack growth tests since the stretch of the two legs can be directly related to the crack propagation velocity. Things are less straightforward on notched pure shear (PS) geometry or tensile specimens. In this case, the estimate of the propagation velocity requires a direct measurement of the crack length as a function of time. “Static cut growth test” corresponds to the measurement of the crack propagation velocity after a cut is made in a statically strained PS specimen. In so called “fatigue crack growth tests”, the notched test-piece is subjected to a cyclic loading, controlled by deformation or stress, with or without polarization. (i.e. with or without complete unloading).The stabilised propagation rate is then measured per cycle [18] for different loading levels. Such protocols are built to mimic the conditions encountered in numerous applications, where loading levels are relatively low. In these applications, the load frequencies are often signicantly higher than 1 Hz. This can lead to a significant rise in temperature of the material. To avoid it, or at least to limit it, haversine type loading conditions are often used. The term "stabilized" is important: indeed, faster propagation is generally observed during the first cycles, and the crack growth rate decreases more or less rapidly towards a “stabilized” value. This is ascribed to a modification of the crack geometry (initially created from a razor cut), and of the mechanical properties of the material in its vicinity.

Whether static, monotonic or cyclic solicitation are applied, these experiments therefore enable to relate Vp, expressed per time unit (for instance in static crack growth experiment) or per number of cycles (in fatigue crack growth tests) to a strain energy release rate G, defined as the variation of potential energy in the specimen per advanced crack area. Note that G is noted T (for tearing energy) in many articles. The resulting Vp(G) curve is indeed considered to be independent on the geometry [18, 19], at least for those commonly used [20], if certain conditions on the geometries are fulfilled [21]. Using a Pure Shear (PS) geometry, [20, 22, 23] of initial height h_0 submitted to a stretching λ, G associated with the propagation of a crack of length c, is the product of $W(\lambda)$ by h_0, where $W(\lambda)$ is the strain energy density of the unnotched PS test piece submitted to the same stretching. For a tensile strip geometry, the expression becomes $2kW(\lambda)c$, k being a parameter depending smoothly on λ [24, 25]. In the case of an elastic material, $W(\lambda)$ simply is the area under the loading curve of the unnotched test piece, and G is then the stored elastic energy. The estimate is less trivial for viscoelastic material, or when the mechanical behavior irreversibly depends - over the time scale of the cycles and/or of the crack propagation - on the maximum loading (as it is the case in filled elastomers due to the Mullins effect). In fatigue crack growth, depending on the authors, $W(\lambda)$ will then be estimated from the area under the loading, or the unloading curve of the material, over a stabilized cycle, and will thus include, or not, the energy dissipated during the cycle (this having important consequences on the interpretation of the Vp(G) curves) [26].

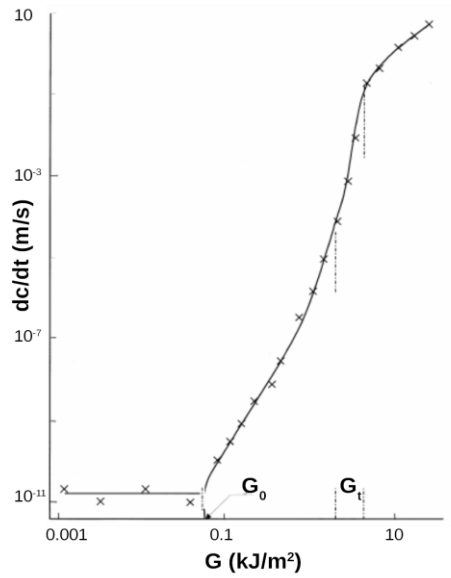

Figure 1 : Crack growth velocity (dc/dt) as a function of the strain energy release rate G for Styrene Butadiene Rubber. G_0 is the threshold energy for mechanical crack growth and G_t indicates the transition region. Figure from reference 30.

There is not a complete consensus in the literature on experimental protocols, whether they are used to assess the properties at break, the tearing resistance or the crack propagation characteristics. However, a generic behavior can be outlined, here introduced in the case of unfilled amorphous elastomers. Their stress and strain at break (ε_b, σ_b), often measured in tensile test, depend on the strain rate ($\dot{\varepsilon}$) and the temperature. A master curves for σ_b (corrected from entropic effects) and for ε_b, can be built, as a function of $1/\dot{\varepsilon}$ [27], using temperature-dependent shift factors from the William-Landels-Ferry law for the α relaxation times. Furthermore, an envelop curve for the couple (σ_b, ε_b) with tests carried out at different speeds and temperatures can be drawn [28]. It highlights the weak rupture properties at high temperature and low velocity, and the existence of optimal temperature and strain rate conditions for the strain energy at break. The latter being related to G via the Greensmith's formula [29], this shows the dependence of the critical strain energy release rate G_c (G value for a catastrophic crack propagation) on temperature and strain rate, or in other words, on the role of the viscoelasticity in the involved processes.

$V_p(G)$ curves (or the reverse, $G(V_p)$ curves) from non-cyclic crack growth tests are found in literature with crack propagation rates which can extend over ten decades (figure 1)[30]. The authors estimate a tearing energy G_t (with a significant error bar), akin to G_c, when Vp reaches several m/s. In the lower or higher velocity domains, the breaking surfaces are respectively rough and smooth, and the velocity is approximatively or completely stable, while stick-slip occur in the transition domain [31, 32]. These different behaviors are related to the material ability to blunt the crack tip by cavitation [33]. This mechanism involving the viscoelastic response of the material, may or may not have the time to occur, depending on the propagation velocity [34]. The width of the transition domain decreases with the increase in the material crosslinking density. Note that the unstable stick-slip process may also result from a non-uniform temperature in the crack vicinity, that interacts with the local viscoelasticity of the material [26]. Below G_t, two different domains can be distinguished : for G above a value named G_0, V_p roughly varies with a power law of G. Below G_0, one observes an extremely low crack propagation rate, independent on G, solely originating from a chemical degradation of the material at the crack tip [35]. $G(V_p,T)$ data obeys the same time-temperature equivalence as dynamic

moduli and makes possible the construction of a master curve over a very large domain. Incidentally, T and V_p being given, G grows with the loss modulus. G_0 has therefore to be estimated when the viscoelastic effects are minimized. The reduction of the dissipation zone can be obtained by pushing an ultra-sharp blade into the open crack. This inspired a new efficient protocol to rapidly evaluate G_0 [36, 37].Values are found between 20 and 100 J / m^2 [38–42]. According to Lake and Thomas [43], they corresponds to the breaking energy of the chains that cross the fracture plane. When a bond breaks, the entire chain between crosslinks relaxes to zero load, making the energy dissipation proportional to the number of Kuhn segments (N) between crosslinks. Recent studies however suggest that chains rupture out of the fracture plane are also involved in the fracture energy [44] (cf. § 3). Despite its simplifying assumption (perfect network without entanglement), the Lake-Thomas model predicts the right order of magnitude for G_0 in unfilled amorphous polymers and the observed dependence of G_0 on $N^{-1/2}$. Our study on γ-irradiated elastomer at different doses suggests that the model also seems to qualitatively work for materials containing a large number of dangling and soluble chains, when these are taken into account in the calculation of N [45].

Regarding fatigue crack growth tests, the curves are generally given as dc/dn (i.e. the crack growth per cycle) versus G [46]. They have a typical shape, similar to those observed for other classes of materials [47] (figure 2). Like in static crack growth, three domains are identified. At G values lower than G_0 (same meaning as in static), crack propagation is again ascribed to chemical degradation processes. Then one observes a transition on a restricted domain of G, where the $V_p(G)$ curve increases, usually according to a linear law. For higher G, dc/dn follows a Paris type law [48], i.e. is equal to $A \cdot G^{\beta}$ where A and β are material parameters. Finally, beyond a certain critical value G_c, the crack propagates in a catastrophic way, causing the sample rupture within few cycles.

As shown by Lake and Lindley [49], in the Paris domain ($dc/dn = A.G^{\beta}$), A decreases rapidly with the frequency increase and then stabilizes for frequencies greater than 10 cycles per minute. At low frequency, crack growth rate evolution can be deduced from the $G(V_p)$ curves obtained in static crack growth tests. For higher ones (above 1 Hz), the evolution of A suggests that this term contains a specific contribution due to the cyclic loading. Thus, the link between static and fatigue crack growth becomes more sophisticated, since the frequency both impacts the time spent at a given G and influences the bulk material viscoelastic response. In addition, the use of a positive non-relaxing loading can lead to a slowdown of the crack propagation (by a factor of up to 18 in experiments carried out at 2 Hz with Styrene Butadiene Rubber). To explain it, Lindley [19] assumed that the dynamic component of dc/dn depends on $(G_{max} - G_{min})^{\beta}$, with β the exponent of the Paris law obtained in non-relaxing conditions. Note that at low frequency, as the static contribution of dc/dn is then preponderant, the increase in G_{min} should lead to a larger dc/dn. The influence of the temperature is more intuitive and similar to that observed in static (A increases with the temperature). Thus, as also deduced from tensile strength measurement, G_c decreases with increasing temperature. Note that the quantification of the temperature influence must be carried out so as to ensure that material ageing is avoided (precaution not always described in publications).

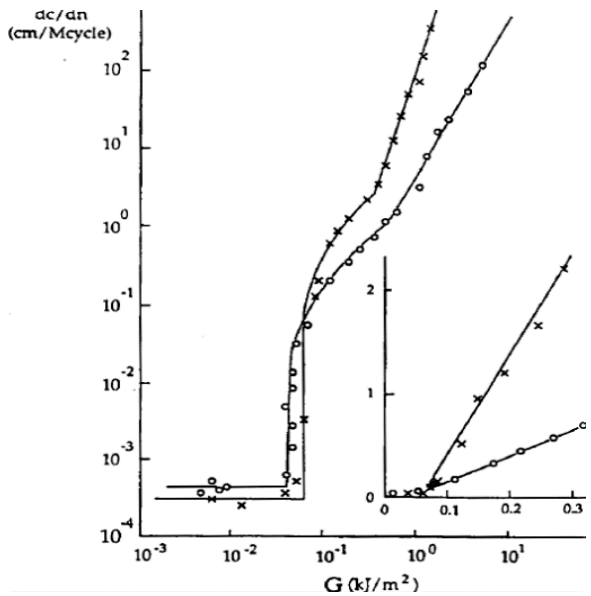

Figure 2: Crack propagation rate as a function of the maximum energy release rate G in fatigue crack growth test for unfilled Styrene Butadiene Rubber (x) and Natural Rubber (o). From reference 6.

3 MATERIAL PARAMETERS

3.1 The polymer and its crosslinking

The strong influence of viscoelasticity in crack propagation can be retrieved in the often used expression of G as the product of G_0 and a function f (V_p, T) (cf. §4). At a macroscopic scale, the viscoelasticity impacts the evolution of the crack tip geometry during the crack advance and therefore the maximum stresses distribution in its vicinity, which causes its further propagation [36]. At the crack tip locus, for the crack to grow, the subchains immediately ahead have to be stretched enough to reach the breaking strain. Since there is internal viscosity, a force higher than that corresponding to the threshold tearing energy must be supplied. The difference between the strain energy density in the bulk and small energy density used for growth of the crack is actually used to overcome the viscosity of the rubber. Viscoelasticity also controls the appearance of other dissipative mechanisms, such as cavitation, fibrillation which may or may not appear in the crack tip and perturb its propagation. Moreover, the chain network density controls G_0 [43] and the deformation level at which strain hardening appears, which seems to decrease the radius of the crack tip and increase a stress triaxiality that promotes cavitation [50].

Thus, from a material design point of view, the key parameters for crack propagation resistance are: crosslinking density, entanglement density, presence of dangling and/or soluble chains, and the glass transition temperature of the polymer. The latter depends on the chemical nature of the polymer chains which also controls the entanglement density (via the chain persistence length), and the energy at break of their bonds. The initial length distribution of the polymer chains controls the presence of chain ends or soluble fraction at a given crosslinking level. The ingredients, the different crosslinking recipes (sulfur, peroxide, disulphide tetramethylthiuram…) and protocols (thermal curing, radiation…) can also be important. Thus, for a same crosslinking density, some authors claim that "conventional" vulcanization system with sulfur (sulfur / accelerator ratio > 1) leads to better breaking properties and tearing energy (with the Rivlin protocol) than efficient vulcanization system [40]. Interpretations differ on the reasons: more or less spatially homogeneous networks [51], crosslinks formed in a more or less irreversible manner, which may result in more or less built-in/ stresses or strains [52]. Playing with the chemistry of the polymer chains, one can also create physical crosslinks. Their associ-

ation/dissociation dynamics should enable a redistribution of the stresses in the elastomer network and therefore slow down the crack propagation. Studies are nevertheless necessary to confirm this. Chemical aging has also large consequences on crack resistance, since it induces, through complex chemical processes, additional crosslinks and/or chain scissions [53–56] . The characterization of molar masses between crosslinks remains however a challenge, even if it has recently benefited from advances in Nuclear Magnetic Resonance [57]. Aging can also be spatially heterogeneous, especially in sulfur vulcanized systems. Characterizing these heterogeneities is also difficult, although they influence the mechanical properties. To sum up, aging and curing conditions can lead to network structures very far from the perfect networks described in most models. This explains apparently contradictory results in the literature [45, 58].

In many cases, the network topology in elastomers results from more or less random crosslinking and/or chain scissions. Nervetheless, better control of this topology is possible.[59] Thus, toughness have been improved with elastomers made of telechelic chains with bimodal length distribution. This improvement comes from a stress redistribution due to the lower extensibility of short chains. The requirements to achieve exceptional toughness seem to be that the components have very different cross-link densities and the morphology is uniform down to the segmental level. With this idea, Buckley et al [60] produced ethylene-propylene double networks with improved rupture properties (at constant modulus). The beneficial effect of multiple networks has also been evidenced in hydrogels [10] and in acrylate elastomers [61] (cf. § 3.4).

3.2 Specificity of polymers which can crystallize with strain

The ability of the polymer for strain induced crystallization (SIC) appears to be another important parameter for crack growth resistance. All elastomers that crystallize with temperature can - under certain strain rate and temperature conditions (near their melting temperature) - crystallize under deformation [62]. Among them, poly-cis isoprene 1,4 (NR) has two advantages: a melting temperature (35°C) very close to ambient, and a reversible crystallinity which can reach several tens of %. NR crystallization kinetics [63] is slow, especially at ambient temperature. This explains, with the presence of crosslinking nodes that restrict chain diffusion, that in most cases, NR remains amorphous despite a melting temperature higher than the ambient. When the material is deformed, the chains stretching reduces the system entropy and makes crystallization thermodynamically more favorable. Crystallites can therefore nucleate and grow, for stretch ratio usually above 4, until they reach a size limited by the presence of the crosslinking nodes. This size is small enough for the crystallites to be unstable and melt during unloading, even at room temperature. The NR SIC (and its various parameters) has been the subject of special attention in recent years [64–74] both from an experimental and theoretical point of view. SIC leads to a significant strain hardening, explained by the creation of a network of percolating crystallites within the material (even if questions remain on this topic). It is preceded, at the very beginning of the crystallization phase, by a slight decrease in stress due to the alignment of the crystallized chains portions in the stretching direction (as this decreases the ‘effective’ stretching of amorphous chains) [75], mostly visible at slow stretching rate.

As shown by the comparison of NR and Styrene Butadiene Rubber (SBR) data [32, 76–78], SIC is the reason for a very strong increase in strain and stress at break and a slower crack propagation velocity, in static as well as in cyclic test [79]. Unlike an amorphous polymer, in a NR Pure Shear specimen submitted to a static loading, after a short growth, the crack stops. In cyclic loading, in the Paris domain, the literature studies suggest an exponent close to 4, for an amorphous elastomer like SBR while it may be around 2 for NR. Note that these exponents can significantly vary, depending on the experimental conditions. In addition, the application of a non-relaxing loading ($G_{min} > 0$) leads to a more important slowing down of the crack propaga-

tion than with an amorphous elastomer [25]. Non-relaxing conditions also leads to crack deviations [80] (absent with unfilled amorphous elastomer). That makes less trivial the monitoring of the crack length, which may or may not include secondary cracks. All these behaviors are related to SIC which occurs at the crack tip, even at low macroscopic strain, due to the important stress concentration created by the tip geometry. Several studies investigated cristallinity at the crack tip in NR [81, 82]. In particular, Rublon et al. [14, 78] have implemented a clever method in order to map it during a dynamic test at 0.1 Hz. Directly compared to crack propagation tests performed at 2 Hz for different energy release rates G, they showed a good correlation between G, the crystallized volume, and the thickness decrease at the crack tip, which also suggests that cavitation occurs.

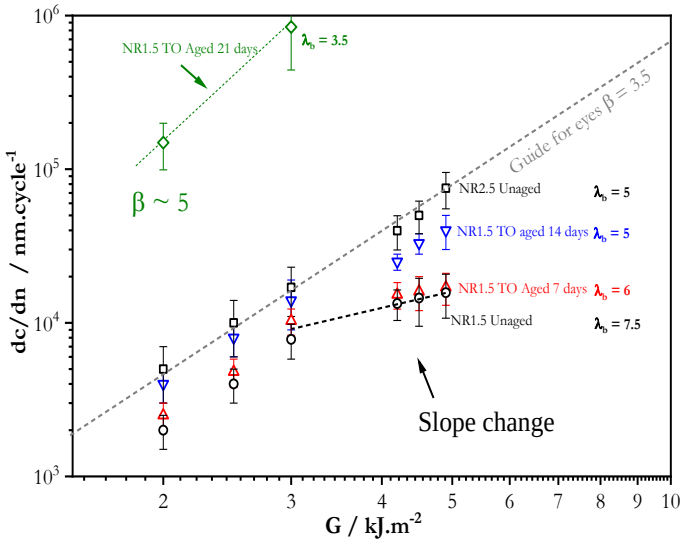

Figure 3: Crack propagation rate as a function of the strain energy release rate G, in fatigue tests, on pure shear sample at 0.01 Hz, for aged and unaged unfilled NR. Tensile stretch at break λ_b measured in tensile test at 4.2 x10^{-3} s^{-1} is also reported. Data from references 83 and 85.

We have studied a conventionally vulcanized NR (noted NR1.5 on figure 3, with the recipe: 100 phr NR + 3Phr Sulfur + 6phrPPD + 2phr stearic acid + 3 phr CBS + 5phr ZnO). This material has a lower ability to crystallize than an efficiently vulcanized rubber (CBS/Sulfur concentration ratio<1), both during cold crystallization (at -25°C) and during a tensile test experiment, the crystallinity being lowered by a factor of ca. 3. This may be due to a different distribution of the active chain length, and/or the presence of more grafted species on the chains which hinder their crystallization. The fatigue crack growth resistance of the material has been tested in pure shear geometry[83]. As shown in figure 3, in the Paris domain, at low G, the slope of the log(G)-log(V_p) curve at 0,01 Hz and at few Hz (not shown), is surprisingly large, around 3.5, i.e. close to the slope reported for amorphous materials. A new slope can however be deduced for G values above 3500 J/m^2, which tends to be closer to the value expected for NR (around 2). The crystallization at the crack tip, measured through in-situ experiments (ZnS has been used as a probe to correctly estimate the material thickness at the crack tip) is reported on figure 4 as a function of G. The slope change in the log(G)-log(V_p) curve corresponds to the detection of the crystallinity. Interestingly, the maximal measured crystallinity is twice larger than the maximal one measured during tensile test at rupture. As reported in literature [84, 85] and as shown by the SAXS images collected during the WAXS measurements [85], cavities develop in the crack tip vicinity. Thus, some amorphous chains are broken and highly stretched fibrils with large crystallinity remain. A careful examination of the crack tip morphology and of the fracture surface may be of interest to confirm this. For unknown reasons, to the best of our knowledge, such studies only exist for fatigued *filled* NR or for unfilled one in non relaxing

condition[80, 86]. Even though fillers likely introduce some differences in crack propagation mechanisms, Xiang et al. conclusion can still be considered. In particular, they resume an interesting parallel, initially proposed by Zhou et al. [87], between the mechanisms induced by SIC and those occurring with double networks. At the front of the crack tip, *s*oft domains which might contain cavities, micro-cracks and amorphous or less crystallized rubber parts alternate with hard domains of highly orientated and more crystallized ligaments. The soft domains may act like a damper to absorb energy and thus slow down the crack propagation.

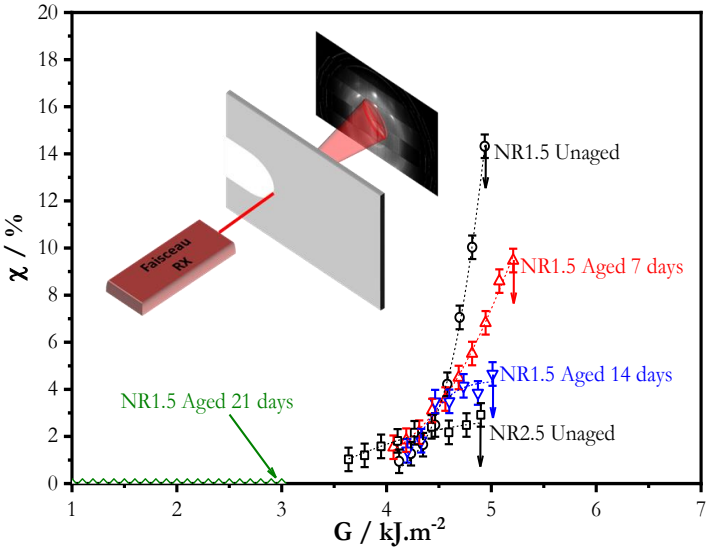

Figure 4: Crystal volume fraction measure by SAXS in situ at the crack tip as a function of the strain energy released rate for aged and unaged NR. Measurements were performed on pure shear specimen at $1.7*10^{-3}$ s^{-1}. Experimental details in references 83 and 85

The close relationship between SIC and crack propagation resistance has also been confirmed with aged NR1.5 samples whose characteristics have been deeply studied by Grasland [88]: ageing in air at 350K enhances the heterogeneity of the spatial distribution of the crosslinks already existing in the initial material, and creates highly crosslinked domains which limits the ability for strain induce crystallization. The consequence is an increase in the crack propagation rate (figure 3) which is consistent with a decrease in the crystallinity measured at the crack tip (figure 4). Moreover, the results suggest that a minimum crystallised volume is needed to observe an inflexion on the log(G)-log(V_p) curve. This is confirmed by the study of another conventionally vulcanized elastomer, so called NR2.5 (same recipe as NR1.5 except a doubled sulfur content). This material is more crosslinked, and therefore less crystallized than NR1.5 (figure 4). Its crystallization at the crack tip is too low, in the G domain explored, to lead to any slope change in the log(G)-log(V_p) curve. Moreover, for all these tested materials, the crack propagation resistance at 0,01Hz is correlated to the energy and stretch at break, obtained from tensile test at strain rate corresponding to the maximum strain rate in the fatigue test (values reported on figure 3). This is quite expected if one considers that ageing did not change the intrinsic flaw at the origin of the material rupture in tensile test, and therefore that its evolution is mostly related to a change in its crack growth resistance [89].

SIC being a kinetic process [90], in “static” experiments, the crack growth velocity in the domain where it is very large (above 0.1 m/s) does not depend on it [30], as SIC does not have the time to proceed. Moreover, concerning fatigue crack growth, we have found with the previous NR1.5 material that an increase in frequency by around 3 decades leads to a decrease in dc/dn by a factor 10 (figure 5). However, expressed in dc/dt instead of dc/dn, these data indicates a much faster crack growth which can be ascribed to a less important SIC. This is also suggested by the increase in the G value at which a change in the slope of the log(G)-log(V_p)

curve is observed (this one being ascribed to a strong increase in crystallinity at the crack tip). In addition, with the NR2.5 material, one observes the decrease in the G value above which there is a fast acceleration of the crack growth rate. In other words, a higher frequency leads to a decrease in the tearing energy of this material, for which strain induced crystallization is so weak that it actually behaves like an amorphous material.

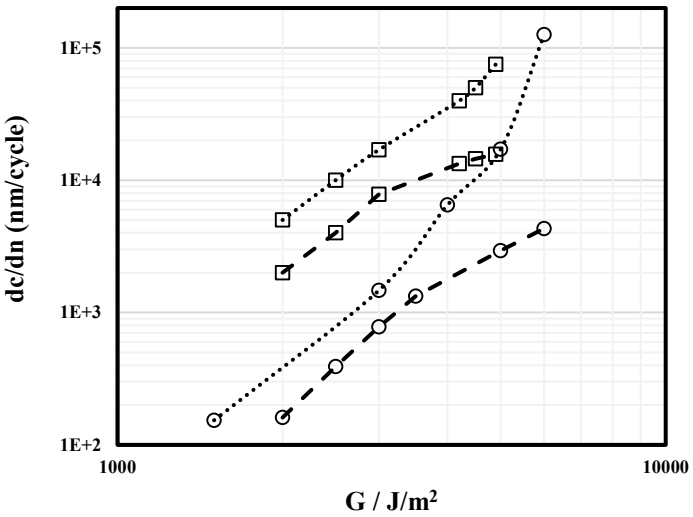

Figure 5 : Influence of the cycle frequency on the crack propagation rate as a function of the strain energy release rate for two unfilled NR (same material as in figure 4), unaged NR1.5 (○) and unaged NR2.5 (□), at rate 0.01 Hz (dotted line) and around 5Hz (----). Data from reference 91

Going back to literature, an increase in temperature has the same consequences on SIC than an increase in frequency. Thus, both can lead to an even greater increase in the crack growth rate than in the case of amorphous elastomers, as they do more than reducing the material viscosity. However, this is dependent on the level of local deformation in the crack vicinity (i.e. on G) and, in fatigue, on the local strain rate that will result from the frequency/shape of the macroscopic cycle.

3.3 Fillers influence

In most applications, elastomers contain reinforcing fillers. They can be of very diverse natures, the most commonly used in the rubber industry being carbon black or silica nanoparticles. Thus, elastomers are most often nano-composites, with specific viscoelastic properties [91, 92]. An abundant literature has been devoted to their nonlinear viscoelastic properties, so called Payne effect [93]. In addition, they exhibit the so-called Mullins effect, i.e. a progressive modification of the strain-stress curve and an hysteresis during the first loading cycle which increases with the increase in the maximum strain [94]. Both Payne and Mullins effects are very dependent on the filler content and characteristics (size, aspect ratio, physico-chemical interactions with the polymer). They considerably influence the rupture and crack resistance properties of these materials since they induce additional energy dissipation mechanisms.

Thus, the introduction of rigid nanoparticles is particularly efficient for increasing the tensile strength. Less intuitively, even though they lead to a significant amplification of local deformation in the matrix, nanofillers can also improve the elongation at break (when their content is not too large, i.e. usually below 50 phr). This is all the more remarkable given that nanofillers can form agglomerates of large sizes acting as crack initiators. Their beneficial effect is also observed in static and fatigue crack growth on various elastomers whether these ones can or cannot crystallize under deformation [3]. The fillers, by amplifying the local strain, enables SIC and therefore a larger crystallized volume at lower macroscopic strain [95]. Nanofillers may

also induce larger crystallized volume at a given G, beneficial to fatigue properties [81] (although G indirectly takes into account strain amplification). A combination of SIC and of reinforcement by nanometric fillers can also lead to tear rotation in tearing test on notched tensile specimen or trouser test-piece [96], not observed without fillers. This enables the relaxation of the local strain (or stress) which is otherwise larger at the crack tip, as shown by a sharper crack tip geometry. Thus, for Medalia [97], tear strength improvement in reinforced elastomer is even mostly associated to tear deviation rather than to energy dissipation (i.e. viscous strengthening or high strain hysteresis). In fatigue tests, more complex crack paths are also observed with fillers, which can lead, in non-relaxing conditions and with crystallizing rubber, to a complete stop of the crack propagation in the direction of the initial cut. Fillers form in the matrix a percolating network (whose connections are potentially ensured by a polymer matrix with modified mobility) which can play the role of a second network. Through decohesion mechanisms and voids formation [95, 98, 99] in the confined material in between the fillers, this network is gradually destroyed. This leads to the creation of a complex fibrillated structure [100] in which the crosslinked network of the polymer matrix is the last defense against the crack advance [101].

Several filler characteristics (shape, dispersion, polymer/filler interactions) influence the crack growth resistance in a way which depends a lot on the material processing. Bad dispersion may induce stress concentrations and microcracks [102], harmful to rupture properties and crack resistance. The literature indicates a positive influence of larger filler specific surface (i.e. smaller filler size) [79, 103–105] and of higher form factors (like in carbon nanotubes, graphene, graphene oxide or nanoclays) on the resistance to crack initiation and propagation [106, 107]. Combination of nanofillers can also be used to obtain synergistic effect [108], like in the work of Xu et al. [102], who designed a compact hybrid filler network of graphene and Multi-Wall NanoTubes to toughen NR.

To conclude this paragraph, different mechanisms govern the fracture properties and the propagation of cracks in filled elastomers, and modeling approaches will therefore be essential to allow the evaluation of their respective contributions [5]. The next paragraph aims at devising a theoretical framework explaining crack growth and underlining the connection between resistance to crack growth and the ability of a material to dissipate energy. Such theoretical approach can then suggest which bulk material properties should be correlated to crack growth resistance.

4 THEORIES CONNECTING RESISTANCE TO CRACK GROWTH WITH HYSTERESIS

The models that we are reviewed in this paragraph are all built (sometimes implicitly) on the energy budget associated with a propagating crack, and were all devised for static crack growth. To our knowledge, their generalization to cyclic crack growth, which seems possible due to the universality of the energy conservation principle, has not been attempted yet. The theories dedicated to isotropic linear viscoelastic materials are associated with the names of Knauss [38, 109, 110], Christensen [111, 112], De Gennes [113, 114], Hui [115], Persson [116, 117] and their coworkers. More recently, they have been extended outside this range of materials by Long [118], Qi [119] and Zhang [120]. All these theories start from the decomposition $\mathbf{G = \Gamma_{intrinsic} + \Gamma_{dissipation}}$ with $\mathbf{\Gamma_{intrinsic}}$ the intrinsic energy required to break molecules at the crack tip (noted G_0 in most of the experimental works, $\Gamma_{intrinsic}$ being tacitly assumed constant) and $\mathbf{\Gamma_{dissipation}}$ the portion of G being consumed by the motion of the material surrounding the crack tip as the latter moves ahead ($\mathbf{\Gamma_{dissipation}}$ is a peculiarity of dissipative materials). These theories aim (sometimes implicitly, as in Knauss and Hui theories) at explaining quantitatively how $\mathbf{\Gamma_{dissipation}}$ can be deduced from the material hysteresis and the loading applied to the specimens.

4.1 Power budget approach

The key idea is the recognition that as a crack propagates, the stress singularity accompanying the crack tip [121] translates accordingly, so that any material point in the specimen is successively loaded and unloaded, and the hysteresis associated to this cycle participates to $\Gamma_{dissipation}$. The figure 6, taken from Qi [119] (see also Long [118]) draws explicitly the hysteresis associated with each horizontal "flow line": the closer this line gets to the crack plane, the greater the maximal loading, and therefore the greater the hysteresis.Indeed, by writing in details the energy and entropy budgets of the notched specimen[119], one gets explicitly (Einstein convention of implicit summation over repeated indices being employed)

$$G = \Gamma_{intrinsic} + 2\int_0^{H_0}\int_{-\infty}^{+\infty} \varphi_p \, dX \, dY$$

$$\text{where} \quad \varphi_p \equiv \sigma_{ij}\frac{\partial \varepsilon_{ij}}{\partial X_p} - \frac{\partial W}{\partial X_p} = \frac{\partial W}{\partial X} - \sigma_{ij}\frac{\partial \varepsilon_{ij}}{\partial X} \quad (1).$$

Here $2H_0$ is the specimen height (typically a PS specimen), X_p is the crack tip abscissa (so that $V_p = dX_p/dt$), φ_p is the dissipation associated to the crack tip motion divided by V_p, and finally $\partial/\partial X_p = -\partial/\partial X$ since we focus on the stationary regime.

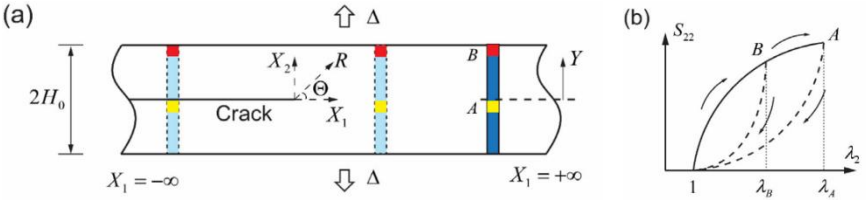

Figure 6 : (a) Two points A and B moving horizontally during steady state crack propagation, shown in the undeformed configuration and in a translating coordinate system centered on the crack tip. (b) Loading histories experienced by points A and B, illustrated by S_{22} versus λ_2 curves. The maximum stress experienced by A is larger due to stress concentration at the crack tip.

Equation (1) can be further simplified by noting that the integral of φ_p over X is the total amount of energy by unit volume dissipated into heat during the matter motion from right to left, that is the mechanical hysteresis associated with this loading-unloading cycle, simply noted "hysteresis". Thus

$$\boxed{G = \Gamma_{intrinsic} + 2\int_0^{H_0} \text{hysteresis}(Y)dY} \quad (2).$$

It is worth underlining the **connection between this approach and the so-called configurational mechanics**[122]. Introducing the Eshelby stress tensor $\Sigma_{ij} = W\,\delta_{ij} - \sigma_{kj}\,\partial u_k/\partial X_i$, then making use of the mechanical equilibrium $\partial\sigma_{kj}/\partial X_j = 0$ and of the stress tensor symmetry, one gets

$$\frac{\partial \Sigma_{1j}}{\partial X_j} = \frac{\partial W}{\partial X_1} - \underbrace{\frac{\partial \sigma_{kj}}{\partial X_j}}_{=0}\frac{\partial u_k}{\partial X_1} - \sigma_{kj}\frac{\partial^2 u_k}{\partial X_j \partial X_1} = \frac{\partial W}{\partial X_1} - \sigma_{kj}\frac{\partial}{\partial X_1}\frac{1}{2}\left(\frac{\partial u_k}{\partial X_j} + \frac{\partial u_j}{\partial X_k}\right)$$

$$\text{that is} \quad \frac{\partial \Sigma_{1j}}{\partial X_j} = \frac{\partial W}{\partial X} - \sigma_{kj}\frac{\partial \varepsilon_{kj}}{\partial X} = \varphi_p \quad (3).$$

In the literature, the contributions to $\partial\Sigma_{1j}/\partial X_j$ of the various internal variables appearing in W are called "local material volume forces", up to a sign. Hence, it is demonstrated that $\Gamma_{dissipation}$ equals the integral on the whole specimen of these material forces (see also in [5] Horst et al. contribution [123]). That is, the material forces approach is equivalent to the energy and entropy budgets employed here.

4.2 Application to isotropic linear viscoelastic materials

Christensen, De Gennes, Persson and their collaborators applied these budgets to **isotropic linear viscoelastic materials**. In the sequel we will follow mostly De Gennes intuitive approach.

The material isotropy and linearity imply that the stress field satisfies the same equations as in the elastic case. Especially, the dominant term in the stress next to the crack tip is given by the well-known formula plotted above. Hence, if K is the stress-intensity factor, the amplitude of loading-unloading cycle at vertical coordinate Y (perpendicularly to crack axis) goes like **K / √|Y|** and its wave length goes like |Y|, so its **pulsation ω goes like V_p / |Y|**.

Far from the crack tip, the material remains at equilibrium, i.e. it behaves like an elastic material of Young modulus E_0. So LEFM theorems apply there. Especially, computing the Rice- or $\mathcal{J}$-integral [121] away from the crack tip gives $G = \mathcal{J} \propto K^2 / E_0$ (this integral must not be confused with compliance J introduced below).

Next, assume the cycle to be harmonic. If $E^*(\omega) = E'(\omega) + i\, E''(\omega)$ is the complex Young modulus and $J^*(\omega) = 1 / E^*(\omega)$ is the complex compliance, the hysteresis at vertical coordinate Y reads

$$\text{hysteresis}(Y) \propto \frac{K^2}{|Y|}|J''(\omega)| = \frac{GE_0}{|Y|}|J''(\omega)| = \frac{GE_0}{|Y|}\frac{E''(\omega)}{|E^*(\omega)|^2} \quad \text{with} \quad \omega \propto \frac{V_p}{|Y|} \quad (4).$$

Inserting this relation into equation (2), and noticing that $dY/Y = d\omega/\omega$, one finally gets

$$G = \Gamma_{\text{intrinsic}} + A \cdot GE_0 \int_0^{\omega_c} \frac{E''(\omega)}{|E^*(\omega)|^2}\frac{d\omega}{\omega} \quad \text{with} \quad \omega_c = B \cdot \frac{\sigma_{\text{rupture}}^2 V_p}{GE_0} \quad (5),$$

A and B being some undetermined numerical constants. The boundaries of the ω-integral require some explanations. Far from the crack tip, we assumed the material to remain at equilibrium, prompting us to take $\omega_{min} = 0$. Close to the integral, the LEFM fields cannot hold when reaching the zone ahead of the crack tip where the material effectively breaks, the so-called cohesive zone, that is when $|Y| = Y_{rupture}$ such that $\sigma_{rupture}^2 \propto K^2 / Y_{rupture}$, and we must therefore take $\omega_{max} \propto V_p / Y_{rupture}$. Persson set the A coefficient by combining the **expected value of the catastrophic tearing energy Γ_c** (G limit for infinite V_p, neglecting inertial effects, also noted G_c in experimental work) guessed by De Gennes with a **"viscoelastic sum rule"** : some examples of such rules are provided by equations (8) and (10) below.

On the one hand, when V_p grows without limit, the material close to the crack tip should reach its high frequency limit, which is the glassy plateau for the polymers. Thus, it should behave there as an elastic (brittle) material of Young modulus E_∞. Hence computing the $\mathcal{J}$-integral close to the crack tip gives now $\Gamma_{intrinsic} = \mathcal{J} \propto K^2 / E_\infty$, with the same K since the dominant term in the stress field has a unique expression. Combining this relation for K with the preceding one, applicable in full generality, one gets

$$G \to \boxed{\Gamma_c = \Gamma_{\text{intrinsic}} \frac{E_\infty}{E_0}} \quad \text{when} \quad V_p \to +\infty \quad (6).$$

The constant A appearing in (5) must be chosen so that (5) reduces to (6) for "infinite" crack growth rate.

On the other hand, if the material can be represented by a set of Kelvin solids (a spring in parallel to a damper) in series, the complex compliance reads

$$J^*(\omega) = \frac{1}{E_\infty} + \int_0^{+\infty} \frac{k(\tau)}{1 + i\omega\tau} d\tau = \frac{1}{E_\infty} + \int_0^{+\infty} \frac{(1 - i\omega\tau)}{1 + (\omega\tau)^2} k(\tau) d\tau \quad (7).$$

$k(\tau)\, d\tau$ is the equilibrium stiffness of the Kelvin solid of time constant τ.

Some elementary manipulations of this decomposition provide

$$\frac{1}{E_0} = J^*(\omega = 0) = \frac{1}{E_\infty} + \int_0^{+\infty} k(\tau)d\tau$$

$$\text{and thus} \quad \int_0^{+\infty} |J''(\omega)| \frac{d\omega}{\omega} = \frac{\pi}{2}\int_0^{+\infty} k(\tau)d\tau = \frac{\pi}{2}\left(\frac{1}{E_0} - \frac{1}{E_\infty}\right) \quad (8).$$

This latter equation is the sum rule we needed. Indeed, making $\omega_c = +\infty$ in (5) and reporting the sum rule into it, (6) will be recovered provided we choose $A = 2/\pi$. Hence the final formula

$$\boxed{G = \Gamma_{intrinsic} + \frac{2}{\pi} G E_0 \int_0^{\omega_c} \frac{E''(\omega)}{|E^*(\omega)|^2} \frac{d\omega}{\omega}} \quad \text{with} \quad \boxed{\omega_c = B \frac{\sigma_{rupture}^2 V_p}{G E_0}} \quad (9).$$

ω_c can be rewritten $\omega_c = 2B\, W_{rupture}\, V_p / G$ where by introducing an "equilibrium" energy of rupture $W_{rupture} \equiv \frac{1}{2}\, \sigma_{rupture}^2 / E_0$ (the "equilibrium" adjective underlines the presence of E_0 in this expression). However, keep in mind that this $W_{rupture}$ can, like $\sigma_{rupture}$, vary with the local temperature and strain rates at the crack tip.

The more sophisticated computations in Persson[116, 117] produced an extra $\sqrt{1 - \frac{\omega^2}{\omega_c^2}}$ factor inside the integral, with little impact on the final theoretical predictions.

4.3 Paris Law

As noted by De Gennes for a specific rheological model (a so-called Zener solid) [113, 114], and later by Persson in greater generality [116, 117], **this theory predicts the occurrence of a Paris law**, in agreement with experiments. (Strictly speaking, the Paris law originates from cyclic crack growth experiments; here, we use this terminology as a shorthand for "V_p proportional to some power of G"; as seen in the preceding chapters, such law can also be encountered experimentally in static crack growth.) This is best seen by making use of an approximate sum rule :

$$J'(\omega_2) - J'(\omega_1) = \int_0^{+\infty} \left(\frac{1}{1 + (\omega_2\tau)^2} - \frac{1}{1 + (\omega_1\tau)^2}\right) k(\tau)d\tau \approx \int_{1/\omega_1}^{1/\omega_2} k(\tau)d\tau$$

$$\frac{2}{\pi}\int_{\omega_1}^{\omega_2} |J''(\omega)| \frac{d\omega}{\omega} = \frac{2}{\pi}\int_0^{+\infty} [\tan^{-1}(\omega_2\tau) - \tan^{-1}(\omega_1\tau)] k(\tau)d\tau \approx \int_{1/\omega_2}^{1/\omega_1} k(\tau)d\tau$$

$$\Longrightarrow \quad \frac{2}{\pi}\int_{\omega_1}^{\omega_2} |J''(\omega)| \frac{d\omega}{\omega} \approx J'(\omega_1) - J'(\omega_2) \approx \frac{1}{E'(\omega_1)} - \frac{1}{E'(\omega_2)} \quad (10).$$

The first line was obtained by assuming $1 / (1 + x^2) \approx \mathcal{H}(1 - x)$ for $x \geq 0$ where $\mathcal{H}$ is the Heaviside step function. The second line used a similar trick, namely $(2/\pi) \tan^{-1}(x) \approx \mathcal{H}(x - 1)$ for $x \geq 0$. The last approximation on the third line is more questionable. Reporting (10) into (9), one finally gets

$$\boxed{\frac{G}{\Gamma_{intrinsic}} \approx \frac{E'(\omega_c)}{E_0}}$$

$$\text{and thus} \quad \boxed{E'(\omega) \approx E_1 \left(\frac{\omega}{\omega_1}\right)^{\alpha} \Longrightarrow V_p \approx \frac{\omega_1 G}{2B W_{rupture}} \left(\frac{E_0}{E_1} \frac{G}{\Gamma_{intrinsic}}\right)^{1/\alpha}} \quad (11).$$

Hence **the Paris exponent β equals $\beta = 1 + 1/\alpha$**. For $\alpha = 0.5$ (typical of Rouse dynamics), $\beta = 3$; and for $\alpha = 0.4$, $\beta = 3.5$: as noted by Persson, these values are typical of SBR in both static and cyclic crack growth. Note also that this approximation yields the same Γ_c expression as the equation from which it is derived. **Gent**[124, 125] **proposed on purely phenomenological grounds an equation similar to (11) to fit the results of his peeling experiments** : we thus provide here a justification of his intuition. However, Gent used $\omega_c = V_p / d$ with d some material

constant, which should be contrasted with our d proportional to G. Actually, (11) brings theory closer to experiments as will be shown below !

4.4 Dissipation confinement and finite size effects

The theories developed by Knauss [38, 109, 110] and Hui [115] do not use explicitly the energy and entropy budgets. Rather, they carefully write the mechanical equilibrium of the cohesive zone, using exact results in LEFM (Kolosov-Mushkelishvili formulae and Westergaard functions applied to localized forces along crack lips). In this respect, they provide a more rigorous treatment of the problem. Yet, they yield essentially the same results: same shape for $V_p(G)$ curves, same expression for G_c (apart for one of the four theories studied in Knauss [109, 110]), etc. This is presumably so because energy and entropy conservation remains necessarily in the background.

For instance, Hui and his coworkers demonstrate graphically [115] that **the dissipation is confined to the corona $0.05\ V_p\ \tau_r <$ radius $< 3.5\ V_p\ \tau_r$** where τ_r is the retardation time occurring in the creep compliance (the authors employ a Zener model) and the radius is counted from the crack tip : this region has a negligible area at low V_p and grows in size with V_p, until becoming eventually macroscopic. This explains qualitatively the trend of our $\Gamma_{dissipation}$ (recall that the r dr dθ surface element compensates the decrease of energy like 1/r). This discussion makes also clear that **the size of the specimen will impact the crack growth curves when $V_p\ \tau_r$ becomes comparable to it**. Indeed, so far we have ignored finite size effects, the discussion focusing on "infinite specimens". But finite size effects can be encountered experimentally, in which case the experimental results are not characteristics of the material alone. They are treated in De Gennes [113, 114], who was chiefly interested in peeling tests [126]. We will review quickly this treatment, using however a slightly more general constitutive law (see e.g. [127]§ 5.5 pp. 188-226) :

$$E^*(\omega) = E_0 + (E_\infty - E_0)\frac{(i\omega\tau)^\alpha}{1+(i\omega\tau)^\alpha} \quad (12).$$

In the original articles, $\alpha = 1$, but we expect $\alpha < 1$ for a glass transition. This model has three remarkable limits : soft solid at low frequencies, hard solid at high frequencies, liquid-like behavior in between. From now on, **$m \equiv E_\infty / E_0 >> 1$** and we reason exclusively in **scaling** terms, so that **"=" will often stand for "∝"**. The computation of the $G(V_p)$ relation is based on the following principles.

Approximation	Soft solid	Liquid	Hard solid
Constitutive law	$\sigma = E_0\ \varepsilon$	$\sigma = (E_\infty - E_0)\ (\omega\tau)^\alpha\ \varepsilon$	$\sigma = E_\infty\ \varepsilon$
Pulsation interval	$\omega\tau < m^{-1/\alpha}$	$m^{-1/\alpha} < \omega\tau < 1$	$1 < \omega\tau$
Spatial domain	$r_s \equiv m^{1/\alpha}\ V_p\ \tau < r$	$V_p\ \tau < r < m^{1/\alpha}\ V_p\ \tau$	$r < V_p\ \tau \equiv r_h$
Stress	$\sigma = \frac{K}{\sqrt{r}}$	$\sigma = \frac{K}{\sqrt{r}}$	$\sigma = \frac{K}{\sqrt{r}}$
Displacement	$u = \frac{K\sqrt{r}}{E_0}$	$u = \frac{K\sqrt{r}}{E_\infty}\left(\frac{r}{V_p\tau}\right)^\alpha$	$u = \frac{K\sqrt{r}}{E_\infty}$
G_{local}	$G_{local} = \frac{K^2}{E_0}$	$G_{local} = \frac{K^2}{E_\infty}\left(\frac{r}{V_p\tau}\right)^\alpha$	$G_{local} = \frac{K^2}{E_\infty}$
L defining condition	$\frac{\sigma_p}{\delta} = \frac{E_0}{L}$	$\frac{\sigma_p}{\delta} = \frac{E_\infty}{L}\left(\frac{V_p\tau}{L}\right)^\alpha$	$\frac{\sigma_p}{\delta} = \frac{E_\infty}{L}$
Cohesive length	$L = \frac{E_0\delta}{\sigma_p} \equiv L_0$	$L = L_\infty^{\frac{1}{\alpha+1}}(V_p\tau)^{\frac{\alpha}{\alpha+1}}$	$L = \frac{E_\infty\delta}{\sigma_p} = mL_0 \equiv L_\infty$
V_p range	$V_p\ \tau < m^{-1/\alpha}\ L_0$	$m^{-1/\alpha}\ L_0 < V_p\ \tau < m\ L_0$	$m\ L_0 < V_p\ \tau$

Step 1. We have $\omega = \frac{V_p}{r}$, $\sigma = \frac{K}{\sqrt{r}}$ and $\varepsilon = \frac{u}{r}$ everywhere in the specimen. Thus, for each asymptotic constitutive law, we can compute its spatial domain of existence, as well as the expressions of ε, u and $G_{local} \equiv \sigma\ u$ (the "local energy release rate") in the domain. Proceeding this way, we

fill the first six lines of the table 1.

Step 2. Let L be the length of the cohesive zone. It is set by the condition $\sigma_p / \delta = \sigma(r = L) / u(r = L)$ where σ_p and δ are material constants such that $\Gamma_{intrinsic} = \sigma_p \delta$. Its detailed expression will therefore depend on the domain (defined as in step 1) surrounding the cohesive zone. Doing so, we obtain the next two lines of the table.

Step 3. The three expressions of L obtained in step 2 are a priori different, implying that L varies with the load applied to the specimen. One deduces from these expressions the range of crack growth rate for which each domain is immediately surrounding the cohesive zone. This leads to the last line of the table.

Step 4. Let W be the specimen size, typically a PS specimen height. The $G(V_p)$ relation is found by taking $\mathbf{\Gamma_{intrinsic} = G_{local}(r = L)}$ and $\mathbf{G = G_{local}(r = W)}$. Various situations can be encountered depending on how W compares with the spatial limits L, r_h (hard solid outer radius) and r_s (soft solid inner radius).

For an infinite specimen, $G = \frac{K^2}{E_0}$ and thus $\frac{G}{\Gamma_{intrinsic}} = \frac{K^2}{E_0 G_{local}(r=L)}$ in any case, since the zone near the clamps will always remain in the soft solid domain. One readily finds

$$\boxed{\frac{G}{\Gamma_{intrinsic}} = \begin{cases} 1 \\ m\left(\frac{V_p\tau}{L_\infty}\right)^{\frac{\alpha}{\alpha+1}} = m\left(\frac{V_p\tau}{L_\infty}\right)^{\frac{1}{\beta}} \\ m \end{cases} \quad \text{if} \quad \begin{cases} V_p\tau < m^{-1/\alpha}L_0 \\ m^{-1/\alpha}L_0 < V_p\tau < mL_0 \\ mL_0 < V_p\tau \end{cases}} \quad (13).$$

Remarkably, **we end up with the same result as with our former treatment**, including the occurrence of a Paris regime characterized by the same exponent β and the same expression for Γ_c.

For a finite specimen however, the preceding results will stop holding once r_s reaches W. The exact consequences depend on the W value.

Assuming first $\mathbf{m^\beta L_0 < W}$, $r_s = W$ happens only after the cohesive zone is surrounded by hard solid, so that the $G = \Gamma_c$ plateau is still observable experimentally. Once the liquid domain has reached the clamps, $\Gamma_{intrinsic} = \frac{K^2}{E_\infty}$ and $\frac{G}{\Gamma_{intrinsic}} = \frac{E_\infty G_{local}(r=W)}{K^2}$, and (13) must be supplemented by

$$\frac{G}{\Gamma_{intrinsic}} = \begin{cases} \left(\frac{W}{V_p\tau}\right)^{\alpha} \\ 1 \end{cases} \quad \text{if} \quad \begin{cases} m^{-1/\alpha}W < V_p\tau < W \\ W < V_p\tau \end{cases} \quad (14).$$

The corresponding $G(V_p)$ curve therefore exhibits a decreasing portion after having reached the plateau of height $m\,\Gamma_{intrinsic}$. It is qualitatively consistent with results of peeling tests carried on poorly crosslinked polymers, to which this study aimed at.

This was the only situation envisaged in the original papers. Yet, it can be unrealistic in practice, since for L_0 = 10 nm it requires W > 10 mm to 10 meters (!) with the above-mentioned m and β values.

Assuming next $\mathbf{L_0 < W < m^\beta L_0}$, $r_s = W$ now happens before the cohesive zone is surrounded by hard solid, so **the previous plateau is not observable anymore, and the material exhibits a different "effective" Γ_c depending on the specimen dimensions**. More precisely, the second line in (13) holds only until $V_p\,\tau = m^{-1/\alpha}\,W$ ($< m\,L_0$), where the "effective" Γ_c is attained :

$$\boxed{\frac{\Gamma_c}{\Gamma_{intrinsic}} = \left(\frac{W}{L_0}\right)^{\frac{\alpha}{\alpha+1}} = \left(\frac{W}{L_0}\right)^{\frac{1}{\beta}}} \quad (15).$$

For example, with L_0 = 10 nm, W = 10 mm and β = 3 for instance, $\Gamma_c / \Gamma_{intrinsic}$ would be limited to 100. Besides, the third line in (13) must be modified.

If $\mathbf{m\,L_0 < W < m^\beta L_0}$, it is replaced by

$$\frac{G}{\Gamma_{intrinsic}} = \begin{cases} \left(\frac{W}{L}\right)^{\alpha} = \left(\frac{W}{L_\infty}\right)^{\alpha}\left(\frac{L_\infty}{V_p\tau}\right)^{\frac{\alpha^2}{\alpha+1}} \\ \left(\frac{W}{V_p\tau}\right)^{\alpha} \\ 1 \end{cases} \text{ if } \begin{cases} m^{-1/\alpha}W < V_p\tau < mL_0 \\ mL_0 < V_p\tau < W \\ W < V_p\tau \end{cases} \quad (16).$$

Whereas if $\mathbf{L_0 < W < m\,L_0}$, it is replaced by

$$\frac{G}{\Gamma_{intrinsic}} = \begin{cases} \left(\frac{W}{L}\right)^{\alpha} = \left(\frac{W}{L_\infty}\right)^{\alpha}\left(\frac{L_\infty}{V_p\tau}\right)^{\frac{\alpha^2}{\alpha+1}} \\ 1 \end{cases} \text{ if } \begin{cases} m^{-1/\alpha}W < V_p\tau < \left(\frac{W}{L_\infty}\right)^{1/\alpha}W \\ \left(\frac{W}{L_\infty}\right)^{1/\alpha}W < V_p\tau \end{cases} \quad (17).$$

4.5 Introducing non-linearity in the constitutive equation

Focusing exclusively on linear viscoelasticity is far too restrictive for filled polymers, which exhibit various nonlinearities at high strains as well as a supplementary source of hysteresis : Mullins effect. In the framework presented here, **the better resistance to static crack growth of a filled polymer in comparison to its unfilled homolog is attributed – at least partially – to an increase of $\Gamma_{dissipation}$ brought by Mullins effect**. Interestingly, as previously mentioned, the so-called multi-networks (various standard polymer networks interpenetrated into each other) also enjoy a high toughness and a mechanical behavior reminiscent of Mullins effect [61]. The microscopic origin of Mullins effect may be different in these two classes of materials (cavitation in filled polymers vs. localized chains ruptures in multi-networks), but a beneficial impact of Mullins hysteresis onto $\Gamma_{dissipation}$ is expected in both cases.

Once again, this line of reasoning prompted different works [119, 120, 128]. Zhang [120] starts with the decomposition $G = \Gamma_{intrinsic} + \Gamma_{dissipation}$. $\Gamma_{dissipation}$ is assumed proportional to the "ultimate" hysteresis $H(Y_{rupture})$, where like in equation (5), $Y_{rupture}$ denotes the minimum height at which the material reaches there its stress at break, with a front factor homogeneous to a length. A length scale manifestly relevant to this problem is $G / W_{rupture}$. Therefore the authors were led to guess $\Gamma_{dissipation} = \alpha\, G\, h_{rupture}$ where $h_{rupture} \equiv \frac{H(Y_{rupture})}{W_{rupture}}$ (< 1). α was found by fitting the results of a campaign of Finite Element Analyses during which the material parameters describing the Mullins effect (modeled with an Ogden-Roxburgh law) and the cohesive zone were systematically varied. They obtained eventually

$$G = \frac{\Gamma_{intrinsic}}{1 - \alpha\, h_{rupture}} \quad \text{with} \quad \alpha \approx 0.33 + \frac{0.034}{m/W_{rupture} + 0.045} \quad (18).$$

r, m and β (set to 0.1 in the article) are material parameters quantifying the Mullins hysteresis : if the energy density provided during the first loading equals W, the Mullins hysteresis reads "h(W) W" where

$$h(W) = \frac{1}{r} f\left[\left(\beta + \frac{m}{W}\right)^{-1}\right] \quad \text{with} \quad f(x) \equiv \frac{1}{x}\int_0^x \mathrm{erf}(y)\,dy \quad (19).$$

Especially, the smaller m, the greater the hysteresis of small amplitude cycles, and thus the greater the hysteresis far from the crack tip. This remark will soon be useful.

Qi [119] **gave an analytic derivation of this result based on equation (2)**. The maximum energy density along a line parallel to a mode I crack in a Neo-Hookean material reads $W(Y) = \frac{G}{2\pi Y}$ according to asymptotic developments. Using a slightly modified version of this expression to take far fields and Mullins softening into account, the authors reported it into (19), and (19) into (2). Proceeding this way, they obtained an α expression comparing well with (18).

Besides, **if $m \to 0$, we noted above that the dissipation zone can extend until the clamps, so the measured G can depend on the specimen geometry**, ceasing to be an intrinsic material

property. Some FEA confirmed this intuition, FEA that were themselves well reproduced by the analytic theory. $\frac{G}{\Gamma_{intrinsic}}$ appears to depend on a dimensionless parameter $\chi = \frac{2H_0}{\Gamma_{intrinsic}/W_{rupture}}$ which is the ratio of the PS specimen height to the cohesive zone length.

4.6 Experimental tests of the preceding theories

Viscoelastic behavior: Knauss and his co-workers applied successfully various theories to a polyurethane. The model developed in Mueller and Knauss [38] matched well the experimental points. It rested on an analysis of the viscoelastic relaxation in the cohesive zone and its prediction read (Δa being a material constant, set to 13.4 nm by the fitting procedure):

$$G(V_p) = \frac{\Gamma_{intrinsic}}{2E_0 D(\Delta a/V_p)} \quad \text{where} \quad D(t) \equiv \frac{1}{t}\int_0^t \left(1 - \frac{u}{t}\right) J(u)du \quad (20).$$

Contrary to the appearances, this result is actually quite similar to (9). Indeed, using a Kramers-Kronig relation, one can recast the denominator of (20) :

$$J(t) = \frac{1}{E_0} + \frac{2}{\pi}\int_0^{+\infty} J''(\omega)\cos(\omega t)\frac{d\omega}{\omega} \Longrightarrow D(t) \approx \frac{1}{2E_0} - \frac{1}{\pi}\int_0^{1/t} |J''(\omega)|\frac{d\omega}{\omega} \quad (21).$$

(We used the approximation $(1 - \cos(x))/x^2 \approx ½\ \mathcal{H}(1 - x)$.) The only distinct feature is the constancy of Δa. So this success suggests also a success of (9).

Later[109, 110], they developed a refined version of this early model, which proved to be equally successful. In both cases, the model predicts a correct Paris exponent β. In fact, these data are consistent with the rule $\beta = 1 + 1/\alpha$: experiments suggest $\alpha \approx 0.8$ (read on master curves of dynamic moduli) and $\beta \approx 2.4$ (read on curves of V_p vs. ε_∞, ε_∞ being the macroscopic strain applied to the PS specimen, so that $G \propto \varepsilon_\infty^2$), in reasonable agreement with the theoretical prediction $\beta \approx 2.25$. With this material, $m \approx 1725$ MPa / 2.75 MPa ≈ 627, and the predicted Γ_c ($= m\,\Gamma_0$) seems in agreement with experiment, though the final plateau is not sufficiently well observed to be categorical. Assuming $L_0 = 10$ nm for the cohesive length at low V_p, the De Gennes criterion to avoid finite size effects reads $W > 627^{2.25} \times 10$ nm = 2 cm : it was indeed satisfied in Knauss experiments, where W = 3.5 cm. Incidentally, Christensen [112] also managed to fit this set of experimental results using a theory of his own, explicitly relying on an energy budget.

Saulnier [129] carried adhesion experiments on an un-crosslinked polydimethylsiloxane (PDMS) of large molecular weight. They confirmed De Gennes predictions (with $\alpha = 1$) regarding the decrease of fracture energy at high crack growth rates – equation (14) – as well as the opening displacement of the crack lips : $u \propto x^{1/2}$ near the crack tip where the material behaves as a hard solid, $u \propto x^{3/2}$ farther from the crack tip where the material becomes liquid-like.

Gent[124, 125] carried peeling tests on various crosslinked polymers of variable T_g. He found that the $G / \Gamma_{intrinsic}$ vs. V_p master-curves were relatively independent of the polymer, like the $E'(\omega) / E_0$ vs. ω master-curves (though to a smaller extent), and speculated, from the resemblance between these, that $\frac{G}{\Gamma_{intrinsic}} = \frac{E'(V_p/d)}{E_0}$ with d some material constant. Unfortunately the exponents of the power laws fitting the glass transition regime did not match : $\beta^{-1} = 0.3$ for the peeling energy, $\alpha = 0.6$ for the storage modulus. Trying anyway to fit the model onto experiment, he found $d \approx 0.1$ nm, or more largely $0.01\ \text{nm} < d < 1$ nm, some unrealistically low values. Besides, $\Gamma_c / \Gamma_{intrinsic}$ appears slightly greater than E_∞ / E_0. But the theories explored in the preceding paragraphs point rather to $d \propto G$, implying $\frac{1}{\beta} = \frac{\alpha}{\alpha+1}$, i.e. $\beta^{-1} = 0.375$ in the present case, which is closer to experiment. One can hope that this improvement will also bring the d range towards more sensible values. In fact, this improvement could be combined with other features not addressed by the models we reviewed but envisaged by Gent : nonlinear effects near the

crack tip, intermittent propagation "in a stick-slip fashion". This last feature implies that the instantaneous V_p can be much higher than the average V_p, which is the one measured : one should keep this idea in mind when considering cyclic crack growth.

Extension to cyclic crack growth and to Mullins effect dissipation: Klüppel surveyed the ability of the models we reviewed to reproduce the cyclic crack growth curves measured on filled and unfilled polymer[130]. The author used crosslinked S-SBR and Ethylene Propylene Diene Monomer (1.7 phr S + 2.5 phr CBS) filled or not with 60 phr of N550 carbon black. He focused his attention on Paris law slopes, and found that the theory matched reasonably with experiment. This is particularly striking because the theory in question has been devised exclusively for static crack growth, and besides it ignores the nonlinearities and the Mullins effect typical of filled polymers. This remark suggests to check if the Paris law intercepts with the Y-axis are equally well reproduced by the theory, namely equation (11) with B = 1. It is an uncertain task since some key quantities ($\Gamma_{intrinsic}$ and $W_{rupture}$) are missing in the article : we must guess them and see what we get. Using notably $\Gamma_{intrinsic} \approx 50$ (resp. 100) $J.m^{-2}$ in the unfilled (resp. filled) case, we find at $G \approx 3$ $kJ.m^{-2}$, 4 Hz and ambient temperature : in unfilled S-SBR, $V_p \approx 40$ $m.s^{-1}$ theoretically vs. $V_p \approx 10$ $nm.cycle^{-1} = 40$ $nm.s^{-1}$ experimentally ; in filled S-SBR, $V_p \approx 4$ $m.s^{-1}$ theoretically vs. $V_p \approx 4$ $nm.cycle^{-1} = 40$ $nm.s^{-1}$ experimentally. These estimates must be taken with caution owing to the mentioned uncertainties. Nevertheless, the discrepancy between our estimates and the measurements is such that we can consider that the theory fails to reproduce the intercept with the Y-axis of the Paris law.

Zhang [120] checked that it could reproduce by FEA the onset of crack propagation in a multi-network hydrogel considered to exhibit Mullins effect only. Constitutive law parameters were identified on cycles of increasing maximum strain applied in pure shear. The propagation threshold G was measured after various pre-strains – applied to the uncracked specimen – between 0 and the strain at break (as high as 8 here). It appears to decrease with pre-strain, reaching a plateau (400 $J.m^{-2}$) for the highest pre-strains, to be identified with the virgin $\Gamma_{intrinsic}$ (though one could argue that high pre-strains could damage enough the material to diminish its $\Gamma_{intrinsic}$). FEA results appeared to be consistent with the G = 1 063 $J.m^{-2}$ value measured with the virgin material. Incidentally, this experiment proves that the intrinsic resistance to crack growth represents here only 38 % of G in the virgin state, the remaining 62 % being brought by macroscopic dissipation.

Qi [119] put the pre-strain effect in equations. The line of reasoning is as follows: the horizontal strips whose strain remains below the pre-strain cannot dissipate by Mullins effect (strips close to the clamps), the dissipation being thus confined to a central strip, where it is moreover smaller than in the virgin state. These statements explain qualitatively why $\Gamma_{dissipation}$ must decrease with pre-strain : the pre-strain diminishes the capacity of the material to dissipate when a crack propagates. The agreement with experiment is even quantitative, as shown in the article.

Wunde et al. [131, 132] carried experiments on cured CB-filled NR-based polymer blends allowing an estimation of $\Gamma_{dissipation}$ / G. For the 4 mixes of the study and various macroscopic strain, they measured by Digital Image Correlation the displacement and strain fields in notched and loaded PS specimens, that they combined with the constitutive laws – modelling Mullins effect and viscoelasticity – identified independently to compute the Rice- or $\mathcal{J}$-integral on various circles C centered on the crack tip. (They considered both components of $\int_C \Sigma_{ij}\, ds_j$, but we focus here on the sole forward component). $\mathcal{J}$ appears to increase with the circle radius R, consistently with $\mathcal{J}(R = 0) = \Gamma_{intrinsic}$ and $G = \mathcal{J}(R = +\infty)$ by construction of $\mathcal{J}$ and with the inequality $\Gamma_{intrinsic} < G$ for a dissipative material. Actually, the difference between these limits is $\Gamma_{dissipation}$. The analysis is complicated by a lack of resolution for R < 0.5 mm and by the fact that $\mathcal{J}$(R =

+∞) becomes greater than G (computed by the Rivlin-Thomas formula) above 40 % macroscopic strain. Despites these difficulties, the authors estimate that all in all, $\Gamma_{dissipation}$ represents 90 % of G. These experiments also demonstrate that $\mathcal{J}$ reaches G for R > 1 to 5 mm (for macroscopic strains between 10 and 60 %) : these are macroscopic dimensions, which legitimate the qualification of $\Gamma_{dissipation}$ as a macroscopic dissipation. Especially, these dimensions demonstrate clearly that crack growth can be accompanied by energy dissipation quite far from the crack tip, where no macroscopic breakage occurs.

Slootman [44] introduced in mono- and multi-networks of polymers a known amount of a mechanophore having the property of becoming fluorescent upon breakage. The materials being transparent, they could be measured by optical confocal microscopy the spatial distribution of this fluorescence, and therefore (via an appropriate calibration) the spatial distribution of the number of broken mechanophores, and finally of overall broken bonds. These distributions were measured along the lips of a crack propagated for various loadings and temperatures. $\Gamma_{intrinsic}$ is deduced by integrating the distribution (for a unit propagated surface) and multiplying the integral by 64 kJ.mol^{-1}, the energetic cost of a single breakage according to Wang[137]. Most remarkably, the author demonstrated that : $\Gamma_{intrinsic}$ increases with the loading, that is with G or V_p, going from the Lake and Thomas estimate for $V_p \rightarrow 0$ up to 100 times this value at high V_p ; and that the number of covalent bond scissions varies in the same proportion, with rupture occurring up to a few 100 µm far from the crack plane for the highest V_p. Especially, **$\Gamma_{intrinsic}$ cannot be treated as a material constant, as was done in the works reviewed so far, but as a function of V_p**. Notice however that equation (2) and the ones stemming from it can easily accommodate a V_p dependent $\Gamma_{intrinsic}$. It seems very likely that this phenomenology also applies to filled polymers, whose filler network is analogous to the first network here and whose polymer matrix is analogous to the second and third networks here. Depending on the tested Single-, Double- or Triple- Network, she found that **$\Gamma_{intrinsic}$ / G varies between a few % and a few 10 %, and therefore $\Gamma_{dissipation}$ / G varies between 50 and more than 90 %**.

5 CONCLUSION

A synthesis of the phenomenology of ultimate and crack growth properties of elastomers is not straightforward given the diversity of elastomers and used protocols. Nevertheless, despite this difficulty, the huge literature on the topic, completed by some our own experimental works, allows to well identify the different interrelated and complex mechanisms involved in crack growth. In connection with these observations, the theories reviewed in the last part link quantitatively the resistance to crack growth to:

- the ability of the material to dissipate energy, either by viscoelasticity or by Mullins effect ;
- the distribution of strain and stress around the crack tip (dictated by the constitutive law), which weights the contribution of each horizontal line to the total dissipation accompanying the crack growth ;
- the break properties (limit strain / stress / energy), which define an upper bound for the dissipation integrals.

These theories have been validated experimentally in various situations. They can be useful to material designers because they allow the replacement of lengthy or sophisticated crack growth experiments by faster and simpler mechanical characterization of unnotched specimen until break, and because they offer a mean to infer what “customary” material property (moduli, break properties) to tune and in which direction to achieve an enhanced resistance to crack growth. Especially, the theories involving dynamic moduli can suggest compromises between Rolling Resistance (RR) and endurance in tires via the difference of frequency ranges relevant to each performance. This situation is reminiscent of the known compromise between RR and grip. And in fact, the analogy goes deeper : the well-known viscoelastic contribution to the friction coefficient µ is equivalent to the viscoelastic contribution in $\Gamma_{dissipation}$ (see e.g. our equation (9)), the role of crack tip singularity in endurance is played by road asperities in grip,

and the integral over all distances Y from the crack plan is replaced in the grip case by the integral over asperity sizes and tread band depth.

Though these theories are encouraging, they still suffer of various shortcomings. The most obvious from a practical standpoint is their inability so far to handle cyclic crack growth : they have been thought for static crack growth, and their generalizations to the cyclic case is not straightforward. They also often treat $\Gamma_{intrinsic}$ and $W_{rupture}$ as material constants, although they are susceptible to vary with strain rate and thus V_p. Finally, it is highly desirable to now quantitatively relate them to the differents fields measurable at the crack tip and reviewed in chapters 2 and 3 (including cavitation and degree of Strain Induced Crystallization). These missing features are as many subjects for future researches.

6 REFERENCES

1. Creton C, Ciccotti M (2016) Fracture and adhesion of soft materials: a review. Rep Prog Phys 79:046601
2. Gent AN, Mars WV (2013) Strength of Elastomers. In: The Science and Technology of Rubber. Elsevier, pp 473–516
3. Mars WV, Fatemi A (2004) Factors that Affect the Fatigue Life of Rubber: A Literature Survey. Rubber Chem Technol 77:391–412
4. Tee YL, Loo MS, Andriyana A (2018) Recent advances on fatigue of rubber after the literature survey by Mars and Fatemi in 2002 and 2004. Int J Fatigue 110:115–129
5. Grellmann W, Heinrich G, Kaliske M, Klüppel M, Schneider K, Vilgis ThA (2013) Fracture Mechanics and Statistical Mechanics of Reinforced Elastomeric Blends. Springer-Verlag Berlin Heidelberg, Berlin; Heidelberg
6. Lake GJ (1995) Fatigue and Fracture of Elastomers. Rubber Chem Technol 68:435–460
7. Nonoyama T, Wada S, Kiyama R, Kitamura N, Mredha MdTI, Zhang X, Kurokawa T, Nakajima T, Takagi Y, Yasuda K, Gong JP (2016) Double-Network Hydrogels Strongly Bondable to Bones by Spontaneous Osteogenesis Penetration. Adv Mater 28:6740–6745
8. Kamat S, Su X, Ballarini R, Heuer AH (2000) Structural basis for the fracture toughness of the shell of the conch Strombus gigas. Nature 405:1036–1040
9. Sen D, Buehler MJ (2011) Structural hierarchies define toughness and defect-tolerance despite simple and mechanically inferior brittle building blocks. Sci Rep 1:35
10. Gong JP, Katsuyama Y, Kurokawa T, Osada Y (2003) Double-Network Hydrogels with Extremely High Mechanical Strength. Adv Mater 15:1155–1158
11. Higuchi Y, Saito K, Sakai T, Gong JP, Kubo M (2018) Fracture Process of Double-Network Gels by Coarse-Grained Molecular Dynamics Simulation. Macromolecules 51:3075–3087
12. Lavoie SR, Millereau P, Creton C, Long R, Tang T (2019) A continuum model for progressive damage in tough multinetwork elastomers. J Mech Phys Solids 125:523–549
13. Laiarinandrasana L, Morgeneyer TF, Proudhon H, N'guyen F, Maire E (2012) Effect of Multiaxial Stress State on Morphology and Spatial Distribution of Voids in Deformed Semicrystalline Polymer Assessed by X-ray Tomography. Macromolecules 45:4658–4668
14. Rublon P, Huneau B, Verron E, Saintier N, Beurrot S, Leygue A, Mocuta C, Thiaudière D, Berghezan D (2014) Multiaxial deformation and strain-induced crystallization around a fatigue crack in natural rubber. Eng Fract Mech 123:59–69
15. Kallungal J, Chazeau L, Chenal J-M, Adrien J, Maire E, Barres C, Cantaloube B, Heuillet P (2019) Methodology for 3D characterization of microstructural defects in filled polymer using X-ray Tomography. In: Huneau B, Le Cam J-B, Marco Y, Verron E (eds) Constitutive Models for Rubber XI, 1st ed. CRC Press, pp 77–81
16. Saintier N (2001) Fatigue multiaxiale dans un élastomère de type NR chargé : mécanismes d'endommagment et critère local d'amorçage de fissure. 225
17. Saintier N, Cailletaud G, Piques R (2006) Crack initiation and propagation under multiaxial fatigue in a natural rubber. Int J Fatigue 28:61–72
18. Lake GJ, Lindley PB (1964) Cut growth and fatigue of rubbers. II. Experiments on a noncrystallizing rubber. J Appl Polym Sci 8:707–721
19. Lindley PB (1974) Non-Relaxing Crack Growth and Fatigue in a Non-Crystallizing Rubber. Rubber Chem Technol 47:1253–1264
20. Rivlin RS, Thomas AG (1953) Rupture of rubber. I. Characteristic energy for tearing. J Polym Sci 10:291–318
21. Roucou D, Diani J, Brieu M, Witz J-F, Mbiakop-Ngassa A (2018) Experimental investigation of elastomer mode I fracture: an attempt to estimate the critical strain energy release rate using SENT tests. Int J Fract 209:163–170

22. Thomas AG (1994) The Development of Fracture Mechanics for Elastomers. Rubber Chem Technol 67:50–67
23. Yeoh OH (2003) Fracture Mechanics of Bond Failure in the “Pure Shear” Test Piece. Rubber Chem Technol 76:483–494
24. Greensmith HW (1963) Rupture of rubber. X. The change in stored energy on making a small cut in a test piece held in simple extension. J Appl Polym Sci 7:993–1002
25. Lindley PB (1972) Energy for crack growth in model rubber components. J Strain Anal 7:132–140
26. Carbone G, Persson BNJ (2005) Crack motion in viscoelastic solids: The role of the flash temperature. Eur Phys J E 17:261–281
27. Smith TL (1958) Dependence of the ultimate properties of a GR-S rubber on strain rate and temperature. J Polym Sci 32:99–113
28. Bueche F, Halpin JC (1964) Molecular Theory for the Tensile Strength of Gum Elastomers. J Appl Phys 35:36–41
29. Kok CM, Yee VH (1986) The effects of crosslink density and crosslink type on the tensile and tear strengths of NR, SBR and EPDM gum vulcanizates. Eur Polym J 22:341–345
30. Lake GJ, Lawrence CC, Thomas AG (2000) High-Speed Fracture of Elastomers: Part I. Rubber Chem Technol 73:801–817
31. Tsunoda K, Busfield JJC, Davies CKL, Thomas AG (2000) Effect of materials variables on the tear behaviour of a non-crystallising elastomer. J Mater Sci 35:5187–5198
32. Papadopoulos IC, Thomas AG, Busfield JJC (2008) Rate transitions in the fatigue crack growth of elastomers. J Appl Polym Sci 109:1900–1910
33. Fukahori Y, Sakulkaew K, Busfield JJC (2013) Elastic–viscous transition in tear fracture of rubbers. Polymer 54:1905–1915
34. Horst T, Heinrich G (2008) Crack propagation behavior in rubber materials. Polym Sci Ser A 50:583–590
35. Mullins L (1959) Rupture of rubber – Part IX : role of hysteresis in the tearing of rubber. Trans Proc Inst Rubber Ind 35:213–222
36. Lake GJ, Yeoh OH (1978) Measurement of rubber cutting resistance in the absence of friction. Int J Fract 14:509–526
37. Robertson CG, Stoček R, Kipscholl C, Mars WV (2019) Characterizing the Intrinsic Strength (Fatigue Threshold) of Natural Rubber/Butadiene Rubber Blends. Tire Sci Technol 47:292–307
38. Mueller HK, Knauss WG (1971) The Fracture Energy and Some Mechanical Properties of a Polyurethane Elastomer. Trans Soc Rheol 15:217–233
39. Ahagon A, Gent AN (1975) Threshold fracture energies for elastomers. J Polym Sci Polym Phys Ed 13:1903–1911
40. Bhowmick AK, Gent AN, Pulford CTR (1983) Tear Strength of Elastomers under Threshold Conditions. Rubber Chem Technol 56:226–232
41. Gent AN, Tobias RH (1982) Threshold Tear Strength of Some Molecular Networks. In: Mark JE, Lal J (eds) Elastomers and Rubber Elasticity. American Chemical Society, Washington, D. C., pp 367–376
42. Stoček R, Stěnička M, Zádrapa P (2020) Future trends in predicting the complex fracture behaviour of rubber materials. Contin Mech Thermodyn
43. Lake GJ, Thomas AG (1967) The strength of highly elastic materials. Proc R Soc Lond Ser Math Phys Sci 300:108–119
44. Slootman J (2019) Quantitative detection of damage in soft materials using mechano-fluorescence. l’Ecole Supérieure de Physique et de Chimie Industrielles de la ville de Paris (ESPCI Paris)
45. De Almeida A, Chazeau L, Vigier G, Marque G, Goutille Y (2017) Ultimate and toughness properties of γ-irradiated EPDM. Eur Polym J 97:178–187
46. Kadir A, Thomas AG (1981) Tear Behavior of Rubbers Over a Wide Range of Rates. Rubber Chem Technol 54:15–23
47. Lake GJ, Lindley PB (1965) The mechanical fatigue limit for rubber. J Appl Polym Sci 9:1233–1251
48. Paris P, Erdogan F (1963) A Critical Analysis of Crack Propagation Laws. J Basic Eng 85:528–533
49. Lake GJ, Lindley PB (1964) Cut growth and fatigue of rubbers. II. Experiments on a noncrystallizing rubber. J Appl Polym Sci 8:707–721
50. Long R, Hui C-Y (2015) Crack tip fields in soft elastic solids subjected to large quasi-static deformation — A review. Extreme Mech Lett 4:131–155
51. Horiuchi S, Dohi H (2006) Nanoimaging and Spectroscopic Analysis of Rubber/ZnO Interfaces by Energy-Filtering Transmission Electron Microscopy. Langmuir 22:4607–4613
52. Tobolsky AV, Lyons PF (1968) Tensile strength of rubbers. J Polym Sci Part -2 Polym Phys 6:1561–1566
53. Colin X, Audouin L, Verdu J (2007) Kinetic modelling of the thermal oxidation of polyisoprene elastomers. Part 3: Oxidation induced changes of elastic properties. Polym Degrad Stab 92:906–914

54. Howse S, Porter C, Mengistu T, Pazur RJ (2018) Experimental determination of the quantity and distribution of chemical crosslinks in unaged and aged natural rubber, part 1: Peroxide vulcanization. Polym Test 70:263–274
55. Kaidou H, Ahagon A (1990) Aging of Tire Parts during Service. II. Aging of Belt-Skim Rubbers in Passenger Tires. Rubber Chem Technol 63:698–712
56. Langley NR, Polmanteer KE (1974) Relation of elastic modulus to crosslink and entanglement concentrations in rubber networks. J Polym Sci Polym Phys Ed 12:1023–1034
57. Saalwächter K (2012) Microstructure And Molecular Dynamics Of Elastomers As Studied By Advanced Low-Resolution Nuclear Magnetic Resonance Methods. Rubber Chem Technol 85:350–386
58. Legorjujago K (2002) Fatigue initiation and propagation in natural and synthetic rubbers. Int J Fatigue 24:85–92
59. Mark JE, Tang M-Y (1984) Dependence of the elastomeric properties of bimodal networks on the lengths and amounts of the short chains. J Polym Sci Polym Phys Ed 22:1849–1855
60. Buckley GS, Fragiadakis D, Roland CM (2011) Strength enhancement from heterogeneous networks of ethylene–propylene/ethylene–propylene–diene. Rubber Chem Technol 84:520–526
61. Ducrot E, Chen Y, Bulters M, Sijbesma RP, Creton C (2014) Toughening Elastomers with Sacrificial Bonds and Watching Them Break. Science 344:186–189
62. Le Gac P-Y, Albouy P-A, Petermann D (2018) Strain-induced crystallization in an unfilled polychloroprene rubber: Kinetics and mechanical cycling. Polymer 142:209–217
63. Candau N, Chazeau L, Chenal J-M, Gauthier C, Munch E (2016) A comparison of the abilities of natural rubber (NR) and synthetic polyisoprene cis-1,4 rubber (IR) to crystallize under strain at high strain rates. Phys Chem Chem Phys 18:3472–3481
64. Behnke R, Berger T, Kaliske M (2018) Numerical modeling of time- and temperature-dependent strain-induced crystallization in rubber. Int J Solids Struct 141–142:15–34
65. Brüning K, Schneider K, Roth SV, Heinrich G (2012) Kinetics of Strain-Induced Crystallization in Natural Rubber Studied by WAXD: Dynamic and Impact Tensile Experiments. Macromolecules 45:7914–7919
66. Candau N, Laghmach R, Chazeau L, Chenal J-M, Gauthier C, Biben T, Munch E (2015) Temperature dependence of strain-induced crystallization in natural rubber: On the presence of different crystallite populations. Polymer 60:115–124
67. Candau N, Chazeau L, Chenal J-M, Gauthier C, Munch E (2016) Complex dependence on the elastically active chains density of the strain induced crystallization of vulcanized natural rubbers, from low to high strain rate. Polymer 97:158–166
68. Das A, Le HH, Vuorinen J, Heinrich G (2017) Comment on "Monitoring Network and Interfacial Healing Processes by Broadband Dielectric Spectroscopy: A Case Study on Natural Rubber." ACS Appl Mater Interfaces 9:14547–14551
69. Huneau B (2011) Strain-Induced Crystallization Of Natural Rubber: A Review Of X-Ray Diffraction Investigations. Rubber Chem Technol 84:425–452
70. Khiêm VN, Itskov M (2018) Analytical network-averaging of the tube model: Strain-induced crystallization in natural rubber. J Mech Phys Solids 116:350–369
71. Laghmach R, Candau N, Chazeau L, Munch E, Biben T (2015) Phase field modelling of strain induced crystal growth in an elastic matrix. J Chem Phys 142:244905
72. Li X, Schneider K, Kretzschmar B, Stamm M (2008) Deformation Behavior of PP and PP/ZnO Nanocomposites As Studied by SAXS and WAXS. Macromolecules 41:4371–4379
73. Roth SV, Rothkirch A, Autenrieth T, Gehrke R, Wroblewski T, Burghammer MC, Riekel C, Schulz L, Hengstler R, Müller-Buschbaum P (2010) Spatially Resolved Investigation of Solution Cast Nanoparticle Films by X-ray Scattering and Multidimensional Data Set Classification. Langmuir 26:1496–1500
74. Sotta P, Albouy P-A (2020) Strain-Induced Crystallization in Natural Rubber: Flory's Theory Revisited. Macromolecules 53:3097–3109
75. Flory PJ (1947) Thermodynamics of Crystallization in High Polymers. I. Crystallization Induced by Stretching. J Chem Phys 15:397–408
76. Gent AN, Hindi M (1990) Effect of Oxygen on the Tear Strength of Elastomers. Rubber Chem Technol 63:123–134
77. Kim SG, Lee S-H (1994) Effect of Crosslink Structures on the Fatigue Crack Growth Behavior of NR Vulcanizates with Various Aging Conditions. Rubber Chem Technol 67:649–661
78. Rublon P, Huneau B, Saintier N, Beurrot S, Leygue A, Verron E, Mocuta C, Thiaudière D, Berghezan D (2013) In situ synchrotron wide-angle X-ray diffraction investigation of fatigue cracks in natural rubber. J Synchrotron Radiat 20:105–109
79. Hamed GR, Park BH (1999) The mechanism of carbon black reinforcement of SBR and NR vulcanizates. Rubber Chem Technol 72:946–959
80. Xiang F, Schneider K, Heinrich G (2020) New observations regarding fatigue crack paths and their fracture surfaces in natural rubber: Influences of R-ratio and pre-load. Int J Fatigue 135:105508

81. Lee DJ, Donovan JA (1987) Microstructural Changes in the Crack Tip Region of Carbon-Black-Filled Natural Rubber. Rubber Chem Technol 60:910–923
82. Trabelsi S, Albouy P-A, Rault J (2002) Stress-Induced Crystallization around a Crack Tip in Natural Rubber. Macromolecules 35:10054–10061
83. Grasland F, Chenal J-M, Chazeau L, Caillard J, Schach R (2017) Role of SIC on the fatigue properties of NR after realistic aerobic ageing. In: Lion A, Johlitz M (eds) European Conference on Constitutive Models for Rubbers X. CRC Press, Munich, Germany
84. Le Cam J-B, Toussaint E (2010) The Mechanism of Fatigue Crack Growth in Rubbers under Severe Loading: the Effect of Stress-Induced Crystallization. Macromolecules 43:4708–4714
85. Grasland F (2018) Vieillissement du caoutchouc naturel parthermo-oxydation: Etudes de ses conséquences sur lacristallisation sous déformation, la fissuration et larupture. PhD Thesis, Université de Lyon
86. Beurrot S, Huneau B, Verron E (2010) In situ SEM study of fatigue crack growth mechanism in carbon black-filled natural rubber. J Appl Polym Sci NA-NA
87. Zhou W, Li X, Lu J, Huang N, Chen L, Qi Z, Li L, Liang H (2015) Toughening mystery of natural rubber deciphered by double network incorporating hierarchical structures. Sci Rep 4:7502
88. Grasland F, Chazeau L, Chenal J-M, schach R (2019) About thermo-oxidative ageing at moderate temperature of conventionally vulcanized natural rubber. Polym Degrad Stab 161:74–84
89. Grasland F, Chazeau L, Chenal J-M, Caillard J, Schach R (2019) About the elongation at break of unfilled natural rubber elastomers. Polymer 169:195–206
90. Candau N, Laghmach R, Chazeau L, Chenal J-M, Gauthier C, Biben T, Munch E (2015) Influence of strain rate and temperature on the onset of strain induced crystallization in natural rubber. Eur Polym J 64:244–252
91. Chazeau L, Gauthier C, Chenal J-M (2010) Mechanical Properties of Rubber Nanocomposites: How, Why … and Then?
92. Stöckelhuber KW, Das A, Klüppel M, Basu D (2017) Designing of elastomer nanocomposites: from theory to applications. In: Designing of elastomer nanocomposites: from theory to applications, 1st ed. 2017. Springer, Cham
93. Chazeau L, Brown JD, Yanyo LC, Sternstein SS (2000) Modulus recovery kinetics and other insights into the payne effect for filled elastomers. Polym Compos 21:202–222
94. Diani J, Fayolle B, Gilormini P (2009) A review on the Mullins effect. Eur Polym J 45:601–612
95. Chenal J-M, Gauthier C, Chazeau L, Guy L, Bomal Y (2007) Parameters governing strain induced crystallization in filled natural rubber. Polymer 48:6893–6901
96. Gabrielle B, Guy L, Albouy P-A, Vanel L, Long DR, Sotta P (2011) Effect of Tear Rotation on Ultimate Strength in Reinforced Natural Rubber. Macromolecules 44:7006–7015
97. Medalia AI (1986) Effect of Carbon Black on Ultimate Proper.Pdf. Rubber Div Am Chem Soc 60:45–60
98. Ramier J, Chazeau L, Gauthier C, Stelandre L, Guy L, Peuvrel-Disdier E (2007) In situ SALS and volume variation measurements during deformation of treated silica filled SBR. J Mater Sci 42:8130–8138
99. Zhang H, Scholz AK, de Crevoisier J, Vion-Loisel F, Besnard G, Hexemer A, Brown HR, Kramer EJ, Creton C (2012) Nanocavitation in Carbon Black Filled Styrene–Butadiene Rubber under Tension Detected by Real Time Small Angle X-ray Scattering. Macromolecules 45:1529–1543
100. Le Cam J-B, Huneau B, Verron E, Gornet L (2004) Mechanism of Fatigue Crack Growth in Carbon Black Filled Natural Rubber. Macromolecules 37:5011–5017
101. Millereau P, Ducrot E, Clough JM, Wiseman ME, Brown HR, Sijbesma RP, Creton C (2018) Mechanics of elastomeric molecular composites. Proc Natl Acad Sci 115:9110–9115
102. Xu Z, Jerrams S, Guo H, Zhou Y, Jiang L, Gao Y, Zhang L, Liu L, Wen S (2020) Influence of graphene oxide and carbon nanotubes on the fatigue properties of silica/styrene-butadiene rubber composites under uniaxial and multiaxial cyclic loading. Int J Fatigue 131:105388
103. Dizon ES, Hicks AE, Chirico VE (1974) The Effect of Carbon Black Parameters on the Fatigue Life of Filled Rubber Compounds. Rubber Chem Technol 47:231–249
104. Nie Y, Wang B, Huang G, Qu L, Zhang P, Weng G, Wu J (2010) Relationship between the material properties and fatigue crack-growth characteristics of natural rubber filled with different carbon blacks. J Appl Polym Sci n/a-n/a
105. Agnelli S, Ramorino G, Passera S, Karger-Kocsis J, Ricco T (2012) Fracture resistance of rubbers with MWCNT, organoclay, silica and carbon black fillers as assessed by the J-integral: Effects of rubber type and filler concentration. Express Polym Lett 6:581–587
106. Dong B, Liu C, Lu Y, Wu Y (2015) Synergistic effects of carbon nanotubes and carbon black on the fracture and fatigue resistance of natural rubber composites. J Appl Polym Sci 132:n/a-n/a
107. Zhou X, Wang L, Cao X, Yin Q, Weng G (2019) Crack resistance improvement of rubber blend by a filler network of graphene. J Appl Polym Sci 136:47278

108. Rooj S, Das A, Morozov IA, Stöckelhuber KW, Stocek R, Heinrich G (2013) Influence of "expanded clay" on the microstructure and fatigue crack growth behavior of carbon black filled NR composites. Compos Sci Technol 76:61–68
109. Knauss WG (1973) On the Steady Propagation of a Crack in a Viscoelastic Sheet: Experiments and Analysis. In: Kausch HH, Hassell JA, Jaffee RI (eds) Deformation and Fracture of High Polymers. Springer US, Boston, MA, pp 501–541
110. Knauss WG (2015) A review of fracture in viscoelastic materials. Int J Fract 196:99–146
111. Christensen RM (2003) Theory of viscoelasticity, 2nd ed. Dover Publications, Mineola, N.Y
112. Christensen RM, Wu EM (1981) A theory of crack growth in viscoelastic materials. Eng Fract Mech 14:215–225
113. De Gennes PG (1996) Soft Adhesives. Langmuir 12:4497–4500
114. De Gennes PG (1988) Fracture d'un adhésif faiblement réticulé. Comptes Rendus Académie Sci Sér 2 Mécanique Phys Chim Sci Univers Sci Terre 307:1949–1953
115. Hui C, Xu D, Kramer EJ (1992) A fracture model for a weak interface in a viscoelastic material (small scale yielding analysis). J Appl Phys 72:3294–3304
116. Persson BNJ, Albohr O, Heinrich G, Ueba H (2005) Crack propagation in rubber-like materials. J Phys Condens Matter 17:R1071–R1142
117. Persson BNJ, Brener EA (2005) Crack propagation in viscoelastic solids. Phys Rev E 71:036123
118. Long R, Hui C-Y (2016) Fracture toughness of hydrogels: measurement and interpretation. Soft Matter 12:8069–8086
119. Qi Y, Caillard J, Long R (2018) Fracture toughness of soft materials with rate-independent hysteresis. J Mech Phys Solids 118:341–364
120. Zhang T, Lin S, Yuk H, Zhao X (2015) Predicting fracture energies and crack-tip fields of soft tough materials. Extreme Mech Lett 4:1–8
121. Anderson TL (2005) Fracture Mechanics: Fundamentals and Applications, Third Edition, 3rd ed. CRC Press
122. Maugin GA (1993) Material inhomogeneities in elasticity, 1. ed. Chapman & Hall, London
123. Horst T, Heinrich G, Schneider M, Schulze A, Rennert M (2013) Linking Mesoscopic and Macroscopic Aspects of Crack Propagation in Elastomers. In: Grellmann W, Heinrich G, Kaliske M, Klüppel M, Schneider K, Vilgis T (eds) Fracture Mechanics and Statistical Mechanics of Reinforced Elastomeric Blends. Springer Berlin Heidelberg, Berlin, Heidelberg, pp 129–165
124. Gent AN (1996) Adhesion and Strength of Viscoelastic Solids. Is There a Relationship between Adhesion and Bulk Properties? †. Langmuir 12:4492–4496
125. Gent AN, Lai S-M (1994) Interfacial bonding, energy dissipation, and adhesion. J Polym Sci Part B Polym Phys 32:1543–1555
126. Creton C, Ciccotti M (2016) Fracture and adhesion of soft materials: a review. Rep Prog Phys 79:046601
127. Haupt P (2002) Continuum Mechanics and Theory of Materials. Springer Berlin Heidelberg, Berlin, Heidelberg
128. Roucou D (2020) Caractérisation et modélisation du comportement à la déchirure de matériaux élastomères endommagés par chargement multiaxiaux. Ecole Centrale de Lille
129. Saulnier F, Ondarçuhu T, Aradian A, Raphaël E (2004) Adhesion between a Viscoelastic Material and a Solid Surface. Macromolecules 37:1067–1075
130. Klüppel M (2009) Evaluation of viscoelastic master curves of filled elastomers and applications to fracture mechanics. J Phys Condens Matter 21:035104
131. Wunde M, Plagge J, Klüppel M (2019) The role of stress softening in crack propagation of filler reinforced elastomers as evaluated by the J-Integral. Eng Fract Mech 214:520–533
132. Klüppel M, Wunde M (2020) Phase morphology and frature mechanics of rubber blend, book chapter In : Fatigue crack growth in rubber materials; experiments and modelling, Heinrich G, Stocek R (eds). Springer
133. Wang S, Panyukov S, Rubinstein M, Craig SL (2019) Quantitative Adjustment to the Molecular Energy Parameter in the Lake–Thomas Theory of Polymer Fracture Energy. Macromolecules 52:2772–2777

APPENDIX 2
EPDM formulation with oil: Influence of oil on the crack rotation?

TABLE OF CONTENTS

1. INTRODUCTION

Various instabilities are found during crack propagation in rubber, such as crack rotation, knotty tearing, crack deviation, stick-slip etc.. The tear rotation or "hammer head" cracking or sideways occurs in single-edge-notched tension samples (SENT) subjected to a tensile loading at constant strain rate. The crack can even propagates perpendicular to the standard trajectory, i.e. in a direction parallel to the applied tensile loading. In the literature such phenomena is commonly described for Natural rubber under tensile loading and usually explained by its strain-induced crystallization[1].

In case of amorphous elastomers, crack rotation behavior similar to NR is generally not observed. Nevertheless, stretched polymer chains at the crack tip can orient and thereby produce an anisotropic reinforcement[2,3]. This was found out to be reason for a small crack deviation in SBR filled with carbon black or silica during a crack propagation test using a SENT sample specimen[4]. Sideways cracking happens if the crack propagation resistance for forward direction (G_f) is higher than sideways propagation (G_s). Gent *et al.*[5] and Lee *et al.*[6] have found that the ratio of G_s/G_f is around 40-60% at which the crack turn sideways.

During our study, we actually observed crack rotation for the industrial material (filled amorphous EPDM elastomer containing oil) during the crack propagation tests using a single edge notched tensile specimen. Such rotation was not observed with all the samples we studied that did not contain any oil. Since this was unexpected, we performed some additional work to understand this phenomenon. Due to time constraints this study is incomplete but some results are sufficiently interesting to be described this appendix.

2. MATERIALS AND TESTING

2.1 Composition and materials processing

We choose to compare two materials with and without oil. Their formulation is given in Table 1. The material without oil was fabricated at INSA Lyon. Due to the unavailability of ingredients of sulphur based curing system, we decided to cure the material with peroxide. The details of their processing is given in Chapter section 2.2. I_no oil is a material with properties quite similar to I_oil from which oil has been extracted (so called "I_oil after swelling" sample), in the low deformation range (below 50% strain).

Ingredients	*'I_oil'*	*I_no_oil*
	(Phr)	*(Phr)*
EPDM KELTAN 4450	*100*	*100*
N326	*100*	*100*
Oil Parffin Torilis	*40*	
ZnStearate	*4.5*	
MBTS 80	*1.5*	
TBzTD 70	*2*	
Soufre	*1.5*	
ZBEC 70	*1*	
Peroxide		*3.2*
Volume Fraction	*24.8%*	*31.0%*

Table 1: Material formulation for model and industrial materials.

2.2 Differential scanning calorimetry (DSC) analysis

Pyris Diamond Calorimeter (Perkin Elmer, U.S.A) is used for the analysis of phase transitions in the material. 2 protocols of measurements are used in this chapter.
1st protocol is to measure the Tg by heating the sample from -80°C to 20°C at a temperature rate of 10°C/min.
2nd protocol is to confirm the crystallization phenomena in the material. During this protocol, the material is cooled down to -20°C at 10°C/min cooling rate, then heated from -20°C to 20°C. and further cooled back to -20°C at the same rate, where it is kept at an isotherm temperature for 16hr. After 16hr, the sample is again heated from -20°C to 20°C. The difference in the heatflux measured during the heating ramp performed immediately after the sample cooling at -20°C and after maintaining the sample 16hr at -20°C is calculated to evidence any crystallization in the material. In the case of material I_no_oil, the protocole is the same except that the sample is kept at -16°C for 48hr. The difference in the temperature of isothermal treatment (-16°C instead of -20°C) is equivalent to the difference in Tg of both materials since both are obtained from the calculation $(T_{amb} + T_g)/2$. At this temperature, there is a possibility of seeing crystallization in the material, if there is any. Such protocols has been successfully used to study the thermal crystallization of NR [7].

The weight crystallinity ratio X_C , in the matrix (without fillers), can be deduced from heating scans using the relationship $X_c = \frac{\Delta H_f}{(1-y)*\Delta H_f^0}$, where y is the mass fraction of fillers, ΔH_f is the specific melting enthalpy of the sample and ΔH_f^0 is the specific melting enthalpy for perfect polyethylene crystal, since the assumption is that only polyethylene segments can crystallize. It is taken as 290J/g [8,9].

1.1 *Swelling: estimation of crosslinking density*

Measurements of swelling of a crosslinked material in a good solvent is a useful technique to obtain the network active chain density (swelling ratio), the degree of crosslinking and the fraction of chains that do not belong to the elastomer network (soluble fraction). The degree of swelling depends on the affinity of the solvent and the polymer as well as the average length of polymer chains between the crosslinking nodes.

The solvent used for swelling is Xylene which is very suitable for EPDM elastomers[10]. *The protocol for swelling experiment is as follows: a sample (3-4 samples for repeatability) with initial weight M_i is introduced into xylene at ambient temperature and let for swelling until it reaches a swelling equilibrium, i.e. constant mass. After weighing of the swollen sample (mass M_s), it is dried in a chamber for 24hrs for the evaporation of the solvent. The partially dry sample is completely dried in a vacuum chamber at 60°C for another 24hrs, to obtain the final dry mass M_d.*

Figure 5: Swelling ratio for the model material F1 as a function of time (days)

The swelling ratio Q and soluble fraction F_s are obtained using:

$$Q = \frac{1}{V_2} = 1 + \frac{\rho_{polymer}}{\rho_{xylene}} . \frac{(M_s - M_d)}{M_d} \quad (1)$$

$$F_s = 100 . \frac{M_i - M_d}{M_i} \quad (2)$$

Where, $\rho_{polymer}$, ρ_{xylene} are the densities of the elastomer and the solvent respectively ($\rho_{polymer}$ = 0.86, ρ_{xylene} = 0.73). When the elastomer is reinforced with carbon black, it introduces a phase in the materials which cannot be swelled. If we consider that the interaction

between the filler and elastomer is perfect, the swelling ratio of the elastomer matrix is given by

$$Q_p = \frac{Q_{composite} - \phi}{1 - \phi} \quad (3)$$

Where ϕ corresponds to the volume fraction of carbon black in the materials and $Q_{composite}$ is the swelling ratio of the material.

One can determine the number of elastically effective crosslinks from equilibrium swelling data by use of the equation of Flory and Rehner,

$$\nu_{swelling} = -\frac{[ln(1-V_2)+V_2+\chi*V_2^2]}{V_1*(V_2^{1/3}-0.5*V_2)} \quad (4)$$

Where $\nu_{swelling}$ is the number of active network chain segments expressed in mols.cm^{-3}, V_1 is the molar volume of the solvent (123.4 cm^3 / mol for xylene), χ is elastomer-solvent interaction parameter[10] *($\chi_{Xylene-EPDM}$ = 0.49) and V_2 is the volume fraction of elastomer network in the swollen material given by equation 1.*

2.3 Tensile test

Tensile tests are conducted on an MTS 1/ME machine equipped with 100N load cell. The nominal stress is defined as $\sigma_n = F/S_0$, where F is the force and S_0 is the initial section of the sample. In most cases, true stress is used, which is defined as $\sigma(t) = F(t)/S(t)$ where S(t) is the current section area of the sample. In elastomeric materials whose deformation is isochoric, the true stress can be defined as $\sigma_n(1+\epsilon_n)$, where σ_n is the nominal stress and ϵ_n is the nominal strain defined as $\epsilon_n = \frac{\Delta L}{L_0}$ (L is the nominal length and ΔL is the displacement). The nominal strain is obtained using digital image correlation. The strain rate is around 0.002 s^{-1}. The sample specimen dimension used for this experiment is shown in Figure 1. The notch in the Single Edged Notch Tensile (SENT) sample is made by a sharp razor. The notch length is varied between 0.5-2.5mm. The thickness of the sample is around 1.5mm.

2.3.1 Strain energy release rate

For a tensile strip geometry, the G associated with the propagation of a crack of length c is 2kW(λ)c, k being a parameter depending smoothly on λ [11,12]. W(λ) is the strain energy density that is calculated from the area under the curve of the stress-strain plot.

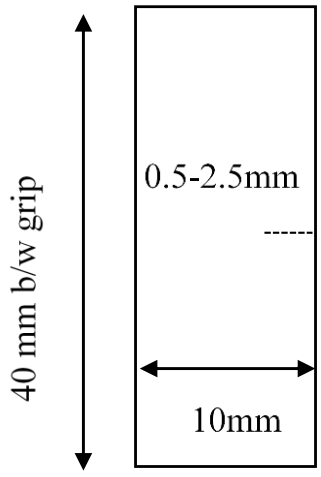

Figure 1: SENT specimen

3. RESULTS

3.1 Crosslinking density and fraction soluble

The estimated crosslinking density for I_oil and I_no_oil materials is 1.9×10^{-4} mol.cm^{-3} and 3.7×10^{-4} mol.cm^{-3} respectively. They have different crosslinking densities because the two materials are crosslinked using 2 system of vulcanization and because one material is crosslinked in presence of oil, which swell the polymer chains, thus reducing the entagelement density. The soluble fraction for I_oil and I_no_oil after 45 days of swelling is 17.6% and 1.9% respectively. The introduced mass fraction of oil in I_oil is around 15.9%. The difference may be due to the extraction of polymer chains that does not take part in crosslinking, and to residual products of the vulcanization recipe.

3.2 DSC analysis

The Table 2 shows the Tg of the materials before and after swelling tests, along with the Tg of the oil, EPDM elastomer, and EPDM elastomer with oil. The oil is miscible in the matrix, since the difference in the Tg between the material with and without oil can be explained based on on flory-fox equation ($\frac{1}{T_g} = \frac{w_{epdm}}{T_{g1}} + \frac{w_{oil}}{T_{g2}}$, For EPDM with oil: $w_{epdm}$and w_{oil} is 0.728 and 0.272, Tg is -56.5). These Tg values are confirmed by DSC (cf Figure 2)

Table 2: Tg for various materials

Materials Name	Tg (°C)
I_oil	-55.9
I_no_oil	-52.4
I_oil_after swelling	-51.9
I_no_oil_ after swelling	-52.7
Oil	-68.3
EPDM pure	-51.7
EPDM with oil	-56.1

Figure 3 shows that the material I_oil seems to have a slightly higher tendency for thermal crystallization than I_no oil (for which crystallization should be confirmed). If the material is kept 16hs at -20°C, X_c in I_oil can reach 0.22% (for I_no_oil 0.02% is measured which is in the error bar). When the % content of polyethylene (PE) is high (>65%)[10], EPDM is semi crystalline. The EPDM Keltan 4450 used here only contains 52% of PE in it, which implies it is an amorphous elastomer. Here, compared to a semi crystalline EPDM (X_c is around 10%)[8], the crystallinity ratio is negligible.

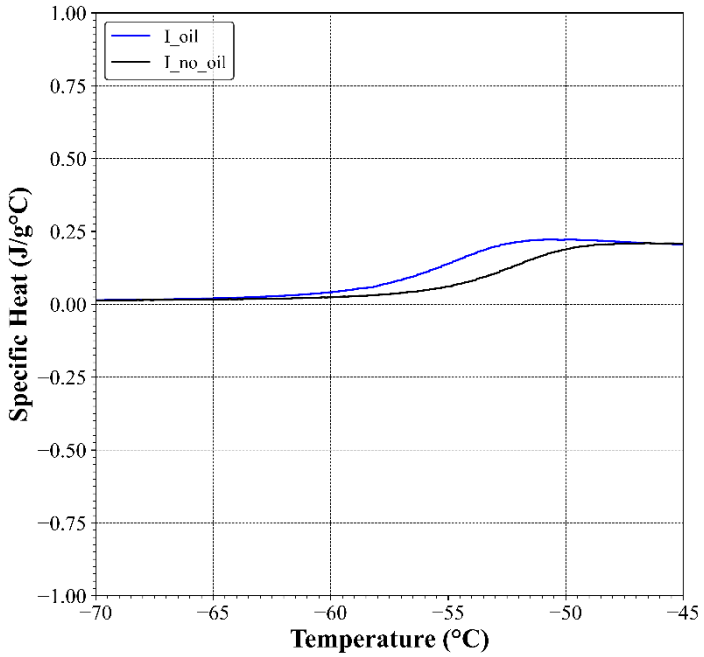

Figure 2: DSC curves for I_oil and I_no_oil

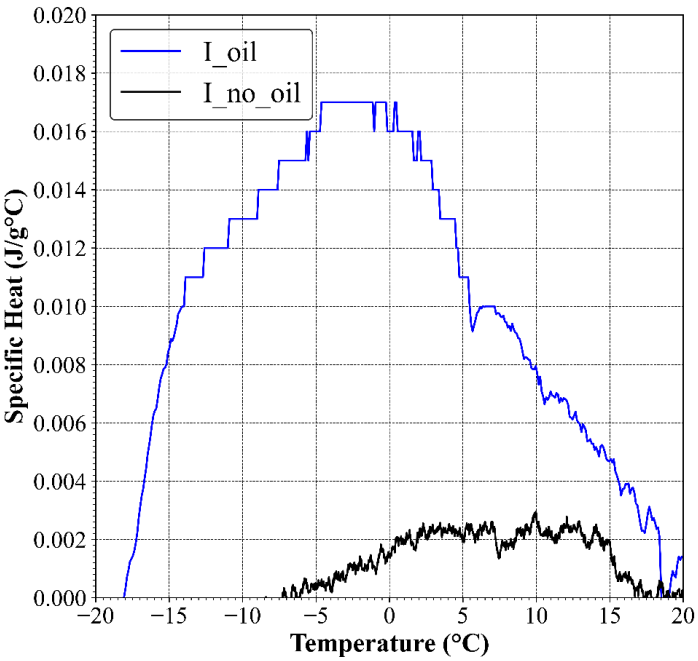

Figure 3: Difference in specific heat measured as function of Temperature when doing a ramp at 10°/min for samples maintained 0min, and 16h at -20°C(for I_oil) and 48h at -16°C (for I_no oil) at -20°C (for I_oil) and -16°C (for I_no oil) .

3.3 Mechanical properties

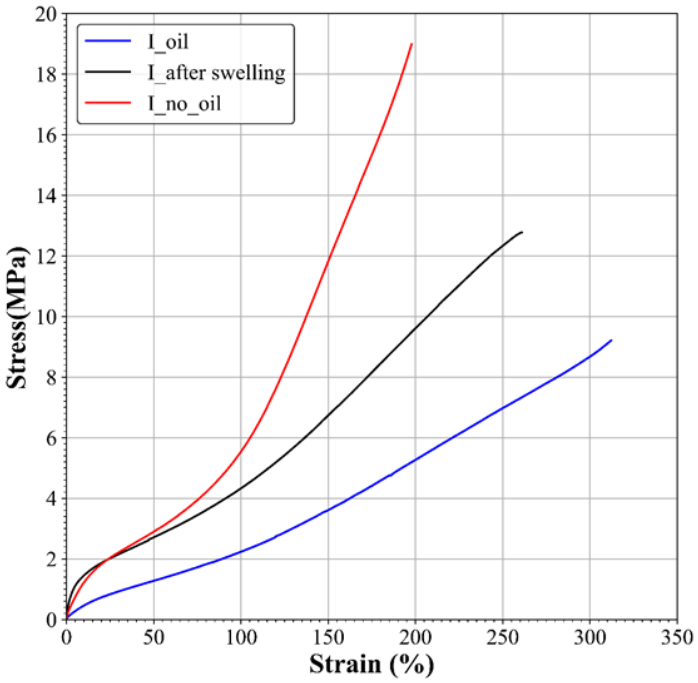

Figure 4: a) representative Stress-strain curve for I_oil, I_oil_after_swelling, I_no_oil using an unnotched tensile strip specimen.

Figure 4 shows the mechanical properties of the material I_oil before and after swelling. The strain at break is 283%±24% and 253%±12% for I_oil and for "I_oil after swelling" respectively. The difference in the stress-strain curve is coherent with the literature[13,14].

3.4 Crack propagation

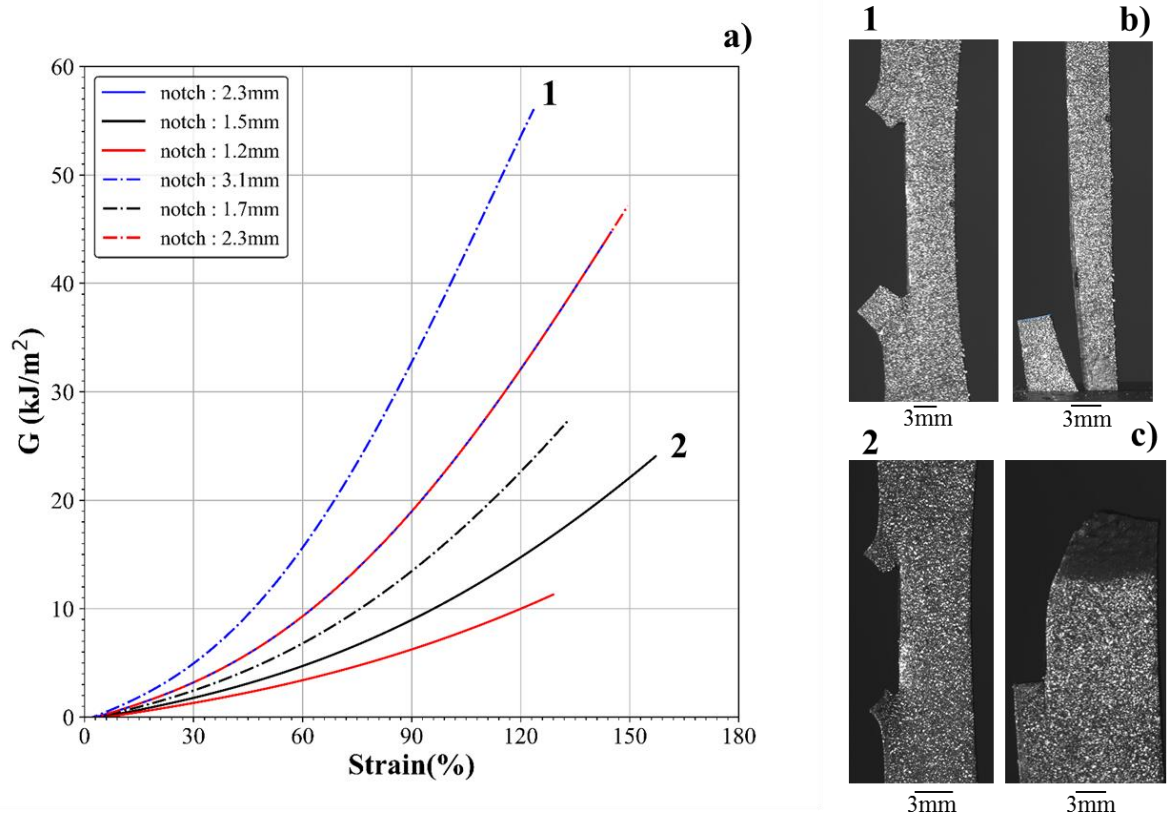

Figure 5: a) Stress-strain curve for I_oil using a SENT specimen. The notch length is mentioned in the legend. b) and c) corresponds to the crack rotating sideways during the test for the SENT sample with notch 3.1mm and 1.5mm respectively.

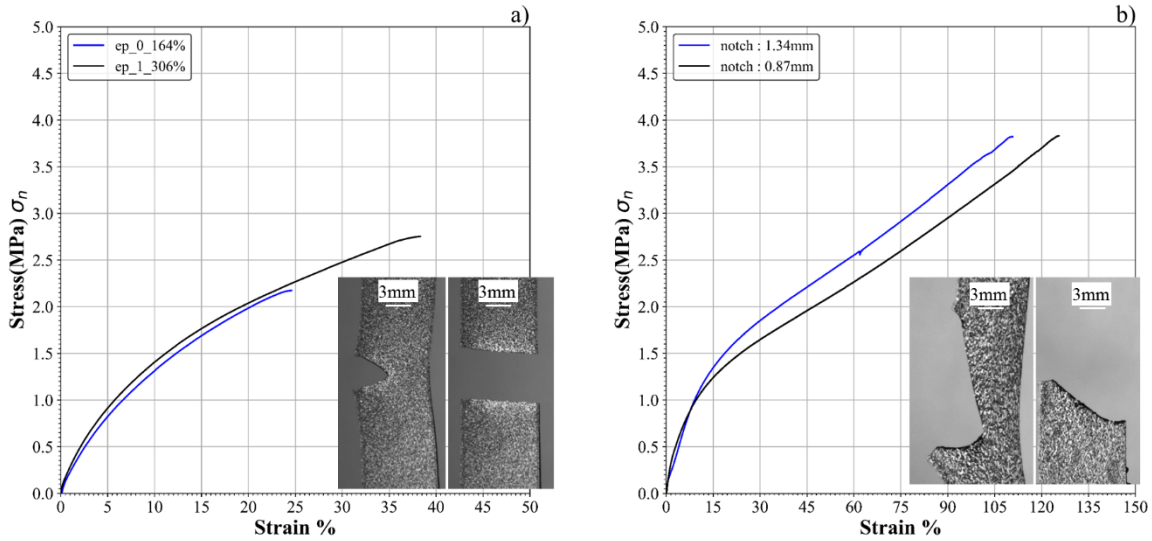

Figure 6: a) & b) Stress-strain curve of SENT sample with 2 notch sizes for I_ no_oil and for I_oil after swelling respectively. The inset picture shows the crack propagation path during and after the rupture

Figure 5 presents the results of crack propagation test using SENT samples with different notch sizes for the materials I_oil. The notched samples breaks at a strain range of 180-250%. (Note that the sample with notch size 3.1mm slips in the clamps at the end of the tensile tests). The images in Figure 5b and 45c are taken during the crack propagation test. These figures clearly show that crack rotates at 90° and continue propagating in the direction of the applied strain. The material is ruptured by crack reaching the head of the tensile specimen as shown in figure 5c. There is no catastrophic crack growth during the test. When the oil is removed partially from the material, there is still a certain degree of crack deviation. The crack rotates less than 50° during the propagation. When the material initially contains no oil at all, as in the case of the material I_no_oil, there is no crack rotation (Figure 6a). The crack propagates perpendicular to the applied stress direction.

We calculated G when the crack starts to propagate, for these material (from only two specimen for I_oil_after swelling and I_no_oil). It is found 4.35±1.7kJ/m^2, 4.6±0.3kJ/m^2, and 1.8±0.2 kJ/m^{2}for I_oil, I_oil after swelling and I_no_oil respectively. The value is lower for I_no oil compared to I_oil after swelling because the crack starts to propagate from the notch at a much lower strain (I_oil_after_swelling: 53% strain, I_no_oil: 22% strain) .

3.5 SEM analysis

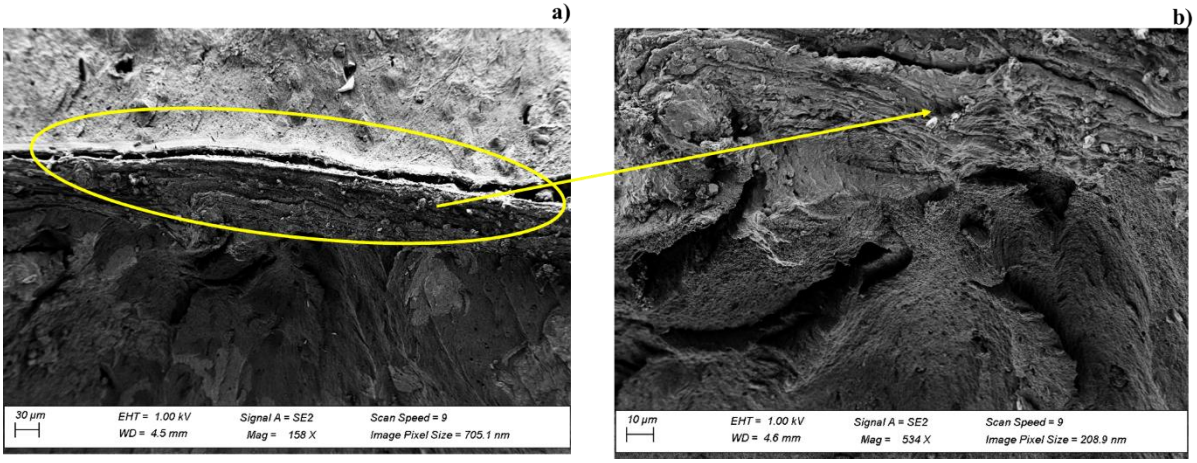

Figure 7: a) SEM image of the crack propagation from the crack notch, b) magnified image of the surface just after the crack notch

SEM images shows there are striations just at the beginning of the crack propagation for I_oil . The striations might be due to the breakage of ligaments formed at the crack tip, similar to the phenomena observed for NR during the crack propagation[15]. No comparison have been made with the other materials.

4. DISCUSSION

A crack deviation occurs at the crack tip when there is a presence of crystallization[1,3,16] or anisotropy resistance due to orientation of the polymer chains at the crack tip [4,17]. Oil can facilitate the chain mobility (as shown by the Tg decrease) and their orientation in the tensile direction. Studies have also shown oil can influence the crystallization kinetics (faster) by changing the polymer chain mobility like in the study by Qin et. al[18] in PLA matrix with essential oil. Oil facilitate crack rotation in our filled amorphous EPDM. Initial hypothesis is that this phenomena can be attributed to the increased chain mobility at the crack tip. Due to the high orientation of polymer chains in the presence of oil, there can be certain degree of

crystallization. However, this hypothesis is yet to be confirmed using microfocused WAXS measurement. Without oil, crack propagation direction has no deviation.

5. REFERENCES

[1] Chenal, J. M.; Gauthier, C.; Chazeau, L.; Guy, L.; Bomal, Y. Parameters governing strain induced crystallization in filled natural rubber *Polymer* **2007**, *48*, 6893, 10.1016/j.polymer.2007.09.023.

[2] Medalia, A. I. Effect of Carbon Black on Ultimate Proper.Pdf *Rubber Division, Americal Chemical Society* **1986**, *60*, 45.

[3] Gabrielle, B.; Guy, L.; Albouy, P. A.; Vanel, L.; Long, D. R.; Sotta, P. Effect of tear rotation on ultimate strength in reinforced natural rubber *Macromolecules* **2011**, *44*, 7006, 10.1021/ma2010926.

[4] Gherib, S.; Chazeau, L.; Pelletier, J. M.; Satha, H. Influence of the filler type on the rupture behavior of filled elastomers *Journal of Applied Polymer Science* **2010**, *118*, 435, 10.1002/app.31606.

[5] Gent, A. N.; Razzaghi-Kashani, M.; Hamed, G. R. Why do cracks turn sideways? *Rubber Chemistry and Technology* **2003**, *76*, 122, 10.5254/1.3547727.

[6] Lee, D. J.; Donovan, J. A. Microstructural Changes in the Crack Tip Region of Carbon-Black-Filled Natural Rubber. *Rubber Chem. Technol.* **1987**, *60*, 910–923.

[7] Grasland, F. Thesis,. Vieillissement du caoutchouc naturel parthermo-oxydation: Etudes de ses conséquences sur lacristallisation sous déformation, la fissuration et larupture, Université de Lyon, **2018**.

[8] Planes, E. Influence des charges sur l ' évolution des propriétés mécaniques des EPDM chargés lors de leur vieillissement par irradiation Remerciements **2008**, 244.

[9] Bandrup, J.; Immergut, E.; Grulke, E. *Polymer Handbook*; **1999**; 10.3159/TORREY-D-18-00011.1.

[10] André, D. A. Propriétés mécaniques et dégradation des élastomères EPDM chargés ATH **2014**, 237.

[11] Greensmith, H. W. Rupture of rubber. X. The change in stored energy on making a small cut in a test piece held in simple extension *Journal of Applied Polymer Science* **1963**, *7*, 993, 10.1002/app.1963.070070316.

[12] Lindley, P. B. Energy for crack growth in model rubber components *Change* **1972**, *132*.

[13] Loo, M. S.; Le Cam, J. B.; Andriyana, A.; Robin, E.; Afifi, A. M. Fatigue of swollen elastomers *International Journal of Fatigue* **2015**, *74*, 132, 10.1016/j.ijfatigue.2014.11.015.

[14] Andriyana, A.; Chai, A. B.; Verron, E.; Johan, M. R. Interaction between diffusion of palm biodiesel and large strain in rubber: Effect on stress-softening during cyclic loading *Mechanics Research Communications* **2012**, *43*, 80, 10.1016/j.mechrescom.2012.03.004.

[15] Le Cam, J. B.; Huneau, B.; Verron, E.; Gornet, L. Mechanism of fatigue crack growth in carbon black filled natural rubber *Macromolecules* **2004**, *37*, 5011, 10.1021/ma0495386.

[16] Lee, S.; Pharr, M. Sideways and stable crack propagation in a silicone elastomer *Proceedings of the National Academy of Sciences of the United States of America* **2019**, *116*, 9251, 10.1073/pnas.1820424116.

[17] Stacer, R. G.; Yanyo, L. C.; Kelley, F. N. Observations on the Tearing of Elastomers. *Rubber Chem. Technol.* **1985**, *58*, 421–435.

[18] Qin, Y.; Li, W.; Liu, D.; Yuan, M.; Li, L. Development of active packaging film made from poly (lactic acid) incorporated essential oil *Progress in Organic Coatings* **2017**, *103*, 76, 10.1016/j.porgcoat.2016.10.017.

FOLIO ADMINISTRATIF

THESE DE L'UNIVERSITE DE LYON OPEREE AU SEIN DE L'INSA LYON

NOM : Kallungal Abdul Jaleel — DATE de SOUTENANCE : 02/03/2022

Prénoms : Muhamed Jesbeer

TITRE: X-ray Tomography study on the impact of microstructural defects on the rupture and fatigue properties of a filled elastomer

NATURE : Doctorat — Numéro d'ordre : 2022LYSEI015

Ecole doctorale : Matériaux de Lyon

Spécialité : Génie des matériaux : microstructure, comportement mécanique

RESUME : La dispersion des charges dans les élastomères reste un problème pour l'industrie : la plupart des produits industriels contiennent des défauts de type agglomérats de charges, qui peuvent provoquer leur défaillance prématurée. Récemment, les industriels ont commencé à explorer des techniques non destructives telles que la tomographie à rayons X pour caractériser les défauts du matériau. Cependant, une méthodologie appropriée doit encore être développée. En outre, des travaux supplémentaires sont nécessaires pour établir un lien entre les caractéristiques des défauts et la durabilité des matériaux. Ainsi, en utilisant largement la tomographie à rayons X, nous avons développé un nouveau protocole pour identifier les classes morphologiques distinctes d'agglomérats de noir de carbone dans les matériaux élastomères et pour mieux comprendre l'influence des paramètres du procédé de mise en œuvre sur leur morphologie. Ensuite, en utilisant une combinaison de tests de traction/fatigue in-situ/ex-situ, nous avons étudié des matériaux avec différentes concentrations d'agglomérats de noir de carbone. Nous avons montré que les agglomérats sont les seuls précurseurs de l'initiation des fissures et que la décohésion observée aux pôles d'inclusions d'oxyde métallique n'initie pas de fissure. De plus, les propriétés de rupture (en traction) sont indépendantes de la concentration en agglomérats (dans la gamme étudiée). Des cavités s'initient à l'intérieur des agglomérats de noir, et se développent pour devenir des fractures internes. Pour observer l'initiation d'une fissure, l'agglomérat fracturé doit être dans ou près d'un champ de contrainte favorable et avoir une taille critique supérieure à 40µm. La structure et l'excentricité ne sont pas aussi critiques que la taille. De plus, la transition d'une fracture interne dans un agglomérat à une fissure dans le matériau semble retardée si l'agglomérat subit des fractures multiples. Comme attendu, le mécanisme d'initiation des fissures en fatigue est similaire. En outre, l'ajout d'huile dans la formulation modifie la morphologie des agglomérats de noir de carbone (plus gros, moins structurés et plus sphériques), mais ne change pas le mécanisme d'initiation des fissures, même si un plus grand nombre de cycles de fatigue est nécessaire pour fracturer les agglomérats. Enfin, la fracturation interne des agglomérats au voisinage de la pointe de fissure est un mécanisme dissipatif qui réduit la vitesse de propagation de la fissure pour un taux de restitution d'énergie (G) macroscopique donné, ce qui a un impact significatif à G élevé. La déviation/arrêt des fissures par les agglomérats (fracturés ou non) augmente également l'énergie nécessaire à la rupture du matériau.

MOTS-CLÉS : Elastomer, carbon black agglomerates, defects, crack propagation, crack initiation, X-ray Tomography

Laboratoire (s) de recherche : MATEIS, PVMH, INSA de Lyon and LRCCP, Vitry-sur-Seine
Directeur : Eric Maire

Directeur de thèse: Laurent CHAZEAU

Président de jury : Yann Marco

Composition du jury : Sylvie Castagnet, Edith Peuvrel-Disdier, Yann Marco, Fabien Wilde, Laurent Chazeau, Jean-Marc Chenal, Claire Barrès,